Interactions and collisions of cold molecules: lithium + lithium dimer

Marko Tomislav Cvitaš

Interactions and Collisions of Cold Molecules: Lithium + Lithium Dimer

Marko Tomislav Cvitaš

Ustinov College

Department of Chemistry

University of Durham

2004

A thesis submitted in partial fulfillment of the requirements for the degree of Ph.D.

Interactions and Collisions of Cold Molecules: Lithium + Lithium Dimer

Marko Tomislav Cvitaš

Abstract

There is at present great interest in the properties of ultracold molecules. Molecules are created in traps in excited rovibrational states and any vibrational relaxation results in the trap loss. This thesis provides a theoretical study of interactions and collisions in the spin-polarized lithium + lithium dimer system at ultralow energies.

Potential energy surface of the electronic quartet ground state of lithium trimer is generated *ab initio* using the CCSD(T) method and represented by an IMLS/Shepard fit. Long-range nonadditive interactions are modelled using a symmetric global form with coefficients taken from a fit to the atom-molecule dispersion coefficients.

The surface allows barrierless atom-exchange reactions. It has a global minimum of ≈ 4000 cm^{-1} at equilateral geometries with $r_e = 3.1$ Å. The nonadditive interactions are very strong near equilibrium. They increase the well depth by a factor of 4 and reduce the interatomic distance by ≈ 1 Å. Another surface of A' symmetry in C_s meets the ground state surface at linear geometries at short range. Part of the seam, near $D_{\infty h}$ geometries, is in an energetically accessible region for cold collisions. Inside the seam, the lowest A' surface correlates with $^4\Pi$ rather than $^4\Sigma$ state.

Inelastic and reactive collisions are investigated using a quantum mechanical coupled channel method in hyperspherical coordinates. Bosonic and fermionic systems in the spin-stretched states are considered. The inelastic rate coefficients from the rovibrationally excited states of dimer at ultralow collision energies are large, often above 10^{-10} cm^{3}s^{-1}. The elastic cross sections are ≈ 3 orders of magnitude lower at 1 nK. Atom-molecule mixtures, at the densities found in Bose-Einstein condensates of alkali metal atoms that were recently produced, would last only a fraction of a second. Classical Langevin model describes semi-quantitatively the energy dependence of inelastic cross sections above ≈ 50 mK. No systematic differences between the bosonic and fermionic systems were found. Sensitivity of the results on potential was investigated.

Reactions in isotopic mixtures of lithium may be exothermic even from the molecular ground state. The reactive rate coefficients are $1-2$ orders of magnitude smaller than those in systems involving an initially vibrationally excited dimer.

Declaration

The material contained within this thesis has not previously been submitted for a degree at the University of Durham or any other university. The research reported within this thesis has been conducted by the author unless indicated otherwise.

Statement of copyright

Acknowledgements

I would like to thank my supervisor Jeremy Hutson for guidance and advice. I am grateful to Pavel Soldán for daily discussions and help. I am also grateful to Jean-Michel Launay and Pascal Honvault for all the help and discussions on molecular collisions and to the JML group for their hospitality in Rennes.

I also wish to thank all my room-mates from the CG207 and other people working in the Chemistry Department in Durham who helped me in any way. I am grateful to the IT service for the support in computer matters.

I thank my family, Jelena and my friends from Durham and from Zagreb for support throughout my years in Durham.

Finally, I would like to extend my gratitude to the opportunity that has been given to me by the Durham Research Studentship and the ORS award from Universities UK toward my research.

Contents

List of Tables

List of Figures

Chapter 1

Introduction

1.1 Background

It was first recognized with the acceptance of the kinetic theory in 19th century that intermolecular collisions are the underlying mechanism for all rate phenomena involving gases and liquids. In kinetic theories individual particle motions are replaced with average quantities based on statistics. In this way it was possible to give quantitative explanations for phenomena such as thermal conductivity, viscosity, diffusion and also rates of chemical change. Understanding the dynamics of collisions at molecular level is the key to interpretation of macroscopic phenomena.

The development of experimental techniques in the 20th century made it possible to study elementary collisional processes in laboratory. Detailed knowledge on elementary chemical reactions may be obtained using the techniques of crossed molecular beams and laser spectroscopy. In a molecular beam experiment, gas at around 1 bar pressure is expanded into a vacuum through a nozzle of aperture of around 50 μm. Under such conditions, almost all the thermal energy is converted into translational motion of molecules, while the relative velocities of molecules in the beam are low, corresponding to temperatures $1 - 10$ K. In experiments with molecular beams, one can control the energies of reagents, investigate the dependence of reactivity on molecular orientation, explore the nature of reaction intermediates and their subsequent decay, and identify reaction mechanisms [1]. Recent reviews are in Ref. 2, 3.

Theoretical treatment of collisions of atoms and molecules usually relies on the quantum mechanical calculation of interaction potential today (earlier calculations used empirical potentials). The motion of nuclei of a system of atoms and molecules is governed by the energetics of their electron clouds. Exact quantum mechanical treatment of nuclear motion on *ab initio* potential energy surface has recently demonstrated a remarkable agreement between theory and experiment for the simplest triatomic reaction, $H + H_2$, [4]. Reaction mechanisms have been explored in many small systems and results compared with experiment. A recent review is in Ref. 5. With the development of modern computers, it has also become possible to treat more complex systems accurately. Reactions involving metastable C, N, O, and S atoms with hydrogen molecules proceed over a deep well via formation of a collision complex [6]. Such reactions have also been well described by a recently-

developed statistical model [7]. The study of these systems finds its application in astrophysical, atmospheric, and combustion chemistry. Reactions were studied at energies of around 1000 K and above.

In the past decade, advances in the cooling and trapping of neutral atoms and molecules opened the field of research on matter at ultralow temperatures. It is possible now to slow down the translational motion of atoms to temperatures below 1 μK. At such ultracold temperatures the effects of quantum statistics become important and atoms can undergo a phase transition into a degenerate quantum gas. Most of the experimental efforts in this field have so far concentrated on alkali atoms. Applications of this research include high-resolution spectroscopy, exploration of fundamental symmetries in nature, new many-body physics [8], and novel possibilities in manipulation of quantum information [9].

Collisions play an important role in cooling processes and properties of matter at low temperatures. Atoms involved in such collisions interact for a long time with one another and collisions depend on fine details of potential energy surface. A lot of work has concentrated on atomic collisions in presence of external electric, magnetic, and radiation fields [10]. Formation of molecules at ultracold temperatures offers new possibilities including exploring chemical reactivity in this new regime of ultracold temperatures [11]. The topic of this thesis is to extend the knowledge about atom-diatom exchange collisions in the new regime of ultracold collision energies in connection with the on-going efforts to create stable molecules at rest.

1.2 Cold atoms and molecules

Before defining the objectives of our research and the organization of the material in this thesis, we briefly describe several cooling methods and some experimental achievements in creation of cold atoms and molecules. Research activity in this field has been so extensive that it is impossible to review all ideas and realizations here. Instead, we bring up only the major achievements that stimulated our research in the past years. Interactions and collisions prove to be of central importance in creating and understanding cold matter.

The quest for reaching ever lower temperatures culminated in the creation of a Bose-Einstein condensate (BEC) of ^{87}Rb atoms by Cornell et al. in 1995 [12]

and soon afterwards in ^{7}Li by Hulet et al. [13] and in ^{23}Na by Ketterle et al. [14]. BEC is a macroscopic quantum state where all atoms are in the ground level of the trapping potential. Transition to BEC occurs at a critical temperature, typically below 1 μK, where de Broglie wavelength reaches the interatomic separations and indistinguishability of particles becomes important as a consequence of quantum statistics. Formation of BEC is possible for bosons, which are entities of integer composite spin (the sum of nuclear and electronic spin).

Creation of BEC is achieved by cooling a gas of atoms below the critical temperature. Various cooling and trapping methods have been developed [9]. In Cornell's experiment atoms are stored in a combination of magnetic and radiation fields called a magneto-optical trap (MOT). Radiation pressure arises from the transfer of photon momentum to atoms and a weak inhomogeneous magnetic field in a MOT serves as a spatially dependent control of this force. The method of laser cooling (and laser sub-Doppler and side-band cooling [9]) is used to cool atoms to the kinetic energies corresponding to a few times the one-photon recoil momentum ($\approx$ 10 μK). Atoms are bombarded with photons tuned just below the atomic resonance frequency. In this way, the photon momentum is transferred selectively to the fast-moving atoms, that will see the light Doppler shifted towards the resonance. Photons are then spontaneously reemitted in random directions. Condensates were first achieved in alkali atoms because their relatively simple energy level structure allows repeated absorption and emission in cooling cycles. At the next stage, atoms are stored in a magnetic bottle and evaporative cooling is used to cool atoms to BEC temperatures. The principle is to change the spin state of the most energetic atoms with a radio-frequency pulse, which expels them from the magnetic trap. The remaining atoms rethermalize through elastic collisions thereby lowering the temperature.

Evaporative cooling technique has also been used to evaporatively cool ^{40}K to ultracold temperatures to create a degenerate Fermi gas [15]. In a binary collision of two identical fermions, s-wave collisions are prohibited by symmetry. Thermalisation in the cooling process was achieved by simultaneously trapping of two different spin states. The other component was selectively removed at the end.

It is important that a sufficient number of atoms is conserved in the cooling process. Typical magnetic trap depths are $\approx$ 1 K and below, so that various inelastic processes may contribute to loss of atoms from trap or heating. Inelasticity in atom-

atom collisions and in the interaction of system with light has been extensively studied [10]. The dominant trap-loss mechanism in BEC is the loss by three-body recombination. Two atoms form a molecule giving up its binding energy to the relative motion of molecule and the third atom, which results in the ejection from condensate. This process has also been studied, e.g. in Ref. 16.

Interatomic interactions play an important role on the road to condensation and influence the properties of BEC. In a dilute gas where the range of interactions is much smaller than the interatomic separations, interactions may be modelled by an effective contact potential described in terms of scattering length. A number of mean-field and Hartree-Fock approaches have been developed [17] that use the mean-field interaction term proportional to the scattering length and explain some of the observed properties of condensates such as, for example, their stability and shape.

Creating cold molecules by laser cooling is not possible because the spontaneous emission that is crucial for cooling populates a range of rovibrational levels of the molecular ground state destroying the cycle. We describe some of alternative cooling methods designed for molecules below. Cold molecule formation has been reviewed in Ref. 18.

One way to obtain cold molecules is to create them from cold atoms. Creating a molecule from two colliding atoms by a laser-driven free-bound transition is called photoassociation [19, 20]. Heinzen and co-workers used stimulated Raman transition to photoassociate atoms in the BEC of rubidium [21]. The atom pair is electronically excited and brought back in a bound state on the electronic ground surface. Molecules produced in this way are formed in a single rovibrational state. Photon recoil is minimized by placing lasers in an arrangement in which the two photon momenta cancel. The transition linewidth is very narrow because the kinetic energy spread of the colliding atoms is very low. This allows a very precise measurement of the binding energy of molecule. An example is determination of the $v = 10$ level in the triplet potential of lithium dimer [22]. One of the future goals is to produce stable ultracold molecules by photoassociation. In Heinzen's experiment inelastic atom-molecule collisions destroyed the condensate and the first measurement of the inelastic rate coefficient of atom-molecule collisions in a condensate provided the upper limit $K_{\text{inel}} < 8 \cdot 10^{-11}$ cm^{3}s^{-1}. It has been proposed

to create molecules in an optical lattice (Mott insulator) [23] to prevent destructive atom-molecule collisions. Photoassociation was recently employed to produce first ultracold heteronuclear molecules $^{6}Li^{7}Li$ [24], $^{85}Rb^{39}K$ [25], $^{85}Rb^{133}Cs$ [26], and $^{23}Na^{133}Cs$ [27].

Magnetic fields can be used to change the scattering length and properties of condensate. Wieman et al. [28] managed to tune the molecular and atomic states in a resonance and create a quantum superposition of atomic and molecular states. Later, Grimm et al. [29] managed to create a pure molecular gas by sweeping with a magnetic field through a Feshbach resonance. Starting from the degenerate Fermi gas of ^{6}Li, Grimm et al. created Li_2 molecules in a weakly bound level by recombination of atoms. Scattering length was tuned with a magnetic field to a large value, which ensures stability against collisional decay in fermionic molecules [30]. Molecules were cooled evaporatively to create the first molecular BEC [31]. Simultaneously, BECs have been created in $^{6}Li_2$ by Ketterle et al. [32] and in $^{40}K_2$ by Jin et al. [33]. All of them used fermionic atoms to build the molecules, since the molecules made of weakly bound bosonic atoms quickly undergo inelastic transitions into deeply bound states [29].

Another way to produce cold atoms and molecules has been developed by Doyle and co-workers [34]. An advantage of his scheme is that it applies to a wide range of species, because it uses a cooling mechanism independent of the electronic energy-level structure. The sample is vaporised by a laser in the presence of helium buffer gas. The density of the buffer gas must be such that thermalisation occurs before the species reaches the container wall where it would stick. This places a lower limit on the temperature which is around few hundred mK. Molecules produced in this way are translationally, vibrationally and rotationally cold. The whole process takes place in a magnetic trap so it is applicable only to paramagnetic species (while ground states of homonucelar diatomics are usually singlets). CaH molecule was cooled in such an experiment to 400 mK. Atom-molecule collisions with the helium buffer gas have been studied theoretically by Dalgarno and co-workers, e.g. in CO_2 [35, 36], and H_2 [37].

Another cooling technique, which has been developed by Meijer and co-workers, is deceleration of molecular beams using time-varying electric fields [8]. The underlying principle is that molecules in an inhomogenous electric field lose their kinetic

energy by converting it to Stark-shift energy and not regaining it fully when the field is switched off. Electrodes in the Stark decelerator are carefully arranged in a linear array about 35 cm long and as molecules go through, time-varying electric field effectively provides a travelling potential well that slowly decreases its velocity. Molecules usually go through $\approx 50 - 100$ electric field stages. The technique applies to polar molecules, e.g. CO and NH_3, and they can be slowed down to mK temperatures in this way.

Other cooling and trapping methods are also being developed [38]. For example, slowing of molecular beams by means of a rapidly rotating source was used to decelerate O_2 molecule to temperatures below 10 K [39]. Molecules at ≈ 400 mK have also been formed in collisions of Ar atoms with NO molecules in crossed molecular beams experiment by Chandler et al. [40], but have not yet been successfully isolated.

Theoretical work on atom-molecule collisions at ultracold temperatures started with the work of Balakrishnan et al. on vibrational quenching and threshold laws in $H + H_2$ [41, 42], and the complex scattering length and Feshbach resonances by Forrey et al. [43]. The content of this work is described briefly in Chapter 7 of this thesis. The first study of chemical reactivity at ultracold temperatures was also done by Balakrishnan et al. [11] on $F+H_2$. The work on atom-diatom collisions is reviewed further in Chapter 8 of the thesis, when discussing our results.

1.3 Objectives

The aim of this theoretical project is to generate a potential energy surface for three spin-polarized lithium atoms and study reactive and inelastic collisions at kinetic energies below 1 K. In particular, the dependence of the inelastic rate coefficients on the initial molecular state will be investigated to assess the possibility of trapping a triplet Li_2 molecule, motivated by recent experiments that produce cold internally excited molecules. Differences between the bosonic and fermionic systems will be explored as well as the reactivity of isotopic mixtures at ultralow energies.

1.4 Outline

The construction of the potential energy surface of lithium trimer is divided in four chapters. Chapter 2 deals with the qualitative aspects of potential. Conical intersections in the quartet potentials and the symmetry of states involved are discussed, as well as the physical origin of the interactions and comparison with other systems. Chapter 3 is involved with the technical details of obtaining accurate electronic energies of the quartet ground state potential. Chapter 4 deals with the fitting of the potential energy surface. Chapter 5 is devoted to the long-range dispersion interactions. Expressions for the nonadditive dispersion interaction for triatomic systems coming from different orders in perturbation theory and many-body expansions are rewritten in the atom-diatom limit. From here, asymptotic expression for the atom-diatom dispersion coefficients is derived and a symmetric form used to represent long-range interaction of lithium trimer.

The following two chapters are involved with the theory of scattering. Chapter 6 describes the theory of scattering in hyperspherical coordinates for atom-diatom reactions. In Chapter 7 we introduce concepts important in the low-energy scattering such as the Wigner laws, scattering length and resonances.

Reactive scattering calculations on the $Li + Li_2$ system at subkelvin collision energies are presented in Chapter 8. Inelastic cross sections for low-lying rovibrational states have been studied in the pure bosonic system, pure fermionic system, and isotopic mixtures. Results are compared with other atom-diatom systems studied so far. The sensitivity of cross sections in the Wigner regime to the nonadditive interactions is discussed in Chapter 9. The thesis ends with conclusions.

Chapter 2

Adiabatic quartet potential of lithium trimer: a qualitative study

2.1 Introduction

A prerequisite for doing dynamics calculations is knowledge of potential energy surface. We are interested in atom-diatom collisions of three spin-aligned lithium atoms in their ground state at low energies. The relevant surface for this study is that of an S atom and the triplet state of dimer that goes to an $S + S$ limit. The energetically accessible region of this potential for cold atom-molecule collisions is below the atomic $S + S + S$ dissociation limit. However, the topology of this surface proved to be more involved than if it was composed just of a single ground state Born-Oppenheimer quartet potential. Conical intersections and topology of the quartet potentials are therefore discussed in this chapter.

The first indication that a $^4\Pi$ state might be low compared to the $S + S + S$ dissociation limit comes from considering Li_2 triplet states. The first MCSCF calculations on low-lying states of Li_2 were done by Konowalow et al. [44]. A more accurate study was done later employing an open-shell coupled-cluster method [45]. Both studies show that the $^3\Sigma_u^+$ and $^3\Pi_u$ states of Li_2 intersect at ≈ 2.5 Å. In this chapter it is shown that this intersection leads to a seam that cuts into the ground state $^4\Sigma_u^+$ surface in all important region for the scattering on ground state quartet potential. The most recent *ab-initio* calculations on Li_2 triplet ground state were performed by Halls et al. [46].

Spectroscopic studies of the triplet states of Li_2 molecules have been carried out in the laboratories of W. C. Stwalley and R. W. Field. A review by Li and Lyyra [47] summarizes the experimental results. A set of low-lying vibrational levels were spectroscopically studied in $^7Li_2$ [48] and $^6Li_2$ [49] and an empirical (RKR) potential has been constructed from the data. A full potential including the long-range interactions was also constructed [50] and improved later [51]. The high-lying vibrational levels have been studied using photoassociation spectroscopy in $^6Li_2$ and $^7Li_2$ by Hulet and co-workers [52, 53]. Binding energy of the uppermost level in the triplet ground states of $^7Li_2$ [22] and $^6Li_2$ [54] have been determined experimentally and used with the RKR data to obtain the scattering lengths of $^7Li_2$, $^6Li_2$, and $^6Li^7Li$. Scattering lengths in the singlet ground state of homonucear lithium have been determined experimentally [55]. The most recent potential of the triplet ground state of Li_2 is by Colavecchia et al. [56]. It combines the RKR data with the data

from photoassociation experiments. Photoassociation of heteronuclear lithium dimer has been recently performed by Zimmermann et al. [24]. Experimental information on the potential of lithium dimer has been ever increasing.

Lithium trimer is a much less studied system. Only the doublet ground state surfaces had been studied experimentally and *ab initio* [57] before our work was undertaken. Recently, Colavecchia et al. published an *ab-initio* ground state quartet surface [56], but no conical intersection was reported and a topological study is still missing in the literature.

In the next section we overview methods for calculating *ab-initio* electronic energies in the Born-Oppenheimer approximation. These methods were used in *ab-initio* calculations in this and the following chapter. Our topological study begins with symmetry considerations. A brief discussion of the conditions under which electron states may intersect is given and applied to our system in the subsequent section. Special attention is given to the analysis of the quartet ground state surface. This is followed by a discussion on the importance of nonadditive interactions and electron-correlation effects in the bonding of the trimer.

2.2 Brief survey of electronic structure methods

2.2.1 Born-Oppenheimer approximation

The total Hamilton operator of a system of nuclei and N electrons in the centre of mass system of nuclei neglecting the relativistic effects [58] (and employing the usual atomic units) is

$$\mathbf{H}_{\mathrm{tot}} = \mathbf{T}_{\mathrm{n}} + \mathbf{H}_{\mathrm{e}} + \mathbf{H}_{\mathrm{mp}}, \tag{2.1}$$

$$\mathbf{H}_{\mathrm{e}} = \mathbf{T}_{\mathrm{e}} + \mathbf{V}_{\mathrm{ne}} + \mathbf{V}_{\mathrm{ee}} + \mathbf{V}_{\mathrm{nn}}, \tag{2.2}$$

$$\mathbf{H}_{\mathrm{mp}} = -\frac{1}{2M_{\mathrm{tot}}}\left(\sum_{i=1}^{N}\nabla_i\right)^2. \tag{2.3}$$

Here, $\mathbf{H}_{\mathrm{e}}$ is the electronic hamiltonian which depends on the position of nuclei, through nuclei-electron, $\mathbf{V}_{\mathrm{ne}}$, and nuclei-nuclei, $\mathbf{V}_{\mathrm{nn}}$, interactions. It does not depend on nuclear momenta. $\mathbf{H}_{\mathrm{mp}}$ is called the mass-polarization and it is introduced by our choice of coordinate system. In equation (2.3), M_{tot} is the total mass of nuclei and the sum is over all the electrons. $\mathbf{T}_{\mathrm{n,e}}$ are kinetic energy operators of nuclei and

electrons respectively and $\mathbf{V}_{\mathrm{ee}}$ represents all electron-electron interactions.

The solution of the time-independent Schrödinger equation may be expanded in the eigenstates of the electronic hamiltonian. The full wavefunction of the system is then

$$\Psi_{\mathrm{tot}}(\mathbf{r}, \mathbf{r}_{\mathrm{e}}) = \sum_{i=1}^{\infty} \Psi_{\mathrm{n}i}(\mathbf{r}) \Psi_i(\mathbf{r}, \mathbf{r}_{\mathrm{e}}), \tag{2.4}$$

where $\mathbf{r}$ and $\mathbf{r}_{\mathrm{e}}$ are vectors of nuclear and electronic coordinates, respectively, and Ψ_i are orthonormal basis functions defined by

$$\mathbf{H}_{\mathrm{e}}(\mathbf{r}, \mathbf{r}_{\mathrm{e}}) \Psi_i(\mathbf{r}, \mathbf{r}_{\mathrm{e}}) = E_i(\mathbf{r}) \Psi_i(\mathbf{r}, \mathbf{r}_{\mathrm{e}}). \tag{2.5}$$

When the ansatz in (2.4) is inserted in the full Schrödinger equation, we obtain a set of differential equations for coefficients Ψ_{ni}, ($\mathbf{T}_{\mathrm{n}} = \sum_a -1/2 M_a \nabla_a^2 \equiv \nabla_{\mathrm{n}}^2$, where a is nuclear index)

$$\begin{aligned} &\nabla_{\mathrm{n}}^2 \Psi_{\mathrm{n}j} + E_j \Psi_{\mathrm{n}j} + \sum_{i=1}^{\infty} \{ 2 \langle \Psi_j | \nabla_{\mathrm{n}} | \Psi_i \rangle (\nabla_{\mathrm{n}} \Psi_{\mathrm{n}i}) + \\ &\langle \Psi_j | \nabla_{\mathrm{n}}^2 | \Psi_i \rangle \Psi_{\mathrm{n}i} + \langle \Psi_j | \mathbf{H}_{\mathrm{mp}} | \Psi_i \rangle \Psi_{\mathrm{n}i} \} = E_{\mathrm{tot}} \Psi_{\mathrm{n}j}. \end{aligned} \tag{2.6}$$

The curly bracket in (2.6) contains terms that couple different electronic states. The first two are called first-order and second-order non-adiabatic couplings. In the Born-Oppenheimer approximation all terms in the curly brackets are neglected. The assumption is that other electronic states are energetically sufficiently far away that non-diagonal terms may be neglected. The diagonal terms are often neglected because they are expected to be smaller than E_j by a factor that is roughly equal to the ratio of electron and nuclear masses. In the Born-Oppenheimer approximation, nuclei move on a potential energy surface $E_j(\mathbf{r})$ which is determined by solving electronic hamiltonian for a set of nuclear geometries.

2.2.2 Electronic structure methods

There has been an enormous progress in last few decades in numerical methods for solving the electronic Schrödinger equation. Computer program packages with a set of built-in methods for obtaining electronic energies are commercially available today and have become a tool in chemistry for obtaining information on properties and potential energy landscapes of molecules. This section is intended to provide information on the electronic structure methods we employed for studying the potential

energy surface of lithium trimer in its quartet ground state. This survey relies on Ref. 59 and a recent review by Knowles et al. [60]. For more detailed information on the methods, the reader is referred to Ref. 61 and the references cited below in connection with the methods used in this work.

The usual starting point in reviews of electronic structure methods is Hartree-Fock theory. Hartree-Fock (HF) is a mean field theory in which each electron has its own wavefunction, an orbital, which obeys a one-particle Schrödinger equation. The effective hamiltonian contains an average field of all the other electrons in the system, where Coulomb and exchange interactions are included. The total electronic wavefunction is an antisymmetrized product of orbitals, a Slater determinant. The assumption lying behind HF theory is that the probability density for a given electron is independent of the other electrons (ignoring the Pauli principle here). However, in reality electrons interact with each other and their motion is correlated.

A well known example of the failure of HF to include electron correlation effects is the calculation of dissociation curves in singlet states of diatomic molecules (for example H_2). If the restriction is made that each spatial orbital contains two electrons, the so-called restricted Hartree-Fock (RHF) wavefunction will contain spurious ionic terms. This is because at long internuclear separations in the mean field approximation each electron has equal probability of being on both atoms. This does not exclude the probability of both of them being on the same atom. Allowing the spatial orbitals of electrons in different spin states be different solves this problem. The method is then called the unrestricted Hartree-Fock (UHF). However, the UHF wavefunction is not a spin eigenstate and this can cause a failure in more advanced methods that build on UHF wavefunction. The correlation energy that arises from long-range correlation effects is usually referred to as the non-dynamical correlation.

Another problem of HF theory is the inability of the HF wavefunction to describe the so-called interelectronic cusp. This is the Coulomb hole connected with the singularity of repulsive Coloumb potential between two electrons. The HF wavefunction overestimates the electron repulsion at short interelectronic separations. This problem is less pronounced in triplet diatomic states since the spatial wavefunction is then antisymmetric and the probability of finding two electrons close together is small. The short-range correlation effects are usually referred to as dynamical correlation.

The electron correlation energy is usually defined as the difference between the

exact energy and the one obtained from HF calculation.

There are many methods that go beyond HF and the choice of which to use depends on the purpose. The most commonly used methods for potential energy surfaces are configuration interaction (CI), many-body perturbation theory (MBPT), and coupled cluster (CC) methods.

In configuration interaction theories, the wavefunction is a mixture of several Slater determinants or configuration state functions (linear combinations of Slater determinants that are a spin eigenstate). The additional determinants, beyond HF, are constructed by replacing occupied molecular orbitals in the HF wavefunction by un-occupied ones. We may generate singly, doubly, triply, and other multiply excited determinants relative to HF in this way. The coefficients in the linear combination may be determined variationally. Because of the large number of configurations usually involved, the lowest eigenvalues of the hamiltonian matrix in the basis of the Slater determinants are found using iterative methods. The ground-state energy determined in this way is an upper bound to the exact energy and the procedure also allows approximate determination of electronically excited states. The dissociation problem is solved using CI theories, but the problem with the interelectronic cusp is only partially solved because convergence to the exact wavefunction is slow. Non-dynamical correlation in CI theories is recovered by a minimum CI expansion that qualitatively correctly describes correlation effects. The dynamical correlation is recovered by increasing the size of the CI expansion to include the remaining correlation energy.

MBPT methods have also been developed in many forms. An important class is Møller-Plesset perturbation theory. In second and third order (MP2, MP3), only doubly-excited determinants contribute to the energy calculations. In fourth order (MP4), singly-, doubly-, triply-, and quadruply-excited determinants contribute. To go beyond MP4 becomes prohibitively expensive. A drawback is also that the MP series is not guaranteed convergence.

In CC theories all the corrections to energy from a given type of excited determinants are included to infinite order in the MBPT sense. The coupled cluster wavefunction, obtained by including the single- and double-excitation operators in the cluster operator, will encompass all the contributions from singly and doubly excited determinants, and also some contributions from triply, quadruply, and other multi-

ply excited determinants. The CCSDT method, which includes the triple-excitation operator in the cluster operator, is too expensive at present, except for the smallest systems. The most important contribution missing in CCSD wavefunction comes from the so-called connected triples (simultaneous interaction of three electrons). Several variants that include the contribution of the triples in a perturbative way have been developed. The most widely used method is CCSD(T), where a term describing the coupling between singles and triples is also included. CCSD(T) scales as the seventh power with the number of basis functions used to describe the system in the large basis set limit, which is same as MP4, but gives more accurate results.

Size extensivity is important in obtaining accurate energies. Since the interaction energy is defined as the difference between the energy of the full molecule and of its constituents, it is important that both are treated with the same accuracy. Size extensivity means that the method scales properly with the size of the system. CI theories are not size extensive. They recover less and less of the correlation energy as the size of the system grows. Only in the limit of full CI, which includes all the excited determinants, do CI theories become size extensive. MP (but not all the MBPT theories) and CC theories are size extensive and that is an important advantage of them. There have been efforts to include additional terms in the CI theories that make them approximately size extensive. An example is Davidson's correction for quadruple excitations. Other examples include the averaged coupled-pair functional (ACPF) and coupled electron pair approximation (CEPA), which may be regarded as approximate versions of CCSD.

Electron correlation methods may be based either on a single-reference or on a multi-reference wavefunction. Single-reference methods build on an HF wavefunction and are suitable for systems where non-dynamical correlation effects are small. An important multi-reference method is the multi-configuration self-consistent field method (MCSCF). It can be considered as a CI method where not only the coefficients in front of determinants, but also the molecular orbitals making up the determinants are optimized. Orbital optimization does not recover a large part of correlation energy (it recovers the non-dynamical correlation energy). A more efficient way to recover the correlation is to keep the orbitals constant and include more excited configurations. Multi-reference configuration interaction (MRCI) is a CI performed on an MCSCF reference function (usually only single and double excitations

are included, i.e., CISD). With inclusion of more configurations, the method quickly becomes very computationally expensive.

Different approaches are often used in treating closed-shell and open-shell systems, the latter being usually more involved.

Many existing methods have been omitted in this brief survey. Some of the promising methods are currently being developed. An important one is symmetry-adapted perturbation theory (SAPT), which is close to reaching CCSD(T) accuracy, but still more expensive. It is currently developed for closed-shell systems only. Theories are being developed for treating excited states, such as the propagator methods, involving Green's functions theory. The R12 methods are being developed in which interelectronic distance is included explicitly in the trial wavefunctions. The advantage gained in this way is to achieve a faster convergence with the basis set. These methods presently give accurate results only when large basis sets are used. Density functional theory has enjoyed a lot of success in calculating molecular properties at a relatively low computational cost.

In this work, electronic structure calculations have been performed using the MOLPRO suite of *ab-initio* programs [62]. Natural atomic population analysis was performed using Gaussian [63] on wavefunctions at the HF level. For qualitative studies of ground and excited states we have used complete active space self consistent field, $[n, m]-$CASSCF as implemented in MOLPRO [64]. This is an MCSCF method which includes all excitations of n electrons within the active space formed of m molecular orbitals. A subsequent internally contracted MRCI [65] was employed if we wanted to recover more correlation energy. For accurate calculations of the quartet ground state of lithium trimer, the partially spin-restricted open-shell coupled cluster method, RCCSD(T) [66], was used. Results were compared to the spin-unrestricted UCCSD(T) method for a few arrangements of lithium atoms. The difference was ≈ 1 cm^{-1} at the global minimum of the quartet surface of lithium trimer.

All computational methods for electronic energies scale at least as M^4, where M is the size of the basis set used to expand the orbitals and represent the wavefunction. The quality and size of the basis set is therefore crucial for accurate calculations. This topic is considered in more detail in the next chapter.

2.3 Symmetry considerations

Electronic structure of lithium atom in the ground state consists of an electron pair in the $1s$ atomic orbital and an unpaired electron in the $2s$ orbital. The term symbol is ^2S.

When two identical S-state atoms approach, the symmetry of the system is $D_{\infty h}$. Molecular orbitals may be formed that span the irreducible representations of the symmetry group and in this way two diatomic electron terms are derived, $^1\Sigma_g^+$ and $^3\Sigma_u^+$. Atomic $2s$ orbitals may be combined in σ_g and σ_u molecular orbitals. The two terms result then from $(\sigma_g 2\mathrm{s})^2$ and $(\sigma_g 2\mathrm{s})(\sigma_u 2\mathrm{s})$ configurations, respectively.

When we bring up a third lithium atom, forming an isosceles triangle geometry with the pair, we label the symmetries of the individual terms as irreducible representations of the C_{2v} group. Placing the pair on y axis, the diatomic states of $^1\Sigma_g^+$ and $^3\Sigma_u^+$ symmetry in the group $D_{\infty h}$, become of $^1A_1$ and $^3B_2$ symmetry in C_{2v}. Atomic state is of $^2A_1$ symmetry in C_{2v}. Combining the multiplicities of atomic state with that of the pair, we obtain $^2A_1$, $^2B_2$, and $^4B_2$ terms from three ground state lithium atoms at C_{2v} geometries. When the three atoms form an equilateral triangle, the doublet states combine into a $^2E'$ degenerate representation of the D_{3h} group and the quartet state becomes $^4A_2'$, which is a spin symmetric and spatially antisymmetric state. Both states span A' irreducible representations in the C_s group. The most stable configurations of the quartet state are of D_{3h} symmetry.

The molecular orbitals of lithium trimer formed from the s and p atomic orbitals and their corresponding symmetry species are given in Table 2.1. Lithium atoms are placed in the yz plane. For D_{3h} configurations of lithium trimer, we refer to labels in Figure 2.1 a). Tangential and radial $p_{t,r}$ orbitals are formed from linear combinations of p_y and p_z orbitals. Two linear combinations of either $p_{t,r,x}$ or s orbitals of form $2p_1 - p_2 - p_3$ and $p_2 - p_3$, form an orthogonal basis for E representations, and $p_1 + p_2 + p_3$ for A representations. When we move the atom along the z axis, we produce C_{2v} configurations. The degeneracy of e orbitals is removed, $e' = a_1 + b_2$ and $e'' = a_2 + b_1$. Inserting the atom on z axis between the two on the y axis brings the system to $D_{\infty h}$ geometries. For the purpose of assigning the symmetry labels to the orbitals we relabel the axes in the conventional way as in Figure 2.1 b), although the results in Table 2.1 refer to the Figure 2.1 a) case. Now a_1 and b_1 orbitals consisting

of atomic p orbitals become degenerate forming π_u molecular orbitals. Similarly, $\pi_g = a_2 + b_2$. We also give the symmetry labels in Table 2.1 for orbitals in the D_{2h} and the C_{2v} group in which the principal axis is taken to be along the molecule in its linear configurations. They are useful for specification of orbital symmetries of a molecule in linear configurations, $D_{\infty h}$ and $C_{\infty v}$, in input to the computer package MOLPRO for *ab-initio* calculations, since MOLPRO works with finite groups only. C_s configurations describe the rest of the arrangements needed to describe the whole reactive Li_3 potential energy surface.

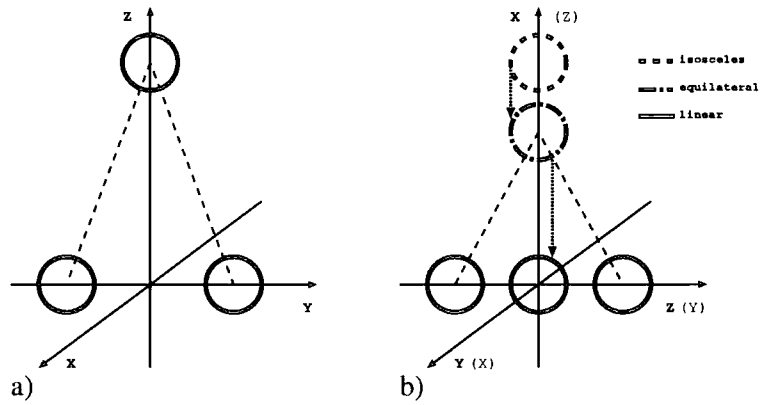

Figure 2.1: Geometrical arrangements of three lithium atoms: a) C_{2v} geometry, and b) $D_{\infty h}$, with the corresponding axis labels.

orbitals	D_{3h}	C_{2v}	$D_{\infty h}$	D_{2h}	C_{2v} (z)	C_s (σ_{yz})
	a_1'	a_1	σ_g	a_g	a_1	a'
s	e'	b_2	σ_u	b_{1u}	a_1	a'
		a_1	σ_g	a_g	a_1	a'
	(a_2'', a_1')	(b_1, a_1)	π_u	(b_{2u}, b_{3u})	(b_2, b_1)	(a'', a')
$(p_x, p_{z\,(\mathrm{or}\,r)})$	(e'', e')	(a_2, b_2)	π_g	(b_{3g}, b_{2g})	(b_2, b_1)	(a'', a')
		(b_1, a_1)	π_u	(b_{2u}, b_{3u})	(b_2, b_1)	(a'', a')
	e'	b_2	σ_u	b_{1u}	a_1	a'
$p_{y\,(\mathrm{or}\,t)}$		a_1	σ_g	a_g	a_1	a'
	a_2'	b_2	σ_u	b_{1u}	a_1	a'

Table 2.1: Symmetry species of molecular orbitals arising from $1s$, $2s$ and $2p$ atomic orbitals of three lithium atoms, placed in the yz plane, in different point groups.

The symmetry assignments we have just given are important to understand the topology of lithium surface.

2.4 Intersection of electronic states

Electronic states as functions of interatomic separations can cross. We analyze here the conditions under which this can happen.

The energies of adiabatic electronic states, E, are eigenfunctions of the hamiltonian. We assume that the Hilbert space is spanned by two orthogonal functions, for example a diabatic basis, see section 2.8. The adiabatic energies are obtained from a secular determinant which, for a two-state problem, reads

$$\begin{vmatrix} H_{11}(\mathbf{r}) - E & H_{12}(\mathbf{r}) \\ H_{12}(\mathbf{r}) & H_{22}(\mathbf{r}) - E \end{vmatrix} = 0, \tag{2.7}$$

where $H_{ij}(\mathbf{r})$ are matrix elements of the hamiltonian in the diabatic basis and $\mathbf{r}$ is a vector describing the nuclear configuration. From equation (2.7), we get two adiabatic energies in form

$$E_{1,2} = \frac{1}{2}(H_{11}(\mathbf{r}) + H_{22}(\mathbf{r})) \pm \frac{1}{2}\sqrt{(H_{11}(\mathbf{r}) - H_{22}(\mathbf{r}))^2 + 4\,|H_{12}(\mathbf{r})|^2}. \tag{2.8}$$

If the adiabatic energies are to become equal, the expression under the radical in (2.8) must vanish. The two conditions to be met are

$$H_{11}(\mathbf{r}) - H_{22}(\mathbf{r}) = 0, \quad \text{and} \quad H_{12}(\mathbf{r}) = 0. \tag{2.9}$$

If we consider a diatomic molecule, the only free parameter to satisfy the above conditions (2.9) is the interatomic distance. This means that two states of diatomic molecule cannot intersect (except accidentally), unless H_{12} vanishes identically because of symmetry. Thus only states that belong to different irreducible representations of the symmetry group of the hamiltonian of our system are allowed to cross.

In a polyatomic molecule consisting of N atoms, the number of free parameters is $N_f = 3N - 6$. Any two states may intersect. If the states are of different symmetry, one condition needs to be satisfied and intersection occurs in $N_f - 1$ dimensions. If the states are of same symmetry, both conditions in (2.9) need to be satisfied and intersection occurs in $N_f - 2$ dimensions.

For lithium trimer $N = 3$, so the number of parameters is $N_f = 3$, the three interatomic distances. In the space of all possible geometries, the surfaces of interest to us are of A' symmetry. Two of them can intersect along a line ($N_f - 2$ dimensions). For some particular symmetry arrangements, for example linear, belonging

to $C_{\infty v}$ group, or isosceles, belonging to C_{2v}, the matrix element H_{12} may vanish due to additional symmetry operations that now distinguish the two A' states. Then the two states belong to different irreducible representations in these higher-order groups. The condition to confine the geometrical arrangement into higher symmetry reduces also the number of free parameters, in our examples by one to $N_f = 2$. Intersection again occurs along a line at most ($N_f - 1$ dimensions), as it should, but the reduced number of free parameters facilitates the process of locating the position of intersection.

2.5 Topology of the quartet electronic states of Li_3

In this section, we compute electronic energies of quartet states of lithium trimer in certain high-symmetry arrangements to gain a qualitative picture of the potential energy surface. We are interested in the states that asymptotically tend to three S-state atoms or to two S-state and a P-state atom at long range.

In the atom-molecule limit of a quartet trimer potential, where one interatomic distance is small and the other two are large, the molecule will be in one of the triplet states that may be constructed from either the $S+S$ or $S+P$ atoms. We have calculated the triplet curves of Li_2 in a state-averaged [3,8]-CASSCF, where three valence electrons where correlated and all orbitals optimized. The active space comprised of all molecular orbitals made of atomic $2s$ and $2p$ orbitals of three atoms. Optimization was simultaneously performed on all states in Figure 2.2. Subsequently, an MRCI that included single and double excitations from the CASSCF wavefunction was performed. Electrons in atomic $1s$ orbitals were frozen. The basis set we employed was aug-cc-pVTZ [67]. At ≈ 2.7 Å, the $^3\Pi_u$ state of the dimer intersects the ground triplet state $^3\Sigma_u^+$ at ≈ 2800 cm^{-1}. At distances larger than ≈ 4.7 Å, $^3\Pi_u$ crosses the $^3\Sigma_g$ state and the order of the four states correlating with the atomic $S + P$ limit does not change on longer distances anymore. The ground triplet state has small amount of bonding present. The ro-vibrational states of this potential energy curve will be the initial and final states in our dynamics investigations later.

In order to investigate the strong interaction region of lithium trimer, we performed calculations of electronic energies in C_{2v} configurations. We have plotted the dependence of electronic energies on the two equal distances at a fixed angle between

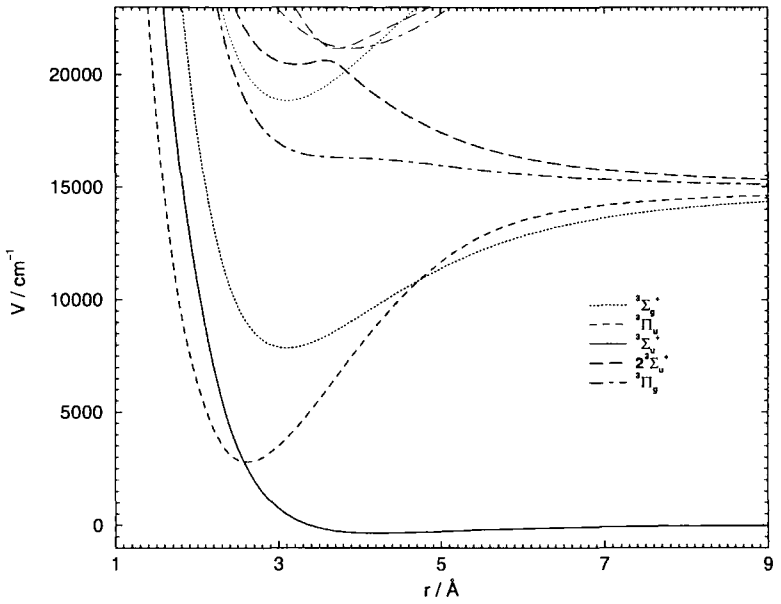

Figure 2.2: Triplet potential energy curves of Li_2 from atomic $S + S$ and $S + P$ dissociation limits.

them in Figure 2.3 for 180°, 170°, 150°, 120°, 90°, and 60°. The calculations on the trimer were performed using [3,24]-CASSCF in connection with an aug-cc-pVTZ basis set. Active space was constructed from all molecular orbitals made of atomic $2s$, $2p$, $3s$, and $3p$ orbitals. State-averaging included all states shown in the figures.

At 180°, states may be labelled by $D_{\infty h}$ irreducible representations. The $^4\Sigma_u^+$ state is derived from the atomic $S + S + S$ limit, while six different states correlate with the $S + S + P$ limit, $^4\Pi_g$, $^4\Sigma_g$, $^4\Pi_u$, $2^4\Sigma_u$, $2^4\Pi_g$, and $2^4\Sigma_g$. The last three of these interact strongly with states correlating with the asymptotic $S + P + P$ and $S + S + 2S$ limits, at short range (less than 6 Å in $D_{\infty h}$). The Π_g state crosses the ground state at $\approx$ 3 Å and a Σ_g state at $\approx$ 4.3 Å. The ground state may be described by the electron configuration in which three electrons sit in the three orbitals derived from atomic $2s$'s, σ_g, σ_u, and σ_g.

By bending the trimer to C_{2v} geometry at an angle slightly smaller than 180°, the degeneracy of the Π states is removed. The Π_g state breaks into $A_2 + B_2$ and Π_u into $A_1 + B_1$. The Σ_u and Σ_g states become B_2 and A_1, respectively. Now, the above mentioned $\Pi_g - \Sigma_g$ crossing remains because all three states involved are of different symmetry in C_{2v}. At the $\Pi_g - \Sigma_u$ crossing, when the geometry is slightly bent from 180°, the A_2 state does not change appreciably, but two B_2 states are not allowed to cross and an avoided-crossing of the two curves may be observed in Figure

2.3 extended over the angles 170° – 120°.

The B_1 state arising from the degenerate Π_u state at 180° interacts strongly with a state from an upper asymptotic limit at short range. As the angle decreases, this state moves downwards in energy and at 60°, this state forms a degenerate pair of E'' symmetry in D_{3h} group, with the A_2 state that was a Π_g at 180°. The B_2 state derived from Π_g at 180° forms a degenerate pair of E' symmetry with the A_1 state that was Σ_g at 180°. The two E symmetry states cross at $\approx$ 4.9 Å and are both intersected by the A_1' state that was an A_1 state arising from the degenerate Π_u at 180°. Intersections happen at $\approx$ 4.0 Å and 4.5 Å with E' and E'', respectively. It may be seen from Figure 2.4, where the curves are shown for the angle fixed at 70° and 55° on the two graphs, that the two states which are degenerate at 60° swap places in energetic order at short distances (in the range of their minima).

In C_{2v}, the ground state is a state of B_2 symmetry. There are three B_2 states, three A_1 states, two A_2 states, and a B_1 state, that correlate with the atomic $S+S+P$ limit. In the C_s group all the A_1 and B_2 states become of A' symmetry, while A_2 and B_1 become A''. This means that as soon as we deform the configuration out of C_{2v} symmetry the terms of the same symmetry in C_s that were crossing will avoided-cross. For example, the A_1 state that was a Σ_g at 180° crosses at a seam the state of B_2 symmetry derived from the degenerate Π_g at 180°. If one of the equal distances in C_{2v} is slightly increased, the two states will avoided-cross.

In the D_{3h} group, the ground state is a product $a_1' \times e' \times e' = a_1' + [a_2'] + e'$, as can be seen from Table 2.1 and direct product tables [68]. A quartet state is a spin symmetric state and is therefore combined with a spatially antisymmetric state giving the term symbol $^4A_2'$. In the same manner as above, the states that asymptotically correlate with the atomic $S + S + P$ limit are two E', an E'', an A_1', an A_2', and an A_1''. The non-degenerate terms of D_{3h} symmetry correlate with the C_{2v} terms in the following way: $A_1' = A_1$, $A_2' = B_2$, $A_1'' = A_2$, and $A_2'' = B_1$, and as stated above $E' = A_1 + B_2$ and $E'' = A_2 + B_1$. For example, the lowest $A_1' - E'$ crossing at 60° involves three states of A' symmetry in C_s. This means they all avoided-cross when an angle and an interatomic distance are displaced from D_{3h} symmetry to C_s. Both A_1 surfaces cross the B_2 surface at a seam at C_{2v} configurations away from D_{3h} configurations, while the two A_1 surfaces touch at a point in the D_{3h} configuration.

After we have seen how quartet states of lithium trimer correlate with their

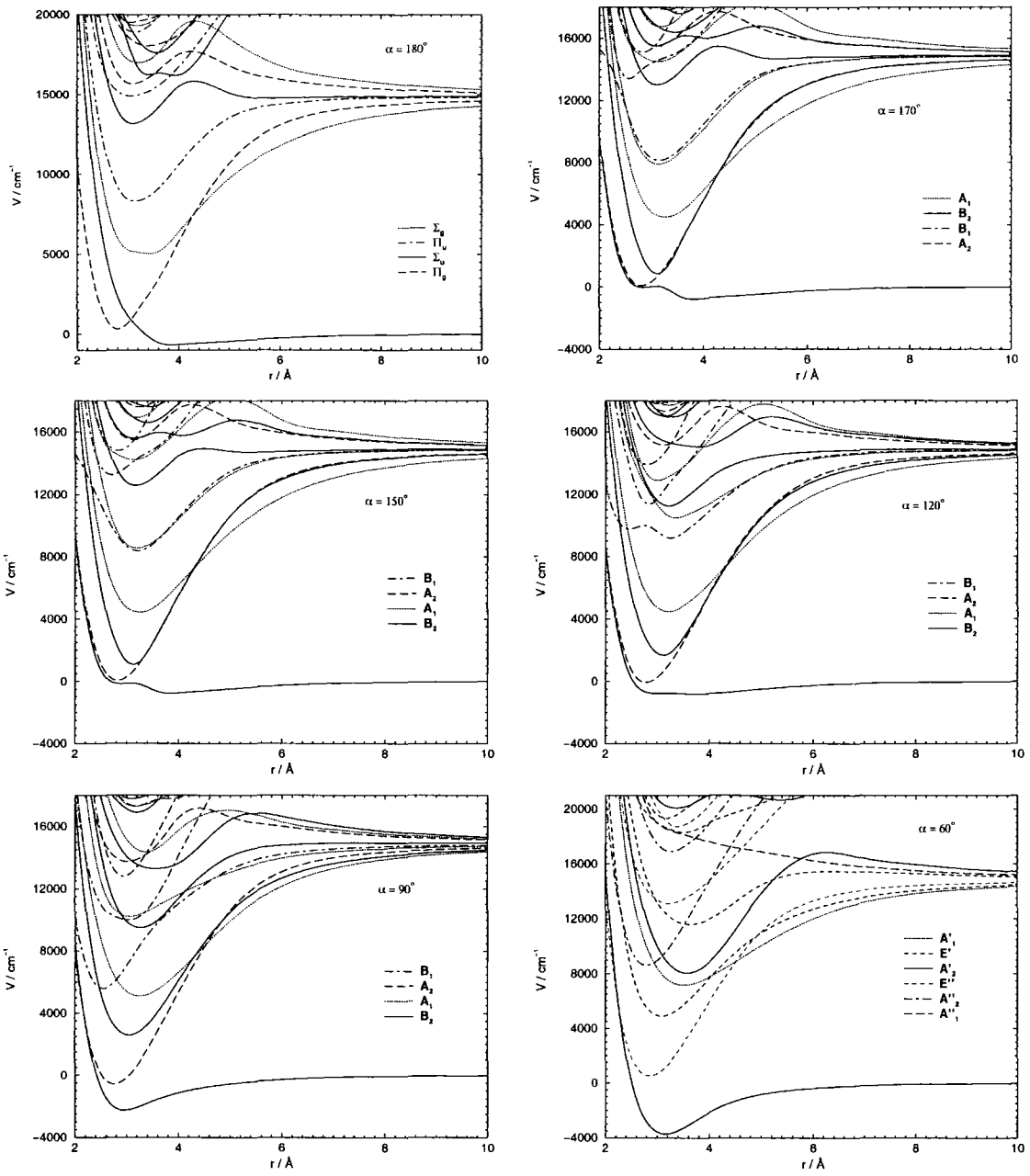

Figure 2.3: CASSCF quartet potentials of Li_3 from atomic $S+S+S$ and $S+S+P$ asymptotic limits at C_{2v} configurations. The two equal interatomic distances r are varied and the angle, α, between them is fixed on each graph at 180°, 170°, 150°, 120°, 90°, and 60°.

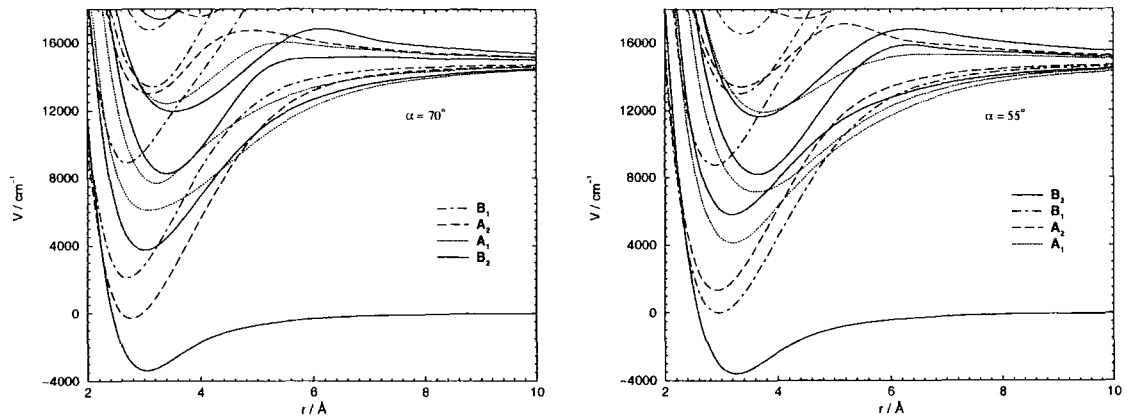

Figure 2.4: CASSCF quartet potentials of Li_3 from atomic $S+S+S$ and $S+S+P$ asymptotic limits at C_{2v} configurations. The two equal interatomic distances r are varied and angle between them is fixed at 70° (left) and 55° (right).

three-body atomic limits at long range, it remains to be seen how they correlate with their atom-diatom limits. The correlation diagram is shown in Figure 2.5. In the first panel (leftmost), we extend one distance away from the $D_{\infty h}$ geometry while preserving linearity, with the other one fixed at 6 Å. The geometries encompassed in this diagram are away from the strong interaction region to avoid interaction with states correlating with higher asymptotic limits. The preserved symmetry is $C_{\infty v}$ and the term symbols (not shown) are same as in $D_{\infty h}$ with g and u labels disposed. On the second panel (middle), we extend two distances from D_{3h} configuration, keeping them equal in the process, with the third fixed at 6 Å. The preserved symmetry is C_{2v} in this case. Here further term crossings occur before the atom-diatom limit is reached. In the third panel, the end configurations are D_{3h} and $D_{\infty h}$ and they are connected by keeping two distances equal (6 Å) and changing the angle between them. C_{2v} symmetry is preserved in the process. This situation has already been discussed above in the text pertaining to Figure 2.3.

2.6 Ground state quartet surface of Li_3

The lowest adiabatic quartet state of lithium trimer of A' symmetry in C_s group has a derivative discontinuity at linear geometries. The $^4\Pi$ state cuts through $^4\Sigma$ as was shown in Figure 2.3 at 180°. It seems that the intersection occurs above the three-body $(S+S+S)$ dissociation limit, but CASSCF calculations underestimate

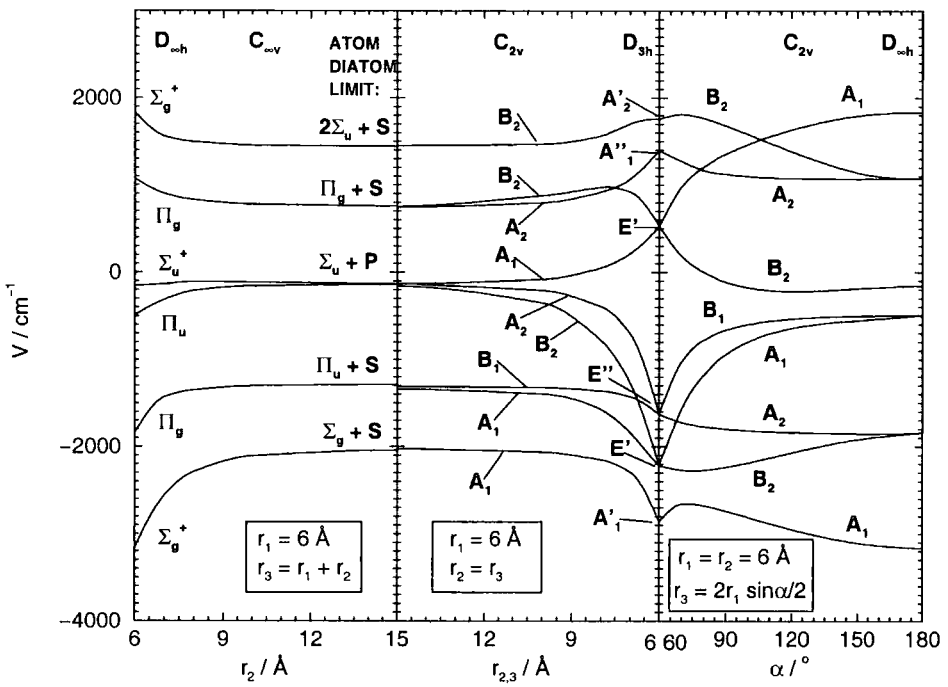

Figure 2.5: Correlation diagram of quartet potentials of Li_3 from atomic $S + S + P$ dissociation limit. The first panel connects the $D_{\infty h}$ terms with the atom-diatom limit, with an interatomic distance fixed at 6 Å and $C_{\infty v}$ symmetry preserved. The second panel connects the D_{3h} terms with the atom-diatom limit, with an interatomic distance fixed at 6 Å and C_{2v} symmetry preserved. The third panel connects D_{3h} and $D_{\infty h}$ terms. Here two interatomic distances are fixed at 6 Å and the angle between them, α, is varied.

the dynamical correlation effects. We performed an RHF followed by RCCSD(T) calculations with an aug-cc-pVTZ basis set to obtain a better estimate of electron correlation effects. The electron energies at $D_{\infty h}$ geometries with respect to the $S + S + S$ limit are shown in Figure 2.6. The energy dependence on the shorter interatomic distances is shown and the solid curve shows the lowest eigenvalue of A' symmetry. The intersection now occurs below zero, at geometries that are energetically accessible in low-energy atom-diatom collisions.

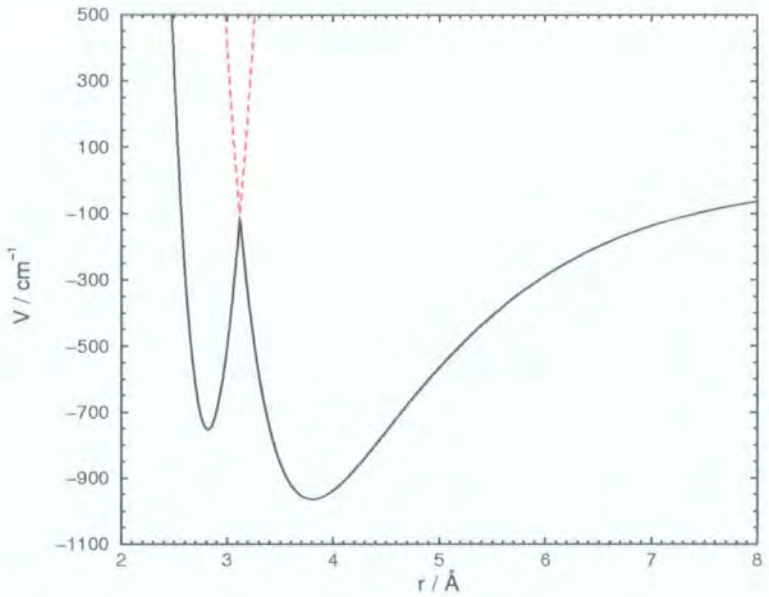

Figure 2.6: RCCSD(T) electron energies of two lowest $^4A'$ states of lithium trimer at $D_{\infty h}$ configurations (r is the smaller interatomic distance).

Figure 2.7 shows both surfaces, $^4\Sigma^+$ and $^4\Pi$, in $C_{\infty v}$ geometries. r_1 and r_2 are the two shorter interatomic distances, the third one being $r_3 = r_1 + r_2$. The diagonal on the graphs indicates $D_{\infty h}$ geometries. The two surfaces intersect along a seam. The line of intersection and the lower A' eigenvalue are shown in Figure 2.8 on the first panel. The seam at $C_{\infty v}$ geometries joins the two intersections, the one between $^4\Sigma_u^+$ and $^4\Pi_g$ in $D_{\infty h}$, shown in Figure 2.6, and the intersection of Li_2 potential curves, $^3\Sigma_g^+$ and $^3\Pi_u$, shown in Figure 2.2, when either r_1 or $r_2 \to \infty$.

The other panels in Figure 2.8 show slices of the potential energy surface where the angle between r_1 and r_2 is fixed at 170°, 150°, 120°, 90°, and 60° (in this order in the reading direction). The two surfaces of A' symmetry avoided-cross and as the angle is lowered, traces of the crossing are less prominent. Technical details of

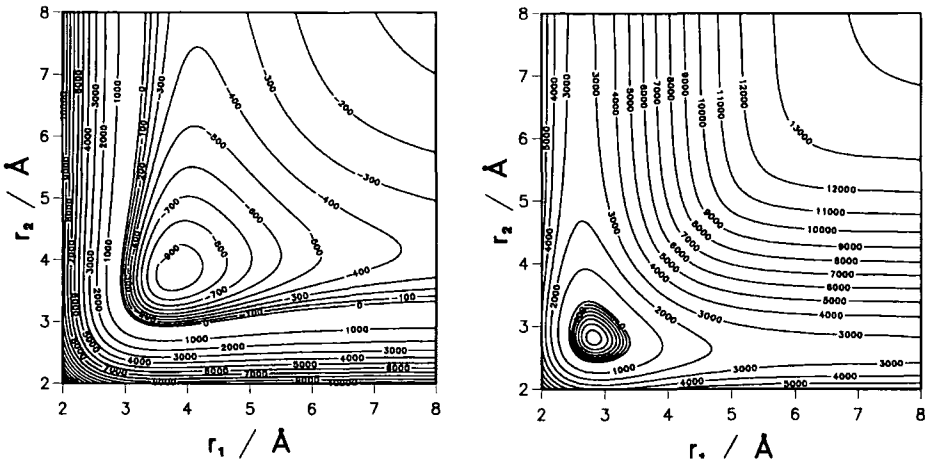

Figure 2.7: RCCSD(T) surfaces of $^4\Sigma_u^+$ (left) and $^4\Pi_g$ (right) states of lithium trimer at $C_{\infty v}$ configurations. Electronic energies are in cm^{-1}.

the grid points where electronic energy is evaluated *ab initio* and the methods of interpolation used for visualization of the surface will be discussed in Chapter 4. In *ab initio* calculations, the HF energy near and inside the avoided crossing jumps in an uncontrollable fashion between the lowest A' surfaces for different geometries. In order to have an automated computation of a large number of energies for the whole reactive surface, it was found useful to do an ionic Li_3^+ HF calculation beforehand to obtain convergence on the lower eigenvalue.

The quality of single-reference-based methods, such as CCSD(T), in the vicinity of conical intersections may be questioned. The T1 diagnostic is a measure that determines where multireference effects become large and may compromise the results [69]. It is related to the norm of amplitudes of singly excited determinants in configuration interaction theory. It has been stated [69] that if T1 is greater than 0.02, single-reference electron correlation methods are probably unreliable and will not yield highly accurate results. CCSD has been tested on alkaline-earth metal clusters [70] and it was shown that when $T_1 > 0.02$ inclusion of perturbative triples in CCSD is important and gives surprisingly good results. It was suggested that CCSD(T) may be useful when MRCI calculations are impractically expensive. We report T1 diagnostics in Figure 2.9. The dots in the figure indicate the positions where T1 diagnostics were evaluated. The angle between the interatomic distances r_1 and r_2 on each graph corresponds to the one on the corresponding graph in Figure 2.8. It can be seen that the electronic energies are less reliable at short distances

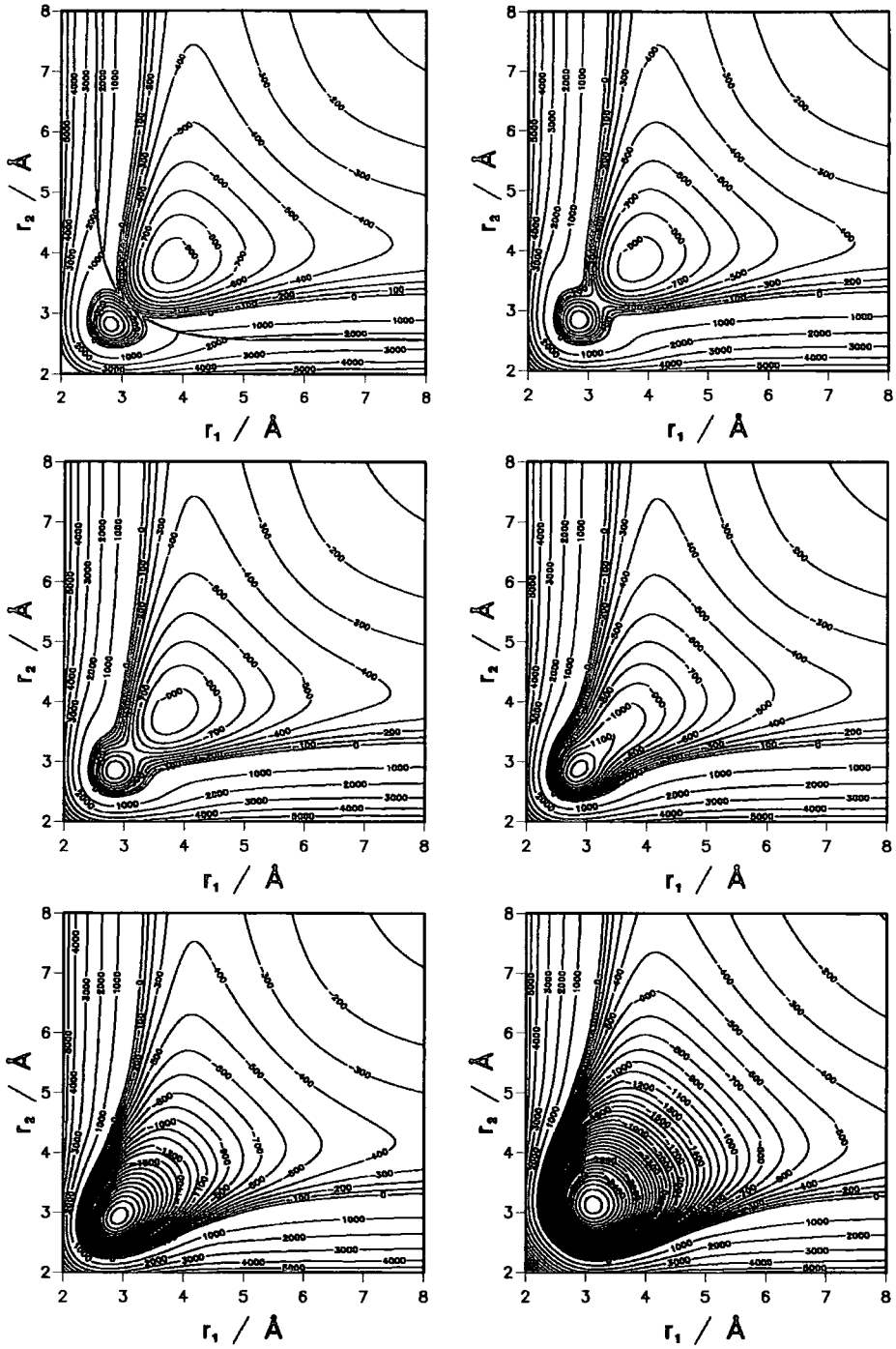

Figure 2.8: Angular slices through RCCSD(T) surface of the lowest $^4A'$ state of lithium trimer. r_1 and r_2 are interatomic distances and the angle between them is fixed on each graph at 180° (top left), 170° (top right), 150° (middle left), 120° (middle right), 90° (bottom left), and 60° (bottom right). Electronic energies are in cm^{-1}.

and at angles close to 60°. A part of the configuration space of low reliability is outside the relevant region for low-energy scattering, below the three-body dissociation limit. The two lowest A' states are of different character at 180° and away from the crossing their character becomes mixed. Regions of high T1 at angles other than 180° are at configurations where the two A' surfaces avoided-cross. The energy difference may be less than 1000 cm^{-1} in high-T1 regions at 60°. The butterfly-like wings extend towards the end of the seam correlating with the $\Sigma - \Pi$ intersection in the atom-diatom limit.

We have recalculated electronic energies using [3,12]-CASSCF, followed by an MRCI including Davidson's correction, for the same configurations. We show surface slices at 60° and 90° in Figure 2.10 where T1 diagnostics yielded high numbers. There are no visible qualitative differences. The MRCI surface is lower at all configurations. The MRCI energies differ from RCCSD(T) (with $1s$ electrons frozen) at $r_{1,2} = 3.8$ Å in $D_{\infty h}$ geometries by 16 cm^{-1} or 1.66 %, while at $r = 3.2$ Å in D_{3h} by 64 cm^{-1} or 1.64 %. Towards the configurations at 60° with large T1 diagnostics, the difference between the MRCI and RCCSD(T) energies increases, but the steepness of the curves is increased proportionally. Another research group employed CCSD(T) method near a conical intersection recently [71] (ClHCl potential) and found the results satisfactory. We have checked that the T1 diagnostics, calculated here using an aug-cc-pVTZ basis, do not change significantly when using larger basis sets.

2.7 Nonadditivity and nature of bonding of Li_3 quartet ground state

Potential energy of a system of atoms may be written in a many-body expansion. Specifically for three atoms, we may write

$$V_{\mathrm{TOT}}(r_1, r_2, r_3) = V_2(r_1) + V_2(r_2) + V_2(r_3) + V_3(r_1, r_2, r_3), \qquad (2.10)$$

where r_i are interatomic distances, V_2 is dimer potential, and V_3 is the nonadditive part of potential.

Nonadditive interactions have been studied in rare-gas trimers and proved to be small. The leading term of nonadditive dispersion interactions, the Axilrod-Teller term [72], has proved to work remarkably well in simulations of rare-gas solids and

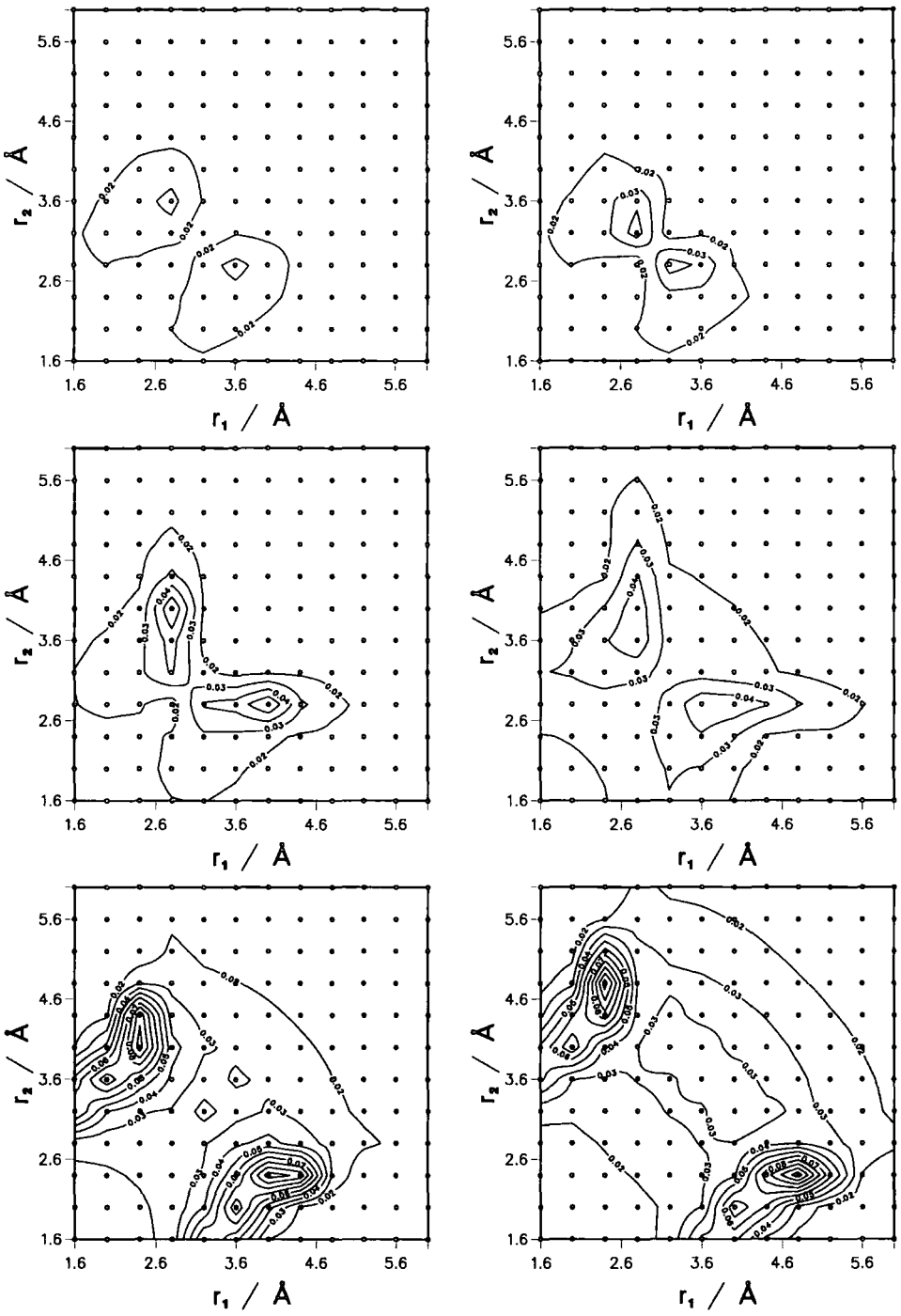

Figure 2.9: T_1 diagnostics at angular slices of potential energy surface. Angle between interatomic distances r_1 and r_2 is fixed on each graph at 180° (top left), 170° (top right), 150° (middle left), 120° (middle right), 90° (bottom left), and 60° (bottom right).

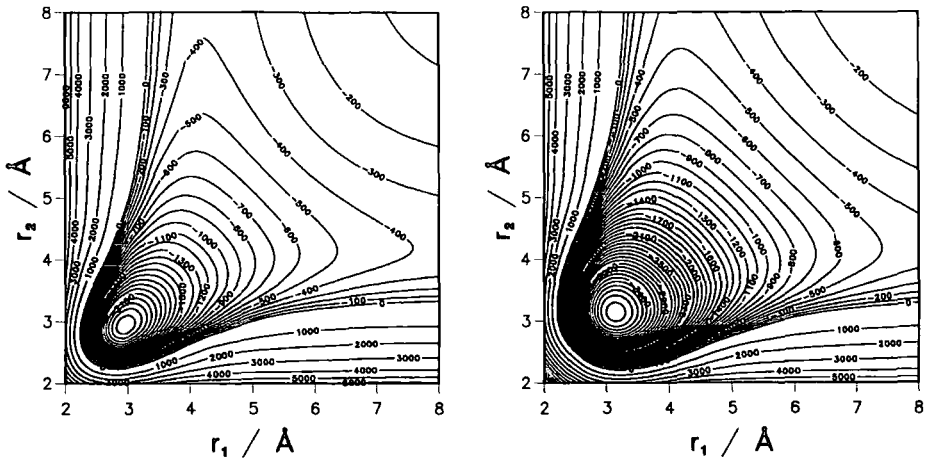

Figure 2.10: Angular slices of the CASSCF + MRCI surface of the lowest $^4A'$ state of lithium trimer. r_1 and r_2 are interatomic distances and the angle between them is fixed at 90° (left) and 60° (right). Electronic energies are in cm^{-1}.

liquids [73]. Its contribution is positive at equilateral geometries and negative at linear. It was shown [74] that other nonadditive interaction terms are not negligible, but cancel one another at the minimum and larger distances.

Surprisingly large nonadditive interactions were found in small metal clusters. In the doublet ground state of lithium trimer, it was found [75] that nonadditive effects are destabilizing and large. Kaplan et al. [76] found that electron correlation must be taken into account to determine the sign of nonadditive interactions in small metal clusters. Lithium trimers are stabilized by pairwise interactions. In the tetramers, two-body attraction is smaller than three-body repulsion and four-body interactions are essential for their stabilization. There is an increase in the equilibrium distances in the sequence Li_2, Li_3, and Li_4, in order to reduce the repulsive three-body interactions which diminish more sharply with the distance than the pairwise interactions.

Alkaline-earth metal dimers and trimers are unstable at the Hartree-Fock level, but electron correlation effects stabilize them [77]. Three-body interactions are attractive and are the main contributors to bonding in the trimers. It was found [78] that the mixing of *ns* and *np* orbitals leading to an *sp* hybridization is likely to be the mechanism responsible for binding in alkaline-earth clusters.

In lithium trimer in the quartet state, three-body nonadditive interactions are large and attractive at equilibrium. Pairwise additive and nonadditive contribu-

tions at D_{3h} configurations are shown in Figure 2.11 at Hartree-Fock and CCSD(T) level (in this section we use the cc-pV5Z basis set with non-contracted p functions, see Chapter 3). Pairwise interactions are repulsive at the Hartree-Fock level at all distances. Nonadditive interactions in the vicinity of the equilibrium are large and attractive and lead to stabilization of trimers even at Hartree-Fock level with a binding energy of ≈ 1280 cm^{-1} at $r \approx 3.09$ Å in the D_{3h} configuration. Electron correlation introduces lowering of the additive energy and contributes bonding. Nonadditive interactions are less influenced by electron correlation. The nonadditive correlation energy is positive at D_{3h} geometries and lowers the binding energy. Nonadditive dispersion interactions also make a positive contribution at D_{3h} geometries and are the dominant nonadditive effect at large separations. Three-body interactions are larger in magnitude than pairwise interactions at intermediate distances between 2.5 Å and 4.1 Å. They are responsible for the large well depth, four times the one suggested by pairwise additivity. The well is shifted to 3.1 Å from 4.2 Å in the pairwise additive model.

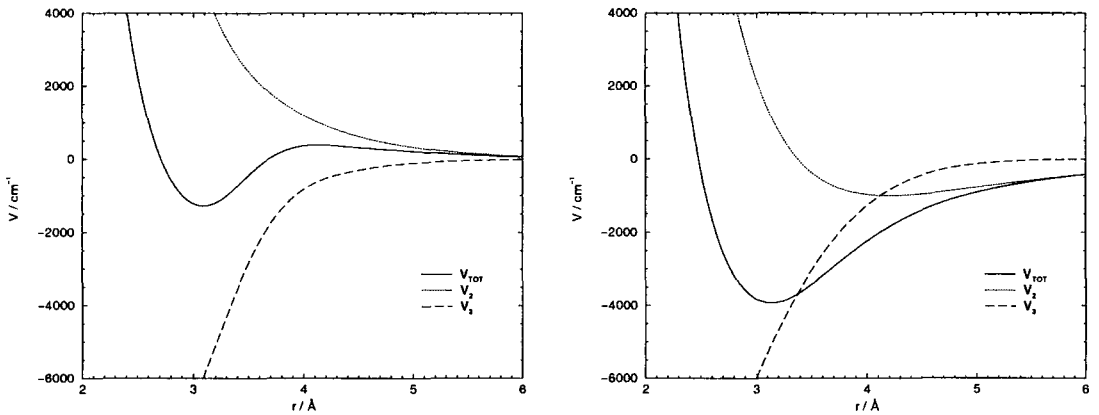

Figure 2.11: Total (V_{TOT}), pairwise-additive (V_2), and nonadditive (V_3) interaction potential of Li_3 in the quartet ground state at D_{3h} geometries as a function of interatomic distance in Hartree-Fock (left) and RCCSD(T) (right).

Additive and nonadditive interaction energy at the $D_{\infty h}$ configurations of lithium trimer in the $^4\Sigma_u^+$ state on Hartree-Fock and CCSD(T) level are shown in Figure 2.12. Interaction energy at Hartree-Fock level is positive for all distances. The pairwise-additive interactions are positive and larger than attractive nonadditive interaction at distances shown in the figure ($r > 2$ Å). Electron correlation lowers the additive and raises the nonadditive energy, with the net effect of bonding for distances larger

than ≈ 3.1 Å. Here, the nonadditive interactions exhibit a minimum at -1100 cm^{-1} at 2.5 Å. The nonadditive dispersion contribution remains negative at long distances.

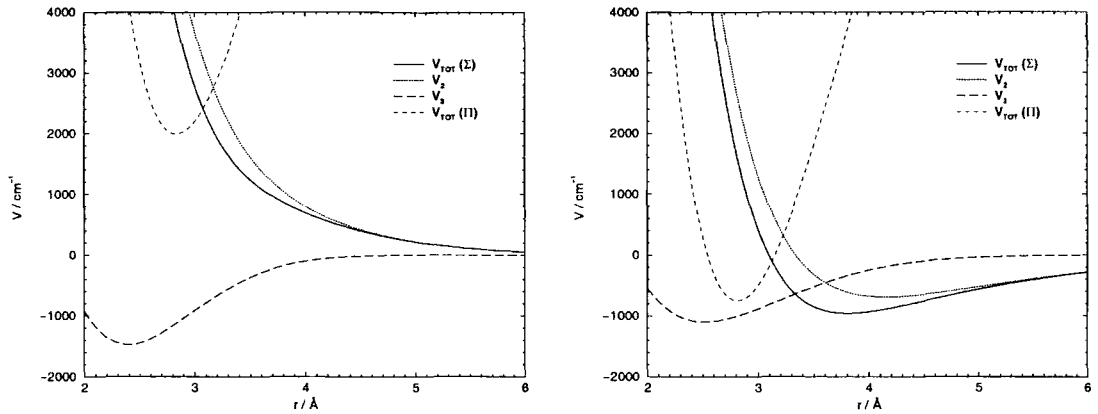

Figure 2.12: Total (V_{TOT}), pairwise-additive (V_2), and nonadditive (V_3) interaction potentials of Li_3 in the quartet ground state at $D_{\infty h}$ geometries as a function of (smaller) interatomic distances in Hartree-Fock (left) and RCCSD(T) (right).

We summarize characteristics of lithium dimer and trimer spin-polarized potentials together with those of other alkali metals obtained (by others) in our group [79] in Table 2.2 and 2.3 for comparison. (At $D_{\infty h}$ geometries in lithium trimer, there is a second minimum, $V = -760$ cm^{-1}, at 2.80 Å. Σ and Π states cross at 3.104 Å and $V = -96$ cm^{-1}.) The results for sodium agree well with those obtained by Higgins et al. [80]. Discrepancy at the global minimum is less than 1.5%. The equilibrium bond lengths in the quartet trimers are substantially shorter than those of the triplet dimers, by an amount that decreases steadily down the series from 1.07 Å in Li_3 to 0.59 Å in Cs_3. All alkali-metal trimers are predominantly bonded by nonadditive interactions. The nonadditive contributions to the interaction energies at the equilibrium vary between ≈ 130 % for Li and ≈ 50 % for Cs. For rare-gas trimers these figures are in range 0.5–2.5 % [74, 81] and produce a weakening rather than a strengthening of the binding. In alkaline-earth metal trimers, the figures are more similar. They range from 100% for Be_3 to 60% for Ca_3 [77].

The potential curves of quartet alkalis at D_{3h} and $D_{\infty h}$ configurations are shown in Figures 2.13 and 2.14. Pairwise-additive and full potentials are shown to emphasize the importance of nonadditive interactions. The effects are smaller at $D_{\infty h}$ configurations, but still substantial in all alkali trimers.

Nonadditive interactions at long range are dominated by dispersion forces, but

	Dimer	
	r_e / Å	V_{min} / cm^{-1}
Li	4.177	−328.922
Na	5.214	−174.025
K	5.786	−252.567
Rb	6.208	−221.399
Cs	6.581	−246.786

Table 2.2: Characteristics of CCSD(T) triplet potentials of alkali dimers.

	Trimer D_{3h}			Trimer $D_{\infty h}$		
	r_e / Å	V_{min} / cm^{-1}	V_3 / cm^{-1}	r_{sp} / Å	V_{sp} / cm^{-1}	V_3 / cm^{-1}
Li	3.103	−3970	−5224	3.79	−950	−344
Na	4.428	−837	−663	5.10	−381	−27
K	5.084	−1274	−831	5.67	−569	−52
Rb	5.596	−995	−513	6.13	−483	−15
Cs	5.992	−1139	−562	6.52	−536	−32

Table 2.3: Characteristics of CCSD(T) quartet potentials of alkali trimers.

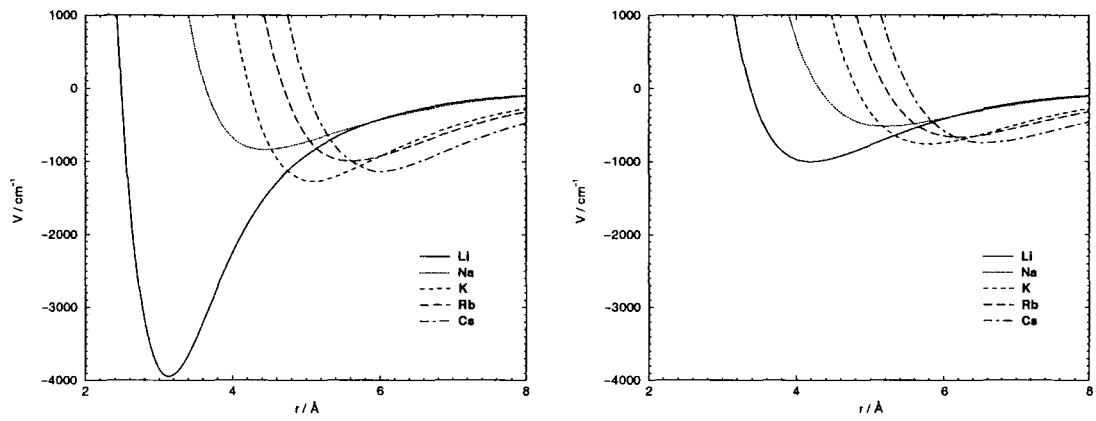

Figure 2.13: Total (left) and pairwise-additive (right) interaction potentials of alkali trimers in the quartet ground state at D_{3h} geometries as a function of the interatomic distance.

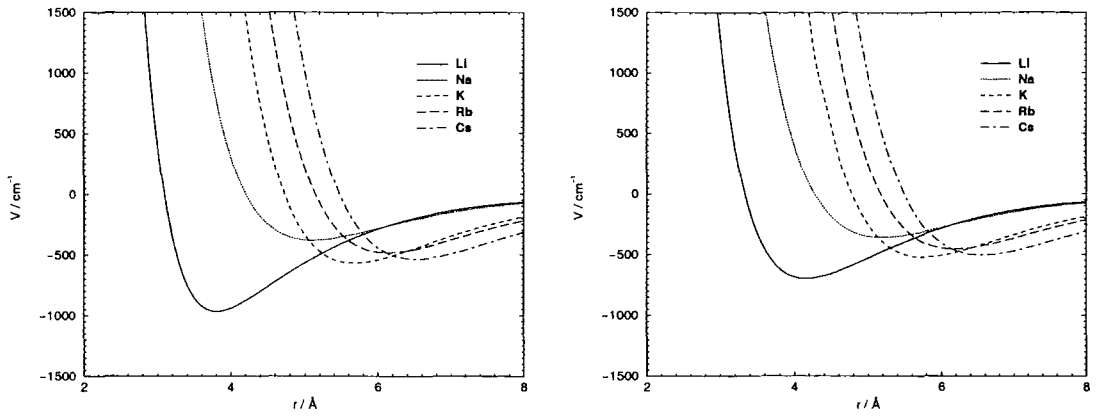

Figure 2.14: Total (left) and pairwise-additive (right) interaction potentials of alkali trimers in the quartet ground state at $D_{\infty h}$ geometries as a function of (smaller) interatomic distances.

the short range nonadditivity is present even at the Hartree-Fock level. Hartree-Fock values for nonadditive potential at the minimum are $\sim$ 110% for Li, $\sim$ 90% for Na, $\sim$ 100% for K and Rb, and $\sim$ 120% for Cs of the CCSD(T) values.

The chemical bonding effect arises because in alkali-metal atoms there are vacant np orbitals that lie relatively close to ns orbitals. The np orbitals form bonding molecular orbitals of the same symmetry as those formed from ns orbitals. The e' orbital is formed from p_t orbitals and the a_1' from p_r orbitals, see Table 2.1. The sets of orbitals of the same symmetry interact, lowering the energy of the occupied molecular orbitals and contributing to the bonding. This is the mechanism of sp hybridization in chemical terms.

We have carried out natural atomic orbital population analysis [82] of the Hartree-Fock wavefunction. The results, shown in Table 2.4, display significantly larger populations of p-type functions than in the corresponding dimers. The effect is largest in lithium where the s and p orbitals are closest. The interaction with p_t orbitals introduces a mixed character in the occupied orbitals of e' symmetry.

2.8 Future work: comment on diabatization

The Born-Oppenheimer approximation breaks down in the vicinity of conical intersections. The coupling between intersecting states is large and the states are mixed in character. One way to describe the electronic states is to use the adiabatic basis,

	Trimer			Dimer	
	ns	np_r	np_t	ns	np_z
Li	0.743	0.046	0.197	0.992	0.005
Na	0.985	0.003	0.009	0.998	0.005
K	0.949	0.011	0.034	0.995	0.003
Rb	0.975	0.006	0.014	0.996	0.003
Cs	0.947	0.012	0.030	0.995	0.003

Table 2.4: Natural atomic orbital populations of quartet alkali trimers and dimers at the corresponding global minima.

defined in equation (2.5). In this case, the dynamical equations involve non-adiabatic coupling matrix elements, inside the curly brackets in equation (2.6), which involve derivative operators and are rapidly varying near the intersections. They are therefore inconvenient to use in dynamical calculations. Alternatively, we may transform to a diabatic basis, Φ_i, by an orthogonal transformation. In the case that two states are involved, we have

$$\begin{pmatrix} \Phi_1 \\ \Phi_2 \end{pmatrix} = \begin{pmatrix} \cos\gamma & \sin\gamma \\ -\sin\gamma & \cos\gamma \end{pmatrix} \begin{pmatrix} \Psi_1 \\ \Psi_2 \end{pmatrix}. \tag{2.11}$$

The mixing angle γ may be determined to make the non-adiabatic couplings as close to zero as possible. For a one-dimensional problem, this condition reads,

$$\langle \Phi_1 | \frac{\mathrm{d}}{\mathrm{d}Q} | \Phi_2 \rangle = -\frac{\mathrm{d}\gamma}{\mathrm{d}Q} + \langle \Psi_1 | \frac{\mathrm{d}}{\mathrm{d}Q} | \Psi_2 \rangle \approx 0, \tag{2.12}$$

where we have taken only the first-derivative non-adiabatic coupling matrix element into account. The mixing angle is then obtained by integration of the non-adiabatic matrix element. Corresponding integral in more than one dimension is in general path dependent, leading to an arbitrariness in definition of diabatic basis [83, 84]. Diabatic basis simplifies the dynamical equations, but it does not diagonalize the electronic hamiltonian. For the two-state case, matrix elements of the electronic hamiltonian in diabatic basis are

$$\begin{aligned} H_{11} &= \cos^2\gamma E_1 + \sin^2\gamma E_2, \\ H_{22} &= \sin^2\gamma E_1 + \cos^2\gamma E_2, \\ H_{12} &= \sin\gamma\cos\gamma(E_2 - E_1), \end{aligned} \tag{2.13}$$

where E_1 and E_2 are adiabatic energies, i.e. eigenvalues of electronic hamiltonian.

We have used an adiabatic representation in the subsequent dynamical calculations in this work, neglecting all the non-adiabatic couplings. It would be interesting to perform the full dynamical calculations on the coupled surfaces in the future once it becomes feasible with increase in computer power. A comparative study of methods for constructing diabatic representations is given in Ref. 85. Direct evaluation of the non-adiabatic coupling matrix elements is expensive and requires a dense grid of geometries. Other methods analysed in Ref. 85 are either based on the analysis of CI vectors or on diagonalization of a property matrix. Application of these methods is not straight-forward in the case of three identical lithium atoms. For example, using the transition angular momentum, the mixing angle is [71]

$$\gamma = \arctan\left[\frac{|\langle 1B_2|L_y|A_2\rangle|}{|\langle 2B_2|L_y|A_2\rangle|}\right]. \tag{2.14}$$

In Figure 2.15, we show the adiabatic and diabatic potentials involved in the conical intersection in the quartet ground state at ≈ 3.1 Å, for C_{2v} arrangements and $\alpha = 170°$. The molecule is in the yz plane and z axis bisects the obtuse angle α. We also show the mixing angle as a function of two equal interatomic distances r, for different angles between them, α. For smaller angles, away from the intersection at $\alpha = 180°$, the method become less useful. This problem persists when using other methods. The reason is that the character of states cannot be described as a Σ or Π far away from linear geometries. Near $r \approx 4$ Å at C_{2v} geometries, other states may need to be included in the diabatization scheme.

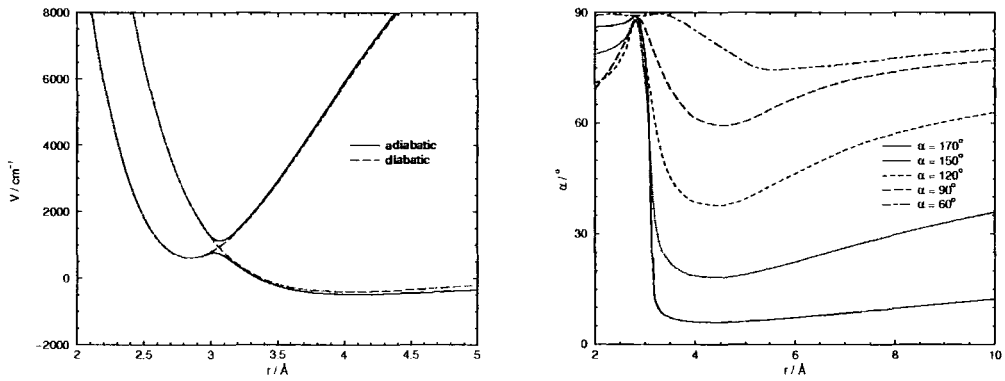

Figure 2.15: CASSCF adiabatic and diabatic potentials for Li_3 at C_{2v} configurations for $\alpha = 170°$ (left) and the mixing angle as a function of r for different angles α (right).

Chapter 3

Adiabatic quartet potential of lithium trimer: a quantitative study

3.1 Introduction

Having discussed the qualitative aspects of the quartet potential energy surface of lithium trimer in the last chapter, our next task is to try and be as accurate as possible in calculation of electronic energies. Potential energy surfaces for reactive systems are usually represented using electronic energies calculated at several hundred geometries that cover all important regions of the system. The strategy is to find the optimum method and basis set for producing the electronic energies in a reasonable time by doing convergence and performance tests at a few important geometries of the system.

Following the results given in the last chapter, we decided to use the RCCSD(T) method. From widely used and tested methods, it is the best for our purpose in terms of the compromise between the computer time and accuracy. In connection with a method, a basis set must be chosen for representing the functional form of the wavefunction. Theoretical CPU scaling of the CCSD(T) method with the basis set size is $\sim M^7$, in the large basis set limit, where M is the number of basis functions. This sets a serious limit on the size that may be used. It is therefore important that the quality of the basis set is high and that the finite size we can use describes the system well.

The most common types of basis functions that are used to represent the atomic orbitals are Slater type orbitals (STO) and Gaussian type orbitals (GTO). While the former have more appealing physical behaviour at short and long range, the latter are much more convenient for calculating electronic integrals. Usually three times more GTOs than STOs are needed to achieve the same level of accuracy, but the disadvantage is compensated by the efficiency of integral calculation so that GTOs are now universally used. The GTOs are of the form

$$\chi_{\zeta nlm}(r,\theta,\varphi) = NY_{lm}(\theta,\varphi)r^{(2n-2-l)}\mathrm{e}^{-\zeta r^2}, \tag{3.1}$$

where Y_{lm} is a spherical harmonic. The disadvantage of GTOs in comparison with STOs is that the r^2 dependence of the exponential produces a zero slope at the nucleus, so GTOs have a problem describing the wavefunction at short range. GTOs also have a difficulty describing the tail of the wavefunction because they fall off too rapidly at long range. Linear combinations of the above *primitive* GTOs (3.1) with

different zeta coefficients (ζ) have been combined to form many different *contracted* basis sets.

The basis sets used in this work are the correlation-consistent basis sets developed by T. H. Dunning and co-workers [86]. They are briefly described in the next section. The rest of the chapter is concerned with the application of the basis sets in calculation of the atomic, diatomic, and triatomic potential characteristics with the aim of studying the convergence and accuracy of the interaction energies.

3.2 Correlation consistent basis sets

Correlation-consistent (cc) basis sets [86] are geared to recover the correlation energy of electrons in connection with an electron correlation method. It has been recognized that individual basis functions fall into well-defined groups that recover similar amounts of correlation energy. Correlation-consistent polarized valence basis sets cc-pVXZ, where X is D, T, Q, or 5, for double, triple, quadruple, and quintuple, respectively, have been designed by adding such groups of functions on the previous basis set in the sequence. Another property of the cc basis sets is that the *sp*-basis increases together with the polarization space, the higher angular momentum functions, and the errors of incompleteness in the two spaces should be comparable. The consistent nature of the increase in the basis set size enables accurate predictions of errors and also extrapolation to infinite basis set size. The cc basis sets have become popular and are a tested and reliable tool to use in the electronic energy calculations.

In a well balanced basis set, different functions may be given different physical purposes. The *sp*-basis describes fundamental electron distribution in an atom. Polarization functions are important for directionality in the bonding and are essential for correlated-electron treatments. The correlation can also be divided into radial and angular correlation. The radial part is responsible for near- and far-from nucleus correlation, while the angular part describes opposite parts of nucleus correlation. Radial correlation is recovered by using basis functions of the same type with different exponents. Angular correlation is recovered using functions of different angular momenta.

Properties such as the polarizability, which is important for the description of the dispersion forces, originating from the correlated induced multipole moments

interaction, depend on the tail of the wavefunction. The description of the tail requires diffuse functions, those with small exponents. In Dunning's terminology addition of diffuse functions is called augmentation. The augmentation we have used in this work is even-tempered, where the exponent of the added function of a given type is determined by keeping the ratio of exponents constant and determined from the two smallest exponents of functions of the same type. If there is only one function of a type, ratio is taken to be 2.5.

The basis sets can also be augmented with additional tight functions with large exponents for a better description of core-valence (simultaneous excitations from core and valence orbitals included, in the CI terminology) and core-core (excitations of core orbital electrons only) correlation. Basis sets optimized for treatments including core correlation are called correlation-consistent polarized core-valence basis sets, cc-pCVXZ, where X remains the same as above.

The convergence of energies in terms of angular momentum is slower for correlated methods than for HF [59]. The correlation energy converges with an inverse power law, $\sim 1/(L+1)^3$, for a basis set that is complete up to angular momentum L. Convergence at the HF level is exponential, $\sim \exp(-L)$.

Lithium basis sets, cc-pVXZ and cc-pCVXZ, up to quintuple zeta have been developed by D. Feller [67] by optimizing the exponents in HF and CISD calculations as described by Dunning in Ref. 86, 87. Basis sets are available from the EMLS Library [67]. We have obtained the cc-pCV5Z basis set for lithium from K. A. Petersen. Recently, new cc-pCVXZ up to $X = 5$, have been published by J. M. L. Martin and co-workers [88] for all alkali and alkaline-earth metals and are available online [89]. Here the successive optimizations were performed using the CCSD(T) energy. Basis sets from all these authors have been tested in this work. Results using the cc-pCVXZ basis sets are shown only using the ones developed by Martin rather than those by Feller and Petersen, but the differences between them are minor. The composition of basis sets in terms of numbers of primitive and contracted basis functions is shown in Table 3.1.

basis	uncontracted	contracted
cc-pVDZ	(9s, 4p, 1d)	[3s, 2p, 1d]
cc-pVTZ	(11s, 5p, 2d, 1f)	[4s, 3p, 2d, 1f]
cc-pVQZ	(12s, 6p, 3d, 2f, 1g)	[5s, 4p, 3d, 2f, 1g]
cc-pV5Z	(14s, 7p, 4d, 3f, 2g, 1f)	[6s, 5p, 4d, 3f, 2g, 1h]
cc-pCVDZ	[cc-pVDZ] + [1s,1p]	
cc-pCVTZ	[cc-pVTZ] + [2s,2p,1d]	
cc-pCVQZ	[cc-pVQZ] + [3s, 3p, 2d, 1f]	
cc-pCV5Z	[cc-pV5Z] + [4s, 4p, 3d, 2f, 1g]	

Table 3.1: Composition of the correlation-consistent polarized valence, cc-pVXZ, and core-valence, cc-pCVXZ, basis sets in terms of primitive and contracted basis functions.

3.3 Basis set convergence

The basis sets described in the previous section are employed in the RCCSD(T) calculations below. We investigate atomic, diatomic, and triatomic properties. Convergence was tested on chosen geometries in both short- and long-range regions of the potential. Convergence was tested with respect to the basis-set size and the level of augmentation. The effect of contraction was investigated and also the addition of tight functions with large exponents, geared to describe the cusp at the nuclei and recover core-valence and core-core correlation. We examine the applicability of the frozen-core approximation in which the core electrons are not included in the electron-correlation calculation and the size of the basis set superposition error.

3.3.1 Atomic properties

Electronic energies of atomic lithium in S and P states calculated using cc-pVXZ and cc-pCVXZ basis sets, where X is T, Q, or 5, are listed in the Table 3.2 and 3.3. The effect of uncontracting the s and p functions (denoted by nc in the tables) is also shown. The RCCSD(T) energies were obtained by correlating all three electrons.

We first look at the results using cc-pVXZ basis sets. Energies at the HF level are well converged. Differences between subsequent basis sets of S-state atom energies are 4 cm^{-1} and 6 cm^{-1}. Contraction coefficients are taken from the atomic HF calculations so the RHF energies are the same irrespective of whether the basis set

basis	E_{RHF}/E_h	$E_{\mathrm{RCCSD(T)}}/E_h$ (nc)	$E_{\mathrm{RCCSD(T)}}/E_h$ (c)
T	−7.43267886	−7.47026503	−7.44606570
Q	−7.43269514	−7.47253409	−7.44982668
5	−7.43272264	−7.47343378	−7.45990753
CT	−7.43267887	−7.47535674	−7.47456905
CQ	−7.43269514	−7.47686218	−7.47673203
C5	−7.43272264	L.D.	−7.47744177

Table 3.2: Basis set convergence of electronic energies of the atomic ^2S state using cc-pVXZ (X) and cc-pCVXZ (CX) basis sets in RHF and RCCSD(T) with (c) and without (nc) contraction of s and p functions. (L.D. denotes failure due to the linear dependency of the basis set.)

basis	E_{RHF}/E_h	$E_{\mathrm{RCCSD(T)}}/E_h$ (nc)	$E_{\mathrm{RCCSD(T)}}/E_h$ (c)
T	−7.36499072	−7.40220586	−7.37861542
Q	−7.36502972	−7.40457286	−7.38238935
5	−7.36505889	−7.40551388	−7.39231881
CT	−7.36499451	−7.40724654	−7.40656314
CQ	−7.36503198	−7.40891354	−7.40879123
C5	−7.36506039	L.D.	−7.40952285

Table 3.3: Basis set convergence of electronic energies of the atomic ^2P state using cc-pVXZ (X) and cc-pCVXZ (CX) basis sets in RHF and RCCSD(T) with (c) and without (nc) contraction of s and p functions. (L.D. denotes failure due to the linear dependency of the basis set.)

is contracted or not. The RCCSD(T) energy of an S-state atom converges steadily when non-contracted basis sets are used, the differences in the subsequent steps being 498.00 cm^{-1} and 197.46 cm^{-1}. The corresponding energy differences for a P-state atom are only slightly larger, 519.50 cm^{-1} and 206.53 cm^{-1}. Convergence in the contracted basis sets is not steady.

For cc-pCVXZ basis sets, the HF energies do not change significantly in comparison with the corresponding energies calculated using the cc-pVXZ basis sets. Addition of the tight functions is geared towards recovering the correlation energy, while the HF wavefunction is already well represented by functions in the cc-pVXZ basis sets. The cc-pCV5Z basis set becomes linearly dependent (L.D.) if the s and p functions are not contracted. The energy differences for the contracted CV basis sets are steadily converging. The energy lowerings in sequential increases in the basis-set size are 474.72 cm^{-1} and 155.77 cm^{-1} for the S-state atom and 489.01 cm^{-1} and 160.572 cm^{-1} for the P-state atom.

The convergence of the correlation energy, the difference between the RCCSD(T) and the RHF energies, is shown in Table 3.4. Contracted cc-pVXZ basis sets recover a considerably smaller amount of correlation energy than their non-contracted cc-pVXZ counterparts. They were designed and optimized for recovering the valence correlation energy only, which is zero for an atom with one valence electron. At the quintuple zeta level, the non-contracted cc-pV5Z recovers 91% of the correlation energy obtained using the cc-pCV5Z basis set. The contracted cc-pV5Z recovers only 61%. It may be noted that the correlation energy is similar for atoms in S and P states at all levels. This means that the correlation energy is due to core-core correlation and the cores of atoms in both states are similar.

Very accurate non-relativistic calculations assuming an infinite nuclear mass have been performed by Yan et al. [90]. Their S- and P-state energies of lithium are $-7.47806032310(31)$ E_h and $-7.4101565218(13)$ E_h, respectively. The values obtained using cc-pCV5Z basis sets are both within 0.0086%.

The differences between the electronic energies calculated using different basis sets are high when compared with the chemical accuracy which we would like to achieve. The hope is that in a well-balanced basis set errors will cancel when calculating interaction energies. The transition energy from the ^2S to ^2P state of an atom is shown in Table 3.5. The RHF value is 14850 cm^{-1} using either the cc-pV5Z

	S state		P state	
basis	$E_{\rm corr}/E_h$ (nc)	$E_{\rm corr}/E_h$ (c)	$E_{\rm corr}/E_h$ (nc)	$E_{\rm corr}/E_h$ (c)
T	−0.03758617	−0.01338684	−0.03721514	−0.01362470
Q	−0.03983895	−0.01713154	−0.03954314	−0.01735963
5	−0.04071114	−0.02718489	−0.04045499	−0.02725992
CT	−0.04267711	−0.04189018	−0.04223895	−0.04156863
CQ	−0.04416685	−0.04403689	−0.04387785	−0.04375925
C5	L.D.	−0.04471913	L.D.	−0.04446246

Table 3.4: The RCCSD(T) correlation energy of Li atom in ^2S and ^2P states using cc-pVXZ (X) and cc-pCVXZ (CX) basis sets; contracted (c) and non-contracted (nc).

or cc-pCV5Z, while X=T value is 5 cm^{-1} larger. The results obtained using the non-contracted cc-pVXZ basis sets are now in closer agreement with the cc-pCVXZ basis, particularly for $X = 5$. This means that the error in the remaining correlation energy that was not recovered in atomic calculations is similar for both atomic states and therefore cancels. The experimental value taken from Ref. 91 is 14903.66 cm^{-1} for the $J = 1/2$ state and 14904.00 cm^{-1} for $J = 3/2$, which is close to the value obtained by the largest basis sets.

	E_{SP}/cm^{-1} (nc)	E_{SP}/cm^{-1} (c)
T	14937.26	14803.63
Q	14915.77	14800.78
5	14906.69	14834.01
CT	14948.46	14925.57
CQ	14913.00	14911.28
C5	L.D.	14906.48

Table 3.5: The $^2S \rightarrow {}^2P$ RCCSD(T) transition energy using cc-pVXZ (X) and cc-pCVXZ (CX) basis sets; contracted (c) and non-contracted (nc).

Augmentation of the basis set made a negligible difference on the atomic energies. We examined the influence of augmentation on the polarizability of lithium atom. A good representation of polarizability may be important for accurate energies at long range that are dominated by the dispersion interaction. Results are shown in Table 3.6. One level of augmentation proved to be sufficient to saturate the basis sets.

We found that the effect of augmentation is less pronounced for larger basis sets. This is so because there are already sufficient diffuse functions in the non-augmented basis sets needed for the description of electron-cloud deformation. The experimental value taken from Ref. 92 is $(164.0 \pm 3.4)\ a_0^3$, while the best calculated value from Ref. 93 is $164.111(2)\ a_0^3$. These values are in close agreement with those obtained here using the non-contracted cc-pVXZ basis sets and the contracted cc-pCVXZ in correlated calculations.

	contracted basis		non-contracted basis	
basis	$\alpha_{\mathrm{RHF}}/a_0^3$	$\alpha_{\mathrm{RCCSD(T)}}/a_0^3$	$\alpha_{\mathrm{RHF}}/a_0^3$	$\alpha_{\mathrm{RCCSD(T)}}/a_0^3$
T	168.790	167.492	169.390	163.827
AT	169.559	168.189	170.140	164.568
AAT	169.533	168.147	170.111	164.548
AAAT	169.518	168.128	170.096	164.536
Q	169.837	166.572	169.946	164.342
AQ	169.974	166.668	170.081	164.424
AAQ	169.978	166.664	170.085	164.425
5	170.029	165.518	170.031	164.336
A5	170.097	165.549	170.100	164.375
CT	169.210	164.288	169.469	163.507
ACT	169.973	165.040	170.186	164.198
CQ	169.939	164.225	169.971	164.140
ACQ	170.075	164.303	170.097	164.220
C5	170.036	164.152	L.D.	L.D.
AC5	170.104	164.189	L.D.	L.D.

Table 3.6: Static dipole polarizabilities of lithium S-state atom in RHF and RCCSD(T) using cc-pVXZ (X) and cc-pCVXZ (CX), contracted and non-contracted, basis sets.

Lithium cation Li^+ is the core of a lithium atom. We performed the Li^+ energy calculations and report them in Table 3.7. The non-contracted cc-pVXZ basis sets display again a steady convergence in steps of 470.30 cm^{-1} and 182.51 cm^{-1}. The contracted cc-pCVXZ basis sets converge in slightly smaller steps 396.84 cm^{-1} and 138.38 cm^{-1}. The ionization energy is reported in Table 3.8. It converges towards the experimental value of 43487.150 cm^{-1} [91].

The correlation energy of the Li^+ ion is shown in Table 3.9. It is very similar to

basis	E_{RHF} / E_h	$E_{\mathrm{RCCSD(T)}}$ / E_h (nc)	$E_{\mathrm{RCCSD(T)}}$ / E_h (c)
T	−7.23638019	−7.27244813	−7.24935339
Q	−7.23638442	−7.27459097	−7.25249283
5	−7.23641110	−7.27542256	−7.26217708
CT	−7.23638009	−7.27740432	−7.27690241
CQ	−7.23638441	−7.27881046	−7.27871054
C5	−7.23641110	L.D.	−7.27934105

Table 3.7: Basis set convergence of electronic energies of Li^+ ion using cc-pVXZ (X) and cc-pCVXZ (CX) basis sets in RHF and RCCSD(T) with (c) and without (nc) contraction of s and p functions.

basis	$E^{\mathrm{ionizat.}}_{\mathrm{RSSCD(T)}}$ / cm^{-1} (nc)	$E^{\mathrm{ionizat.}}_{\mathrm{RSSCD(T)}}$ / cm^{-1} (c)
T	43415.79	43173.36
Q	43443.49	43309.77
5	43458.44	43396.82
CT	43445.53	43382.81
CQ	43467.33	43460.69
C5	L.D.	43478.08

Table 3.8: Basis set convergence of the ionization energy of Li using cc-pVXZ (X) and cc-pCVXZ (CX) basis sets in RHF and RCCSD(T) with (c) and without (nc) contraction of s and p functions.

the correlation energy reported for S- and P-state atoms in Table 3.4. This confirms that the core-core correlation dominates the core-valence correlation in the atoms.

basis	$E_{\rm corr}/E_h$ (nc)	$E_{\rm corr}/E_h$ (c)
T	−0.03606794	−0.01297320
Q	−0.03820655	−0.01610841
5	−0.03901146	−0.02576598
CT	−0.04102423	−0.04052232
CQ	−0.04242605	−0.04232613
C5	L.D.	−0.04292995

Table 3.9: The RCCSD(T) correlation energy of Li^+ ion using cc-pVXZ (X) and cc-pCVXZ (CX) basis sets; contracted (c) and non-contracted (nc).

We have seen here that uncontracting s and p functions enables recovery of the core-core correlation energy in lithium. We have also tried uncontracting only s functions and only p functions from the cc-pVXZ basis sets. When the basis set is large, i.e. using cc-pV5Z, we have discovered that uncontracting only p functions gives electron energies that are close to the non-contracted basis. Uncontracting s functions only gives considerably poorer results, close to the fully contracted basis sets. The RHF and RCCSD(T) energies of an S-state atom, using cc-pV5Z with s functions contracted only, are $-7.43272264\ E_h$ and $-7.47241840\ E_h$, respectively. They are $-7.36505884\ E_h$ and $-7.40451252\ E_h$ for a P-state atom, respectively. This give the $S-P$ transition wavenumber of 14903.6179 $\rm cm^{-1}$ in close agreement with experiment. The polarizability of lithium, using s-contracted basis set, is 170.031 a_0^3 in HF and 164.396 a_0^3 in RCCSD(T). The ionic energies are $-7.23641104\ E_h$ in RHF and $-7.27442174\ E_h$ RCCSD(T). All the values agree closely with those obtained by the non-contracted cc-pV5Z.

3.3.2 Diatomic properties

In this subsection, the triplet ground-state potential curves obtained using the RCCSD(T) method with different correlation consistent basis sets will be compared to recent experimental data.

The basis sets used in calculations of interaction energies are centred on the two nuclei. In this way, the basis set on one centre can help compensate for the basis

set incompleteness on the other centre. This introduces a systematic error called basis set superposition error (BSSE). BSSE can be approximately corrected using the counterpoise correction (CC) by Boys and Bernardi [94]. The dimer interaction energy is defined as

$$V_{\rm int}(r) = V_{\rm dim}(r) - 2V_{\rm at}, \tag{3.2}$$

where $V_{\rm dim}$ is the total dimer energy with respect to all electrons and nuclei break-up and $V_{\rm at}$ is lithium atomic energy. The CC corrected interaction energy is obtained using (3.2) with both the dimer and atomic energy calculated using the same two-centre basis set. The atomic energy becomes dependent on the distance between the centres and the BSSE per atom, using CC, is

$$V_{\rm BSSE}(r) = V_{\rm at} - V_{\rm at}^{(2)}(r). \tag{3.3}$$

The superscript indicates the number of basis-set centres. All reported interaction energies in this work are CC corrected.

We have calculated dimer interaction energies and BSSE using (3.2), for the $^3\Sigma_u^+$ state, using different correlation-consistent basis sets near equilibrium, at $r = 4.2$ Å, and at short range for $r = 3.3$ Å. The results are shown in Table 3.10.

Contracted cc-pVXZ basis sets all have a large BSSE that is comparable to the magnitude of the interaction energies. The BSSE is larger at smaller separations and when basis sets are augmented with diffuse functions. Then the basis functions from the other centre significantly overlap with the electronic density on the atom and compensate for the inadequacies of the one-centre basis. This is inappropriate and the basis sets that give large BSSE should not be used.

In the frozen core (FC) approximation, core electrons are excluded from the correlation treatment and only two valence electrons are correlated. BSSE in the FC approximation is very small for all basis sets. It is somewhat bigger, but still small, for cc-pCVXZ basis sets, in all-electron calculations.

The cc-pCVXZ basis sets are constructed to include the functions that represent the core-core correlation effects well. We have seen that core correlation effects are not well represented by the contracted basis sets in atomic calculations in the preceding subsection. We calculated the BSSE in HF and RCCSD(T) for an S-state atom, a P-state atom and Li^+ ion using the contracted cc-pV5Z basis set. BSSE in HF is plotted as a function of intercentre distance in Figure 3.1. It is small for all

	$r = 4.2$ Å		$r = 3.3$ Å	
	V / cm^{-1}	V_{BSSE} / cm^{-1}	V / cm^{-1}	V_{BSSE} / cm^{-1}
T	−318.2808	23.7514	111.9954	56.6317
T unc p	-	-	-	-
T unc all	−310.0849	0.8436	106.1144	1.8205
FC T	−318.7930	0.3435	125.4594	0.4865
CT	−310.5019	2.7306	109.4956	5.3647
AT	−333.8039	59.7620	95.0010	110.3248
AT unc p	-	-	-	-
AT unc all	−322.7682	1.8562	95.5283	3.0113
FC AT	−334.0051	0.5975	110.1737	0.8160
ACT	−324.6038	0.6081	95.5952	10.8017
Q	−332.4916	33.5759	73.8057	125.6963
Q unc p	−325.4764	13.9910	81.1159	45.3722
Q unc all	−324.8495	0.6577	81.8652	2.2691
FC Q	−334.8093	0.0523	103.4009	0.0755
CQ	−325.4004	0.5010	77.2602	1.4366
AQZ	−337.1347	98.0681	71.1426	248.4343
AQ unc p	−329.2576	44.6784	78.4953	98.5989
AQ unc all	−328.5029	1.4460	79.1350	3.5058
FC AQ	−339.1725	0.0622	99.9892	0.0772
ACQ	−329.0942	1.0490	74.4931	2.2991
5	−333.8321	41.4517	67.4659	111.0671
5 unc p	−328.8170	2.5533	73.7552	9.6466
5 unc all	−328.6265	0.8015	74.0185	1.8544
FC 5	−338.4712	0.0136	99.6626	0.0191
C5	−328.8147	0.1386	70.4171	0.2998
A5	−335.5736	85.4620	65.6835	186.0677
A5 unc p	−330.4757	8.7942	72.5456	16.2187
A5 unc all	−330.2446	1.4885	72.7985	3.0041
FC A5	−340.2752	0.0201	98.3219	0.0245
AC5	−330.4193	0.2335	69.2717	0.4283

Table 3.10: The RCCSD(T) energy of $^3\Sigma_u^+$ state of Li_2 and the basis set superposition error for an S-state atom in the two-centre basis set at $r = 4.2$ Å and 3.3 Å, using different cc-pVXZ (X) and cc-pCVXZ (CX) basis sets; augmented (A), contracted, non-contracted (unc all), and with s functions contracted only (unc p) and either with all electrons correlated or with a frozen core (FC).

three species. In CCSD(T), when correlation effects are included, BSSE is similar and large for all three species and at all distances. For example, at $r = 4.2$ Å, it is 41.45 cm^{-1} for an S-state atom, 40.61 cm^{-1} for a P-state atom, and 40.41 cm^{-1} for the ion. This confirms that BSSE is mainly due to core-core correlation effects and its origin is in an inadequate representation of these effects by a single-centre basis set. We have also investigated how uncontracting s and p functions in the cc-pV5Z basis set influences BSSE. In Figure 3.1, it can be seen that uncontracting only the s functions in the set makes no significant difference to the magnitude of the BSSE. Uncontracting only the p functions reduces BSSE significantly, from 41.45 cm^{-1} to 2.55 cm^{-1} at $r = 4.2$ Å. But only the cc-pCV5Z basis sets eliminates the problem of having a large BSSE.

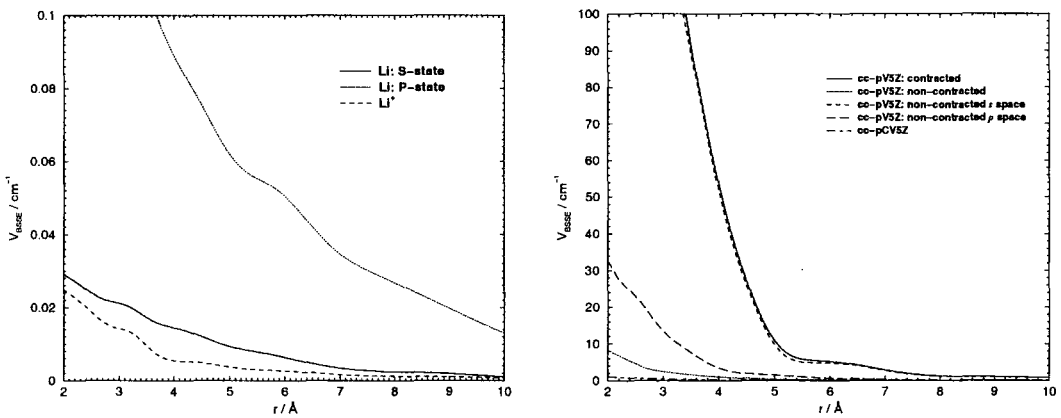

Figure 3.1: Basis set superposition error of an atom in two-centre basis as a function of intercentre distance in RHF (left) and RCCSD(T) (right) using cc-pV5Z basis set and different contraction schemes.

Turning our attention back to Table 3.10, it may be noted that interaction energies calculated using the cc-pCVXZ basis sets are similar to those obtained using the non-contracted cc-pVXZ at all levels X at $r = 4.2$ Å, near equilibrium. The agreement is poorer at short range, where the inadequacy of the basis set becomes apparent in the BSSE as well (see Figure 3.1).

Ignoring the core-correlation effects does not seem to bring the desired accuracy. In frozen core approximation, the interaction energies $r = 4.2$ Å are underestimated and at $r = 3.3$ Å they are overestimated.

Convergence with the size of the basis set, increasing X, is established for all types of basis sets considered, and is slower at short range.

Augmentation lowers the interaction energies at both distances considered in Table 3.10. It has a smaller effect for larger basis sets because more functions with small exponents have already been included. We have also tried doubly augmenting the basis, but it does not bring a significant further energy lowering. Augmenting the non-contracted cc-pVQZ basis set lowers the energy at $r = 4.2$ Å by 1.4%. Double augmentation lowers it by further 0.1%.

Potential characteristics of curves calculated using different types and sizes of correlation consistent basis sets are summarized in Table 3.11. Dissociation energy measured from the bottom of potential well, D_e, and position of the minimum, r_e, have been calculated from Morse potential, of form

$$V(r) = D_e(1 - \mathrm{e}^{-a(r-r_e)})^2 - D_e, \tag{3.4}$$

that interpolates the *ab-initio* energies calculated at $r = 4.1$ Å, 4.2 Å, and 4.3 Å. The position where the interaction energy crosses zero, σ_0, was calculated from Morse potential (3.4) with D_e taken from the above described calculation and two *ab-initio* energies calculated at $r = 3.3$ Å and 3.4 Å. The error in σ_0 and D_e is in the last digit shown in the table. The values for D_e and r_e may be compared with experiment. The most recent RKR potential was published by Linton et al. [48] obtained from perturbation facilitated optical-optical double resonance spectroscopy. They report $D_e = (333.69 \pm 0.10)$ cm^{-1} and $r_e = 4.173$ Å. Abraham et al. [54] obtained $D_e = (333.78 \pm 0.02)$ cm^{-1}, analyzing the data from a photoassociation experiment. Halls et al. [46] published QCISD(T) potential using cc-pV5Z and obtained $D_e = 334.145$ cm^{-1} and $r_e = 4.169$ Å. This result is probably obtained using the contracted basis set and it is in close agreement with our CCSD(T) value of 334.042 cm^{-1} at the same r_e. CCSD(T) and QCISD(T) should be similar methods, but CCSD(T) is more complete [59].

Convergence of r_e and D_e for the non-contracted cc-pVXZ and (contracted) cc-pCVXZ basis sets is towards the experimental values. The contracted cc-pVXZ basis sets converge towards an overestimated D_e. The effect of the first level of augmentation is significant even at the cc-pCV5Z level, deepening the well by 1.6 cm^{-1}.

The potential curve in the frozen core approximation overestimates σ_0 and r_e. The effect of the core-core correlation is to decrease the size of the system and also

basis	σ_0 / Å	r_e / Å	$-D_e$ / cm^{-1}
T	3.3886	4.196	−318.284
T unc p	-	-	-
T unc all	3.3860	4.192	−310.098
FC T	3.3982	4.216	−318.854
CT	3.3886	4.196	−310.505
AT	3.3740	4.195	−333.809
AT unc p	-	-	-
AT unc all	3.3765	4.198	−322.769
FC AT	3.3848	4.216	−334.068
ACT	3.3763	4.198	−324.202
Q	3.3586	4.176	−332.620
Q unc p	3.3653	4.182	−325.543
QZ unc all	3.3658	4.183	−324.914
FC Q	3.3798	4.201	−334.809
CQ	3.3623	4.179	−325.499
AQ	3.3561	4.176	−337.260
AQ unc p	3.3628	4.186	−329.299
AQ unc all	3.3634	4.185	−328.551
FC AQ	3.3768	4.202	−339.173
ACQ	3.3598	4.181	−329.173
5	3.3536	4.169	−334.042
5 unc p	3.3592	4.178	−328.924
5 unc all	3.3594	4.178	−328.732
FC 5Z	3.3766	4.199	−338.471
C5	3.3567	4.175	−328.952
A5	3.3521	4.170	−335.770
A5 unc p	3.3581	4.179	−330.573
A5 unc all	3.3583	4.179	−330.339
FC A5	3.3754	4.200	−340.275
AC5	3.3557	4.176	−330.545

Table 3.11: Well depth, D_e, position of minimum, r_e, and position where potential curve crosses zero energy (atomic $S+S$ limit), σ_0, for $^3\Sigma_u^+$ state of Li_2 in RCCSD(T) using different cc-pVXZ (X) and cc-pCVXZ (CX) basis sets; augmented (A), contracted, non-contracted (unc all), and with s functions contracted only (unc p) and either with all electrons correlated or with a frozen core (FC).

to lower the binding energy at the minimum by $\approx 3\%$.

It is affordable to perform the CCSD(T) calculations for lithium dimer using the largest basis set, aug-cc-pCV5Z, analyzed here. We have obtained potential curves and calculated vibrational bound-state energies and the scattering lengths using aug-cc-pCV5Z basis set, the basis set extrapolated to the complete-basis-set (CBS) limit from aug-cc-pCVQZ and aug-cc-pCV5Z, and also using the cc-pV5Z basis with uncontracted p functions.

The potential was constructed by interpolation from electronic energies calculated on the mesh of 64 interatomic distances. Step of 0.2 Å was applied between 1.6 Å and 2.6 Å , 0.1 Å between 2.7 Å and 6.0 Å, 0.2 Å between 6.2 Å and 8.0 Å, 0.5 Å between 8.5 Å and 10 Å, and 1 Å between 11 Å and 20 Å. The potential was interpolated using reciprocal powers reproducing kernel Hilbert space interpolation (RP-RKHS), described in the next chapter, with the predetermined dispersion coefficients C_6, C_8, and C_{10} to match those of Yan et al. [95]. Potential, represented in this way, extrapolates to a pure dispersion interaction energy determined by the three coefficients. The parameters of the interpolation, in the notation from Chapter 4, are $m = 2$, $n = 3$, $r_a = 15$ Å, $r(65) = 21.5$ Å, $r(66) = 22.5$ Å, and $r(67) = 23.5$ Å. At 16 Å, *ab-initio* electronic energies extrapolated to the CBS limit overestimate the dispersion energy calculated using C_6, C_8, and C_{10} from Ref. 95 by 0.5%. At larger interatomic separations, *ab-initio* energies were replaced by the ones calculated from the dispersion energy expansion. At $r = 16$ Å, the $-C_6/r^6$, $-C_8/r^8$, and $-C_{10}/r^{10}$ terms contribute 93.3%, 6.1%, and 0.6%, respectively, to the dispersion energy approximated by first three leading contributions in the multipole expansion. The dispersion energy is discussed further in Chapter 5.

Basis set extrapolation was performed using a two-parameter formula [59]

$$E_X = A + \frac{B}{X^3}. \tag{3.5}$$

Only the correlation energy was extrapolated. The HF energy was taken from the cc-pCV5Z calculation. It was not extrapolated because the steps in the convergence did not fit well the exponential form. This may be due to slight deficiencies in the *sp* basis at smaller basis size. We have checked first how extrapolation to the CBS limit performs on the atomic energies. Extrapolating the cc-pCVQZ and cc-pCV5Z energies delivered a value 0.001% off the best theoretical value [90], which

is an improvement over the cc-pCV5Z energy (0.0086% off). We have repeated the procedure for all the dimer electronic energies on the mesh using energies obtained by the aug-cc-pCVQZ and aug-cc-pCV5Z basis sets.

Vibrational energies of the potential were obtained by variational expansion onto a sine basis. The sine functions that we used are the eigenfunctions of the hard wall potential delimited by r_{min} and r_{max}. The vibrational energies of the bound levels needed to be converged with respect to the inner and outer limits, r_{min} and r_{max}, the number of sine functions, and the number of integration steps in calculating matrix elements of the diatomic hamiltonian between the sine functions. Integration with sines was performed using fast fourier transform algorithm [96]. The method is not particularly efficient for energy levels close to dissociation, but in most cases it delivers all the bound-state energies by one diagonalization. The scattering length was calculated from the wavefunction propagated at the zero energy as described in Chapter 7. Such a zero-energy wavefunction and the wavefunction of $v = 10$ vibrational state for the potential extrapolated to the CBS limit are shown in Figure 3.2. The vibrational quantum number at dissociation is determined using the phase integral calculated to obtain the scattering length and includes the shift of 1/8 with respect to the number obtained in the near dissociation expansion, as discussed in Ref. 97.

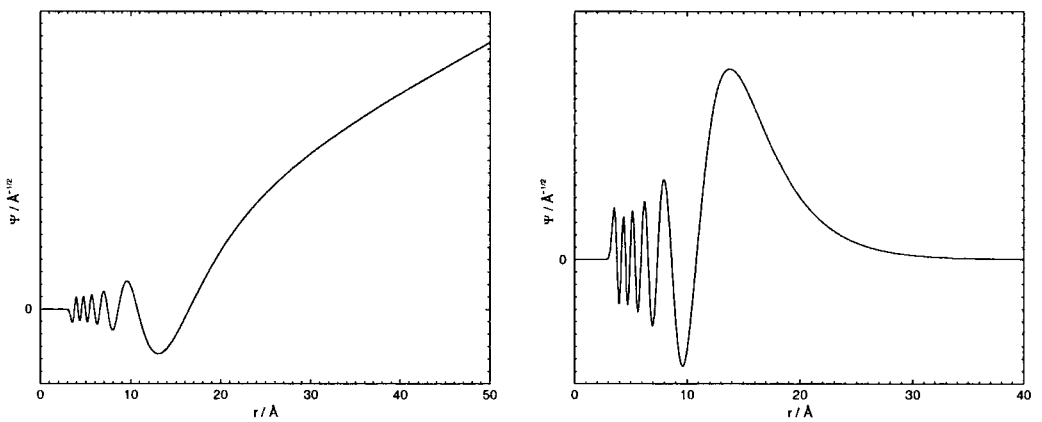

Figure 3.2: Wavefunction at zero energy (left) and of the vibrational level $v = 10$ (right) of lithium dimer.

Vibrational energies of $^7Li_2$ and turning points of the bound levels are shown in Table 3.12 for cc-pV5Z with uncontracted p functions, in Table 3.13 for aug-cc-pCV5Z, and in Table 3.14 for the potential extrapolated to the CBS limit. The

results may be compared to energy levels obtained by Linton et al. [48] using RKR in Table 3.15. Dissociation energies, position of the minimum and scattering lengths for $^7Li_2$ using the same basis sets are reported in Table 3.16.

v	$G(v)$ / cm^{-1}	R_{min} / Å	R_{max} / Å
0	31.785	3.851	4.638
1	90.145	3.674	5.101
2	141.999	3.576	5.512
3	187.522	3.509	5.930
4	226.773	3.461	6.383
5	259.699	3.425	6.900
6	286.165	3.398	7.529
7	306.011	3.380	8.363
8	319.201	3.368	9.610
9	326.262	3.361	11.841
10	328.699	3.359	17.754

Table 3.12: Bound levels (with respect to potential minimum), $G(v)$, and their turning points, R_{min} and R_{max}, for the $^3\Sigma_u^+$ potential of $^7Li_2$. Potential calculated with RCCSD(T) using cc-pV5Z basis set with s functions contracted only.

The scattering length for $^7Li_2$ was determined by Abraham et al. [22] from the combined information from the RKR data and the binding energy of the uppermost vibrational level, $a = (-27.6 \pm 0.5)\ a_0$. The vibrational energy spacings for all basis sets underestimate the experimental results [48]. For the extrapolated potential, the discrepancies with the experiment are smallest. Comparing the vibrational spacings obtained by Halls et al. [46] to the RKR, it may be seen that they are smaller up to $v = 6$, and larger for higher levels. The same is true for the CCSD(T) potential with the contracted cc-pV5Z basis. This is deficiency of the contracted basis sets when used in calculations where all electrons are being correlated. The shape of the well is better represented when core-core correlation is taken into account. Extrapolated potential has a deeper well, compared to the aug-cc-pCV5Z basis, the system is slightly smaller in size, r_e, and the classical turning points of the bound levels, R_{min} and R_{max}, are all smaller. The binding energy of the last vibrational level, $v = 10$, is 0.416 cm^{-1}. This may be compared to 0.223 cm^{-1}, 0.346 cm^{-1}, and 0.374 cm^{-1}, for cc-pV5Z with non-contracted p space, aug-cc-pCV5Z, and the CBS extrapolated

v	$G(v)$ / cm^{-1}	R_{min} / Å	R_{max} / Å
0	31.741	3.849	4.636
1	89.995	3.672	5.100
2	141.727	3.574	5.513
3	187.119	3.507	5.932
4	226.252	3.459	6.385
5	259.124	3.423	6.901
6	285.672	3.397	7.523
7	305.822	3.378	8.330
8	319.580	3.365	9.502
9	327.305	3.358	11.534
10	330.202	3.356	16.561

Table 3.13: Bound levels (with respect to potential minimum), $G(v)$, and their turning points, R_{min} and R_{max}, for the $^3\Sigma_u^+$ potential of $^7Li_2$. Potential calculated with RCCSD(T) using aug-cc-pCV5Z basis set.

v	$G(v)$ / cm^{-1}	R_{min} / Å	R_{max} / Å
0	31.825	3.845	4.631
1	90.238	3.668	5.094
2	142.105	3.570	5.507
3	187.612	3.504	5.925
4	226.836	3.455	6.378
5	259.782	3.419	6.893
6	286.406	3.393	7.513
7	306.661	3.374	8.314
8	320.567	3.361	9.471
9	328.435	3.354	11.469
10	331.428	3.352	16.347

Table 3.14: Bound levels (with respect to potential minimum), $G(v)$, and their turning points, R_{min} and R_{max}, for the $^3\Sigma_u^+$ potential of $^7Li_2$. Potential calculated with RCCSD(T) using the basis extrapolated from aug-cc-pCVQZ and aug-cc-pCV5Z to the complete-basis-set limit.

v	$G(v)$ / cm^{-1}	$R_{\min}$ / Å	$R_{\max}$ / Å
0	31.857	3.846	4.630
1	90.453	3.668	5.092
2	142.523	3.571	5.503
3	188.240	3.505	5.922
4	227.679	3.458	6.373
5	260.837	3.422	6.885
6	287.665	3.395	7.501
7	308.098	3.377	8.297
8	322.155	3.365	9.441
9	330.170	3.358	11.392
10	333.269	3.356	16.052

Table 3.15: The RKR bound levels (with respect to potential minimum), $G(v)$, and turning points, $R_{\min}$ and $R_{\max}$, for the $^3\Sigma_u^+$ potential of $^7Li_2$, taken from Ref. 48.

basis	r_e / Å	$-D_e$ / cm^{-1}	a / a_0	v_D
5 unc p	4.177	−328.922	12.54	10.67
AC5	4.176	−330.548	−8.95	10.79
CBS	4.171	−331.802	−15.80	10.81

Table 3.16: Dissociation energy, D_e, position of the minimum, r_e, scattering length, a, and vibrational quantum number at dissociation, v_D, for $^7Li_2$ molecule calculated using RCCSD(T) with cc-pV5Z basis with s functions contracted, with aug-cc-pCV5Z, and core valence basis set extrapolated to the complete-basis-set limit.

basis, respectively. The binding energy of the last level is connected to the value of the scattering length. The scattering length obtained using cc-pV5Z basis set has a wrong sign. The vibrational spacings are in good agreement with the RKR for $v \leq 6$, but for $v > 6$ they are underestimated by larger amount. The binding energy for this basis is the smallest from the basis sets considered, as is the dissociation energy. The scattering lengths and dissociation energies of the other two basis sets converge towards the value obtained by Abraham et al. [22]. At the CBS limit the well is still not deep enough to reproduce the scattering length. The reasons for that may be due to the deficiencies in the basis sets or the neglect of some of the triply and quadruply excited configurations in the RCCSD(T) method.

We have also calculated the vibrational energies of $^6Li_2$ and $^6Li^7Li$ using the best potential, the one extrapolated to the CBS limit. The results are shown in Tables 3.17 and 3.18. The vibrational energies of $^6Li_2$ have been published by Linton et al. [49]. This results are old and the discrepancies between *ab initio* and RKR are larger. Vibrational spacings are again somewhat smaller for the *ab-initio* potential. The binding energy of the last vibrational level, $v = 9$, is determined by Abraham et al. [54] to be 0.815 cm^{-1}. The *ab-initio* potential gives 0.751 cm^{-1}. The scattering length and vibrational quantum number at dissociation are $a = -266.95\ a_0$ and $v_D = 9.97$. There is a virtual level lying slightly above the dissociation limit as a large negative scattering length indicates. The scattering length obtained by Abraham et al. [54], using RKR data [48] and experimentally determined binding energy of the last vibrational level in $^6Li_2$ and in $^7Li_2$, is $(-2160\pm250)\ a_0$. The discrepancy between the *ab-initio* and value by Abraham et al. [54] is large, but the scattering length changes rapidly (passes through a pole) when a level is near the dissociation limit. The calculated scattering length and vibrational quantum number at dissociation for $^6Li^7Li$ system are $a = 44.11\ a_0$ and $v_D = 10.37$. The scattering length by Abraham et al. [54] is $40.9\pm0.2\ a_0$, in very good agreement. The binding energy of the uppermost vibrational level has not been published to our knowledge and it is -0.0535 cm^{-1} for $v = 10$, determined from our *ab-initio* calculations.

An interesting possibility for future work would be to try to scale these potentials in some way to obtain a better agreement with the experimental data [98]. An alternative way forward might be fitting the electronic energies to an analytic form and subsequently fitting to experimental data with some parameters set to predicate

v	$G(v)$ / cm^{-1}	R_{min} / Å	R_{max} / Å
0	34.303	3.834	4.653
1	96.812	3.654	5.145
2	151.718	3.555	5.589
3	199.230	3.489	6.048
4	239.424	3.441	6.555
5	272.280	3.407	7.150
6	297.737	3.382	7.900
7	315.760	3.366	8.946
8	326.529	3.356	10.679
9	331.051	3.352	14.592

Table 3.17: Bound levels (with respect to potential minimum), $G(v)$, and their turning points, R_{min} and R_{max}, for the $^3\Sigma_u^+$ potential of $^6Li_2$. Potential calculated with RCCSD(T) using the basis extrapolated from aug-cc-pCVQZ and aug-cc-pCV5Z to the complete-basis-set limit.

v	$G(v)$ / cm^{-1}	R_{min} / Å	R_{max} / Å
0	33.089	3.839	4.642
1	93.600	3.660	5.120
2	147.036	3.562	5.548
3	193.594	3.496	5.987
4	233.353	3.448	6.467
5	266.305	3.413	7.021
6	292.396	3.387	7.703
7	311.583	3.369	8.617
8	323.943	3.358	10.024
9	330.072	3.353	12.757
10	331.749	3.352	22.504

Table 3.18: Bound levels (with respect to potential minimum), $G(v)$, and their turning points, R_{min} and R_{max}, for the $^3\Sigma_u^+$ potential of $^6Li^7Li$. Potential calculated with RCCSD(T) using the basis extrapolated from aug-cc-pCVQZ and aug-cc-pCV5Z to the complete-basis-set limit.

values from the fit to *ab initio*. One analytic form that might be used is the modified Lennard-Jones potential [99].

It should be noted that the presented potentials are smooth and predict the correct number of vibrational bound levels. It was noticed that the second derivative of the RKR potential by Linton et al. [48] wiggles between 3.5 Å and 3.7 Å.

3.3.3 Triatomic properties

The aim of the analysis in this chapter is to determine the best basis set to be used in calculation of electronic energies of the quartet ground state of lithium trimer. We have tested the basis sets on atomic and diatomic systems so far and compared the results with the available experimental data. This chapter will be concluded with a report on the performance of the basis sets on calculating trimer energies and the magnitude of the BSSE that is an indicator of inadequacies of the one-centre basis sets. No experimental information is available to our knowledge on this system, so comparisons cannot be made. The choice of the basis set that will be used to calculate electronic energies on the entire grid for representing the reactive potential energy surface of the trimer will be made.

Interaction energies of the trimer are calculated using the counterpoise correction procedure [94],

$$V_{\rm int}(r_1, r_2, r_3) = V_{\rm trim}(r_1, r_2, r_3) - \sum_{i=1}^{3} V_{\rm at}^{i}(r_1, r_2, r_3), \tag{3.6}$$

where $V_{\rm trim}$ is the total trimer energy with respect to all electrons and nuclei break-up and $V_{\rm at}^{i}$ are lithium atomic energies calculated in the same three-centre basis of the trimer. The nonadditive interaction energy, V_3, is

$$V_3(r_1, r_2, r_3) = V_{\rm int}(r_1, r_2, r_3) - \sum_{i<j}^{3} V_2^{ij}(r_1, r_2, r_3), \tag{3.7}$$

where

$$V_2^{ij}(r_1, r_2, r_3) = V_{\rm dim}^{ij}(r_1, r_2, r_3) - V_{\rm at}^{i}(r_1, r_2, r_3) - V_{\rm at}^{j}(r_1, r_2, r_3). \tag{3.8}$$

All energies are calculated in the three-centre basis.

The BSSE for the total interaction energy of the trimer (3.6) is the sum of the BSSE's for each atom,

$$V_{\rm BSSE}^{\rm atom}(r_1, r_2, r_3) = V_{\rm at}^{(1)} - V_{\rm at}^{(3)}(r_1, r_2, r_3). \tag{3.9}$$

The superscripts indicate the number of basis-set centres used for calculation of electronic energies. For C_s geometries all three atoms may be non-equivalent and energy $V_{\rm at}^{(3)}$ must be calculated for each atom of the trimer. The BSSE of the nonadditive part of the potential includes also BSSE for dimers,

$$V_{\rm BSSE}^{\rm diatom}(r_1, r_2, r_3) = V_{\rm dim}^{(3)}(r_1, r_2, r_3) - V_{\rm dim}^{(2)}(r_k), \tag{3.10}$$

with superscripts having the same meaning as above. There are, generally (C_s), three dimers, denoted by k in (3.10), in a trimer and energy must be calculated for each in the CC procedure. The two sources of BSSE in the nonadditive part, (3.9) and (3.10), have opposite signs, positive and negative, respectively, and partially cancel in the expression for nonadditive interaction energy, (3.7) and (3.8) combined.

Convergence of the total and the nonadditive part of the trimer interaction energy with the basis set near stationary points at D_{3h} and $D_{\infty h}$ geometries is shown in Table 3.19. The magnitude of each source of BSSE for different basis sets is reported in Table 3.20 for D_{3h} geometry where all three atoms and three dimers are equivalent. The discussion of the convergence of the interaction energies of the dimer may be extended here without modification. Although the two sources of the BSSE in the case of the nonadditive interaction energies cancel quite well near the D_{3h} minimum, they reveal any inadequacies in the basis sets and those with a large BSSE should preferably not be used. Potential characteristics at D_{3h} configurations, obtained in an analogous manner to those of the dimer potential, are summarized in Table 3.21. Only the largest basis sets are reported between which the final choice must be made.

It is obvious that using the largest basis set considered here, aug-cc-pCV5Z, would yield the most reliable electronic energies, but our computational resources do not allow its use for the trimer. Some computational aspects are summarized in Table 3.22. The real and CPU times and the requirements on the hard-disc space are for the full counterpoise-corrected interaction energies at a D_{3h} geometry near equilibrium, calculated internally in C_{2v} symmetry. For a good representation of reactive surface we will need to evaluate points at C_s configurations, which is more demanding computationally. Calculation of the total counterpoise-corrected interaction energy at C_s with the cc-pV5Z basis where the p space is uncontracted takes 331 minutes of real time, 264 minutes of CPU time, and requires 11.10 GB of hard-disc memory. If no contraction is applied, it takes 630 minutes of real time, 339 of CPU time, and

	D_{3h}: $r = 3.2$ Å		$D_{\infty h}$: $r = 3.8$ Å	
	V_{int} / cm^{-1}	V_3 / cm^{-1}	V_{int} / cm^{-1}	V_3 / cm^{-1}
T	−3866.0931	−4673.0110	−925.4766	−338.3250
T unc p	-	-	-	-
T unc all	−3798.4158	−4579.6808	−898.4560	−325.8667
FC T	−3821.9008	−4680.7072	−919.9465	−338.1248
CT	−3799.5980	−4590.1752	−899.3395	−327.1310
AT	−3920.4770	−4679.7190	−964.7496	−348.5394
AT unc p	-	-	-	-
AT unc all	−3839.6856	−4592.1618	−928.6071	−335.2552
FC AT	−3875.4137	−4693.0558	−958.0661	−348.8676
ACT	−3848.5997	−4599.7928	−933.3482	−336.8339
Q	−3978.4500	−4663.7270	−966.1009	−345.6122
Q unc p	−3897.3487	−4602.2331	−940.1817	−336.4626
Q unc all	−3889.9222	−4596.7614	−938.0014	−335.6772
FC Q	−3903.9343	−4700.6994	−960.0338	−348.2622
CQ	−3905.5957	−4595.7503	−941.4993	−336.0035
AQ	−3986.7604	−4666.6682	−976.4040	−347.3362
AQ unc p	−3909.4182	−4607.8409	−948.3457	−338.1951
AQ unc all	−3902.6682	−4602.3592	−945.6116	−337.4086
FC AQ	−3918.1494	−4706.9432	−969.5392	−350.4303
ACQ	−3918.0605	−4601.1397	−949.1473	−337.7004
5	−3974.8684	−4693.0734	−967.9229	−343.0650
5 unc p	−3922.8694	−4604.1593	−949.4090	−337.4908
5 unc all	−3920.4546	−4602.3998	−948.6674	−337.2356
FC 5	−3918.8787	−4706.7396	−968.0262	−349.4856
C5	−3930.3763	−4599.2264	−950.4851	−337.1051
A5	−3980.1350	−4640.7190	−970.9248	−343.8426
A5 unc p	−3929.1772	−4607.3136	−953.0212	−338.4696
A5 unc all	−3926.7383	−4605.5290	−952.1752	−338.2087
FC A5	−3925.0081	−4709.7208	−971.9110	−350.6064
AC5	-	-	-	-

Table 3.19: Total and nonadditive energy of the quartet ground state of Li_3 at two different nuclear configurations calculated with RCCSD(T) using different cc-pVXZ (X) and cc-pCVXZ (CX) basis sets; augmented (A), contracted, non-contracted (unc all), and with s functions contracted only (unc p) and either with all electrons correlated or with a frozen core (FC).

	D_{3h}: $r = 3.2$ Å	
	$V_{\mathrm{BSSE}}^{\mathrm{atom}}$ / cm^{-1}	$V_{\mathrm{BSSE}}^{\mathrm{diatom}}$ / cm^{-1}
T	−109.6671	98.2983
T unc p	-	-
T unc all	−3.8540	6.4218
FC T	−0.8603	4.5936
CT	−11.3776	14.1693
AT	−204.8927	176.6837
AT unc p	-	-
AT unc all	−5.8753	7.0759
FC AT	−1.2422	3.0748
ACT	−20.8259	20.9884
Q	−278.4277	264.1531
Q unc p	−93.1692	76.3860
Q unc all	−4.8548	5.5527
FC Q	−0.2063	1.2071
CQ	−2.9695	3.6674
AQ	−447.6865	343.7719
AQ unc p	−145.4919	68.8733
AQ unc all	−6.8432	6.6281
FC AQ	−0.1317	0.6628
ACQ	−4.2161	4.0230
5	−225.8723	207.6998
5 unc p	−16.7657	12.5312
5 unc all	−4.0208	4.4553
FC 5	−0.0307	0.5004
C5	−0.6123	0.9811
A5	−316.1137	233.8480
A5 unc p	−21.9365	13.1268
A5 unc all	−5.9324	5.6800
FC A5	−0.0395	0.2568
AC5	-	-

Table 3.20: Basis set superposition error of an S-state Li atom and of a $^3\Sigma_u^+$ Li_2 dimer in the three-centre basis at D_{3h} configuration with $r = 3.2$ Å. Calculated with RCCSD(T) using different cc-pVXZ (X) and cc-pCVXZ (CX) basis sets; augmented (A), contracted, non-contracted (unc all), and with s functions contracted only (unc p) and either with all electrons correlated or with a frozen core (FC).

basis	σ_0 / Å	r_e / Å	D_e / cm^{-1}
5	2.4621	3.102	−4021.49
5 unc p	2.4641	3.102	−3969.77
5 unc all	2.4641	3.102	−3967.40
FC 5	2.4911	3.137	−3937.51
C5	2.4611	3.098	−3980.59

Table 3.21: Well depth, D_e, position of minimum, r_e, and position where D_{3h} potential crosses zero energy (atomic $S+S+S$ limit), σ_0, for $^4A_2'$ state of Li_3 in RCCSD(T) using cc-pV5Z (5) and cc-pCV5Z (C5) basis sets; contracted, non-contracted (unc all), and with s functions contracted only (unc p) and either with all electrons correlated or with a frozen core (FC).

requires 13.64 GB of hard disc. Use of the cc-pCVQZ basis set would be even more demanding, as can be seen in the table. Therefore computational demands limit us to the triple zeta level in the core valence basis sets, cc-pCVTZ, which are optimized to deal with the core-correlation effects. The frozen core approximation allows the use of the non-augmented cc-pV5Z basis set, but the non-contracted cc-pV5Z basis set provides a better description of the potential characteristics, as can be seen in Table 3.21, and is in closer agreement with the results obtained by the largest basis set, cc-pCV5Z, than the cc-pCVTZ. Contracting the s functions provides an important time saving without a significant loss in accuracy, so the decision was made to use this basis set for the calculation of electronic energies for the full potential energy surface of lithium trimer. This task is undertaken in the next chapter.

basis	REAL / min	CPU / min	DISC / GB
FC 5	27	17	4.42
FC A5	166	105	16.67
5	68	53	4.42
5 unc p	78	67	4.80
5 unc all	126	96	7.15
A5	428	236	17.00
A5 unc p	497	286	19.96
A5 unc all	686	394	23.83
CQ	42	36	2.12
ACQ	144	118	7.06
C5	546	354	23.39

Table 3.22: Real and CPU times and usage of hard disc for evaluation of the counterpoise-corrected total and nonadditive interaction energy of lithium trimer on a Sun Fire machine (UltraSPARC-III Cu processor of 1200 MHz) using different correlation consistent basis sets; X = cc-pVXZ, CX = cc-pCVXZ, A = aug, FC = frozen core, unc p = non-contracted p functions, unc all = non-contracted basis set.

Chapter 4

Interpolation and fitting of potential energy surfaces

4.1 Introduction

Quantum chemical calculations of potential energy surfaces of high accuracy are demanding on computer resources. Dynamical studies of the motion of nuclei usually require evaluation of potential energy at a great number of nuclear geometries. Therefore it is desirable to have a way of representing potential energy surfaces based on a relatively small number of *ab-initio* determined electronic energies. This is commonly achieved by either fitting of analytical forms on *ab-initio* energies or by interpolating them.

Our particular problem is finding a representation of potential energy surface for reactive scattering calculations of three identical atoms. In the Born-Oppenheimer approximation the potential is symmetric under exchange of nuclei. To avoid any artificial phenomena in collision dynamics this symmetry must be built into the potential representation. The accuracy of the potential for our problem is particularly important in the strong interaction region and in the asymptotic reactant and product arrangements. The analytic representation of the long-range interactions will be developed in the next chapter and fitted on available data for lithium quartet system. This chapter is concerned with fitting to electronic energies in the strong interaction region. The two regions must be smoothly matched into a global representation of potential.

The potential energy surface that correlates with the quartet ground state of three lithium atoms intersects an excited quartet surface at a seam at linear configurations. The seam passes below the three-body dissociation limit in the strong interaction region. An accurate solution of the nuclear Schrödinger equation for three nuclei would require two diabatic potentials and the non-adiabatic coupling between them. This is currently too expensive to do computationally for this system. We made an approximation and ignored the higher surface and coupling between the two to make the dynamics calculations feasible. In this way, we were able to calculate the lower surface with greater precision using cheaper single-reference methods with a large basis set. This was addressed in the previous chapter. Drawback of this approach is that the lowest adiabatic surface has a derivative discontinuity at the seam, which cannot be easily incorporated in any interpolation or fitting methods available for potential energy surfaces. There are two apparent ways around this

problem. One is to fit or interpolate both diabatic surfaces and the coupling between them and perform calculations on the lower eigenvalue. The other is to sacrifice the quality of the fit in the vicinity of conical intersection. The latter approach was taken here. Near a conical intersection, the Born-Oppenheimer approximation is invalid and dynamics influenced by that region of the potential energy surface is not accurate in any case. We believe that most of the conclusions that we will draw from the scattering calculations will hold even in the presence of the excited surface. The sensitivity of the dynamics to the potential is also explored in the limit of zero collision energy in Chapter 9. But the influence of the excited surface on the dynamics will not be known until the calculations on both surfaces can be performed.

Some techniques for representing potential energy surfaces are described in a review by Schatz [100] and references therein. New methods are still being developed. From a vast choice, we present three methods that we have implemented and comment on their applicability in representing the surface of lithium trimer. The IMLS/Shepard fit is finally described in most detail. The global representation of the potential energy surface is postponed until the next chapter, where the analytic long-range form will be incorporated in our fit.

4.2 Interpolation and fitting of potential energy surfaces of triatomic systems

4.2.1 Reproducing Kernel Hilbert Space interpolation

The reproducing kernel Hilbert space (RKHS) interpolation method is a global method specifically formulated for potential energy surfaces [101]. The potential energy as a function of one coordinate is defined in terms of the reproducing kernel functions $q(x, x')$. The reproducing kernel functions were designed to have desirable properties for interpolation such as smoothness and well-behaved extrapolation properties [102].

A reciprocal power RKHS has been constructed [101] for interpolating in distance-like coordinates in the range $[0, \infty)$. The one-dimensional interpolant for N_d data points at $r(i)$ with potential energies $V(r(i))$ is expressed as a linear combination of

kernel functions,

$$V^{[n,m]}(r) = \sum_{i=1}^{N_d} \alpha_i^{[n,m]} q^{[n,m]}(r, r(i)), \tag{4.1}$$

where

$$q^{[n,m]}(x, x') = \frac{1}{x_<^{m+1}} \sum_{k=0}^{n-1} \beta_k^{[n,m]} \frac{x_<^k}{x_>^k} \tag{4.2}$$

is a reproducing kernel, $x_< = \min(x, x')$, $x_> = \max(x, x')$, and the coefficients $\beta_k^{[n,m]}$ are constants given in Ref. 101. The coefficients $\alpha_i^{[n,m]}$ are found by solving the linear system

$$V(r(j)) = \sum_{i=1}^{N_d} \alpha_i^{[n,m]} q^{[n,m]}(r(i), r(j)). \tag{4.3}$$

It can be seen that the RKHS potential extrapolates to a series in inverse powers of r at long range. The leading power of the asymptotic expansion is $r^{-(m+1)}$ and n is the number of asymptotic terms,

$$V^{[n,m]}(r) = -\sum_{k=0}^{n-1} \frac{\beta_k^{[n,m]} \sum_{i=1}^{N_d} \alpha_i^{[n,m]} r(i)^k}{r^{m+1+k}}. \tag{4.4}$$

For a long-range dispersion interaction between two S-state atoms, interpolation is best performed in the variable r^2 to prevent odd-order terms contaminating the expansion [103]. The choice $m = 2$ and $n = 3$ gives the correct first three terms in the r^{-1} expansion of dispersion interaction.

The set of chosen dispersion coefficients C_s may be built into the interpolation procedure [104] by extending the linear system (4.3) with n additional equations. For this purpose n additional $\alpha_i^{[n,m]}$ coefficients and distances $r(i)$ are introduced. The new system reads

$$\mathbf{Q}\alpha = \mathbf{V}, \tag{4.5}$$

where

$$Q_{ij} = \begin{cases} q^{[n,m]}(r(j), r(i)) & \text{for} \quad i = 1, \ldots, N_d,\ j = 1, \ldots, N_d \\ 0 & \text{for} \quad i = N_d + 1, \ldots, N_d + n,\ j = 1, \ldots, N_d \\ \frac{\beta_k^{[n,m]} r(i)^k}{r_a^{m+1+k}} & \text{for} \quad j = N_d + 1 + k,\ k = 0, \ldots, n-1 \end{cases}, \tag{4.6}$$

and

$$V_j = \begin{cases} V(r(j)) & \text{for} \quad j = 1, \ldots, N_d \\ -\frac{C_{m+1+k}}{r_a^{m+1+k}} & \text{for} \quad j = N_d + 1 + k,\ k = 0, \ldots, n-1 \end{cases}. \tag{4.7}$$

The largest $r(i)$ delimits the asymptotic region, and r_a should be a distance at which different dispersion terms in the sum (4.4) are comparable in magnitude.

The short range extrapolation of the RKHS potential results in a polynomial of order $n-1$. A sufficient number of *ab-initio* points must be included on the repulsive wall to ensure the accuracy of the interpolated potential there [103].

Reproducing kernels in more than one dimension can be constructed as a product of one-dimensional reproducing kernels in each of the coordinates [102]. They have been used for interpolation of the nonadditive part of interaction potential of the quartet ground state potential of sodium trimer [80]. A three-dimensional reproducing kernel,

$$Q^{[n,m]}(\mathbf{r}(i),\mathbf{r}) = q^{[n,m]}(x,x')q^{[n,m]}(y,y')q^{[n,m]}(z,z'), \tag{4.8}$$

was symmetrized and the potential expressed as

$$V(\mathbf{r}) = \sum_{i=1}^{p} \alpha_i^{(3)} \left\{ \frac{1}{3!} \sum_{\{123\}} P^i_{\{123\}} Q^{[n,m]}(\mathbf{r}_i,\mathbf{r}) \right\}, \tag{4.9}$$

where x, y, and z represent interatomic distances scaled by a constant in such a way that α coefficients remain small. $P_{\{123\}}$ is the permutation operator of the indices 1, 2, and 3. The summation is over all possible permutations. The correct powers of the leading term of the nonadditive dispersion interaction at long range, the Axilrod-Teller term, were obtained by choosing $n = 2$, and $m = 2$. However, this potential does not reproduce the correct angular dependence of Axilrod-Teller term and the next order terms at long range are incorrect. Dispersion coefficient C_9 was not fixed to a predetermined value, as described above.

Other reproducing kernel functions have also been developed [102]. An exponentially decaying reproducing kernel over an interval $[0,\infty)$ [102] may be defined as

$$q_n^{\mathrm{ED}} = \frac{nn!}{\beta^{2n-1}} \mathrm{e}^{-\beta x_>} \sum_{k=0}^{n-1} \frac{(2n-2-k)!}{(n-1-k)!k!} [\beta(x_> - x_<)]^k, \quad \beta > 0. \tag{4.10}$$

This may be useful for interpolating potentials where a long-range potential is added on the interpolant in an analytic form.

4.2.2 Fitting of polynomials in symmetric coordinates

An attractive way to fit triatomic potentials with identical atoms is an expansion in an analytic function of symmetric coordinates [105]. Appropriate symmetry coordinates can be defined as

$$Q_1 = \frac{1}{\sqrt{3}}(r_1 + r_2 + r_3),$$

$$
\begin{aligned}
Q_2 &= \frac{1}{\sqrt{2}}(r_2 - r_3), \\
Q_3 &= \frac{1}{\sqrt{6}}(2r_1 - r_2 - r_3).
\end{aligned} \tag{4.11}
$$

It can be shown [105] that any function, symmetric under exchange of any two indices, may be written as sums and products of these three variables,

$$
Q_1, \quad Q_2^2 + Q_3^2, \quad Q_3^3 - 3Q_3Q_2^2. \tag{4.12}
$$

Murrell and co-workers used this fact to fit nonadditive potentials of beryllium [106] and helium trimer [107] to a 15-parameter form,

$$
\begin{aligned}
V &= \exp(-\alpha Q_1)\{c_0 + c_1Q_1 + c_2Q_1^2 + (c_3 + c_4Q_1 + c_5Q_1^2)(Q_2^2 + Q_3^2) \\
&+ (c_6 + c_7Q_1 + c_8Q_1^2)(Q_3^3 - 3Q_3Q_2^2) + (c_9 + c_{10}Q_1 + c_{11}Q_1^2)(Q_2^2 + Q_3^2)^2 \\
&+ (c_{12} + c_{13}Q_1 + c_{14}Q_1^2)(Q_2^2 + Q_3^2)(Q_3^3 - 3Q_3Q_2^2)\}.
\end{aligned} \tag{4.13}
$$

The evaluation of such a potential is very fast. The only non-linear parameter is α, while the coefficients c_i may be determined by solving a linear system for each α.

4.2.3 Interpolant moving least squares / Shepard interpolation

The interpolant-moving least squares (IMLS) method represents the interpolated value at a point in terms of linearly independent basis functions. The coefficients in this expansion are determined by the least-squares method. In the IMLS/Shepard method proposed by Ishida et al. [108], the IMLS interpolant is used only at the data points to evaluate approximate gradients and Hessians of the interpolating function. These numbers together with the functional values at data points are stored (ten values per data point) and used in a Taylor series expansion about each data point. The interpolating function is evaluated at an arbitrary point in the configuration space as a weighted sum of the Taylor expansions about all data points in the set. The final interpolant is a modified version of the Shepard method introduced by Ischtwan et al. [109].

In the IMLS method the interpolated value u at a point $\mathbf{Z}$ is represented as a linear combination of basis functions $b_j(\mathbf{Z})$,

$$
u(\mathbf{Z}) = \sum_{j=1}^{n} a_j(\mathbf{Z}) b_j(\mathbf{Z}) = \mathbf{a}^T(\mathbf{Z})\mathbf{b}(\mathbf{Z}). \tag{4.14}
$$

Here n is the number of basis functions and matrix notation is introduced so that $\mathbf{a}$ is a coefficient vector. We take the basis functions to be polynomials up to second order as in Ref. 108. Then the number of functions for a system with N_f degrees of freedom is $n = (N_f + 1)(N_f + 2)/2$. For a system of three particles, $N_f = 3$ and $n = 10$. The functions are: 1, Z_1, Z_2, Z_3, Z_1^2, Z_2^2, Z_3^2, Z_1Z_2, Z_1Z_3, and Z_2Z_3. The coordinates in which interpolation is performed were chosen to be inverse internuclear distances, $\mathbf{Z} = 1/\mathbf{r}$. This is more efficient than internuclear distances themselves for representing potential energy functions. We also require the second-order derivatives for evaluating the Taylor series, as mentioned above (which vanish if internuclear distances are used).

We denote the coordinates and energy values of the points we are interpolating by $\mathbf{Z}(i)$ and $f(i)$ and the number of them N_d. The coefficients a_j are determined at any point $\mathbf{Z}$ in the configuration space by minimizing the weighted sum of the squared deviations at the data points,

$$\sum_{i=1}^{N_d} w_i(\mathbf{Z})[u(\mathbf{Z}(i)) - f(i)]^2, \tag{4.15}$$

where $w_i(\mathbf{Z})$ are the weights. The requirement that the functional (4.15) be stationary with respect to variation in the parameters $a_j(\mathbf{Z})$ leads to a linear system of equations written in matrix form as

$$BW(\mathbf{Z})B^T\mathbf{a}(\mathbf{Z}) = BW(\mathbf{Z})\mathbf{f}. \tag{4.16}$$

Here, W is a diagonal matrix with weights w_i on the diagonal and B is composed of the basis functions evaluated at data points,

$$B = \begin{pmatrix} b_1(\mathbf{Z}(1)) & b_1(\mathbf{Z}(2)) & \cdots & b_1(\mathbf{Z}(n)) \\ b_2(\mathbf{Z}(1)) & b_2(\mathbf{Z}(2)) & \cdots & b_2(\mathbf{Z}(n)) \\ \cdots & \cdots & \cdots & \cdots \\ b_n(\mathbf{Z}(1)) & b_n(\mathbf{Z}(2)) & \cdots & b_n(\mathbf{Z}(n)) \end{pmatrix}. \tag{4.17}$$

The dependence of the coefficients, $\mathbf{a}$, on coordinates is introduced through weight functions w_i. This approach can be applied to fitting potential energy functions directly and this has recently been done [110]. In this approach, the linear system (4.16) needs to be set up and solved for each configuration and the function evaluated using (4.14). This is computationally expensive.

The weight function may be defined as in Ref. 108, 109, by

$$w_i = \frac{\nu_i}{\sum_{j=1}^{N_d} \nu_j}, \tag{4.18}$$

and

$$\nu_i = \frac{1}{(||\mathbf{Z} - \mathbf{Z}(i)||^2 + \epsilon^2)^p}. \tag{4.19}$$

Here p is a parameter that determines the shape of the weight function and the range in which data points contribute to the interpolant at a point. The parameter ϵ is present to smooth out the singularities of the interpolant at data points. In fact with the introduction of a finite ϵ, u is not strictly an interpolant, but a fitting function. Previous applications involved $p = 3$, 6, and 9, while ϵ was kept small [108, 110–112]. If ϵ is infinitesimal, $w_i(\mathbf{Z}(j)) = \delta_{ij}$ and $0 \leq w_i(\mathbf{Z}) \leq 1$. From the definition (4.18) it follows that

$$\sum_{i=1}^{N_d} w_i(\mathbf{Z}) = 1, \tag{4.20}$$

for all $\mathbf{Z}$.

In the next step, we derive the gradients and Hessians at the data points. Using (4.14) and (4.16) with the weights defined in (4.18,4.19), we get the gradients

$$u_s(\mathbf{Z}) = \mathbf{a}^T(\mathbf{Z})\mathbf{b}_s(\mathbf{Z}). \tag{4.21}$$

The derivatives of coefficients at data points, $\mathbf{a}_s(\mathbf{Z})$ are zero when ϵ is infinitesimal. The Hessian is

$$u_{st}(\mathbf{Z}) = \mathbf{a}_{st}^T(\mathbf{Z})\mathbf{b}(\mathbf{Z}) + \mathbf{a}^T(\mathbf{Z})\mathbf{b}_{st}(\mathbf{Z}). \tag{4.22}$$

Using (4.16), $\mathbf{a}_{st}$ may be found by solving a linear system,

$$BW(\mathbf{Z})B^T\mathbf{a}_{st}(\mathbf{Z}) = BW_{st}(\mathbf{Z})[\mathbf{f} - B^T\mathbf{a}(\mathbf{Z})]. \tag{4.23}$$

In practical applications, the gradients and Hessians of the weight functions (4.18,4.19) are evaluated analytically. This procedure involves calculation with large numbers, so care must be taken that multiplications and divisions are carried out in a proper order to avoid a numerical overflow. The linear systems in (4.16) and (4.23) may be ill-conditioned. They are solved using the singular value decomposition method [96].

Shepard interpolation is an IMLS method where basis functions of zeroth order are adopted, $b(\mathbf{Z}) = 1$. In this case the coefficient a is equal to the interpolant u and for a normalized weight function (4.20) it is

$$u(\mathbf{Z}) = \sum_{i=1}^{N_d} w_i(\mathbf{Z}) f(i). \tag{4.24}$$

This method suffers from the so-called flat-spot phenomenon, meaning that the interpolant has zero gradient at all data points.

Ischtwan et al. [109] have solved the flat-spot problem by using Taylor series expansions instead of the energy values at data points in (4.24). Expansion up to the second order was shown to be necessary and sufficient for generating well-behaved potential energy functions [113]. In the IMLS/Shepard method, the potential is evaluated at an arbitrary point as

$$V(\mathbf{Z}) = \sum_{i=1}^{N_d} w_i(\mathbf{Z}) T_i(\mathbf{Z}), \tag{4.25}$$

where $T_i(\mathbf{Z})$ is a Taylor series expansion about $\mathbf{Z}(i)$ evaluated at $\mathbf{Z}$ up to the second order using potential value $V(\mathbf{Z}(i))$, gradients, and Hessians, precalculated as described above and stored,

$$\begin{aligned} T_i(\mathbf{Z}) &= V(\mathbf{Z}(i)) + \sum_{k=1}^{N_f} [Z_k - Z_k(i)] \left.\frac{\partial V}{\partial Z_k}\right|_{\mathbf{Z}(i)} + \\ &+ \frac{1}{2!} \sum_{k=1}^{N_f} \sum_{l=1}^{N_f} [Z_k - Z_k(i)][Z_l - Z_l(i)] \left.\frac{\partial^2 V}{\partial Z_k \partial Z_l}\right|_{\mathbf{Z}(i)} + \ldots \end{aligned} \tag{4.26}$$

The weights in (4.25) and (4.15) need not be the same. The only parameters of the method are ϵ and p.

The IMLS/Shepard method is easily extendable to more degrees of freedom. It can also be used with arbitrarily scattered data points. The interpolant may be symmetrized by symmetrizing the data points. The disadvantages are that the method becomes more expensive with inclusion of more data points and that asymptotically the interpolant tends to a constant. Therefore an alternative representation is needed at long range and switching or damping functions are needed to eliminate the influence of the interpolant there.

4.3 Choosing coordinates, grid, and method

Diatomic potentials are much easier to represent than triatomic potentials, either by a simple analytical form or by interpolation. It is sometimes useful to represent a potential energy surface of the triatomic system as a sum of the additive and nonadditive parts of the interaction potential. This is especially convenient when additivity is a good approximation and when the magnitude of the additive potential excludes from interest the configuration space where nonadditive interactions are large. In the case of the quartet ground state of lithium trimer, the total interaction

potential near equilibrium and at shorter distances is a result of cancellation of a large and attractive nonadditive part and a large and repulsive additive part of potential (see Chapter 2). Fitting or interpolating the parts separately could results in magnification of the relative errors in the representation of the resultant potential. We have therefore tried to interpolate the total interaction potential.

Choice of the coordinate system, grid of *ab-initio* points, and the method for interpolation or fitting are all intricately connected. It is therefore hard to give any independent statements on those three subjects. In spite of that, we explain here our logic behind these choices.

Generally, a systematic set of grid points should cover the regions of physical interest. If interpolation is performed in an independent set of coordinates, the scan in each of them with the others fixed should not pass through violent changes in the potential. If there are such violent changes, the interpolant is likely to oscillate in other regions of the potential.

The hyperspherical coordinate system is the coordinate system which we will use in the scattering calculations. It maps all the possible nuclear arrangements of the three atoms uniquely in the upper half of the three-dimensional coordinate system ($z > 0$). The origin corresponds to all the nuclei together at the same position. The plane $z = 0$ corresponds to collinear arrangements of nuclei, and the three rays at $\varphi = 30°$, $150°$, and $270°$ (φ is the azimuthal angle) correspond to two nuclei at the same position. Backward extensions of these rays map to $D_{\infty h}$ geometries. The z-axis corresponds to D_{3h} arrangements. The high-energy regions concentrated along the three rays are difficult to avoid if hyperspherical coordinates are used for interpolation. At long range, the physically interesting part of the surface is concentrated in the narrow arrangement valleys while the potential in the remainder of the space is zero. The space, parametrized in this way, seems to be an inefficient and bad choice for interpolation.

Elliptical coordinates (a generalization of Jacobi coordinates) have been used successfully for interpolation in two dimensions [114]. The angular dependence was expanded in Legendre polynomials and the coefficients of the expansion interpolated using the RKHS method for the distance-like variables. A three-dimensional scan would require the distance between the foci of the ellipse as a variable parameter too. For each arrangement of the nuclei we can define three elliptic coordinate systems

with focuses on the line defined with each nuclear pair. The space excluded from the interpolation within the ellipse of smallest size for a given focal distance can be covered by another elliptic system. But interpolation through different elliptic systems would result in an overlap of the same regions in the nuclear configuration space or an un-natural coverage.

Internuclear distances were previously used as coordinates to interpolate the quartet potential of the sodium trimer using the RKHS method in Ref. 80. We use them here to fit the lithium surface.

We formed a three-dimensional grid of internuclear distances, (r_1, r_2, r_3), from the following set of values in Ångstroms: 2.0, 2.4, 2.8, 3.2, 3.6, 4.0, 4.4, 4.8, 5.2, 6.0, 6.8, 8.4, 10.0. The grid at nonlinear geometries was constructed from all 315 possible combinations of r_1, r_2, and r_3, taken from the above set of distances. We have added additional points to the grid in such a way that for r_1 and r_2 from the set, the grid in r_3 included all distances larger than 10 Å in steps of 1.6 Å, which satisfy the triangle inequality, $r_3 < r_1 + r_2$. This produced another 56 points, such as, for example, $(6.0, 6.0, 11.6)$. A grid of 120 linear configurations was formed by taking all possible combinations of r_1 and r_2 from the set that additionally included the distance 5.6 Å. *Ab-initio* electronic energies of the quartet ground-state potential of lithium trimer were evaluated using RCCSD(T) with the cc-pV5Z basis set with un-contracted p functions. Electronic energies at two grid points, $(2.4, 4.4, 4.8)$ and $(2.0, 6.0, 6.8)$ in Ångstroms, failed to converge. The whole grid was based on 489 different electronic energies.

The RKHS method has proven to work well with a small number of grid points on a number of systems [102]. Initially, we tried to interpolate the angular slices of the lithium trimer potential using RKHS. The upper four panels in Figure 2.8 are the result of the reciprocal powers RKHS interpolation. The two-dimensional rectangular grid in the internuclear distances r_1 and r_2 included the points shown on the left panel in Figure 4.1 as well as the horizontal and vertical rows at distances of 1.6 Å, 8.4 Å, and 10 Å, not shown in the figure. On the right panel in Figure 4.1 is the RP-RKHS interpolant at $D_{\infty h}$ configurations. The surface is well-behaved. The derivative discontinuity at the seam did not cause difficulties in the interpolation. On the other hand, the RP-RKHS interpolant for angular slices with the angle between the internuclear distances r_1 and r_2 fixed at 60° and 90° was not well-behaved.

Figure 4.2 shows wiggles around the minimum for 60°. The kernel functions could not accommodate the functional form of the potential at short range. Interpolating the expression $\log(E/\mathrm{cm}^{-1} + 5000) - \log(5000)$, where E are electronic energies on the grid, removed the wiggles from the surface, shown in Figure 4.2, but unphysical features are still present on the repulsive wall. We have tried fitting with the exponential RKHS and got similar results. Extending the RKHS interpolation to fitting three-dimensional surfaces brings additional problems. The interpolant of the quartet ground state of the sodium trimer by Higgins et al. [80] was based on the C_{2v} geometries only. When one includes C_s points in the grid, the quality of the interpolant becomes more difficult to control. Inclusion of closely spaced points, to remove any wiggles in the surface, renders the RKHS method unstable, because the algebraic problem becomes ill-conditioned. Since representing the surface of lithium trimer is expected to be difficult anyway because of the presence of a seam at linear geometries and since we encountered complications in the two-dimensional RKHS interpolation of angular slices at 60° and 90°, we abandoned this approach.

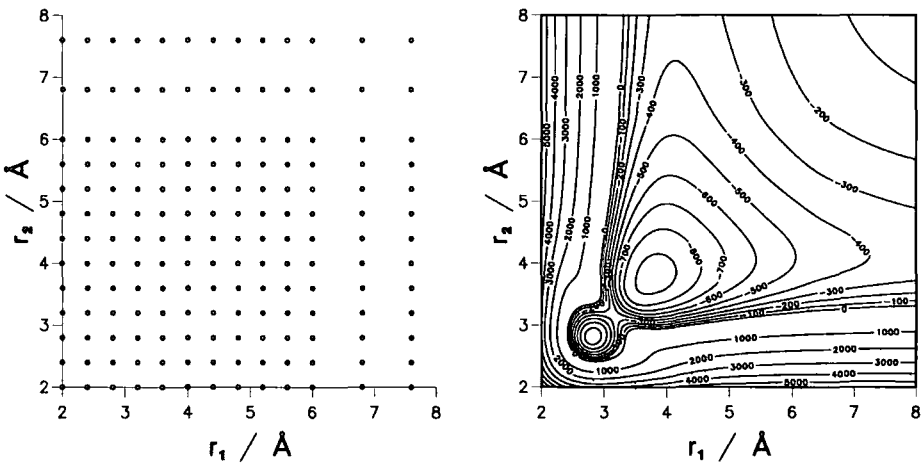

Figure 4.1: The grid of *ab-initio* points used in the interpolation of angular slices of the potential energy surface of lithium trimer in Figure 2.8 (left). RP-RKHS interpolant of the quartet ground state of lithium trimer at $D_{\infty h}$ geometries (right). Electronic energies are in cm^{-1}.

The well-behaved surfaces in the bottom row in Figure 2.8 are obtained using two-dimensional cubic splines method [96]. However, three-dimensional cubic splines would require a large rectangular grid.

Fitting the potential with the symmetric polynomials of Murrell et al. (4.13) is

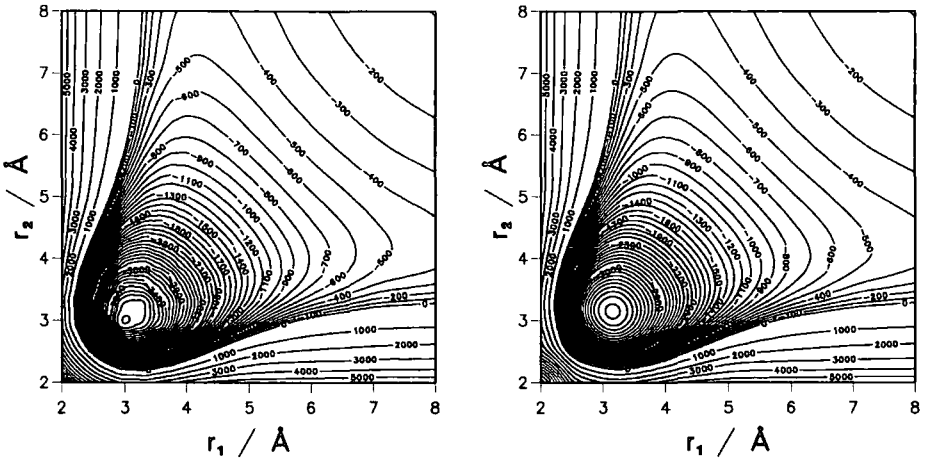

Figure 4.2: RP-RKHS interpolant of the quartet ground-state potential of lithium trimer at a fixed angle of 60° between the internuclear distances r_1 and r_2. Electronic energies, E, are interpolated on the left panel, $\log(E/\mathrm{cm}^{-1} + 5000) - \log(5000)$ are interpolated on the right panel. Electronic energies are in cm^{-1}.

simple and attractive when the desired accuracy is achieved by small number of terms. However, large number of polynomial terms renders the fit highly correlated.

A potential energy surface of lithium trimer in the quartet ground state has recently been published by Colavecchia et al. [56]. The nonadditive part of potential was represented using the multiquadratic interpolation method described by Salazar [115]. The interpolated energies of N_d data points can be represented as

$$V(\mathbf{r}) = \sum_{i=1}^{N_d} c_i \sqrt{||\mathbf{r} - \mathbf{r}(i)||^2 + \Delta}, \tag{4.27}$$

where the parameters c_i are determined by requiring that the energies are exactly reproduced at the grid points. Δ is a free parameter determined by minimizing the first differences in the interpolated higher-order derivatives as described by Salazar et al. [116]. The authors used *ab-initio* energies of lower quality than us, evaluated at 1122 configurations. The interpolant was used at short range. At intermediate distances wiggles in the potential corrupted the surface. Therefore, the authors switched to a fitted symmetric polynomial, similar to that in (4.13), at intermediate distances (the value of the switching function was 1/2, where $r_1+r_2+r_3 \approx 14.2$ Å). We applied this method using our grid. The resulting interpolant wiggled everywhere. The density of points in our grid is too low.

We have found that IMLS/Shepard method gives the most satisfactory results. The fit is described below in more detail.

4.4 IMLS/Shepard fit

In the IMLS/Shepard method, the potential energy surface is constructed from weighted quadratics. There are two parameters at our disposal, p and ϵ, which control the quality of the fit once the grid is chosen. The parameter p determines how quickly the weight function drops off, while ϵ removes the singularity in weights and smooths out the potential near the grid points.

Ishida and Schatz [111] found that for the H_3 potential, $p = 6$ and $\epsilon = 0.03$ Å^{-1} give the best results for randomly scattered data. Their conclusion was based on examining the convergence of classical trajectories, and the root-mean-square deviations of energies and gradients from a previously known potential energy surface. They found that if $\epsilon < 0.03$, precision in gradients is lost near the grid points, because of the divergence in unnormalized weight functions.

We have initially interpolated potential of lithium trimer using $p = 6$ and $\epsilon = 0.03$ Å^{-1}. The interpolated potential is shown in Figure 4.3 for $D_{\infty h}$ geometries. Because of the scarcity of grid points near the seam, Taylor expansions about adjacent grid points have very different behaviour. The unphysical gradients in the figure are caused by a rapid switching between the contributions from different data points as we move on the surface. Since $\epsilon > 0$, the IMLS/Shepard interpolant is, in fact, a fit. The root-mean-square (rms) error at the grid points is 1.47 cm^{-1}. The largest contributions to this error come from the points on the repulsive wall, at short range, and near the conical intersection. The most important part of potential for low-energy collisions is that which lies below zero, defined as the three-body dissociation limit. The rms error at the points where the potential is negative is 0.39 cm^{-1}, with the maximum absolute deviation of 4.91 cm^{-1} at $(2.8, 3.6, 6)$, close to the seam.

To obtain a smooth potential, we have tried increasing the value of ϵ in steps of 0.01 Å^{-1}. Increasing ϵ increases the average number of grid points that significantly contribute to the fitted potential at a point. In this way, the potential value is influenced significantly by other grid points even at grid points and the quality of fit deteriorates where potential varies rapidly. A smooth fit was obtained using $\epsilon = 0.05$ Å^{-1} and is shown in Figure 4.6. The rms error at all points on the grid has increased to 9.72 cm^{-1}. The rms error at points below zero is now 4.33 cm^{-1} with the maximum absolute deviation of 45.53 cm^{-1} at coordinates $(2.8, 3.6, 6)$.

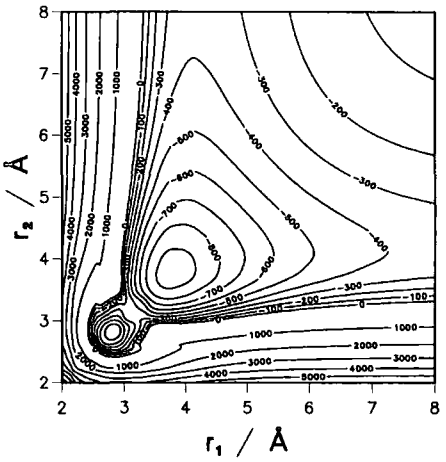

Figure 4.3: IMLS/Shepard interpolant of the quartet ground state of lithium trimer. Parameter of interpolation $p = 6$ and $\epsilon = 0.03$ Å^{-1}. Electronic energies are in cm^{-1}.

We evaluate the quality of the fit in more detail. There are 67 grid points at which the relative error in the fitted potential is greater than 1%. At 46 of them, the potential is negative. In the next chapter the global fit will be constructed from the IMLS/Shepard fit at short range and an analytic form at long range. The two regions will be matched by a switching function. We may divide the whole configuration space into an inner region and an outer region, where the dividing line is defined by the switching function being equal to 1/2 ($r_1 + r_2 + r_3 = 20$ Å). Of the 46 points at negative energies, where the error is greater than 1%, 21 are in the inner region and 25 are in the outer region. Of all the grid points, 323 are in the inner region and 166 are in the outer region. Of 323 points in the inner region, 201 are at negative energies, which means that the relative error is greater than 1% at $\approx 10\%$ of the points in the important region. At 5 points at negative energies the relative error is higher than 10%. At 3 of them, the large relative error is due to a small value of the potential at the point, and 2 of them lie near the conical intersection, $(3.2, 3.2, 6.4)$ and $(2.8, 3.6, 6.0)$. There are another two points, at $(2.8, 3.6, 6.4)$ and $(2.8, 3.6, 6.4)$, where the relative error is greater than 10% ($\approx 20\%$) and the potential is positive.

The fitted potential, the *ab-initio* points, and the potential of Colavecchia et al. [56] are shown in Figures 4.4 and 4.5 at D_{3h} and $D_{\infty h}$ geometries, respectively, for comparison. Near the global minimum, at $r = 3.2$ Å in D_{3h}, the error of the fit is 3.06 cm^{-1} or 0.08%, well within the error of the *ab-initio* energies. It can be seen in

Figure 4.5 that gradients have more physical appeal for the IMLS/Shepard fit with $\epsilon = 0.05$ Å^{-1} than with $\epsilon = 0.03$ Å^{-1}.

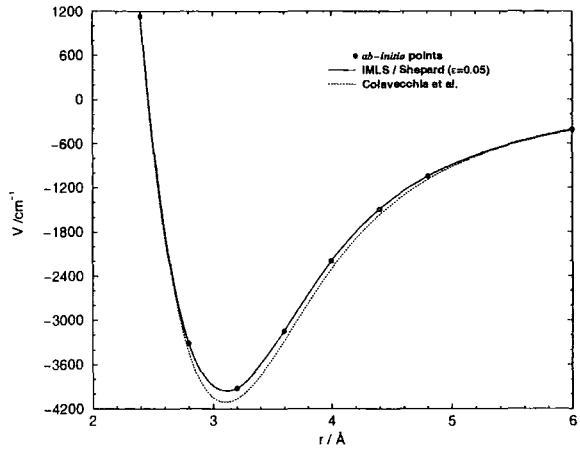

Figure 4.4: IMLS/Shepard fit, $\epsilon = 0.05$ Å^{-1}, and *ab-initio* energies of the quartet ground state of Li_3 at D_{3h} geometries.

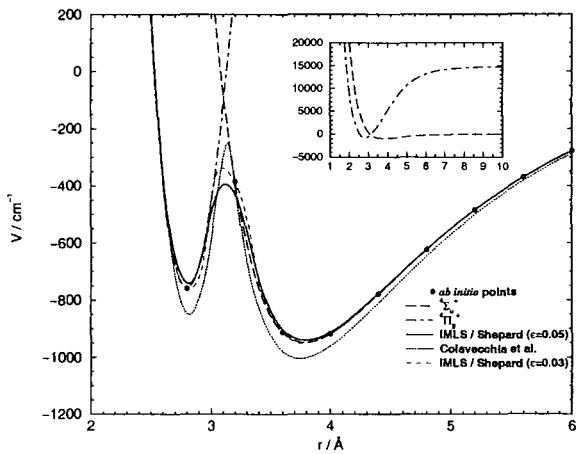

Figure 4.5: IMLS/Shepard fit, $\epsilon = 0.05$ Å^{-1} and 0.03 Å^{-1}, and *ab-initio* energies of the quartet ground state of Li_3 at $D_{\infty h}$ geometries.

The IMLS/Shepard fit is shown in Figure 4.6. We regard this fit as a satisfactory representation of a surface with a discontinuity at a seam. A better representation using this method could be achieved by increasing the density of points. At each panel, the angle between two internuclear distances is fixed. The interpolant may be compared to Figure 2.8 obtained with lower quality *ab-initio* energies, but more points. The potential of Colavecchia et al. [56] is shown in Figure 4.7 for comparison.

The large number of points (25) with a relative error greater than 1% at long

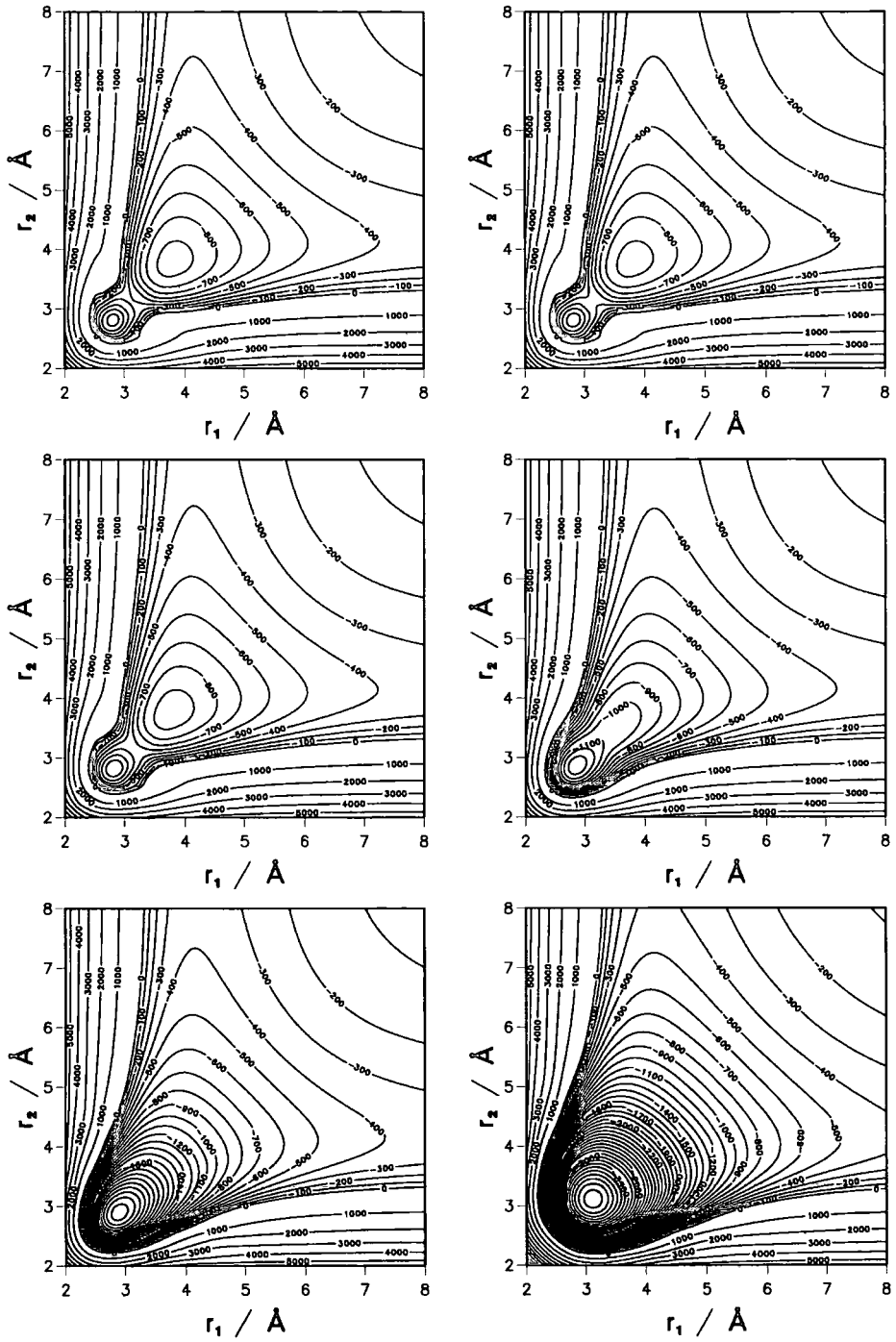

Figure 4.6: The quartet ground-state potential of lithium trimer fitted using the IMLS/Shepard method with $p = 6$ and $\epsilon = 0.05$ Å^{-1}. The angle between the internuclear distances, r_1 and r_2, is fixed at 180° (top left), 170° (top right), 150° (middle left), 120° (middle right), 90° (bottom left), and 60° (bottom right). Electronic energies are in cm^{-1}.

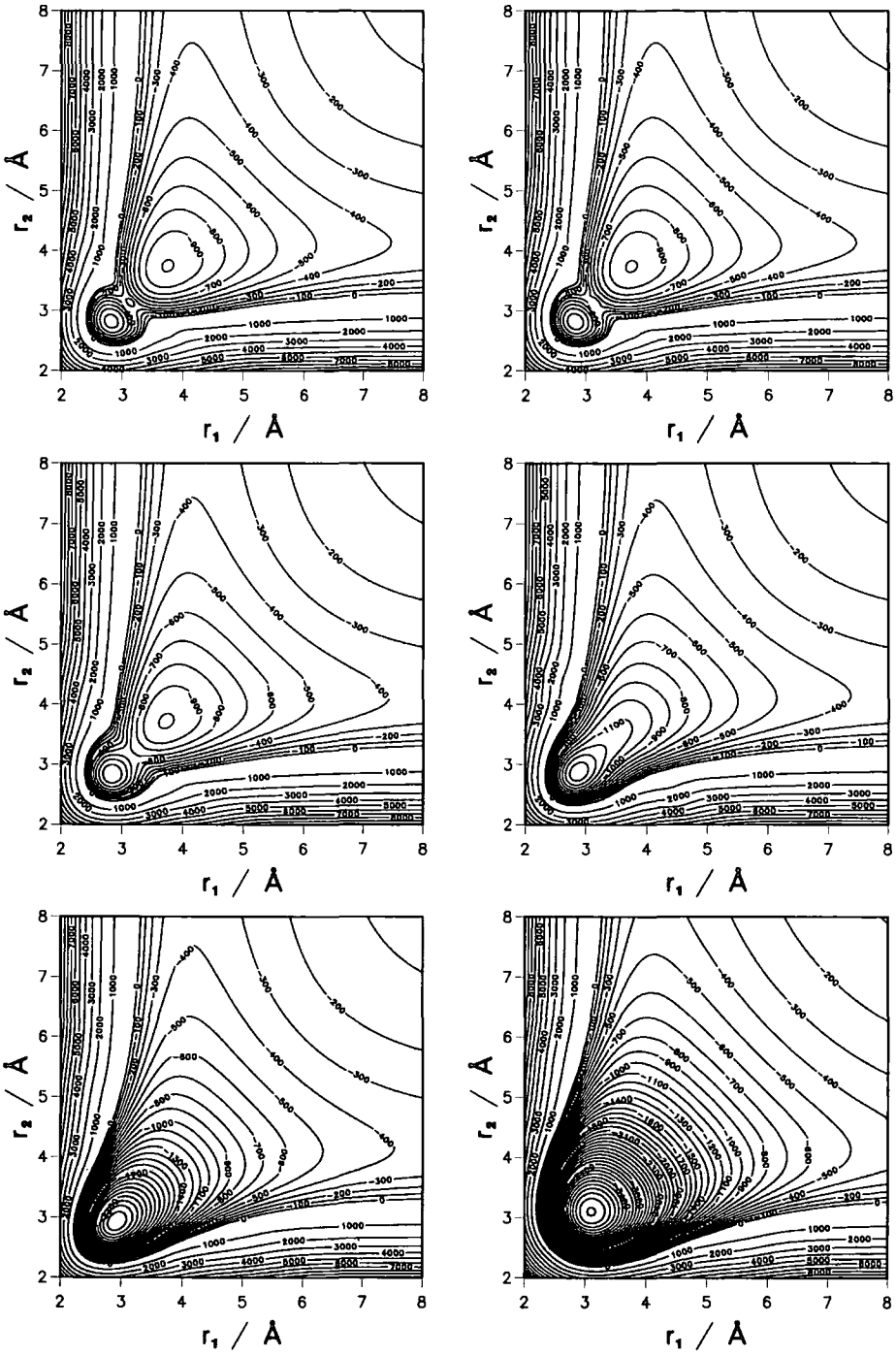

Figure 4.7: The quartet ground-state potential of lithium trimer of Colavecchia et al. [56]. The angle between the internuclear distances, r_1 and r_2, is fixed at 180° (top left), 170° (top right), 150° (middle left), 120° (middle right), 90° (bottom left), and 60° (bottom right). Electronic energies are in cm^{-1}.

range exists because the measure of proximity between the points is in the coordinate system of inverse distances. All long-range points lie close to the origin in that coordinate system. The high value of ϵ results in averaging of the potential contributions coming from nearby points. In this averaging, points that come from very different nuclear configurations and lie far apart in physical space participate. Apart from this drawback, the limiting value of the interpolant at infinity is easily seen to be a constant. These facts demonstrate that switching to a more appropriate form at long range is necessary.

A symmetric potential in all three internuclear distances is obtained by symmetrizing the 489 points. The total number of symmetrized points at which Taylor expansions need to be evaluated is 2398. The potential constructed in this way is expensive to evaluate. The time for evaluation may be reduced by introducing a cut-off distance and redefining the weights in (4.19),

$$\begin{aligned} \nu_i &= \frac{1}{(||\mathbf{Z}-\mathbf{Z}(i)||^2+\epsilon^2)^p} - \frac{1}{(d^2_{\text{cut-off}}+\epsilon^2)^p} \quad \text{for} \quad ||\mathbf{Z}-\mathbf{Z}(i)|| \leq d_{\text{cut-off}} \\ \nu_i &= 0 \qquad\qquad\qquad\qquad\qquad\qquad\quad \text{for} \quad ||\mathbf{Z}-\mathbf{Z}(i)|| > d_{\text{cut-off}}. \end{aligned} \tag{4.28}$$

Small discontinuities in the gradients are introduced in this way. When the cut-off distance is set to $d^2_{\text{cut-off}} = 0.025$ Å^{-2}, the root-mean-square deviation from the surface with original weights in (4.19) at the grid points is 0.0476 cm^{-1} and the maximum deviation is 0.27 cm^{-1} near the global minimum. The average number of points about which the Taylor expansions need to be evaluated is 616.8 for points on the grid, which is 3.9 times less than originally. The factor of decrease would be even larger for surfaces interpolated with a smaller ϵ value.

Chapter 5

Fitting long-range interactions

5.1 Introduction

Properties of cold dilute molecular systems and of weakly bound complexes are very sensitive to long-range interactions [117]. The wavefunction is such that molecules spend long time at large separations. For calculations of cross sections or bound-state energies near dissociation, the accurate representation of long-range interactions is therefore important.

The intermolecular potential may be partitioned in the form [118]

$$V^{\text{int}} = V^{\text{SCF}} + V^{\text{intra}} + V^{\text{disp}}. \tag{5.1}$$

In this expression, V^{SCF} is the interaction energy evaluated in the mean self-consistent-field approximation, V^{intra} is the intramolecular correlation energy of the monomers, and V^{disp} is the dispersion interaction energy of the monomers.

The dispersion energy has its origin in the interaction of the correlated motion of fluctuating multipoles of monomers. It is the dominant contribution to the potential of two neutral S-state atoms at long range where overlap and exchange interaction are negligible. The dispersion interaction is relatively weak and it is common to describe it using perturbation theory. Formal expressions of the long-range interaction terms of an arbitrary number of molecules have been given in three orders of perturbation treatment in Ref. 119, 120. Several lower-order contributions have been evaluated in analytic form and for the case of three equal S-state atoms they will be given below.

The dispersion interaction of two neutral S-state atoms may be written in the form

$$V^{\text{disp}}(r) = -\frac{C_6}{r^6} - \frac{C_8}{r^8} - \frac{C_{10}}{r^{10}} - \dots \tag{5.2}$$

C_6, C_8, and C_{10} are dispersion coefficients and r is the distance between the atoms. The coefficients come from instantaneous dipole-dipole, dipole-quadrupole, and quadrupole-quadrupole and dipole-octupole interactions, respectively, and may be expressed as integrals over products of dynamic polarizabilities at imaginary frequencies [121]. A considerable effort has been made in the last decades in *ab-initio* determination of the dispersion coefficients. In particular, for two lithium atoms, C_6, C_8, and C_{10} have been published in Ref. 93 and also higher order coefficients in [122]. The most recent calculations of the C_6 coefficient for lithium [93, 122, 123] all agree within 2%. They are tabulated in Table 5.1. At large distances, the interactions cannot be regarded

as instantaneous because they propagate with the finite speed of light. The effect of the retardation has also been studied and retardation function that multiplies the C_6 coefficient in (5.2) calculated for two lithium atoms [95]. The magnitude of the effect grows with the distance and amounts to a reduction of the first term in (5.2) by 0.5% at 250 a_0, 1.67% at 500 a_0, $\approx$ 10% at 1500 a_0, and $\approx$ 60% at 10 000 a_0. Its effect will be neglected in our analysis, but may easily be incorporated when known.

reference	$C_6/E_h a_0^6$	$C_8/E_h a_0^8$	$C_{10}/E_h a_0^{12}$
Yan et al. [93]	1393.39	83425.8	7372100
Patil, Tang [122]	1388	81830	7289000
Rérat, Bussery [123]	1419	76142	-

Table 5.1: C_6, C_8, and C_{10} dispersion coefficients for two lithium atoms from recent *ab-initio* calculations.

An analytic expression for the nonadditive dispersion interactions of three neutral S-state atoms, in third-order perturbation theory applied to three interacting dipoles, was obtained by Axilrod and Teller [72]. The well-known formula is

$$V(\mathrm{DDD})_3 = Z_{111} 3 \frac{1 + 3\cos\varphi_1 \cos\varphi_2 \cos\varphi_3}{r_1^3 r_2^3 r_3^3}. \tag{5.3}$$

r_1, r_2, and r_3 are distances between atoms and φ_1, φ_2, and φ_3 are internal angles at atoms and opposite the respective distances. The expression (5.3) has been extensively used in the past to account for the nonadditive dispersion interaction at long range. It is quantitatively good only if all three distances are large enough that any overlap and exchange interactions are negligible. The dispersion coefficient $C_9 \equiv 3Z_{111}$ is often used in the literature.

Further terms coming from the third-order perturbation theory including the interactions of higher order multipoles have been derived by Bell [124] and Zucker et al. [125]. They apply to interactions of three identical S-state atoms. The expressions are

$$V(\mathrm{DDQ})_3 = Z_{112} W(\mathrm{DDQ})_3, \tag{5.4}$$

$$V(\mathrm{DQQ})_3 = Z_{122} W(\mathrm{DQQ})_3, \tag{5.5}$$

$$V(\mathrm{DDO})_3 = Z_{113} W(\mathrm{DDO})_3, \tag{5.6}$$

$$V(\mathrm{QQQ})_3 = Z_{222} W(\mathrm{QQQ})_3, \tag{5.7}$$

where the geometric factors W are

$$\begin{aligned}
W^{123}(\mathrm{DDQ})_3 &= \frac{3}{16r_1^4r_2^4r_3^3}[(9\cos\varphi_3 - 25\cos 3\varphi_3) + 6\cos(\varphi_1 - \varphi_2) \\
&\times (3 + 5\cos 2\varphi_3)], \qquad (5.8) \\
W^{123}(\mathrm{DQQ})_3 &= \frac{15}{64r_1^5r_2^4r_3^4}[3(\cos\varphi_1 + 5\cos 3\varphi_1) + 20\cos(\varphi_2 - \varphi_3) \\
&\times (1 - 3\cos 2\varphi_1) + 70\cos 2(\varphi_2 - \varphi_3)\cos\varphi_1], \qquad (5.9) \\
W^{123}(\mathrm{DDO})_3 &= \frac{5}{32r_1^5r_2^5r_3^3}[9 + 8\cos 2\varphi_3 - 49\cos 4\varphi_3 \\
&+ 6\cos(\varphi_1 - \varphi_2)(9\cos\varphi_3 + 7\cos 3\varphi_3)], \qquad (5.10) \\
W(\mathrm{QQQ})_3 &= \frac{15}{128r_1^5r_2^5r_3^5}\{-27 + 220\cos\varphi_1\cos\varphi_2\cos\varphi_3 \\
&+ 490\cos 2\varphi_1\cos 2\varphi_2\cos 2\varphi_3 \\
&+ 175[\cos 2(\varphi_1 - \varphi_2) + \cos 2(\varphi_2 - \varphi_3) \\
&+ \cos 2(\varphi_3 - \varphi_1)]\}. \qquad (5.11)
\end{aligned}$$

The origin of each term is in the interaction of three multipoles denoted in the above expressions by D, Q, and O for dipole, quadrupole, and octupole, respectively. The terms must be symmetric in the indices of three atoms (1, 2, 3). The full geometric factor for DDQ, DQQ, and DDO interactions includes also the terms generated by cyclic permutations of the atom indices in the expressions (5.8), (5.9), and (5.10),

$$W = W^{123} + W^{231} + W^{312}. \qquad (5.12)$$

Three-body dispersion coefficients to be used with (5.3-5.7) were calculated for alkali atoms by Patil and Tang [122]. The coefficients for lithium are tabulated in Table 5.2.

$Z_{111}/E_h a_0^9$	$5.63 \cdot 10^4$
	$5.6865 \cdot 10^4$ [93]
	$5.90 \cdot 10^4$ [123]
$Z_{112}/E_h a_0^{11}$	$5.81 \cdot 10^5$
$Z_{122}/E_h a_0^{13}$	$6.41 \cdot 10^6$
$Z_{113}/E_h a_0^{13}$	$1.70 \cdot 10^7$
$Z_{222}/E_h a_0^{15}$	$7.86 \cdot 10^7$

Table 5.2: Three-body dispersion coefficients for lithium, taken from Ref. 122 if not indicated otherwise.

The leading fourth-order term for interaction of three atoms through dipolar forces was derived within the Drude model by Bade [126],

$$V(\mathrm{DDDD})_4 = -Z^4_{1111}\frac{45}{64}\left[\frac{1+\cos^2\varphi_1}{r_2^6 r_3^6} + \frac{1+\cos^2\varphi_2}{r_1^6 r_3^6} + \frac{1+\cos^2\varphi_3}{r_1^6 r_2^6}\right]. \tag{5.13}$$

An *ab-initio* value of the Z^4_{1111} coefficient for lithium has not been published to our knowledge.

Recently, dispersion coefficients for alkali atom-diatom and diatom-diatom systems were calculated for S-state monomers and $^3\Sigma$ dimers [123, 127]. The formulae are expressed in Jacobi coordinates. The diatom bond length is denoted by r, the atom-diatom centre-of-mass separation R, and the angle between the two vectors is θ. The angular dependence of the interaction is expanded as a series in Legendre polynomials

$$V^{\mathrm{disp}}(R,\theta) = -\sum_L \sum_s \frac{C_s^L(r)}{R^s} P_L(\cos\theta). \tag{5.14}$$

For the interaction of two dipoles there are two non-zero coefficients C_6^0 and C_6^2 that were evaluated as a function of the diatomic distance. The values are given below in Table 5.3. The four coefficients resulting from a dipole-quadrupole interaction C_8^0, C_8^2, C_8^4 were evaluated at the diatomic equilibrium distance. The authors say that

r/Å	$C_6^0/E_h a_0^6$	$\sqrt{5}C_6^2/E_h a_0^6$
3.6	3304	2549
4.2	3148	1875
4.8	3020	1309
5.6	2919	801
6.4	2871	505
7.0	2852	371
8.2	2839	225
10	2832	121
15	2830	36

Table 5.3: Atom-diatom C_6^0 and C_6^2 dispersion coefficients as a function of diatom distance taken from Ref. 123.

no asymptotic form of the atom-diatom C_6 coefficients exists, and both isotropic and anisotropic coefficients were fitted to the form

$$F(r) = A_\infty + A\exp(-bx) + f_3(b,r)\frac{c_3}{r^3} + f_6(b,r)\frac{c_6}{r^6}, \tag{5.15}$$

with $x = (r - r_0)/r_0$. f_n are Tang-Toennies damping functions [129] (see eq. (5.43)), r_0 is a constant and the other parameters in (5.15) are determined by fitting.

The above form (5.14) for atom-molecule dispersion is valid when the atom-diatom distance R is much bigger than the diatomic separation r. On the other hand, the three-body dispersion expressions (5.3-5.7) are valid when all three distances are large.

As one distance gets shorter, with the other two remaining large, more and more terms in the three-body multipole expansion start to contribute to the atom-molecule interaction. Finally when overlap between two atoms is significant there will be exponential terms that contribute in turn to the diatomic charge distribution, diatomic polarizability and finally to the atom-molecule dispersion interaction described by expression (5.14). Our aim was to develop a form for fitting atom-diatom dispersion coefficients in terms of three-body interactions that is lacking in the literature according to Ref. 123 and to the best of our knowledge. We were also aiming to develop a symmetric analytical form for fitting the long-range nonadditive interactions of triatomic systems for use in scattering calculations that would also be valid when one distance of the three is near equilibrium. Many published potential energy surfaces have not properly accounted for the long-range interactions. In particular the ground-state quartet potential of three lithium atoms of Colavecchia et al. includes only the Axilrod-Teller term for the nonadditive part, which, as will be seen below, does not accurately describe the atom-molecule anisotropy. The ground-state quartet potential for three sodium atoms by Higgins et al. [80] resulting from extrapolation of the RKHS-RP method does not account properly for the anisotropy contained in the Axilrod-Teller term and also contains terms $\sim r_1^{-3} r_2^{-3} r_3^{-4}$ which do not emerge in the perturbation theory of multipole interactions. Accurate global forms are therefore of interest in developing potential energy surfaces for use in scattering calculations. Finally, the aim is also to obtain a symmetric long-range potential for lithium and incorporate it in the ground-state quartet potential fit obtained in the last chapter for subsequent use in scattering calculations.

5.2 Atom-molecule dispersion interaction formulas

In this section, we will cast the atom-atom additive (5.2) and triatomic nonadditive (5.3-5.13) dispersion interaction formulas in the form of the atom-molecule dispersion formula in (5.14). This is done by changing coordinates in the formulae (5.2) and (5.3-5.13) from interatomic distances to Jacobi coordinates and performing a series expansion in the limit $r \ll R$. The full dispersion interaction potential is the sum of all these contributions.

A word about notation is in order here. The atom-molecule dispersion coefficients $C_6^{\rm AM}$ and $C_8^{\rm AM}$ are defined as the complete functions multiplying R^{-6} and R^{-8}, respectively, in the expression for the dispersion energy (5.14). The summation over s in equation (5.14) is performed and we get

$$\begin{aligned} C_6^{\rm AM}(r,\theta) &= C_6^0(r) + C_6^2(r)P_2(\cos\theta), \\ C_8^{\rm AM}(r,\theta) &= C_8^0(r) + C_8^2(r)P_2(\cos\theta) + C_8^4(r)P_4(\cos\theta). \end{aligned} \tag{5.16}$$

Additive and nonadditive interactions of three atoms in different orders of perturbation treatment give separate contributions to $C_6^{\rm AM}$ and $C_8^{\rm AM}$ and higher-order coefficients. The full $C_s^{\rm AM}$ coefficients are the sum of these contributions. We will introduce a symbol $\triangleleft$ with the meaning that everything on the right side of it is a contribution to the quantity on the left. A summary of all the contributions analyzed will be given in tables at the end of the discussion.

5.2.1 Additive contribution to atom-molecule dispersion interaction

The total additive dispersion interaction is

$$V^{\rm disp}(r_1,r_2,r_3) = V^{\rm disp}(r_1) + V^{\rm disp}(r_2) + V^{\rm disp}(r_3), \tag{5.17}$$

where each of the three terms on the right-hand side is of form (5.2). The total additive interaction may also be written in form

$$V^{\rm disp}(R,r,\theta) = V^{\rm disp}(R,\theta) + V^{\rm disp}(r), \tag{5.18}$$

where we have used Jacobi coordinates. The first term on the right-hand side may be associated with the atom-molecule potential, and the second with the intramolecular potential that depends on the separation of the two atoms in the molecule. If we associate one distance in the valence coordinates, say r_3, with the diatomic distance in Jacobi coordinates, r, the first two terms in (5.17) are associated with the atom-molecule potential and the third with the intramolecular potential. Now, we express r_1 and r_2 in terms of R and θ,

$$\begin{aligned} r_1 &= \sqrt{R^2 + \frac{r^2}{4} + Rr\cos\theta}, \\ r_2 &= \sqrt{R^2 + \frac{r^2}{4} - Rr\cos\theta}. \end{aligned} \tag{5.19}$$

When the atom-molecule distance is large, $R \gg r$, we factorize R in the distances (5.19) and expand the atom-molecule dispersion potential in powers of r/R. For example, the contribution to atom-molecule dispersion potential that comes from the leading terms in the atom-atom dispersion potentials is

$$-\frac{C_6}{R^6}\left\{\frac{1}{\left[1+\frac{r}{R}\cos\theta+\frac{1}{4}\left(\frac{r}{R}\right)^2\right]^3}+\frac{1}{\left[1-\frac{r}{R}\cos\theta+\frac{1}{4}\left(\frac{r}{R}\right)^2\right]^3}\right\}, \tag{5.20}$$

which can easily be expanded in powers of r/R. Only even powers survive in this expansion and, by comparison to (5.14), one can extract the contribution of atom-atom dispersion coefficients to atom-molecule dispersion coefficients. The series is infinite and we list the terms up to R^{-10},

$$C_6^{\mathrm{AM}} \lhd 2C_6, \tag{5.21}$$

$$C_8^{\mathrm{AM}} \lhd C_6\left(-\frac{3}{2}+12\cos^2\theta\right)r^2, \tag{5.22}$$

$$C_{10}^{\mathrm{AM}} \lhd C_6\left(\frac{3}{4}-15\cos^2\theta+30\cos^4\theta\right)r^4. \tag{5.23}$$

We see here that terms depending on the diatomic distance, r, appear. When we contract the diatomic distance, ever more terms start to contribute in expansion (5.2), but as a part of last term of the right-hand side of expressions (5.17) and (5.18) which is not a part of atom-molecule potential. Additive dispersion interactions do not account for C_6 anisotropy, but do account for a part of the anisotropy in higher-order coefficients. The angular dependence in (5.14) is contained in Legendre

polynomials of even order which are functions of $\cos^2\theta$,

$$\begin{aligned} P_0(\cos\theta) &= 1, \\ P_2(\cos\theta) &= \frac{1}{2}(3\cos^2\theta - 1), \\ P_4(\cos\theta) &= \frac{1}{8}(35\cos^4\theta - 30\cos^2\theta + 3). \end{aligned} \tag{5.24}$$

It is convenient to have the expressions (5.21-5.23) written in terms of Legendre polynomials. In order to do that, one must invert (5.24). We obtain contributions

$$C_6^{\mathrm{AM}} \lhd 2C_6, \tag{5.25}$$

$$C_8^{\mathrm{AM}} \lhd C_6\left(\frac{5}{2} + 8P_2\right) r^2, \tag{5.26}$$

$$C_{10}^{\mathrm{AM}} \lhd C_6\left(\frac{7}{4} + \frac{50}{7}P_2 + \frac{48}{7}P_4\right) r^4. \tag{5.27}$$

This is done in order to be able to separate the terms that contribute to C_6^0 and C_6^2 since the two are calculated separately in *ab-initio* calculations, and for the same reason for higher-order atom-molecule dispersion coefficients. It may be noticed that the angular dependence does not exceed P_2 in C_6^{AM}, P_4 in C_8^{AM}, as must be the case because of angular momentum couplings in the multipole expansions of the two interacting species.

The same algebra may be performed for the dipole-quadrupole interactions. We find the contribution of pairwise interactions to atom-molecule interactions and express the atom-molecule C_8^{AM} in terms of the atom-atom dispersion coefficient C_8,

$$C_8^{\mathrm{AM}} \lhd 2C_8, \tag{5.28}$$

$$C_{10}^{\mathrm{AM}} \lhd C_8\left(-2 + 20\cos^2\theta\right) r^2. \tag{5.29}$$

The angular dependence may be expressed in terms of Legendre polynomials. Then (5.28,5.29) become

$$C_8^{\mathrm{AM}} \lhd 2C_8, \tag{5.30}$$

$$C_{10}^{\mathrm{AM}} \lhd C_8\left(\frac{14}{3} + \frac{40}{3}P_2\right) r^2. \tag{5.31}$$

This procedure may be extended to higher-order interactions, but we keep the present analysis limited to the atom-molecule C_6^{AM} and C_8^{AM} coefficients.

We have derived terms of different powers in the diatomic distance r that contribute to atom-molecule dispersion interaction, from pairwise additive atom-atom interactions. These are summarized in Table 5.4.

origin	powers in A-M dispersion		
$(DD)_2$	$r^0 \frac{P_0}{R^6}$	$r^2 \frac{(P_0,P_2)}{R^8}$	$r^4 \frac{(P_0,P_2,P_4)}{R^{10}}$
$(DQ)_2$		$r^0 \frac{P_0}{R^8}$	$r^2 \frac{(P_0,P_2)}{R^{10}}$
$(QQ,DO)_2$			$r^0 \frac{P_0}{R^{10}}$

Table 5.4: Summary of terms that appear in the atom-molecule dispersion potential and originate from pairwise additive atom-atom interactions.

5.2.2 Nonadditive contribution to atom-molecule dispersion interaction

The nonadditive interaction of three atoms does not make a contribution to the intramolecular interaction (since the latter is a pairwise interaction) in (5.18), but only to the atom-molecule interaction. One distance in the nonadditive potentials (5.3-5.13) is again associated with the diatomic distance and the other two expressed in terms of Jacobi coordinates using (5.19). Additionally, we need to express the internal angles in terms of interatomic distances using formulae such as

$$\cos\varphi_1 = \frac{r_2^2 + r_3^2 - r_1^2}{2r_2r_3}. \tag{5.32}$$

The cosines of sums and differences between the angles are expanded as trigonometric functions of individual angles, sines are expressed in terms of cosines, and the substitutions (5.32) again performed. The resulting expressions are expanded in powers of r/R.

When this strategy is applied to the Axilrod-Teller term (5.3), the geometric factor is

$$\begin{aligned} &W(\mathrm{DDD})_3 = \\ &3 \times \left[(1 - 3\cos^2\theta)\,\tfrac{1}{r^3R^6} + \left(6\cos^2\theta - \tfrac{15}{2}\cos^4\theta\right)\tfrac{1}{rR^8}\right] + \mathcal{O}\left(\tfrac{r}{R^{10}}\right). \end{aligned} \tag{5.33}$$

The expansion contains even powers of r/R and the angular dependencies can be expressed in even powers of $\cos\theta$. We kept only the terms $\sim R^{-6}$ and R^{-8} in the analysis.

We proceed to do the same with the $(DDQ)_3$ geometric factor (5.4),

$$\begin{aligned} &W(\mathrm{DDQ})_3 = \\ &\tfrac{3}{16} \times \left[(48 - 384\cos^2\theta + 400\cos^4\theta)\,\tfrac{1}{r^3R^8} + (32 - 96\cos^2\theta)\,\tfrac{1}{r^3R^8}\right] + \\ &+\mathcal{O}\left(\tfrac{1}{rR^{10}}\right). \end{aligned} \tag{5.34}$$

All three cyclic permutations in (5.12), W^{123}, W^{231}, and W^{312} in the $(\mathrm{DDQ})_3$ geometric factor (5.4) contribute to the above expression (5.34). The first parentheses in the square brackets in (5.34) contain terms that arise from the expansion of the sum of the two W^{ijk} that are $\sim r^{-4}R^{-7}$ when expressed in Jacobi coordinates. This expansion contains only odd powers in r/R. The second parentheses in the square brackets in (5.34) comes from the remaining geometric factor $\sim r^{-3}R^{-8}$. Same powers of r and R appear in the expansion of this geometric factor as in the expansion of the sum of the other two.

The geometric factor of the $(\mathrm{DQQ})_3$ interactions (5.5) again contains three terms, W^{ijk}, connected by cyclic permutation of atom indices. Only one of them contributes to the $r^{-5}R^{-8}$ term below, while all of them contribute to the next term in the expansion, which is $\sim r^{-3}R^{-10}$,

$$W(\mathrm{DQQ})_3 = \frac{15}{64} \times \left(48 - 480\cos^2\theta + 560\cos^4\theta\right) \frac{1}{r^5R^8} + \mathcal{O}\left(\frac{1}{r^3R^{10}}\right). \qquad (5.35)$$

From the three geometric factors of the $(\mathrm{DDO})_3$ interactions, the combination of two contributes to $r^{-5}R^{-8}$ term below and all contribute in the next order of expansion $\sim r^{-3}R^{-10}$,

$$W(\mathrm{DDO})_3 = \frac{5}{32} \times \left(-96 + 960\cos^2\theta - 1120\cos^4\theta\right) \frac{1}{r^5R^8} + \mathcal{O}\left(\frac{1}{r^3R^{10}}\right). \qquad (5.36)$$

Since the contributions coming from the $(\mathrm{DQQ})_3$ and $(\mathrm{DDO})_3$ nonadditive interactions have the same powers in r and R they may be grouped together. Contributions coming from higher multipole interactions in the third order of perturbation theory do not contribute to C_6^{AM} and C_8^{AM} atom-molecule dispersion coefficients. They start with terms $\sim R^{-10}$.

Next, we consider the terms that come from fourth-order perturbation theory. The $(\mathrm{DDDD})_4$ interaction has a geometric factor made up of three terms connected by cyclic permutations of indices. Two of the terms contribute with $r^{-6}R^{-6}$ leading powers and each subsequent contribution is obtained by multiplying the previous one by $(r/R)^2$. The leading power of the third term is r^0/R^{12}. Keeping only the terms that contribute to C_6^{AM} and C_8^{AM} coefficients, we obtain

$$\begin{aligned} &W(\mathrm{DDDD})_4 = \\ &-\tfrac{45}{64} \times \left[(2 + 2\cos^2\theta)\,\tfrac{1}{r^6R^6} + (-1 + 2\cos^2\theta + 20\cos^4\theta)\,\tfrac{1}{r^4R^8}\right] + \\ &+\mathcal{O}\left(\tfrac{1}{r^2R^{10}}\right). \end{aligned} \qquad (5.37)$$

Geometric factors for the higher multipole nonadditive interactions in fourth order have not been derived. They would contribute to higher inverse powers of r in both C_6^{AM} and C_8^{AM} atom-molecule dispersion coefficients. The powers in the expansion may be determined by noting that the DD interactions are $\sim r^{-3}$, the DQ are $\sim r^{-4}$, and the QQ and DO are $\sim r^{-5}$. Contributions of fourth order in perturbation treatment contain a sum of the products of matrix elements of four pairwise multipole interactions and the summation is over three intermediate states. The powers in interatomic distances may be derived by examining for which combinations of multipole interactions the product of the matrix elements may be non-vanishing.

The next term of fourth order comes from DQ and DD interactions and it will contain terms $\sim r_1^{-8} r_2^{-6} r_3^{0}$, where r_i are interatomic distances. This means that higher-order terms in the asymptotic form of the atom-molecule C_6^{AM} and C_8^{AM} coefficients are $\sim r^{-8}$ and $\sim r^{-6}$, respectively. The fifth-order dipolar interaction contains terms such as $\sim r_1^{-9} r_2^{-3} r_3^{-3}$ and therefore contributes with r^{-9} and r^{-7} to C_6^{AM} and C_8^{AM}, respectively. The results are summarized in Table 5.5.

All the above expressions (5.33-5.37) have an angular dependence which is a function of $\cos^2\theta$. Using (5.24) they can be expressed in terms of even-order Legendre polynomials. Namely,

$$W(\mathrm{DDD})_3 = 3 \times \left(-\frac{2P_2}{r^3R^6} + \frac{\frac{1}{2} - \frac{2}{7}P_2 - \frac{12}{7}P_4}{rR^8} \right) + \ldots, \tag{5.38}$$

$$W(\mathrm{DDQ})_3 = \frac{3}{16} \times \left(\frac{-\frac{192}{7}P_2 + \frac{640}{7}P_4}{r^3R^8} + \frac{-64P_2}{r^3R^8} \right) + \ldots, \tag{5.39}$$

$$W(\mathrm{DQQ})_3 = \frac{15}{64} \times \left(\frac{128P_4}{r^5R^8} \right) + \ldots, \tag{5.40}$$

$$W(\mathrm{DDO})_3 = \frac{5}{32} \times \left(\frac{-256P_4}{r^5R^8} \right) + \ldots, \tag{5.41}$$

$$W(\mathrm{DDDD})_4 = -\frac{45}{64} \times \left(\frac{\frac{8}{3} + \frac{4}{3}P_2}{r^6R^6} + \frac{\frac{11}{3} + \frac{268}{21}P_2 + \frac{32}{7}P_4}{r^4R^8} \right) + \ldots, \tag{5.42}$$

where the grouping of terms of different origin has been retained from (5.33-5.37).

It is clear from this that the Axilrod-Teller term accounts for a part of the anisotropy coming from dispersion interactions described by C_6^{AM} and C_8^{AM} coefficients. The importance of the expressions (5.38-5.42) is that the asymptotic forms for atom-molecule dispersion coefficients may now be extracted and expressed in terms of atomic two-body and three-body dispersion coefficients. In fact, the atomic two-body and three-body dispersion coefficients can be treated as fitting parameters

of atom-molecule dispersion coefficients at large r. Instead of writing more formulae, we collect all the powers of r that contribute to atom-molecule dispersion coefficients C_6^0 and C_6^2 in Table 5.6, and C_8^0, C_8^2, and C_8^4 in Table 5.7. The atomic dispersion coefficients are defined by the relations (5.2) and (5.3-5.13).

origin	powers in A-M dispersion			
$(DDD)_3$	$\frac{1}{r^3R^6}$	$\frac{1}{rR^8}$	$\frac{r}{R^{10}}$	$\frac{r^3}{R^{12}}$
$(DDQ)_3$		$\frac{1}{r^3R^8}$	$\frac{1}{rR^{10}}$	$\frac{r}{R^{12}}$
$(DQQ)_3$		$\frac{1}{r^5R^8}$	$\frac{1}{r^3R^{10}}$	$\frac{1}{rR^{12}}$
$(DDO)_3$		$\frac{1}{r^5R^8}$	$\frac{1}{r^3R^{10}}$	$\frac{1}{rR^{12}}$
$(DDDD)_4$	$\frac{1}{r^6R^6}$	$\frac{1}{r^4R^8}$	$\frac{1}{r^2R^{10}}$	$\frac{1}{R^{12}}$
$(DDDQ)_4$	$\frac{1}{r^8R^6}$	$\frac{1}{r^6R^8}$	$\frac{1}{r^4R^{10}}$	$\frac{1}{r^2R^{12}}$
$(DDDDD)_5$	$\frac{1}{r^9R^6}$	$\frac{1}{r^7R^8}$	$\frac{1}{r^5R^{10}}$	$\frac{1}{r^3R^{12}}$

Table 5.5: Summary of terms that appear in the atom-molecule dispersion potential and have origin in the nonadditive three-body interactions.

	C_6^0	C_6^2
r^0	$2C_6$	-
r^{-3}	-	$6Z_{111}$
r^{-6}	$\frac{15}{8}Z_{1111}^4$	$\frac{15}{16}Z_{1111}^4$
r^{-8}	$(DDDQ)_4$	
r^{-9}	$(DDDDD)_5$	

Table 5.6: Asymptotic r-dependence of atom-molecule C_6^{AM} dispersion coefficients in terms of atomic additive and nonadditive dispersion coefficients.

We are now able to give a physical interpretation of each term in the form (5.15) used by Rérat and Bussery [123] to fit C_6^0 and C_6^2 atom-molecule dispersion coefficients. Their asymptotic form is correct. The constant term in the isotropic coefficient comes from DD interaction between the atoms and is zero in the anisotropic coefficient. The r^{-3} term is zero in the expression for C_6^0, and is connected to the Axilrod-Teller Z_{111} coefficient in the C_6^2 expression. This was already discussed by the original authors [123]. The origin of the anisotropy in the r^{-6} term is in nonadditive dipolar interactions of fourth order; a constraint should be applied on the fitting parameter in C_6^0 and C_6^2 and the fit of both performed simultaneously. This has not been done before and is described below. The exponential term in (5.15)

	C_8^0	C_8^2	C_8^4
r^2	$\frac{5}{2}C_6$	$8C_6$	-
r^0	$2C_8$	-	-
r^{-1}	$-\frac{3}{2}Z_{111}$	$\frac{6}{7}Z_{111}$	$\frac{36}{7}Z_{111}$
r^{-3}	-	$\frac{120}{7}Z_{112}$	$-\frac{120}{7}Z_{112}$
r^{-4}	$\frac{165}{64}Z_{1111}^4$	$\frac{1005}{112}Z_{1111}^4$	$\frac{45}{14}Z_{1111}^4$
r^{-5}	-	-	$-30Z_{122}+40Z_{113}$
r^{-6}	$(\mathrm{DDDQ})_4$		
r^{-7}	$(\mathrm{DDDDD})_5$		

Table 5.7: Asymptotic r-dependence of atom-molecule C_8^{AM} dispersion coefficients in terms of atomic additive and nonadditive dispersion coefficients.

comes from exchange and overlap contributions to the diatomic polarizability.

It may be noted in Table 5.7 that even if C_8^4 was a known function of r, it would not be possible to determine Z_{122} and Z_{113} separately from its asymptotic form.

5.3 Analytic form for long-range interactions

Our objective is to devise an analytic function that accurately represents the potential at geometries when all distances are large, and also when one interatomic distance is short and the others large. The latter geometries are particularly important for atom-diatom collisions. The potential in the region where all atoms are far apart is important for processes such as collision-induced dissociation and three-body recombination which have recently been studied quantum-mechanically [128].

The form representing the long-range interactions of three identical S-state atoms must be symmetric in the atom indices. An obvious choice is to separate the pairwise-additive contribution, the sum of diatomic potentials, and to use the symmetric expressions (5.3-5.13) for the nonadditive part of the potential. If the diatomic potential has the correct asymptotic behaviour (5.2) built in, once we add the damping functions to dispersion terms the only term missing in the leading atom-molecule dispersion term of form (5.15) is the exponential.

The dispersion tail (5.2) can readily be built into the diatomic potential by one of the following methods. When the diatomic potential curve is known on a grid of points at short range, either from *ab-initio* calculations or from an RKR procedure or

some other source, a fit or interpolation can be performed on the difference between the potential and the damped dispersion energy evaluated at the grid points, and the analytic expression of the dispersion energy then added back to the fit or interpolant. There are also interpolation methods available that extrapolate to the desired long-range form. One of them has been described in the last chapter (RKHS). Or a fit can instead be performed onto a function which has the desired long-range tail built in by construction.

Damping functions represent the influence of charge overlap on the multipolar dispersion energy in (5.2). Considerable effort has been devoted to determining the best way to damp the atom-atom dispersion energy. The most popular approach is to use Tang-Toennies damping functions [129],

$$f_s(b,R) = 1 - \mathrm{e}^{-bR} \sum_{k=0}^{s} \frac{(bR)^k}{k!}. \tag{5.43}$$

Each term of the dispersion energy (5.2) proportional to R^{-s} is multiplied by the corresponding damping function f_s. The same b is used for all. It is much less known how the nonadditive dispersion energy should be damped. Several prescriptions have been given [130]. We choose to associate a damping function with every multipolar two-body interaction term appearing in the expression for the energy in the perturbative treatment. The dimer damping functions f_s are recovered if the square root of each, $\sqrt{f_s}$, is used in connection with the associated interaction terms, $R^{-s/2}$, when the second-order perturbation energies are considered. When this recipe is applied to third- and fourth-order terms (5.3-5.13), damped equivalents are obtained by the following replacements in geometric factors

$$\begin{aligned}
\frac{1}{r_1^3 r_2^3 r_3^3} &\rightarrow \frac{\sqrt{f_6(b,r_1) f_6(b,r_2) f_6(b,r_3)}}{r_1^3 r_2^3 r_3^3}, \\
\frac{1}{r_1^4 r_2^4 r_3^3} &\rightarrow \frac{\sqrt{f_8(b,r_1) f_8(b,r_2) f_6(b,r_3)}}{r_1^4 r_2^4 r_3^3}, \\
\frac{1}{r_1^5 r_2^4 r_3^4} &\rightarrow \frac{\sqrt{f_{10}(b,r_1) f_8(b,r_2) f_8(b,r_3)}}{r_1^5 r_2^4 r_3^4}, \ldots \\
\frac{1}{r_1^6 r_2^6} &\rightarrow \frac{f_6(b,r_1) f_6(b,r_2)}{r_1^6 r_2^6}, \ldots
\end{aligned} \tag{5.44}$$

When damping is introduced in this way, the atom-molecule dispersion interaction $\sim R^{-6}$ is damped by $\approx f_6(b,R)$. But in the fitting form (5.15) for C_6^2, term $\sim r^{-3}$ is damped with $\sqrt{f_6}$ instead of f_3.

Symmetric expression that accounts for the exponential term in (5.15) was chosen to be

$$\begin{aligned} V_{\rm exc}({\rm DD}) &= V_{\rm exc}^{123} + V_{\rm exc}^{231} + V_{\rm exc}^{312}, \\ V_{\rm exc}^{123} &= -[A + BP_2(\cos\theta_1)]{\rm e}^{-C\frac{r_1-r_0}{r_0}} \frac{\sqrt{f_6(b,r_2)f_6(b,r_3)}}{r_2^3 r_3^3}. \end{aligned} \tag{5.45}$$

When all three distances are large, this term (5.45) disappears due to exponentials which then vanish. When one distance gets short, two terms disappear, while an exponential remains in the diatomic distance that contributes to C_6^0 and C_6^2. The same exponent was chosen for both components. The reason for this will be explained below. The dependence on the large distance R^{-6} is damped by $f_6(b,R)$, which prevents divergence when all distances are small. The argument of the Legendre polynomial in (5.45) is the cosine of the Jacobi angle. It can be expressed in terms of the distances or in terms of a symmetric expression of internal angles,

$$P_2(\cos\theta_1) \simeq -\frac{1}{2}(1 + 3\cos\varphi_1\cos\varphi_2\cos\varphi_3). \tag{5.46}$$

The advantage of the latter is that the expression (5.46) does not require any extra computational effort since it is already evaluated for the $V({\rm DDD})_3$ term. This symmetric expression introduces additional terms in $C_8^{\rm AM}$ and higher coefficients, see (5.33). This could be avoided by using Jacobi coordinates

$$\cos^2\theta_1 = \frac{(r_3^2 - r_2^2)^2}{r_1^2[2(r_2^2 + r_3^2) - r_1^2]}, \tag{5.47}$$

and $1/R^6$ instead of $1/r_2^3 r_3^3$ in (5.45), where

$$R^2 = \frac{2(r_2^2 + r_3^2) - r_1^2}{4}. \tag{5.48}$$

The coefficients A, B, and C in equation (5.45) may be determined for lithium by fitting to the data in Table 5.3.

The sum of the additive potential and long-range nonadditive terms (5.3-5.13), damped by the substitutions in (5.44) and including the symmetric exponential term (5.45), represent a global potential. It represents the potential energy surface accurately when two distances are large and should be matched at short range to a potential that accurately accounts for short-range nonadditivity.

5.4 Fitting atom-molecule dispersion coefficients in lithium

We have refitted the parameters of the form used by Rérat and Bussery(5.15) using the data in Table 5.3. The exponent parameter b is set to the same value as the damping parameter in f_3 and f_6, and $r_0 = 7$ Å. We replaced the damping function f_3 in (5.15) by $\sqrt{f_6}$, according to the arguments given above. The fitting was performed using NAG subroutines E04YCF and E04FCF. The fitted parameters are summarized in Table 5.8 and the dependence of C_6^0 and C_6^2 on the diatomic distance r is plotted in Figure 5.1. Both fits give excellent agreement with the data. The

	$A_\infty/E_h a_0^6$	$A/E_h a_0^6$	$b/\text{Å}^{-1}$	$c_3/E_h a_0^9$	$c_6/E_h a_0^{12}$
C_6^0	2831.34	28.250	7.012	-	$-3.756 \cdot 10^7$
C_6^2	-	29.703	6.688	$3.520 \cdot 10^5$	$-7.370 \cdot 10^7$

Table 5.8: Parameters of the fit to equation (5.15) for C_6^0 and C_6^2 for lithium to data from Ref. 123, listed in Table 5.3.

root-mean-square (rms) error of the fit for C_6^0 is 0.800 $E_h a_0^6$ and for C_6^2 is 1.839 $E_h a_0^6$. However, several observations can be made. The coefficient Z^4_{1111} is equal to $V\alpha^4$ in the Drude model [126], where V is a characteristic dispersion energy of molecules and α is the atomic polarizability. Within the same model [131], we have

$$C_6 = \frac{3}{4} V\alpha^2, \tag{5.49}$$

$$Z_{111} = \frac{3}{16} V\alpha^3. \tag{5.50}$$

These two expressions, (5.49) and (5.50), can be combined to give an estimate of Z^4_{1111},

$$Z^4_{1111} = \frac{64}{3} \frac{(Z_{111})^2}{C_6}. \tag{5.51}$$

The value for lithium is $Z^4_{1111} = 4.9508 \cdot 10^7 E_h a_0^{12}$ with C_6 and Z_{111} in (5.51) taken from Ref. 93. The number is positive, while the fitted parameters suggest it is negative. The ratio of parameters c_6 from the fit of C_6^0 and C_6^2 is 0.510, while theory predicts it is 2, see Table 5.6. Moreover, since r^{-6} is the leading term in C_6^0 at long range coming from the nonadditive dispersion interaction of three atoms, one would expect that it is the long range that determines the value of Z^4_{1111}, or equivalently

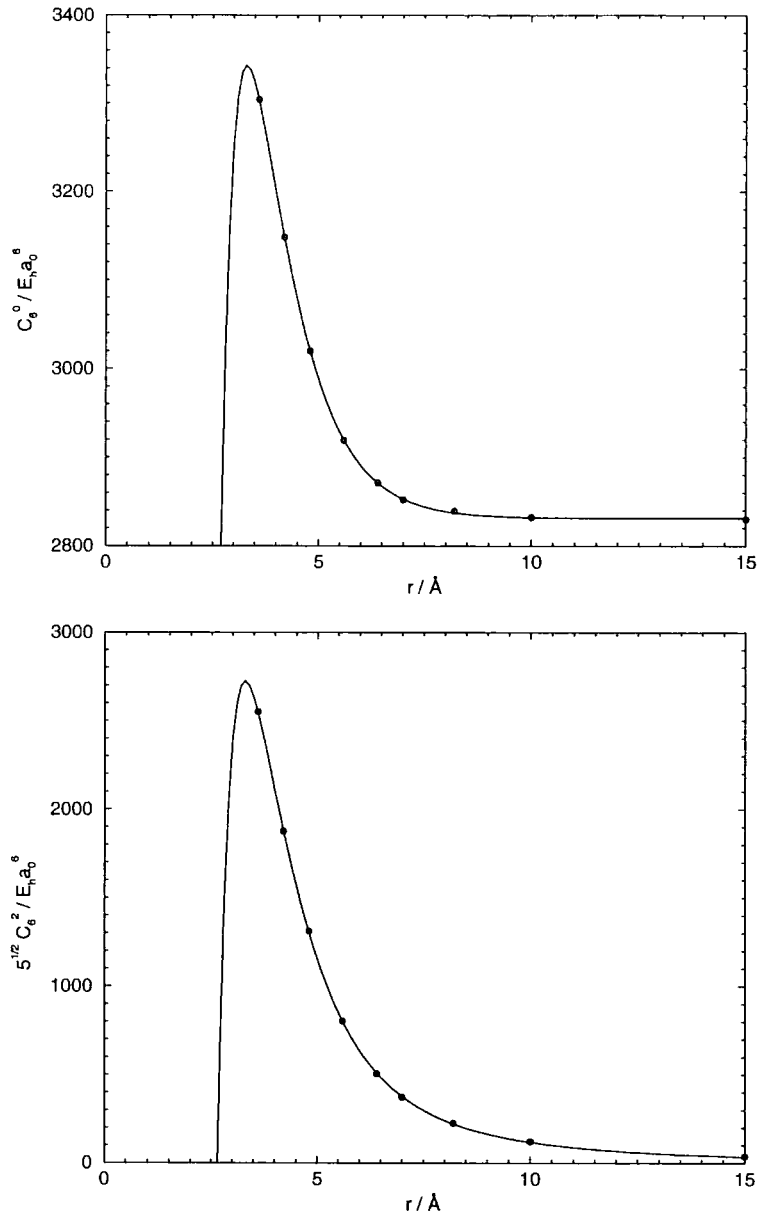

Figure 5.1: Dependence of C_6^0 and C_6^2 for lithium on the diatomic distance: dots are data from Ref. 123, curve is best fit on form (5.15).

c_6 in the fit of C_6^0. The fact that C_6^0 is decreasing towards its asymptotic value from above suggests a positive value for Z_{1111}^4. There is a dramatic decrease in the value of both C_6^0 and C_6^2 at short range just inside the last data point which is governed by the r^{-6} dependence in both fits. So it is actually the exponential that describes the increase of C_6^0 at long range in the fits. The last observation is that the b parameter in the damping functions is 7.012 and 6.688 from C_6^0 and C_6^2 fits, respectively. This is very different from what was determined in *ab-initio* studies of dispersion damping in lithium [132]. If we assume that atom-molecule dipolar interaction is damped in a similar way, i.e. that damping amounts to ≈ 45 % at the minimum of the diatomic ($r \approx 4.2$ Å) then $b \approx 1.5$ Å^{-1} ($f_6 = 0.442$).

We tried to refit the atom-molecule dispersion coefficients using physical insight. The fitting is performed sequentially. If an integer inverse-power law is assumed for the long-range dependence of C_6^0 and C_6^2, it is found that r^{-6} and r^{-3} are indeed the leading terms at long range, respectively, by inspection of the data in Table 5.3. Therefore, we first tried to determine the Z_{1111}^4 coefficient from the long-range behaviour of C_6^0 as a function of r. We performed a fit of $A_\infty + f_6(b,r)c_6/r^6$ to the last 2, 3, 4, and 5 data points in Table 5.3. Initially, we fixed the value of b to 1.5 Å^{-1}, and obtained $10.068 \cdot 10^7$, $13.582 \cdot 10^7$, $13.443 \cdot 10^7$, and $15.191 \cdot 10^7$, for $c_6/E_h a_0^{12}$, respectively. The *ab-initio* values do not lie on an entirely smooth curve and the accuracy of printed digits in Table 5.3 is not very high, which renders the value of c_6 not very accurate. Next, we floated the damping in the fits to 4 and to 5 points. It did not affect much the results for 4 points, $b = 1.514$ Å^{-1}, $c_6/E_h a_0^{12} = 13.365 \cdot 10^7$, $A_\infty/E_h a_0^6 = 2829.50$. But it did so for 5, raising b to 3.619 Å^{-1}. We also tried fitting all points by putting large weights at long range. We chose the weights at each point $f(r)$ to be $\max\{1, 10000[2825 - f(r)]^{-2}\}^2$. The best fit gives parameters $b = 1.713$ Å^{-1}, $c_6/E_h a_0^{12} = 11.896 \cdot 10^7$, $A_\infty/E_h a_0^6 = 2829.71$, and an rms error of 22.51 $E_h a_0^6$. If the damping parameter is not floated and is set to $b = 1.5$ Å^{-1}, we obtain $c_6/E_h a_0^{12} = 13.474 \cdot 10^7$, $A_\infty/E_h a_0^6 = 2829.60$, with an rms error of 39.58 $E_h a_0^6$. The comparison of fits to all points and with the values of $b = 1.5$ Å^{-1} and c_6 obtained from the Drude model are plotted in Figure 5.2. It can be seen that the Drude model and the fit with $b = 1.5$ Å^{-1} underestimate the *ab-initio* values at short range. The difference is fitted to an exponential. If all parameters are left floating, the fit becomes strongly correlated. Therefore we

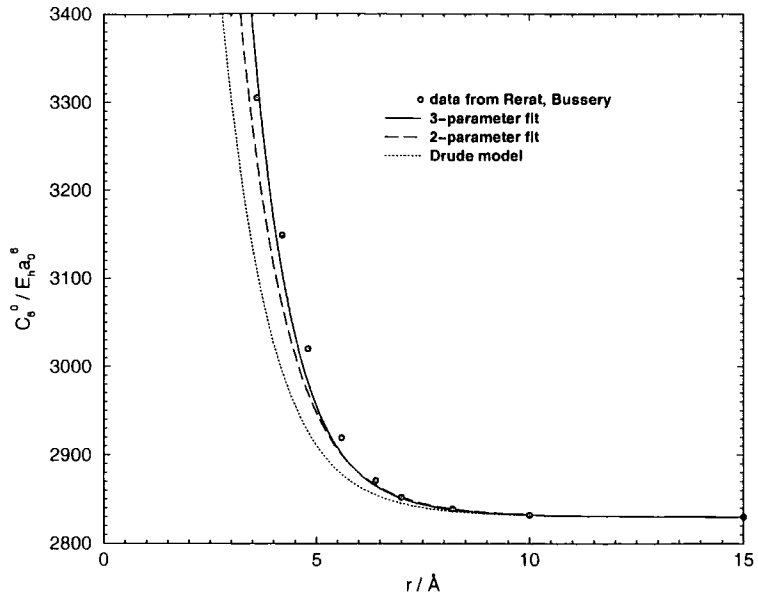

Figure 5.2: Best fit of $A_\infty + f_6(b,r)c_6/r^6$, with b set to 1.5 Å^{-1} and b floated, to C_6^0 data from Ref. 123. Comparison to the function where $b = 1.5$ Å^{-1} and c_6 obtained from the Drude model.

fix the values $b = 1.5$ Å^{-1}, $c_6/E_h a_0^{12} = 13.4 \cdot 10^7$, and $A_\infty/E_h a_0^6 = 2829.6$, and fit $A\exp(-Cx)$, with $x = (r - r_0)/r_0$ and $r_0 = 7$ Å, all points weighted equally. We obtain $A = (10.7 \pm 4.8)\ E_h a_0^6$, $C = 4.28 \pm 1.05$, with an rms error of 10.98 $E_h a_0^6$. If we refit with $c_6/E_h a_0^{12} = 9.283 \cdot 10^7$ as estimated from the Drude model, the properties of the fit are better, $A = (17.5 \pm 3.8)\ E_h a_0^6$, $C = 5.08 \pm 0.49$, with an rms error of 10.11 $E_h a_0^6$. The value of the parameter C is substantially different from b. We therefore relax the constraint of them being set equal as was done in (5.15).

We have made a similar analysis of the C_6^2 coefficient with the data from Ref. 123 listed in Table 5.3. A fit based on physical grounds is obtained by fixing the value of c_6 to one obtained from C_6^0 fit divided by 2, c_3 from the best *ab-initio* calculations ($c_3 = 6Z_{111}$) [93], and $b = 1.5$Å^{-1}. The difference is then fitted to an exponential $B\exp(-Cx)$. We tried fitting with the Drude value for c_6 and the value obtained from the C_6^0 fit with similar results (the fit was slightly better when using c_6 from the Drude model). We obtained $B = (35.2 \pm 5.6)\ E_h a_0^6$ and $C = 5.13 \pm 0.13$, with an rms error of 15.15 $E_h a_0^6$. The value for C obtained from fitting the C_6^0 and the C_6^2 are very similar when c_6 in both models is evaluated using Z_{1111}^4 from the Drude model. Therefore, we fixed C to have the same value in the forms for the C_6^0 and the C_6^2 and fitted all the parameters simultaneously (actually the final fit was to $\sqrt{5} \times C_6^2$

because the data [123] are reported for this quantity) to obtain our final estimates of A, B, and C in (5.45). The values obtained in this way are $A = (17.17 \pm 2.6)\ E_h a_0^6$, $B = (35.2 \pm 3.9)\ E_h a_0^6$, and $C = 5.13 \pm 0.25$, with an rms error of $25.00\ E_h a_0^6$. The fitted curves are plotted in Figure 5.4. The whole set of coefficients is summarized in Table 5.9.

	C_6^0	C_6^2
$A/E_h a_0^6$	17.17	-
$B/E_h a_0^6$	-	35.21
C	5.13	
$A_\infty/E_h a_0^6$		-
$b/\text{Å}^{-1}$	1.5	
$c_3/E_h a_0^9$	-	$3.412 \cdot 10^5$
$c_6/E_h a_0^{12}$	$9.283 \cdot 10^7$	$4.642 \cdot 10^7$

Table 5.9: Parameters of the final fit of atom-molecule dispersion coefficients C_6^0 and C_6^2 for lithium to data from Ref. 123. A, B, and C are fitted, other parameters set to values explained in the text.

It is easily seen that the fit in Figure 5.4 is not nearly as good as the one in Figure 5.1. It is likely that higher-order nonadditive terms contribute significantly at distances between 5 Å and 10 Å. With the inclusion of the higher inverse powers in the fit, the fit becomes highly correlated and accurate determination of the fit parameters is hard. It is desirable therefore to do the *ab-initio* determination of the fourth-order coefficients. Inclusion of such higher terms would probably change the values of the parameters A, B, and C fitted here, but the prescription for determining them would stay the same. *Ab-initio* three-body dispersion coefficients can be used in order to have an accurate representation of the dispersion when three atoms are far apart. Higher order terms become important as one distance is shortened and an exponential term is added with parameters fitted to describe the atom-molecule dispersion accurately. The present values, determined above, are an improvement over long-range potentials used previously [56].

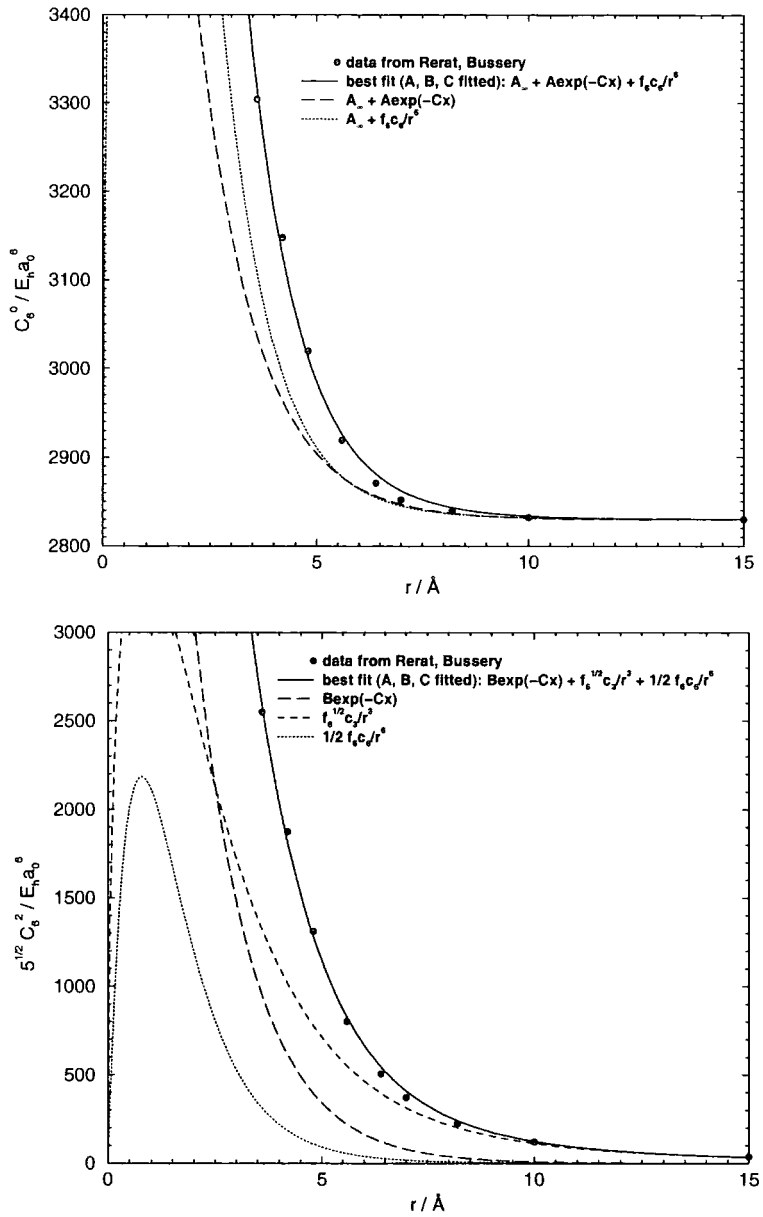

Figure 5.3: Dependence of C_6^0 and C_6^2 for lithium on the diatomic distance: dots are data from Ref. 123, the curve is our best fit. See text for details.

5.5 Global fit of the quartet ground state of lithium trimer

The potential energy surface for an accurate description of atom-diatom scattering at low energies must be accurate at both short and long atom-diatom separations. In order to obtain an accurate global representation, we join the IMLS fit developed in Chapter 4, which suffers from inaccuracy at long range, with the long-range form developed in this chapter.

We adopt a long-range form composed of the nonadditive $V(DDD)_3$ (Axilrod-Teller) (5.3), $V(DDD)_4$ (5.13) and $V(DDQ)_3$ (5.4) terms, in the notation introduced at the beginning of this chapter, the exponential term in (5.45), and the additive lithium potential published by Colavecchia et al. [56]. The dispersion coefficients Z_{111} and Z_{112} were taken from Ref. 93 and 122, respectively, and other parameters from Table 5.9 obtained by fitting to the atom-molecule dispersion coefficients as a function of intermolecular distance [123]. The diatomic potential of Colavecchia et al. is composed of the RKR points [48] in the well region, *ab initio* points on the repulsive wall, and a three-term analytic dispersion potential (5.2), smoothly interpolated and joined together. The advantage of this potential over the *ab initio* potentials is that it accurately reproduces experimental energies of the low-lying vibrational states. It uses the dispersion coefficients from Ref. 93. Colavecchia's potential also includes a correction term that is geared to reproduce the experimental value of the atom-atom (^{7}Li-^{7}Li) scattering length [54].

We used a switching function, S, to join the long-range form, $V_{\rm LR}$, with the IMLS/Shepard fit, $V_{\rm IMLS}$,

$$V = SV_{\rm IMLS} + (1 - S)V_{\rm LR}. \tag{5.52}$$

The switching function was taken to be

$$S(r_1, r_2, r_3) = \frac{1}{2}\tanh[1 - s_1(r_1 + r_2 + r_3 - s_2)]. \tag{5.53}$$

The values of the parameters s_1 and s_2 in (5.53) were determined in such a way that the switching is in the region where both potential forms give reasonably accurate electronic energies. The size of the switching region should preferably be large and its upper limit determined so that the above requirement is satisfied. We have found

that $s_1 = 0.7$ Å^{-1} and $s_2 = 20$ Å satisfy the above criteria. A graphical comparison of different atom-molecule potentials, used to construct the global representation, with the *ab-initio* electronic energies is shown in Figure 5.5. A smooth switching is easier to perform at linear than at T-shape geometries, because contributions other than the pure atom-molecule dispersion are significant there. The switching function is plotted in Figure 5.6 and the short-range, long-range, and global representations of potential are shown together in Figure 5.5 for specific nuclear arrangements as described in the captions. For the final potential to be used in scattering calculations below we have omitted some points to speed up the potential evaluation (we omitted distances 5.2 Å, 6.8 Å, and 8.4 Å, and added 7.6 Å in the set from which we formed the grid as described in Chapter 4).

The nonadditive part of the long-range form we use here is an improvement over using just the Axilrod-Teller term, as has often been done in the past (e.g. [56]), although the exponential term (5.45) contaminates the potential at intermediate distances at equilateral arrangements where the Axilrod-Teller term alone reproduces the *ab-initio* energies better. Whether this can be corrected by changing the parameters in (5.45) or the form itself must be changed remains to be seen. This region of potential does not significantly affect the atom-diatom collisions we intend to study.

In Figure 5.7, our global representation is compared with Colavecchia's potential at the Jacobi angle $\theta = 90°$. The figure illustrates that Li + Li_2 can undergo an insertion reaction, as the collinear Li_3 is at lower energy than the Li + Li_2 reactants. The global representation described in this subsection is used through the remainder of this work.

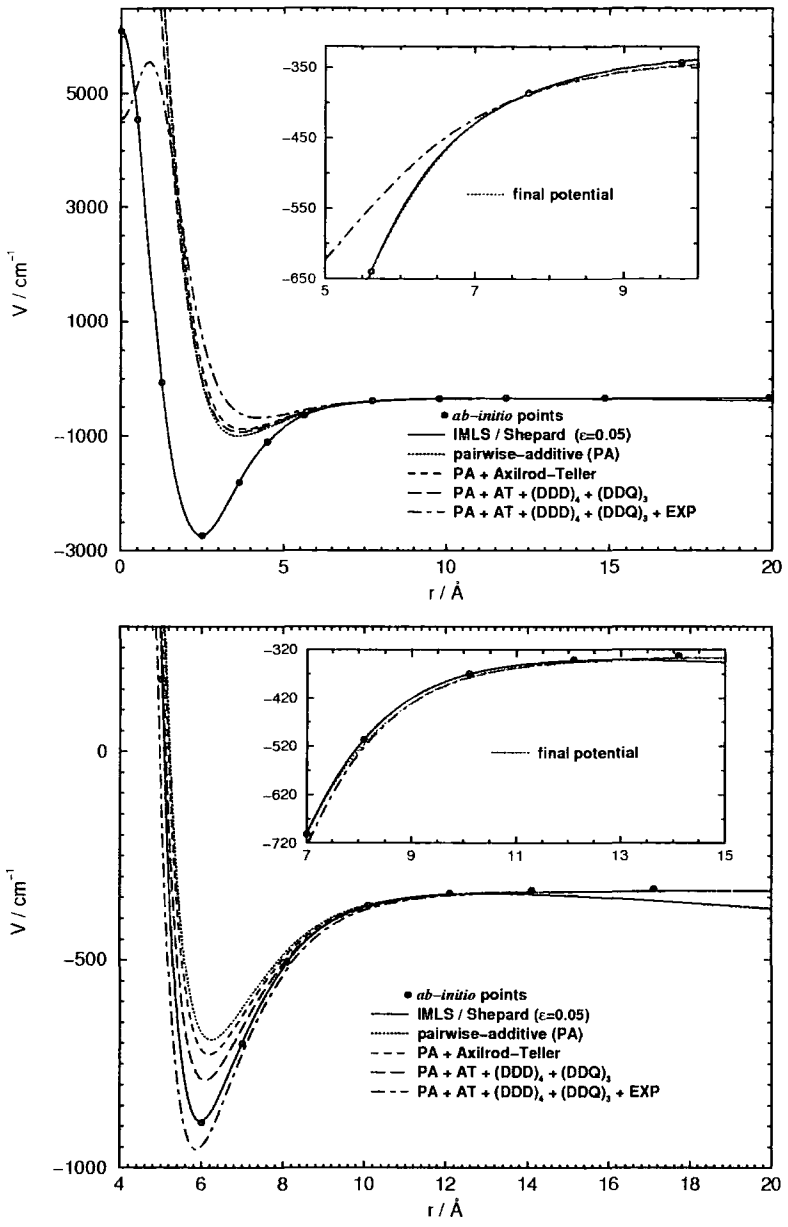

Figure 5.4: Comparison of different atom-diatom lithium potentials described in the text with *ab-initio* electronic energies. One internuclear distance is fixed at 4.2 Å, r is the distance between atom and centre of mass of molecule, Jacobi angle $\theta = 90°$ (top panel) and $\theta = 0°$ (bottom panel).

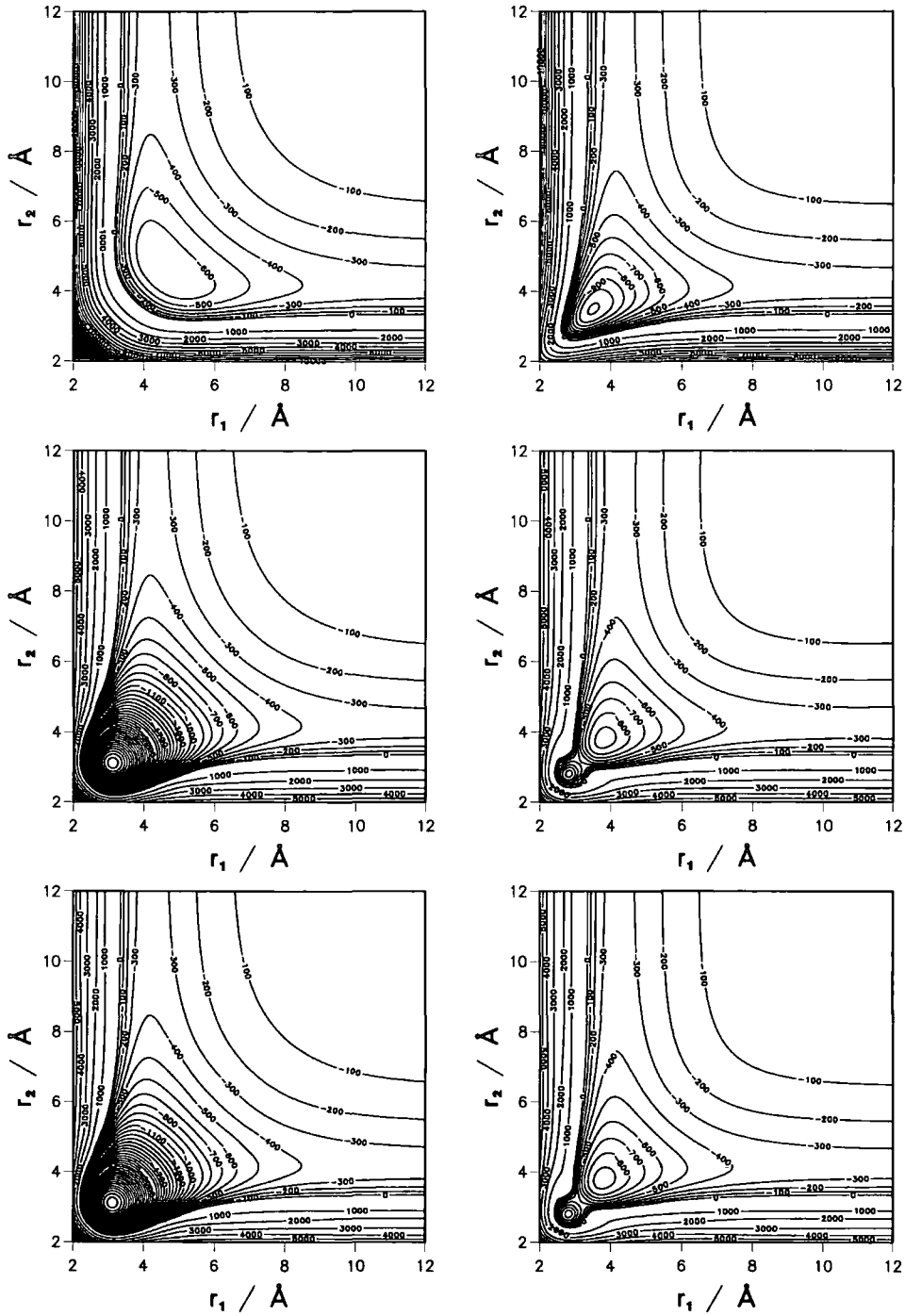

Figure 5.5: Long-range lithium trimer potential, described in the text (top row), the IMLS fit of lithium trimer potential (middle row), and global potential of lithium trimer (bottom row) as a function of internuclear distances r_1 and r_2 with the angle between them fixed at 60° (left column) and 180° (right column). Electronic energies are in cm^{-1}.

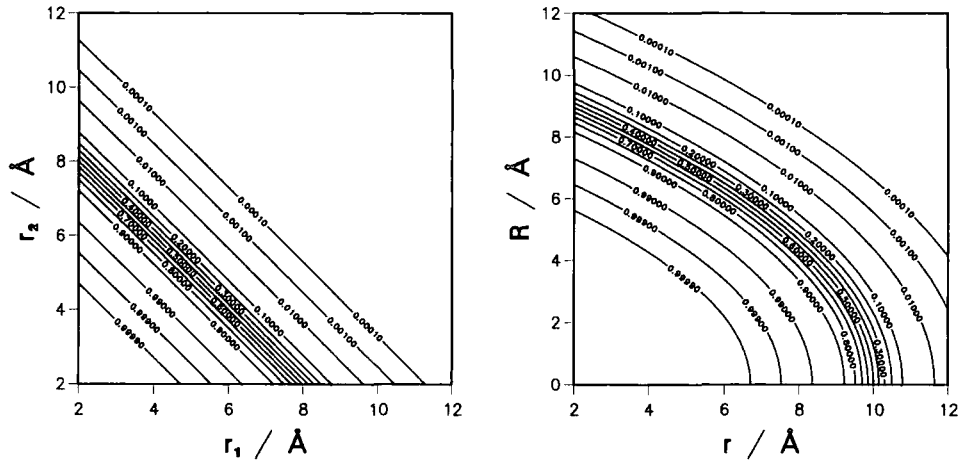

Figure 5.6: Switching function used to join the IMLS fit and long-range form, described in the text, into a global representation of the quartet ground state potential energy surface of lithium trimer at linear geometries as a function of internuclear distances (left) and at T-shape geometries in Jacobi coordinates ($\theta = 90°$) (right).

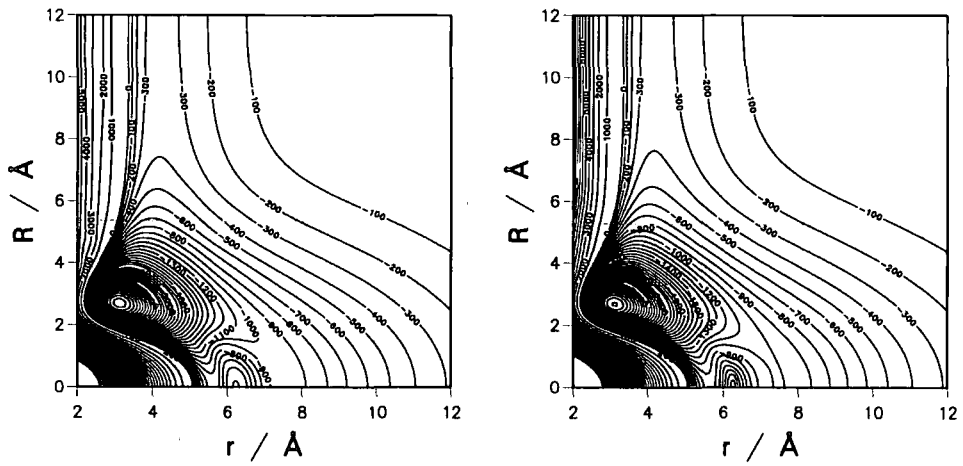

Figure 5.7: The quartet ground state potential of lithium trimer in Jacobi coordinates with $\theta = 90°$ as constructed by us (left) and by Colavecchia et al. [56] (right). Electronic energies are in cm^{-1}.

Chapter 6

Theory of reactive collisions in hyperspherical coordinates

6.1 Introduction

An accurate treatment of the nuclear dynamics in chemical reactions and inelastic collisions that allows for the rearrangement of identical particles is founded on the quantum scattering theory. It involves solving the Schrödinger equation for the motion of nuclei in the Born-Oppenheimer potential of electrons. First converged calculations in a realistic system were performed on $H + H_2$ by Kupperman and Schatz [133] in 1975. Numerous methods for solving the Schrödinger equation have been developed since [134]. They can be divided into the time-dependent and time-independent methods, depending on whether we are propagating an initial wave packet through time or solving the time-independent equation subject to certain boundary conditions.

Time-dependent methods are very inefficient in the limit of very small kinetic energies. The long wave-length and long duration of collision require enormous grids and therefore have not been successfully employed in this regime to our knowledge.

Time-independent methods are usually divided in the algebraic and coupled-channel methods.

In algebraic methods, the wavefunction is expanded in a basis set in all degrees of freedom and the expansion is substituted in the Schrödinger equation. This leads to linear algebraic equations for the expansion coefficients. The coefficients may also be determined variationally.

In coupled-channel methods, the wavefunction is expanded into a basis set in all degrees of freedom but one. This reduces the size of the basis set significantly. The solution in the remaining coordinate is obtained by propagating a set of independent solutions of the coupled ordinary differential equations resulting from the substitution of the expansion in the Schrödinger equation. The particular solution describing the process of interest is obtained by matching to the boundary conditions. These methods are most commonly used today.

This chapter reviews the theory of atom-diatom scattering in hyperspherical coordinates by a coupled-channel method.

Hyperspherical coordinates have been introduced to deal with the problem of describing different arrangements of the products of a reactive process on an equal footing. The hyperspherical coordinate system is described in the next section. The

hyperspherical radius describes the size of the system and is used as a propagation coordinate. When it is large, the products are far apart and asymptotic matching can be performed to obtain the S matrix which contains all information of interest on the scattering process. Dependence of the wavefunction on other, hyperangular, coordinates is described by an expansion in a carefully chosen basis set. The following sections describe the hamiltonian in hyperspherical coordinates of Parker et al. [135], the basis of pseudohyperspherical harmonics introduced by Launay and LeDourneuf [136], and the resulting coupled equations. This is followed by a description of the method of partial waves and the procedure of matching solutions in the asymptotic region, in order to make a connection between the coupled-channel solution and the observables. Propagation methods are briefly described at the end of the chapter.

The theory of scattering in hyperspherical coordinates that we use was developed by Parker and Pack [137] and completed in the form used throughout this work by Launay and LeDourneuf [136, 138]. The chapter heavily relies on these references in theory and detail of numerical implementation.

Another method that differs from our approach in the choice of the hyperspherical coordinate system and basis functions [139] has already been employed in the description of reactive collisions at ultracold temperatures by Balakrishnan et al. [11]. It used diatomic rovibrational wavefunctions as the basis set everywhere and therefore is not suitable for description of collisions where bond lengths are significantly shortened at the transition state, as in the alkali atom-diatom systems in their quartet ground states (see Chapter 2).

6.2 Hyperspherical coordinate system

In the following subsections, we introduce the hyperspherical coordinate system in a stepwise fashion.

6.2.1 Mass-scaled Jacobi coordinates

A quantum-mechanical description of the chemical reaction

$$\mathrm{A} + \mathrm{BC}(m) \rightarrow \mathrm{AB}(n) + \mathrm{C}, \tag{6.1}$$

where m and n denote internal states of the reactant and product diatomics respectively, is obtained by solving the time-independent Schrödinger equation

$$H\Psi = E\Psi. \tag{6.2}$$

The nuclear wavefunction depends on three vectors describing the positions of the nuclei. The centre of mass motion can be separated due to the translational invariance of the physical system and the remaining vectors may be chosen as the two Jacobi vectors,

$$\begin{aligned} \mathbf{R}_\tau &= \mathbf{x}_\tau - \frac{m_{\tau+1}\mathbf{x}_{\tau+1} + m_{\tau+2}\mathbf{x}_{\tau+2}}{m_{\tau+1} + m_{\tau+2}}, \\ \mathbf{r}_\tau &= \mathbf{x}_{\tau+2} - \mathbf{x}_{\tau+1}, \end{aligned} \tag{6.3}$$

where τ = A, B, or C, and τ, $\tau+1$, and $\tau+2$ are cyclic permutations of A, B, and C. $\mathbf{x}_\tau$ are the position vectors of atoms, $\mathbf{r}_\tau$ describes the vibrational motion of the molecule and $\mathbf{R}_\tau$ describes the translational motion of the atom τ relative to the molecule.

The hamiltonian describing three nuclei in a potential in the Jacobi coordinates is

$$H = -\frac{1}{2\mu_\tau}\nabla^2_{R_\tau} - \frac{1}{2\mu_{\tau+1,\tau+2}}\nabla^2_{r_\tau} + V(R_\tau, r_\tau), \tag{6.4}$$

where the reduced masses are given by

$$\mu_\tau = \frac{m_\tau(m_{\tau+1} + m_{\tau+2})}{m_\tau + m_{\tau+1} + m_{\tau+2}}, \tag{6.5}$$

and

$$\mu_{\tau,\tau+1} = \frac{m_\tau m_{\tau+1}}{m_\tau + m_{\tau+1}}. \tag{6.6}$$

This hamiltonian may be simplified in form and made isomorphic to the hamiltonian of one particle by scaling the coordinates,

$$\mathbf{S}_\tau = d_\tau \mathbf{R}_\tau, \quad \mathbf{s}_\tau = d_\tau^{-1}\mathbf{r}_\tau, \tag{6.7}$$

and requiring a common numerical factor multiplying the differential operators in the kinetic-energy part of the hamiltonian (6.4). From there we get three-particle reduced mass

$$\mu = \left(\frac{m_\mathrm{A} m_\mathrm{B} m_\mathrm{C}}{M}\right)^{1/2}, \tag{6.8}$$

where M is the total mass of the three atoms, and the scaling factor

$$d_\tau = \left[\frac{m_\tau}{\mu}\left(1 - \frac{m_\tau}{M}\right)\right]^{\frac{1}{2}}. \tag{6.9}$$

The hamiltonian in the new mass-scaled Jacobi coordinates (MSJ) [140] becomes

$$H = -\frac{1}{2\mu}\nabla^2_{S_\tau} - \frac{1}{2\mu}\nabla^2_{s_\tau} + V(S_\tau, s_\tau). \tag{6.10}$$

Equation (6.10) shows that the motion of three particles is equivalent to the motion of one particle in a six-dimensional space. The scaling factors are usually of the order of unity and, specifically, for the equal-mass system $d_\mathrm{A} = d_\mathrm{B} = d_\mathrm{C} = 1.07457$. The kinetic energy operator is symmetric under the transformations of group O(6) of all 6×6 orthogonal matrices. Three different sets of mass-scaled Jacobi coordinates, each particularly suitable for description of one final arrangement, are connected by an orthogonal transformation belonging to the group O(2),

$$\begin{pmatrix} \mathbf{S}_{\tau+1} \\ \mathbf{s}_{\tau+1} \end{pmatrix} = \begin{pmatrix} \cos(\phi_{\tau+1,\tau})\mathbf{1} & \sin(\phi_{\tau+1,\tau})\mathbf{1} \\ -\sin(\phi_{\tau+1,\tau})\mathbf{1} & \cos(\phi_{\tau+1,\tau})\mathbf{1} \end{pmatrix} \begin{pmatrix} \mathbf{S}_\tau \\ \mathbf{s}_\tau \end{pmatrix}, \tag{6.11}$$

with the kinematic angle

$$\phi_{\tau+1,\tau} = \arctan(m_{\tau+2}/\mu) \tag{6.12}$$

lying in the interval $[\pi, 3\pi/2]$.

Transformation between the space-fixed coordinate system and a suitable molecular frame, the body-fixed system, is achieved by spatial rotations belonging to the group O(3),

$$\begin{pmatrix} \mathbf{S}_\tau{}^{\mathrm{SF}} \\ \mathbf{s}_\tau{}^{\mathrm{SF}} \end{pmatrix} = \begin{pmatrix} \mathrm{R} & \mathbf{0} \\ \mathbf{0} & \mathrm{R} \end{pmatrix} \begin{pmatrix} \mathbf{S}_\tau{}^{\mathrm{BF}} \\ \mathbf{s}_\tau{}^{\mathrm{BF}} \end{pmatrix}, \tag{6.13}$$

where R is a 3×3 orthogonal matrix which connects the Cartesian coordinates of a three-component vector in two coordinate systems. Relative orientations of the two systems are usually expressed with three Euler angles [141],

$$\mathrm{R} = \begin{pmatrix} \cos\alpha\cos\beta\cos\gamma - \sin\alpha\sin\gamma & \sin\alpha\cos\beta\cos\gamma + \cos\alpha\sin\gamma & -\sin\beta\sin\gamma \\ -\cos\alpha\cos\beta\sin\gamma - \sin\alpha\cos\gamma & -\sin\alpha\cos\beta\sin\gamma + \cos\alpha\cos\gamma & \sin\beta\sin\gamma \\ \cos\alpha\sin\beta & \sin\alpha\sin\beta & \cos\beta \end{pmatrix}. \tag{6.14}$$

The direct product of the above O(2) (6.11) and O(3) (6.13) groups is commutative and forms a subgroup of the group O(6) of the full symmetry of the system.

An inversion in the space-fixed axes can be achieved either through an inversion in the group O(3), taking $R = -I$ in (6.13), or by a rotation in the O(2) through the kinematic angle $\pm\pi$, as can be seen from (6.11).

6.2.2 APH coordinates

We are now ready to define three body-fixed (BF) systems of axes requiring the BF z axis to point in the $\mathbf{S}_\tau$ direction. The arrangement index τ is also used to label the three respective BF systems. Transformation from the space-fixed (SF) to the $(\mathrm{BF})_\tau$ system is achieved by rotation through the Euler angles $\alpha_\tau = \phi_{S_\tau}$ and $\beta_\tau = \theta_{S_\tau}$, where ϕ_{S_τ} and θ_{S_τ} are spherical polar angles of $\mathbf{S}_\tau$. The Euler angle γ_τ is chosen to make $\mathbf{s}_\tau$ lie in the $(\mathrm{BF})_\tau$ xz plane with a non-negative x component. The mass-scaled Jacobi vectors have the following components in the so-defined BF systems,

$$\mathbf{S}_\tau = \begin{pmatrix} 0 \\ 0 \\ S_\tau \end{pmatrix} \quad \text{and} \quad \mathbf{s}_\tau = \begin{pmatrix} s_\tau \sin\Theta_\tau \\ 0 \\ s_\tau \cos\Theta_\tau \end{pmatrix}, \tag{6.15}$$

where Θ_τ is the angle between $\mathbf{S}_\tau$ and $\mathbf{s}_\tau$. In this way the BF y axis is perpendicular to the plane of the three particles and common to all three BF systems.

In the next stage we define another BF system as the instantaneous principal axis system. First we extend the definition of the kinematic rotation angle to be the continuous variable defined as to maximize the magnitude of $\mathbf{Q}$ defined through the relation

$$\begin{pmatrix} \mathbf{Q} \\ \mathbf{q} \end{pmatrix} = \mathbf{T}(\phi_\tau) \begin{pmatrix} \mathbf{S}_\tau \\ \mathbf{s}_\tau \end{pmatrix}, \tag{6.16}$$

where the $\mathbf{T}$ matrix is the kinematic transformation matrix in (6.11). The variable ϕ_τ is taken to have its origin in the initial arrangement τ, so the definition for the other arrangements differs only in the translation through the kinematic angle in (6.12). Q is maximum if

$$\sin(2\phi_\tau) = \frac{2\mathbf{S}_\tau\mathbf{s}_\tau}{[(S_\tau^2 - s_\tau^2)^2 + (2\mathbf{S}_\tau\mathbf{s}_\tau)^2]^{1/2}} \tag{6.17}$$

and

$$\cos(2\phi_\tau) = \frac{(S_\tau^2 - s_\tau^2)}{[(S_\tau^2 - s_\tau^2)^2 + (2\mathbf{S}_\tau\mathbf{s}_\tau)^2]^{1/2}}, \tag{6.18}$$

giving

$$Q = \left\{ \frac{1}{2}(S_\tau^2 + s_\tau^2) + \frac{1}{2}\left[(S_\tau^2 - s_\tau^2)^2 + (2\mathbf{S}_\tau\mathbf{s}_\tau)^2\right]^{1/2} \right\}^{1/2} \tag{6.19}$$

and

$$q = \left\{ \frac{1}{2}(S_\tau^2 + s_\tau^2) - \frac{1}{2}\left[(S_\tau^2 - s_\tau^2)^2 + (2\mathbf{S}_\tau\mathbf{s}_\tau)^2\right]^{1/2} \right\}^{1/2}. \tag{6.20}$$

Vectors $\mathbf{Q}$ and $\mathbf{q}$ defined in this way are automatically orthogonal, $\mathbf{Qq} = 0$, and their magnitudes are independent of the arrangement. The choice of angle ϕ_τ in (6.17)

and (6.18) also minimizes q. The range of ϕ_τ is taken in the interval $[0, 2\pi]$, although its definition is not unique there through the above equations. Other choices can lead into difficulties when quantizing angular momenta [137].

The $(\mathrm{BF})_Q$ system can now be defined as the one whose z and x axes coincide with $\mathbf{Q}$ and $\mathbf{q}$. Substituting the angle ϕ_τ from equations (6.17) and (6.18) and $\mathbf{S}_\tau$ and $\mathbf{s}_\tau$ from (6.15) in the upper row of the matrix identity (6.16), we can find the rotation angle β_Q around the common BF y axis which brings the $(\mathrm{BF})_\tau$ z axis into coincidence with $\mathbf{Q}$,

$$\tan \beta_{Q_\tau} = \frac{s_\tau \sin \phi_\tau \sin \Theta_\tau}{S_\tau \cos \phi_\tau + s_\tau \sin \phi_\tau \cos \Theta_\tau}. \tag{6.21}$$

$\mathbf{q}$ is then automatically aligned to the new x axis.

Components of the inertia tensor in the $(\mathrm{BF})_Q$ system are

$$I_x = \mu Q^2, \quad I_z = \mu q^2, \quad \text{and} \quad I_y = I_x + I_z. \tag{6.22}$$

Axes of the $(\mathrm{BF})_Q$ system are aligned to the principal axes of inertia of the three particles. It is valid that $I_z \leq I_x \leq I_y$, so that the z axis is the axis of least inertia.

Asymptotically, when $S_\tau \gg s_\tau$, $\mathbf{Q}$ aligns parallel to $\mathbf{S}_\tau$ in each arrangement, as can be seen from (6.17) and (6.18), but $\mathbf{q}$ does not align parallel to s_τ since it is always orthogonal to $\mathbf{Q}$. Therefore, these coordinates become impractical in the asymptotic region.

Adiabatically adjusting principal axes hyperspherical (APH) coordinates are now defined [135] with three internal and three external coordinates. The three external coordinates are taken to be three Euler angles α_Q, β_Q, and γ_Q of the $(\mathrm{BF})_Q$ system with respect to a space-fixed system. The internal coordinates describe the shape of the three-particle system and they are taken to be ϕ_τ,

$$\rho = \sqrt{Q^2 + q^2}, \tag{6.23}$$

and

$$\theta = 2 \arctan q/Q. \tag{6.24}$$

The above relations, together with the equations (6.17), (6.18), (6.19), and (6.20) define the internal APH coordinates in terms of the mass-scaled Jacobi coordinates. It is worth noting that the hyperradius is the same as in the other hyperspherical systems in literature [142]

$$\rho = \sqrt{S_\tau^2 + s_\tau^2} \tag{6.25}$$

and is independent of the arrangement τ. The way to transform back is through the following relations, that define Cartesian components of $\mathbf{S}_\tau$ and $\mathbf{s}_\tau$,

$$Z_\tau = \rho\cos(\theta/2)\cos\phi_\tau, \tag{6.26}$$

$$X_\tau = -\rho\sin(\theta/2)\sin\phi_\tau, \tag{6.27}$$

$$z_\tau = \rho\cos(\theta/2)\sin\phi_\tau, \tag{6.28}$$

$$x_\tau = \rho\sin(\theta/2)\cos\phi_\tau. \tag{6.29}$$

From (6.29) we can also obtain compact expression for S_τ, s_τ, and the angle Θ_τ between them,

$$S_\tau = \frac{\rho}{\sqrt{2}}\left\{1+\cos\theta\cos(2\phi_\tau)\right\}^{1/2}, \tag{6.30}$$

$$s_\tau = \frac{\rho}{\sqrt{2}}\left\{1-\cos\theta\cos(2\phi_\tau)\right\}^{1/2}, \tag{6.31}$$

$$\cos\Theta_\tau = \frac{\cos\theta\sin(2\phi_\tau)}{\left[1-\cos^2\theta\cos^2(2\phi_\tau)\right]^{1/2}}. \tag{6.32}$$

The domains of the APH internal coordinates are $\rho \in [0,\infty)$, $\theta \in [0,\pi/2]$, and $\phi_\tau \in [0,2\pi)$. ϕ_τ is the only variable dependent on the arrangement. The range of ϕ_τ covers six arrangements, the usual three and the ones connected to them by an inversion. Only internal coordinates are needed for the evaluation of the potential through (6.32). All degrees of freedom but the hyperradius have a finite range and are therefore suitable for expansion into a basis set.

The moments of inertia can easily be evaluated using (6.22) with $Q = \rho\cos(\theta/2)$ and $q = \rho\sin(\theta/2)$. Symmetric top configurations are obtained for $\theta = \pi/2$. Collinear configurations are at $\theta = 0$.

6.3 Hamiltonian

Hamiltonian in the APH coordinates can be obtained by the procedure of Podolsky as described in detail in Ref. 143.

$$H = -\frac{1}{2\mu\rho^5}\frac{\partial}{\partial\rho}\rho^5\frac{\partial}{\partial\rho} + \frac{\boldsymbol{\Lambda}^2}{2\mu\rho^2} + V(\rho,\theta,\phi), \tag{6.33}$$

where V is the interaction potential and $\boldsymbol{\Lambda}^2$ is the square of grand angular momentum [144],

$$\boldsymbol{\Lambda}^2 = \boldsymbol{\Lambda}_0^2 + \frac{4J_z^2}{\sin^2\theta} + \mathcal{R}, \tag{6.34}$$

with

$$\Lambda_0^2 = -\frac{4}{\sin 2\theta}\frac{\partial}{\partial\theta}\sin 2\theta\frac{\partial}{\partial\theta} - \frac{1}{\cos^2\theta}\frac{\partial^2}{\partial\phi^2}, \tag{6.35}$$

$$\mathcal{R} = \frac{J_x^2 - J_z^2}{\cos^2\theta/2} + \frac{J_y^2}{\cos^2\theta} - \frac{2\mathrm{i}\sin\theta J_y}{\cos^2\theta}\frac{\partial}{\partial\phi}. \tag{6.36}$$

Here J_x, J_y, and J_z are angular momentum operators in the principal axes frame $(\mathrm{BF})_Q$. The first term in the hamiltonian in (6.33) is the kinetic energy, $\mathbf{\Lambda}_0^2$ represents the deformation terms, and the last term in (6.36) is the Coriolis coupling that is coupling vibrational and rotational degrees of freedom. The remaining terms in $\mathbf{\Lambda}^2$ are rotational terms of a fluid rotor [137]. The terms in $\mathcal{R}$ are small for linear configurations ($\theta = 0$) and large for symmetric top ($\theta = \pi/2$) configurations. In fact, the singularity at $\theta = \pi/2$ in the terms containing J_y and J_y^2 may cause problems in the convergence depending on the particular basis set used for the angular coordinates. It is called the Eckart singularity.

The procedure used to derive the hamiltonian also provides the volume element for integration over space in the APH coordinates. The integral of a function F over the full space is

$$\int F\mathrm{d}\mathbf{S}_\tau\mathrm{d}s_\tau = \frac{1}{16}\int_0^\infty \rho^5\mathrm{d}\rho\int_{-\pi}^{\pi}\mathrm{d}\phi_\tau\int_0^{\pi/2}\sin 2\theta\mathrm{d}\theta \times\int_0^{2\pi}\mathrm{d}\alpha_Q\int_0^{\pi}\sin\beta_Q d\beta_Q\int_0^{2\pi}\mathrm{d}\gamma_Q F. \tag{6.37}$$

6.4 Basis functions

In order to solve the Schrödinger equation (6.2) with the hamiltonian (6.33), we expand all the degrees of freedom but the hyperradius in a basis set. The ρ-dependent basis functions are taken in the form

$$\Phi_{k\Omega}^{JM\epsilon_I\sigma}(\rho;\theta,\phi,\alpha,\beta,\gamma) = \varphi_k^{\epsilon_I\sigma\Omega}(\rho;\theta,\phi)N_\Omega^{JM\epsilon_I}(\alpha,\beta,\gamma). \tag{6.38}$$

Subscripts on Euler angles and ϕ denoting the $(\mathrm{BF})_Q$ system and arrangement τ have been suppressed. The functions on the right-hand-side of (6.38) are described below.

$N_\Omega^{JM\epsilon_I}(\alpha,\beta,\gamma)$ is a symmetric top wavefunction of the definite parity ϵ_I. The wavefunction of the rotationally invariant hamiltonian can be written as a linear combination of Wigner rotation matrices. The Wigner rotation matrix is a $(2J +$

1)-dimensional irreducible representation of the rotation operator in the angular momentum basis. Using the active rotation conventions from Zare [141], we have

$$\begin{aligned} D^J_{M\Omega}(\mathbf{R}) &= \langle JM|\mathrm{e}^{-\mathrm{i}J_z\alpha}\mathrm{e}^{-\mathrm{i}J_y\beta}\mathrm{e}^{-\mathrm{i}J_z\gamma}|J\Omega\rangle \\ &= \mathrm{e}^{-\mathrm{i}(M\alpha+\Omega\gamma)}d^J_{M\Omega}(\beta), \end{aligned} \tag{6.39}$$

where

$$d^J_{M\Omega}(\beta) = \langle JM|\mathrm{e}^{-\mathrm{i}J_y\beta}|J\Omega\rangle. \tag{6.40}$$

Using (6.39), the rotated wavefunction is

$$\mathbf{R}\psi^{J\Omega}(\alpha,\beta,\gamma) = \sum_M D^J_{M\Omega}(\mathbf{R})\psi^{JM}(\alpha,\beta,\gamma). \tag{6.41}$$

Now, the rotated wavefunction at a particular point in space assumes the value of the original wavefunction evaluated at the coordinates that are brought to that point by the rotation. Choosing the rotation angles to be the same as the argument of the original wavefunction and inverting (6.41) using unitarity of $D^J_{M\Omega}(\mathbf{R})$, we arrive to the wavefunction of an asymmetric top as a linear combination of complex-conjugated rotation matrices,

$$\psi^{JM}(\alpha,\beta,\gamma) = \sum_\Omega D^{J*}_{M\Omega}(\alpha,\beta,\gamma)\psi^{J\Omega}(0,0,0). \tag{6.42}$$

If the body has an axis of symmetry, an arbitrary rotation around that axis can change the wavefunction only up to a phase factor, so that only one term survives in the sum (6.42) and the symmetric top wavefuntion is just a normalized Wigner rotation matrix [141]

$$\sqrt{\frac{2J+1}{8\pi^2}}D^{J*}_{M\Omega}(\alpha,\beta,\gamma). \tag{6.43}$$

M is the projection of the angular momentum on the space-fixed z axis (rotation through α) and Ω on the body-fixed axis (rotation through γ), which can be seen by applying the appropriate angular momentum operators on the explicit form of the rotation matrices in (6.39) [141]. When $\Omega = 0$, the wavefunction of the symmetric top is reduced to a spherical harmonic and describes a linear rigid rotator.

The operation of inversion, Π, as mentioned earlier, can be achieved by either a kinematic rotation through $\pm\pi$, in the group O(2), or through a reflection in the xz plane followed by a rotation through π about the y axis, in the group O(3). The reflection has no effect on the $\mathbf{Q}$ and $\mathbf{q}$ vector, which determine the orientation of

the BF system, because the particles lie in the xz plane. The effect of the rotation follows from

$$\mathbf{R}(0,\pi,0)\mathbf{R}(\alpha,\beta,\gamma) = \mathbf{R}(\alpha+\pi,\pi-\beta,\pi-\gamma). \tag{6.44}$$

Using the properties of the Wigner rotation matrices [141],

$$\Pi D^{J*}_{M\Omega}(\alpha,\beta,\gamma) = D^{J*}_{M\Omega}(\alpha+\pi,\pi-\beta,\pi-\gamma) = (-1)^{J+\Omega} D^{J*}_{M-\Omega}(\alpha,\beta,\gamma). \tag{6.45}$$

Parity-adapted functions, having the definite parity eigenvalue ϵ_I, are obtained from any function F as $F+\epsilon_I \Pi F$. Therefore, the normalized parity-adapted symmetric top wavefunctions suitable for expansion of the rotational part of the wavefunction are

$$N^{JM\epsilon_I}_{\Omega}(\alpha,\beta,\gamma) = \sqrt{\frac{2J+1}{16\pi^2(1+\delta_{\Omega 0})}}\left[D^{J*}_{M\Omega}(\alpha,\beta,\gamma) + \epsilon_I(-1)^{J+\Omega} D^{J*}_{M-\Omega}(\alpha,\beta,\gamma)\right]. \tag{6.46}$$

Functions $\varphi^{\epsilon_I\sigma\Omega}_k(\rho;\theta,\phi)$ in (6.38) are eigenfunctions of the two-dimensional "hypersurface" Schrödinger equation at a fixed hyperradius ρ,

$$H^{\Omega}(\rho)\varphi^{\epsilon_I\sigma\Omega}_k(\rho;\theta,\phi) = \epsilon^{\epsilon_I\sigma\Omega}_k \varphi^{\epsilon_I\sigma\Omega}_k(\rho;\theta,\phi). \tag{6.47}$$

The subscript k labels the eigenfunctions and the hypersurface hamiltonian is

$$H^{\Omega}(\rho) = \frac{1}{2\mu\rho^2}\left(\mathbf{\Lambda}_0^2 + \frac{4\Omega^2}{\sin^2\theta}\right) + V(\rho;\theta,\phi). \tag{6.48}$$

H^{Ω} depends on ρ and Ω and equation (6.47) is solved in each symmetry block $\{\epsilon_I,\sigma,\Omega\}$, where σ labels the irreducible representations of the molecular permutation symmetry group (S_3), by a variational expansion over the eigenfunctions, $\mathcal{Y}$, of $\mathbf{\Lambda}_0^2 + \frac{4\Omega^2}{\sin^2\theta}$. $\mathcal{Y}$ are called pseudohyperspherical harmonics [136] (as opposed to the hyperspherical harmonics which are the eigenfunctions of the full grand angular momentum operator $\mathbf{\Lambda}^2$). The equation (6.47) with $V = 0$ is separable in θ and ϕ and results in two one-dimensional equations,

$$\left(-\frac{4}{\sin 2\theta}\frac{\mathrm{d}}{\mathrm{d}\theta}\sin 2\theta\frac{\mathrm{d}}{\mathrm{d}\theta} + \frac{\nu^2}{\cos^2\theta} + \frac{4\Omega^2}{\sin^2\theta}\right) g^{\nu\Omega}_K(\theta) = K(K+4) g^{\nu\Omega}_K(\theta) \tag{6.49}$$

and

$$\frac{\mathrm{d}^2}{\mathrm{d}\phi^2} h^{\epsilon_P}(\phi) = \nu^2 h^{\epsilon_P}(\phi), \tag{6.50}$$

solutions of which are combined into the pseudohyperspherical harmonics,

$$\mathcal{Y}^{\epsilon_I\epsilon_P}_{K\nu\Omega}(\theta,\phi) = g^{\nu\Omega}_K(\theta) h^{\epsilon_P}(\phi). \tag{6.51}$$

The parity and permutation symmetry have been implied by the indices in the above equations.

In the case of the two identical atoms B and C in (6.1), permutation symmetry is achieved by the simultaneous transformations, $\phi \to -\phi$ and the rotation through π about the BF z axis. Applying this transformation to the parity-adapted symmetric top wavefunctions in (6.46) results in the eigenvalue $(-1)^{\Omega}$. This factor is cancelled by an equal factor when the transformation is applied to h^{ϵ_P}, if they are taken to be trigonometric functions $h^{\epsilon_P}(\nu\phi - \Omega\pi/2)$. Changing the sign of ϕ makes the difference in phase of $\Omega\pi$. Trigonometric solution h^{ϵ_P} is a cos function, if $\epsilon_P = +1$ (symmetric under exchange of B and C), and a sin function, if $\epsilon_P = -1$ (antisymmetric).

Inversion amounts to the transformation $\phi \to \phi + \pi$. The non-negative integer ν must be even for $\epsilon_I = +1$ and odd for $\epsilon_I = -1$ solutions.

When dealing with three different atoms both sets of solutions for $\epsilon_P = \pm 1$ must be taken into the basis, since permutation operator does not commute with the potential.

In case all three atoms are indistinguishable the additional symmetry of the system is the cyclic permutation, which is achieved by the transformation $\phi \to \phi + 2\pi/3$ taking effect on the basis functions h. The index labelling the symmetry block is now $\sigma = (\epsilon_P, \sigma_R)$, where σ_R picks whether we are dealing with the symmetric representation when $\epsilon_P = +1$ and antisymmetric representation when $\epsilon_P = -1$ or with the doubly degenerate representation (E) of the permutation group S_3. In the case of the symmetric or antisymmetric representations, $\nu = 0, 6, 12, \ldots$, if $\epsilon_I = +1$, and $\nu = 3, 9, 15, \ldots$, if $\epsilon_I = -1$. These are the ν values that leave the basis functions h unchanged under a cyclic permutation. The h functions with the remaining ν values span the doubly degenerate representation: $\nu = 2, 4, 8, 10, \ldots$, if $\epsilon_I = +1$, and $\nu = 1, 5, 7, 11, \ldots$, if $\epsilon_I = -1$.

The solution for the $g_K^{\nu\Omega}(\theta)$ in equation (6.49) is known analytically and may be expressed in terms of the Jacobi polynomials of the variable $\sin^2\theta$, with $K = \nu + 2\Omega + 4n$, where n is a non-negative integer. Numerically, it is convenient to solve it by determining the coefficients c in the expansion

$$g_K^{\nu\Omega}(\theta) = a_\nu(\theta) \sum_{k=0}^{[K/4]} b_k(\theta) c_{kK}^{\nu\Omega}, \tag{6.52}$$

variationally [136]. $[x]$ in (6.52) denotes the integer part of x. In the place of $b_k(\theta)$,

$\cos 2k\theta$ is used if $[\nu/2]$ is even and $\cos(2k+1)\theta$ if $[\nu/2]$ is odd, when Ω is even. On the other hand when Ω is odd, $\sin(2k+1)\theta$ is used in place of $b_k(\theta)$ if $[\nu/2]$ is even and $\sin(2k+2)\theta$ if $[\nu/2]$ is odd. The function $a_\nu(\theta)$ is 1 when ν is even and $\sqrt{\cos\theta}$ when ν is odd.

The basis of pseudohyperspherical harmonics (6.51) is orthogonal. Its size is limited in practical calculations by the maximum value for K, $K_{\max}$. Calculation of the matrix elements of the potential V in the $\mathcal{Y}$ basis involves two-dimensional quadratures with trigonometric functions and can be made very efficient using simple trigonometric rules. Integrals may be evaluated using Gauss-composite integration. Outside the fragmentation limit, $K_{\max}$, sufficient to converge a given number of hypersurface states in (6.47), increases linearly with ρ. The basis set size for a given $K_{\max}$ is proportional to $K_{\max}^2$. As the arrangement valleys become increasingly narrow, the wavefunction concentrates in the small region of the configuration space and this basis becomes inefficient. To reduce the problems with the basis set size at large ρ, it was suggested [138] to reduce its size according to the following algorithm. $1/\cos^2\theta$ is diagonalized in the basis of $\mathcal{Y}$ and only those linear combinations are kept that have the eigenvalues close to one. They correspond to the functions localized near $\theta = 0$, i.e. linear configurations.

6.5 Coupled equations

Solution of the Schrödinger equation (6.2) for the total mechanical angular momentum quantum number J and its projection on a SF axis M may be expanded in terms of the basis functions (6.38) described above. Basis functions evaluated at ρ_m are used to represent a solution within the sector $[\rho_{m-1/2}, \rho_{m+1/2}]$ that is centered at ρ_m in form

$$\Psi^{JM\epsilon_I\sigma}(\rho,\theta,\phi,\alpha,\beta,\gamma) = \frac{1}{\rho^{5/2}} \sum_{k\Omega} \Phi_{k\Omega}^{JM\epsilon_I\sigma}(\rho_m;\theta,\phi,\alpha,\beta,\gamma) f_{k\Omega}^{J\epsilon_I\sigma}(\rho_m;\rho). \qquad (6.53)$$

We substitute the above expansion of $\Psi^{JM\epsilon_I\sigma}$ (6.53) and the hamiltonian (6.33) into the Schrödinger equation (6.2), multiply from the left by a basis function (6.38) and integrate using their orthogonality. We arrive to a set of coupled differential equations valid within a sector,

$$\left(-\frac{1}{2\mu}\frac{\mathrm{d}^2}{\mathrm{d}\rho^2} + \frac{15}{8\mu\rho^2} - E\right) f_{k\Omega}^{J\epsilon_I\sigma}(\rho_m;\rho) + \sum_{k'} H_{kk'}^{\epsilon_I\sigma\Omega}(\rho_m;\rho) f_{k'\Omega}^{J\epsilon_I\sigma}(\rho_m;\rho)$$

$$+\frac{1}{2\mu\rho^2}\sum_{k'\Omega'}\mathcal{R}^{J\epsilon_I\sigma}_{k\Omega,k'\Omega'}(\rho_m)f^{J\epsilon_I\sigma}_{k'\Omega'}(\rho_m;\rho)=0, \qquad (6.54)$$

with coupling matrix elements given by

$$\begin{aligned} H^{\epsilon_I\sigma\Omega}_{kk'}(\rho_m;\rho) &= \langle\varphi^{\epsilon_I\sigma\Omega}_k(\rho;\theta,\phi)|\frac{\rho_m^2}{\rho^2}\epsilon^{\epsilon_I\sigma\Omega}_{k'}+ \\ &+ V(\rho,\theta,\phi)-\frac{\rho_m^2}{\rho^2}V(\rho_m,\theta,\phi)|\varphi^{\epsilon_I\sigma\Omega}_{k'}(\rho;\theta,\phi)\rangle_{(\theta,\phi)} \qquad (6.55) \end{aligned}$$

and

$$\mathcal{R}^{J\epsilon_I\sigma}_{k\Omega,k'\Omega'}(\rho_m)=\langle\Phi^{JM\epsilon_I\sigma}_{k\Omega}(\rho_m;\theta,\phi,\alpha,\beta,\gamma)|\mathcal{R}|\Phi^{JM\epsilon_I\sigma}_{k'\Omega'}(\rho_m;\theta,\phi,\alpha,\beta,\gamma)\rangle_{(\theta,\phi,\alpha,\beta,\gamma)}. \qquad (6.56)$$

Matrix elements in (6.55) are calculated at the middle of each sector, where they are diagonal in k and Ω, and at the boundaries, where the small off-diagonal elements in k arise due to the variation of the potential within a sector. At other positions within a sector they are evaluated using the Lagrange interpolation formula. Quadratures involve θ and ϕ and they are independent of J.

Matrix elements in (6.56) couple states with $\Delta\Omega = 0, \pm1, \pm2$ and are computed by expressing J_x and J_y in terms of the raising and lowering operators ($J_\pm$) and regarding them as the quantum-mechanical operators obeying inverse commutation relations, since they operate in the BF frame [141]. They are evaluated only at the middle of each sector. Quadratures involving θ and ϕ are independent of J.

Basis set (6.38) is independent of ρ within a sector and is therefore termed diabatic. Coupled equations (6.54) are in a diabatic representation, resulting from an expansion in the ρ-independent basis. They are easier to solve than the coupled equations that would result from working in an adiabatic representation, with a ρ-dependent basis. In the adiabatic representation, the coupling matrix elements involve the first and second derivatives of the basis functions with respect to ρ. These are rapidly varying functions of ρ, so that the use of an adiabatic basis requires a denser grid on which the basis functions need to be evaluated and is therefore numerically more difficult.

6.6 Partial wave expansion and boundary conditions

It would be computationally too expensive to solve the Schrödinger equation for three atoms directly by discretization in all six degrees of freedom. A way to simplify the problem is to make use of the constants of motion and expand the wavefunction in the eigenfunctions of $\mathbf{J}^2$ and J_z, which in the absence of external fields commute with the hamiltonian (6.33),

$$\Psi^{(+)} = \sum_{JM} A^{JM} \Psi^{JM}. \tag{6.57}$$

The hamiltonian does not couple different components of J and M, so we have effectively reduced the dimensionality of the problem by two. The additional symmetries that reduce the size of the computational effort are parity and permutation, in case we are dealing with identical particles.

A scattering event can be described by the stationary solution of the Schrödinger equation (6.2) at energy E that tends to its asymptotic form

$$\begin{aligned} \Psi^{(+)}_{\mathbf{k}_{\tau vj}\tau vjm} &\simeq \mathrm{e}^{i\mathbf{k}_{\tau vj}\mathbf{S}_\tau} \zeta_{\tau vjm}(s_\tau) \\ &+ \sum_{\tau' v' j' m'} \frac{\mathrm{e}^{ik_{\tau' v' j'} S_{\tau'}}}{S_{\tau'}} f^{(+)}_{\tau vjm \to \tau' v' j' m'}(\mathbf{k}_{\tau vj}; \hat{S}_{\tau'}) \zeta_{\tau' v' j' m'}(s_{\tau'}) \end{aligned} \tag{6.58}$$

as $S_\tau \to \infty$. The first term on the right-hand side is a plane wave describing relative motion of an atom and a diatomic molecule in the initial rovibrational state $\zeta_{\tau vjm}$. The second term is an outgoing spherical wave in the final rovibrational state of the molecule $\zeta_{\tau' v' j' m'}$ multiplied by the scattering amplitude $f^{(+)}$ that depends on the initial momentum and the scattering direction. If $\epsilon_{\tau vj}$ is the internal rovibrational energy of the molecule, the energy conservation implies

$$\frac{1}{2\mu} k^2_{\tau vj} + \epsilon_{\tau vj} = E. \tag{6.59}$$

Differential cross section is related to the scattering amplitude through

$$\left(\frac{\mathrm{d}\sigma}{\mathrm{d}\Omega}\right)_{\tau vjm \to \tau' v' j' m'} = \frac{k_{\tau' v' j'}}{k_{\tau vj}} \left| f^{(+)}_{\tau vjm \to \tau' v' j' m'}(\mathbf{k}_{\tau vj}; \hat{S}_{\tau'}) \right|^2. \tag{6.60}$$

Arthurs and Dalgarno [145] derived how scattering boundary conditions are imposed to the eigenfunctions of $\mathbf{J}^2$ and J_z and how to combine them together to obtain the eigenfunctions of relative momentum and hamiltonian of the diatomic molecule.

The plane wave is a solution of the Schrödinger equation in free space and as such it can be expressed as the linear combination of the spherical Bessel functions j_l and spherical harmonics Y_{lm_l}. The coefficients can be found in textbooks, e.g. [146], and the relation is

$$e^{i\mathbf{k}_{\tau vj}\mathbf{S}_\tau} = 4\pi \sum_{lm_l} i^l j_l(k_{\tau vj}S_\tau) Y^*_{lm_l}(\hat{k}_{\tau vj}) Y_{lm_l}(\hat{S}_\tau). \tag{6.61}$$

Equation (6.61) represents the connection between the spherical-wave and plane-wave formalisms. Using the asymptotic form of the spherical Bessel functions,

$$j_l(x) \simeq \frac{\sin(x - l\pi/2)}{x} = \frac{i}{2x}\left[e^{-i(x-l\pi/2)} - e^{i(x-l\pi/2)}\right], \tag{6.62}$$

and the rovibrational diatomic wavefunction in form

$$\zeta_{\tau vjm}(s_\tau) = \frac{1}{s_\tau}\chi_{\tau vj}(s_\tau) Y_{jm_j}(\hat{s}_\tau), \tag{6.63}$$

the first term of the right-hand side of equation (6.58) can be rewritten as

$$e^{i\mathbf{k}_{\tau vj}\mathbf{S}_\tau}\zeta_{\tau vjm}(s_\tau) \simeq 2\pi i \sum_{lm_l} i^l Y^*_{lm_l}(\hat{k}_{\tau vj})\left[e^{-i(k_{\tau vj}S_\tau - l\pi/2)} - e^{i(k_{\tau vj}S_\tau - l\pi/2)}\right] \times \frac{1}{k_{\tau vj}S_\tau}\frac{1}{s_\tau}\chi_{\tau vj}(s_\tau) Y_{jm_j}(\hat{s}_\tau) Y_{lm_l}(\hat{S}_\tau). \tag{6.64}$$

Spherical harmonics in $\hat{s}_\tau$ and $\hat{S}_\tau$ in this equation can be coupled using Clebsch-Gordan coefficients into the eigenfunction of $\mathbf{J}^2$ and J_z,

$$Y^{JM}_{jl}(\hat{s}_\tau, \hat{S}_\tau) = \sum_{m_j m_l} \langle jm_j lm_l | JM\rangle Y_{jm_j}(\hat{s}_\tau) Y_{lm_l}(\hat{S}_\tau). \tag{6.65}$$

Inverting this equation, using the orthogonality of Clebsch-Gordan coefficients, and substituting it in (6.64), we arrive to

$$e^{i\mathbf{k}_{\tau vj}\mathbf{S}_\tau}\zeta_{\tau vjm}(s_\tau) \simeq \frac{2\pi i}{k^{1/2}_{\tau vj}} \sum_{lm_l JM} i^l Y^*_{lm_l}\langle jlm_j m_l | JM\rangle \times \frac{1}{k^{1/2}_{\tau vj}S_\tau}\left[e^{-i(k_{\tau vj}S_\tau - l\pi/2)} - e^{i(k_{\tau vj}S_\tau - l\pi/2)}\right]\Phi^{JM}_{\tau vjl}(s_\tau, \hat{S}_\tau), \tag{6.66}$$

where

$$\Phi^{JM}_{\tau vjl}(s_\tau, \hat{S}_\tau) = \frac{1}{s_\tau}\chi_{\tau vj}(s_\tau) Y^{JM}_{jl}(\hat{s}_\tau, \hat{S}_\tau). \tag{6.67}$$

The last row of equation (6.66) is a superposition of spherical incoming and outgoing waves. Functions $\Phi^{JM}_{\tau vjl}$, defined in (6.67), can be used as a basis to expand the wavefunction in the mass-scaled Jacobi coordinates, as is usually done in the inelastic scattering problems,

$$\Psi^{JM\epsilon_I\sigma}(\mathbf{S}_\tau, \mathbf{s}_\tau) = \sum_{\tau vjl} \frac{1}{S_\tau}\Phi^{JM}_{\tau vjl}(s_\tau, \hat{S}_\tau) f^{J\epsilon_I\sigma}_{\tau vjl}(S_\tau). \tag{6.68}$$

The boundary conditions applied to the functions $f^{J\epsilon_I\sigma}_{\tau vjl}(S_\tau)$ are

$$f^{J\epsilon_I\sigma}_{\tau vjl}(S_\tau) \simeq \frac{1}{k^{1/2}_{\tau vj}} \mathrm{e}^{-i(k_{\tau vj}S_\tau - l\pi/2)}\delta_{\tau'\tau}\delta_{v'v}\delta_{j'j}\delta_{l'l} - \frac{1}{k^{1/2}_{\tau'v'j'}} \mathrm{e}^{+i(k_{\tau'v'j'}S_\tau - l\pi/2)} S^J_{\tau'v'j'l'\tau vjl}. \tag{6.69}$$

Now, combining the wavefunctions in (6.68) in their asymptotic forms, having substituted f's from (6.69), with the coefficients in (6.57) chosen in such a way to make the incoming part of the spherical wave match the incoming part of the plane wave in (6.66), we obtain

$$\Psi^{(+)}_{\mathbf{k}_{\tau vj}\tau vjm} \simeq \frac{2\pi i}{k^{1/2}_{\tau vj}} \sum_{lm_lJM} i^l Y^*_{lm_l}\langle jlm_jm_l|JM\rangle \Psi^{JM\epsilon_I\sigma}(\mathbf{S}_\tau, \mathbf{s}_\tau). \tag{6.70}$$

From there, we subtract the plane wave part (6.66) of the asymptotic form in (6.58) and compare the terms to extract the scattering amplitude defined now in terms of the S matrices. The result is

$$f^{(+)}_{\tau vjm_j\to\tau'v'j'm'_j}(\mathbf{k}_{\tau vj}; \hat{S}_{\tau'}) = \frac{2\pi i}{(k_{\tau vj}k_{\tau'v'j'})^{1/2}} \sum_{lm_ll'm'_lJM} \{i^{l-l'}(\delta_{\tau\tau'}\delta_{vv'}\delta_{jj'}\delta_{ll'} - S^J_{\tau'v'j'l'\tau vjl}) \times Y^*_{lm_l}(\hat{k}_{\tau vj})\langle jlm_jm_l|JM\rangle Y_{l'm'_l}(\hat{S}_{\tau'})\langle j'l'm'_jm'_l|JM\rangle\}. \tag{6.71}$$

Once S matrices are determined for each J from the coupled equations, the above relation (6.71) provides the link to determine the cross sections (6.60).

The theory of atom-diatom scattering has also been developed in the molecular frame [58, 147]. Expressions for differential and integral cross sections are more conveniently expressed using the T matrix of molecular frame [148],

$$T^J_{\tau'v'j'\Omega'\tau vj\Omega} = \sum_{ll'} i^{l-l'}\langle jJ\Omega - \Omega|jJl0\rangle T^J_{\tau'v'j'l'\tau vjl}\langle j'Jl'0|j'J\Omega' - \Omega'\rangle, \tag{6.72}$$

where

$$T^J_{\tau'v'j'l'\tau vjl} = \delta_{\tau\tau'}\delta_{vv'}\delta_{jj'}\delta_{ll'} - S^J_{\tau'v'j'l'\tau vjl}. \tag{6.73}$$

Differential cross section, averaged over initial m_j and summed over final states m'_j, reads

$$\left(\frac{\mathrm{d}\sigma}{\mathrm{d}\Omega}\right)_{\tau vj\to\tau'v'j'} = \frac{1}{4(2j+1)k^2_{\tau vj}} \left|\sum_{J\Omega\Omega'} (2J+1) T^J_{\tau'v'j'\Omega'\tau vj\Omega} d^J_{\Omega\Omega'}(\vartheta)\right|^2, \tag{6.74}$$

where ϑ is the scattering angle in the centre-of-mass frame, with respect to the initial approach direction. Integral cross section is obtained by integrating the above expression and making use of the orthogonality of the Wigner d functions [141],

$$\sigma_{\tau vj\to\tau'v'j'} = \frac{\pi}{(2j+1)k^2_{\tau vj}} \sum_{J\Omega\Omega'} (2J+1) \left| T^J_{\tau'v'j'\Omega'\tau vj\Omega} \right|^2 . \tag{6.75}$$

6.7 Asymptotic matching

Coupled equations are typically solved by integrating a set of independent solutions outwards, starting from a small hyperradius in the classically forbidden region. At long range the solutions that energetically lie below the three-body dissociation threshold concentrate into the arrangement valleys and anisotropy of the potential becomes low. Linearly independent solutions in the APH coordinates must be matched onto the analytic solutions in the mass-scaled Jacobi coordinates of the remaining potential. Fock coordinates [149] are a convenient intermediate step in the matching procedure that is described below.

The body-fixed Fock coordinates consist of a hyperradius, defined in (6.25), angles ω_τ and η_τ, defined with

$$\omega_\tau = \arctan s_\tau/S_\tau \quad \text{and} \quad \eta_\tau = \arccos \mathbf{S}_\tau \mathbf{s}_\tau, \tag{6.76}$$

and three Euler angles of the $(\mathrm{BF})_\tau$ system.

The potential in the asymptotic region is independent of the bending angle η_τ and equation (6.47) becomes separable. The parenthesis in equation (6.48) can be rewritten in the Fock coordinate system as

$$\begin{aligned} \Lambda_0^2 + \frac{4\Omega^2}{\sin^2\theta} \;=\; & -\frac{1}{\sin^2 2\omega_\tau}\frac{\partial}{\partial\omega_\tau}\sin^2 2\omega_\tau \frac{\partial}{\partial\omega_\tau} \\ & + \frac{4}{\sin^2 2\omega_\tau}\left(-\frac{1}{\sin\eta_\tau}\frac{\partial}{\partial\eta_\tau}\sin\eta_\tau\frac{\partial}{\partial\eta_\tau} + \frac{\Omega^2}{\sin^2\eta_\tau}\right). \end{aligned} \tag{6.77}$$

Hypersurface states at long range, $\rho \to \infty$, converge to the Fock rovibrational states

$$\varphi_k^{\epsilon_I\sigma\Omega}(\rho;\theta,\phi) \to \sum_\tau \chi_{\tau vj}(\rho;\omega_\tau) P_{j\Omega}(\eta_\tau) c_{\tau j}^{\epsilon_I\sigma\Omega}, \tag{6.78}$$

where $P_{j\Omega}(\eta)$ are the associated Legendre functions which represent rotation, and $\chi_{\tau vj}$ are solutions of the one-dimensional equation

$$\begin{aligned} \left[\frac{1}{2\mu\rho^2}\left(-\frac{1}{\sin^2 2\omega_\tau}\frac{\partial}{\partial\omega_\tau}\sin^2 2\omega_\tau\frac{\partial}{\partial\omega_\tau} + \frac{4j(j+1)}{\sin^2 2\omega_\tau}\right) + V_\tau(\rho;\omega_\tau)\right] \times \\ \times\chi_{\tau vj}(\rho;\omega_\tau) = \varepsilon_{\tau vj}(\rho)\chi_{\tau vj}(\rho;\omega_\tau), \end{aligned} \tag{6.79}$$

and represent vibration of the molecule. $c_{\tau j}^{\epsilon_I \sigma \Omega}$ coefficients in (6.78) are obtained by a two-dimensional integration in η and ω with ρ fixed at the middle of the last sector in propagation.

Transformation from the body-fixed frame of the principal axes of inertia to the space-fixed frame, where we apply the boundary conditions is performed in two steps.

The first step is reorientation of the quantization axis z along $\mathbf{S}_\tau$. It is accomplished by rotation about the common y axis by β_Q, defined in (6.21). The transformation matrix is defined with

$$U^J_{\tau v' j' \Omega'_\tau v j \Omega_\tau} = \langle \chi_{\tau v' j'} P_{j' \Omega'_\tau} | d^J_{\Omega'_\tau \Omega_\tau}(\beta_Q) | \chi_{\tau v j} P_{j \Omega_\tau} \rangle_{\omega_\tau \eta_\tau}, \tag{6.80}$$

where Ω_τ and Ω'_τ are projections of the total angular momentum $\mathbf{J}$ on $\mathbf{S}_\tau$ and on the axis of least inertia. $d^J_{\Omega'_\tau \Omega_\tau}$ is the rotation matrix (6.40) about the y axis.

The second step is the standard transformation from the body-fixed frame wavefunction of form

$$\Psi^{JM} = \sum_{\tau v j \Omega_\tau} N^{JM}_{\Omega_\tau}(\alpha, \beta, \gamma) P_{j \Omega_\tau}(\eta_\tau) \chi_{\tau v j}(\omega_\tau) F_{\tau v j \Omega_\tau}(\rho) \tag{6.81}$$

to the space-fixed frame wavefunction of form

$$\Psi^{JM} = \sum_{\tau v j \Omega_\tau} Y^{JM}_{jl}(\hat{S}_\tau, \hat{s}_\tau) \chi_{\tau v j}(\omega_\tau) F_{\tau v j l}(\rho). \tag{6.82}$$

Transformation matrix between the SF and BF representations may be derived by evaluating the coupled angular momentum functions in equation (6.65) in the BF frame,

$$\begin{aligned} Y^{J\Omega}_{jl}(\hat{s}_\tau, \hat{S}_\tau) &= \sum_{m_j} \langle j m_j l \Omega - m_j | J \Omega \rangle Y_{j m_j}(\eta, 0) Y_{l \Omega - m_j}(0, 0) \\ &= \sum_{m_j} \langle j m_j l \Omega - m_j | J \Omega \rangle \frac{1}{\sqrt{2\pi}} P_{j m_j}(\eta) \sqrt{\frac{2l+1}{4\pi}} \delta_{\Omega m_j} \\ &= \langle j \Omega l 0 | J \Omega \rangle \sqrt{\frac{2l+1}{8\pi^2}} P_{j\Omega}(\eta), \end{aligned} \tag{6.83}$$

and proceeding with the same line of arguments that led from equation (6.41) to (6.42). We obtain

$$Y^{JM}_{jl}(\hat{S}_\tau, \hat{s}_\tau) = \sum_\Omega C^{Jj}_{\Omega l} Y^{JM}_{j\Omega}(\alpha, \beta, \gamma; \eta), \tag{6.84}$$

where the BF angular momentum eigenfunctions are defined as

$$Y^{JM}_{j\Omega}(\alpha, \beta, \gamma; \eta) = \sqrt{\frac{2J+1}{8\pi^2}} D^{J*}_{M\Omega}(\alpha, \beta, \gamma) P_{j\Omega}(\eta), \tag{6.85}$$

and the transformation matrix is

$$C_{\Omega l}^{Jj} = \left(\frac{2l+1}{2J+1}\right)^{1/2} \langle j\Omega l0|J\Omega\rangle = (-1)^{j-\Omega}\langle j\Omega J-\Omega|l0\rangle. \tag{6.86}$$

Inserting (6.46) in (6.81) provides a functional form ready to be transformed to (6.82) using (6.84). Boundary conditions (6.68) and (6.69) can be applied directly to the form obtained in (6.82) using coordinate relationships (6.76). Asymptotic functions need to be projected on the vibrational basis of the last sector in propagation,

$$F^{(\pm)}_{\tau v' j' l' \tau v j l} = \delta_{jj'}\delta_{ll'}\langle \chi_{\tau v' j'}(\omega_\tau)|\chi_{\tau v j}(s_\tau)h^{(\pm)}_{\tau v j l}(S_\tau)\rangle_{\omega_\tau}, \tag{6.87}$$

and matching of $F_{\tau v j l}$ from (6.82) to $F^{(\pm)}$ from (6.87) permits extraction of the S matrix.

6.8 Solution of coupled equations

There is a wide array of methods described in the literature for solving coupled differential equations of form

$$\frac{\mathrm{d}^2F}{\mathrm{d}R^2} = W(R)F(R). \tag{6.88}$$

A review with applications in solving bound-state problems is given in Ref. 150. The same methods apply to scattering problems and in particular to the coupled equations in (6.54). Methods that are commonly used today are the renormalized Numerov method [151], the R matrix method [152], and the log-derivative methods [153]. The renormalized Numerov method was improved recently and its new variant, the enhanced Numerov [154], is likely to become the method of choice in the future. The log-derivative method has more natural formulation for initial conditions of the type $F(0) = 0$ than the R matrix method. Moreover R matrix becomes undefined when $W = 0$ [155]. Log-derivative method was used in the present work.

Log-derivative matrix, Y, is defined by

$$F'(R) = Y(R)F(R). \tag{6.89}$$

Differentiating (6.89) with respect to R and using (6.88), we obtain the differential equation for Y,

$$Y'(R) = W(R) - Y(R)^2, \tag{6.90}$$

known as Riccati equation. It can be solved by a form of invariant imbedding technique. We divide the whole integration range in intervals and, within each of the intervals $[a, b]$, define the log-derivative propagator $\mathcal{Y}$ by

$$\begin{pmatrix} F'(a) \\ F'(b) \end{pmatrix} = \begin{pmatrix} \mathcal{Y}_1(a,b) & \mathcal{Y}_2(a,b) \\ \mathcal{Y}_3(a,b) & \mathcal{Y}_4(a,b) \end{pmatrix} \begin{pmatrix} -F(a) \\ F(b) \end{pmatrix}. \tag{6.91}$$

The propagators are used to propagate the log-derivative matrix Y over the interval,

$$Y(b) = \mathcal{Y}_4(a,b) - \mathcal{Y}_3(a,b)[Y(a) + \mathcal{Y}_1(a,b)]^{-1}\mathcal{Y}_2(a,b). \tag{6.92}$$

The coupling matrix can be approximated in an interval by the sum $W = W_0 + W_1$. For W_0, we choose the part of W to be treated exactly by solving the boundary value problem (6.91) for the propagator, and for W_1, the part to be treated perturbatively. To do a perturbative correction on the propagator, an integral needs to be solved using, usually, either the trapezium or modified Simpson's quadrature rule. By choosing different reference potentials with different quadrature rules, the whole range of different methods can be constructed. A thorough discussion can be found in Ref. 155.

Coupled equations in (6.54) may be solved using the diabatic-by-sector method. Deep in the classically forbidden region, we assume that we have a linearly independent set of wavefunctions which is infinitesimally small in each of the channels. We assign them arbitrarily small derivatives and keep the linear independence valid. Looking back at (6.89), we conclude that

$$Y(0) = \infty I, \tag{6.93}$$

where I is the unit matrix. Dimension of the log-derivative matrix is $N \times N$, where N is the number of hypersurface functions, i.e. channels, needed to converge the S matrix elements. Using the initial condition (6.93), a set of N independent solutions is propagated outwards to a point where the couplings due to potential become negligible or have a known analytic form. At that point the independent solutions are linearly combined to give the desired asymptotic form. Propagation within a sector is done using relations (6.91) and (6.92). In each sector different basis functions (6.53) are used and a matrix transformation to change the basis must be applied each time the boundary of a sector is reached . The matrix elements of the transformation are

overlap integrals between the basis functions in different sectors. From the final log-derivative matrix one usually obtains a K matrix using real matrix algebra, which is connected to the S matrix (see (7.80)). Real and symmetric coupling matrix W results in a real and symmetric Y matrix, and the latter produces a real and symmetric K matrix, which guarantees the unitarity of the S matrix. Application of boundary conditions is discussed in more detail in Ref. 137.

6.9 Computer codes

The theory presented in this chapter was implemented into a suite of codes by Launay and LeDourneuf [136, 138]. These codes were used by us to obtain the scattering results in Chapter 8 and 9.

TB program generates the basis by solving the eigenvalue problem (6.47), the rovibrational functions by solving (6.79), and also the coupling matrix elements in (6.55). It is independent of the total angular momentum J and energy E.

TJ program generates the J-dependent couplings in (6.56) and transformation from the SF to BF frame. It is independent of E.

TK solves coupled equations in (6.54) for a set of energies E and obtains the K matrices.

TS transforms K matrices to S matrices and computes the cross sections.

Chapter 7

Topics of collision theory

7.1 Introduction

This chapter is intended to provide a background for understanding and analysis of the scattering results presented in the next chapter. The intention is to make transparent the origin of the principles and phenomenology rather than being rigorous in all mathematical detail.

Potential scattering is presented first because it will be used later to illustrate the points and to emphasize the generality of some results. The energy dependence of cross sections for slow scattering and a way to parametrize them in terms of scattering length are presented next. A method for detection and analysis of scattering resonances is described. The chapter is ended with a classical model for reaction cross sections.

7.2 Potential scattering

Potential scattering is the non-relativistic scattering of two particles interacting through a potential, $V(r)$, that depends only on their distance. Every solution of the Schrödinger equation can then be written as a linear combination of the products of spherical functions and radial functions that satisfy

$$\frac{1}{r^2}\frac{\mathrm{d}}{\mathrm{d}r}\left(r^2\frac{\mathrm{d}R_l}{\mathrm{d}r}\right)+\left[k^2-\frac{l(l+1)}{r^2}-2mV(r)\right]R_l=0, \tag{7.1}$$

with $k=\sqrt{2mE}$, where m is the two-body reduced mass. A particular solution describing a scattering event can be specified by the boundary condition

$$\psi \approx \mathrm{e}^{ikz}+\frac{f(\theta)}{r}\mathrm{e}^{ikr}. \tag{7.2}$$

The first term in (7.2) describes a free particle moving in the positive z direction while the second term is a divergent spherical wave. The function f is called a scattering amplitude and is dependent on the scattering angle θ (polar angle). The differential scattering cross section is

$$\frac{\mathrm{d}\sigma}{\mathrm{d}\Omega}=|f(\theta)|^2. \tag{7.3}$$

Now, the asymptotic form of the functions R_l is (when $V(r)$ falls off faster than $1/r$ in the limit $r\to\infty$ [156])

$$R_l \sim \frac{1}{r}\sin\left(kr-\frac{l\pi}{2}+\delta_l\right). \tag{7.4}$$

The scattering amplitude may be written in terms of the phase shifts δ_l. The general solution is an expansion in $R_l(r)P_l(\cos\theta)$, where P_l are Legendre polynomials. The expansion coefficients are chosen to eliminate the convergent spherical wave from $\psi - \mathrm{e}^{ikz}$ so that the asymptotic form of the solution satisfies the boundary condition (7.2). Using (6.61) and (6.62), the asymptotic form of the solution becomes

$$\psi \approx \frac{i}{2kr}\sum_{l=0}^{\infty}(2l+1)P_l(\cos\theta)\left[(-1)^l\mathrm{e}^{-ikr} - S_l\mathrm{e}^{ikr}\right], \tag{7.5}$$

with

$$S_l = \mathrm{e}^{2i\delta_l}. \tag{7.6}$$

The scattering amplitude is

$$f(\theta) = \sum_l (2l+1)f_l P_l(\cos\theta), \tag{7.7}$$

where

$$f_l = \frac{1}{2ik}(S_l - 1) = \frac{1}{2ik}\left(\mathrm{e}^{2i\delta_l} - 1\right) = \frac{1}{k\cot\delta_l - ik}. \tag{7.8}$$

The total cross section in terms of the phase shifts is

$$\sigma = \frac{4\pi}{k^2}\sum_{l=0}^{\infty}(2l+1)\sin^2\delta_l. \tag{7.9}$$

This series is convergent when the potential $V(r)$ falls off faster than $1/r^2$ [157]. Scattering amplitude (7.7) is infinite for $\theta = 0$ when $V(r) \sim 1/r^3$ and slower [157].

The phase shift, δ_l, is not unique as defined in (7.6). The ambiguity (modulo π) may be removed if we define the phase shift in the high-energy limit as $\lim_{k\to\infty}\delta_l(k) = 0$, and assume the continuity in k. The low-energy limit is then

$$\lim_{k\to 0}\delta_l(k) = n_l\pi, \tag{7.10}$$

where n_l is the number of bound levels of the potential with angular momentum $l > 0$. When there is a level just at the threshold, n_0 assumes half-integer values for $l = 0$. This result, (7.10), is very general (it assumes that $\int_0^\infty r^s|V(r)|\mathrm{d}r$ is finite for $s = 1, 2$) and is called the Levinson's theorem [156].

7.3 Wigner threshold laws

The dynamics of two particles at very low collision energies follow threshold laws. The first derivation of analytical expressions governing the energy dependence of the

cross sections in the short-range potentials was given by Wigner [158]. A line of arguments leading to the description of the behaviour of the cross sections can be simply demonstrated in the one channel case. The wavefunction outside the range of the potential at zero kinetic energy can be written as

$$R_l(E=0) = A_1 r^l + A_2 r^{-(l+1)}, \tag{7.11}$$

A_2/A_1 being independent of energy. At a slightly positive energy the solution in the potential-free zone is a linear combination of spherical Bessel and Neumann functions

$$R_l(E) = j_l(kr) + \tan\delta_l n_l(kr), \tag{7.12}$$

where k is the wavevector, n_l is the solution that is irregular at the origin, and δ_l is the phase shift introduced by the presence of the potential at short range. When $kr \ll 1$, equation (7.12) is

$$R_l(E) = (kr)^l + \tan\delta_l (kr)^{-(l+1)} \tag{7.13}$$

to first order in kr. Smooth matching of the two forms (7.11) and (7.13) requires:

$$\tan\delta_l = (A_2/A_1)k^{2l+1} \quad R_l(E) = k^l R_l(E=0). \tag{7.14}$$

The formulas in (7.14), defining the cross sections, can be generalized for multichannel case within multichannel quantum defect theory [159]. T matrix elements at very low energies follow

$$T_{fi} \sim k_i^{l_i+1/2} k_f^{l_f+1/2}. \tag{7.15}$$

The subscripts i and f denote incident and final channel of the collision. The origin of the factor $1/2$ in the exponents is the reduction in the phase space available for slow particles, while the origin of l's is the hindrance due to the tunneling through the centrifugal barrier [160].

In an elastic collision at low energy, the incoming and outgoing momenta k_i and k_f are equal and they are small quantities. Angular momentum quantum numbers can differ. It follows from (6.75) and (7.15) that

$$\sigma_{nl_i \to nl_f} \sim k^{2l_i+2l_f}. \tag{7.16}$$

Here n denotes all quantum numbers, but l. In an inelastic collision at low energy only the initial momentum k_i is small, so relation (7.15) gives ($m \neq n$)

$$\sigma_{nl_i \to ml_f} \sim k_i^{2l_i-1}. \tag{7.17}$$

The Wigner threshold laws do not hold in the presence of long-range forces. The above derivation rests on the assumption that for large r the second term in the brackets in equation (7.1) times the smallest contribution we have kept in (7.11), $1/r^{l+1}$, is still bigger than the third term in the square brackets times the bigger term from (7.11), r^l. For long-range potential of the form $\sim r^{-s}$ this means that $s > 2l + 3$. The long-range interaction gives an additional contribution to the phase shift [157]. In the one-channel case, it is [159]

$$\tan \delta_l \sim \text{const} k^{s-2} + \text{const} k^{2l+1}. \tag{7.18}$$

This results in the modification of the threshold laws for elastic scattering. Inelastic processes remain governed by the Wigner threshold laws in the presence of the dispersion potential.

In the ultracold temperature regime, the dominant contribution to the cross sections comes from the l=0 partial wave. The elastic cross section tends to a constant while the inelastic one diverges. The rate coefficient for the elastic process is zero and those for inelastic processes are constant (independent of energy).

7.4 Scattering length

The expression for the scattering amplitude in equation (7.8) can be rewritten in form

$$f_l = \frac{1}{g_l - ik}, \tag{7.19}$$

where the function g_l is real for $E > 0$. From the analytical properties of the scattering amplitude for exponentially decaying potentials it follows that f_l is real for $E < 0$ [157]. This means that g_l permits expansion in powers of E or, equivalently, even powers of k. In particular at low energies from (7.8) $f_l \approx \delta_l/k \sim k^{2l}$ so that $g_l \sim k^{-2l}$. Long-range interactions introduce anomalies in the expansion of the function f_l. It follows from the arguments above that for a potential of form $\sim r^{-s}$ there is a term proportional to k^{s-3} in f_l.

Now, we restrict the analysis to s-wave scattering, $l = 0$. For a long-range r^{-6} potential (and smaller potentials), it is justified to keep the first two terms in Taylor expansion of g_0,

$$g_0(k) \approx -\frac{1}{a} + \frac{1}{2} r_0 k^2. \tag{7.20}$$

Here, a is called the scattering length and r_0 is the effective range. We want to examine the significance of these parameters in more detail following Ref. 161.

By making a substitution $u(r) = rR_0(r)$ in equation (7.1) for $l = 0$, we arrive at

$$\frac{\mathrm{d}^2u}{\mathrm{d}r^2} + [k^2 - 2mV(r)]u(r) = 0. \tag{7.21}$$

Let $u_1(r)$ and $u_2(r)$ be solutions for the energies k_1^2 and k_2^2 which vanish at the origin, $u_{1,2}(0) = 0$, and are asymptotically normalized as

$$\begin{aligned} u_1(r) &\approx \frac{1}{\sin\delta_1}\sin(k_1r + \delta_1), \\ u_2(r) &\approx \frac{1}{\sin\delta_2}\sin(k_2r + \delta_2). \end{aligned} \tag{7.22}$$

In the next step we multiply equation (7.21) for u_1 by u_2 and the one for u_2 by u_1, subtract one from another and integrate the whole expression. After integrating by parts the term involving second derivative, we arrive at

$$\left[u_2\frac{\mathrm{d}u_1}{\mathrm{d}r} - u_1\frac{\mathrm{d}u_2}{\mathrm{d}r}\right]_0^R = (k_2^2 - k_1^2)\int_0^R u_1u_2\mathrm{d}r. \tag{7.23}$$

Now, let v_1 and v_2 be free-particle solutions ($V(r) = 0$) defined with

$$\begin{aligned} v_1(r) &= \frac{1}{\sin\delta_1}\sin(k_1r + \delta_1), \\ v_2(r) &= \frac{1}{\sin\delta_2}\sin(k_2r + \delta_2). \end{aligned} \tag{7.24}$$

They satisfy equation (7.23) too. Subtracting equation (7.23) from the analogous one, where u's are replaced by v's, and letting $R \to \infty$, we get

$$(k_2^2 - k_1^2)\int_0^\infty (v_1v_2 - u_1u_2)\mathrm{d}r = k_2\cot\delta_2 - k_1\cot\delta_1. \tag{7.25}$$

The scattering length is defined with (see (7.20))

$$-\frac{1}{a} = \lim_{k\to 0}[k\cot\delta(k)]. \tag{7.26}$$

Letting $k_1 \to 0$ and $k \equiv k_2$, equation (7.25) becomes

$$k\cot\delta = -\frac{1}{a} + \frac{b}{2}k^2 \tag{7.27}$$

with

$$b = 2\int_0^\infty (v_0v - u_0u)\mathrm{d}r. \tag{7.28}$$

The wavefunctions v and u are very different where $V(r)$ is appreciable and if $2m|V(r)| \gg k^2$, $u(r)$ will not depend on energy. At low energy we replace, therefore, u and v by u_0 and v_0

$$b \approx r_0 = 2\int_0^\infty (v_0^2 - u_0^2)\mathrm{d}r. \tag{7.29}$$

The integral in (7.29) vanishes outside the range of the potential. The zero-energy wavefunction $u_0(r)$ has the asymptotic form

$$u_0(r) \to v_0(r) = \lim_{k\to 0}(\cos kr + \cot\delta \sin kr) = 1 - \frac{r}{a}. \tag{7.30}$$

Thus, a and r_0 are insensitive to the exact form of the potential, but they depend on some integrated property of $V(r)$.

At low energies only s-waves scatter. Using (7.19) and (7.20) with (7.3), a useful approximation for cross sections at low energy may be derived. The zero-energy limit is $\sigma = 4\pi a^2$.

Expression (7.30) may be used for numerical determination of the scattering length of diatomic potentials. For a given diatomic potential a wavefunction ψ may be integrated outwards at zero energy to large r and matched onto the function in (7.30), namely $\psi'/\psi = -1/a$. It turns out that for a realistic diatomic ground state potential the propagation needs to be extended far into the long-range interaction region where the analytic solutions for $V(r) = -C_s r^{-s}$ dispersion potentials accurately describe the wavefunction. Therefore, to avoid integration to large distances and reduce the error build-up in the propagation, it is desirable to match onto the two independent solutions of

$$\chi''(r) + \frac{\gamma^2}{r^s}\chi(r) = 0, \tag{7.31}$$

with

$$\gamma = \sqrt{2mC_s}. \tag{7.32}$$

The general solution of equation (7.31) [157] is

$$\chi(r) = \sqrt{r}\left[AJ_{\frac{1}{s-2}}\left(\frac{2\gamma}{s-2}r^{-\frac{s-2}{2}}\right) - BN_{\frac{1}{s-2}}\left(\frac{2\gamma}{s-2}r^{-\frac{s-2}{2}}\right)\right], \tag{7.33}$$

where $J_{\frac{1}{s-2}}(x)$ and $N_{\frac{1}{s-2}}(x)$ are Bessel and Neumann functions and A and B are constants. The ratio A/B is determined from the propagated wavefunction. By expanding the Bessel and Neumann function for large r (small argument), we recover

linear behaviour in (7.30) and get an expression for the scattering length [162]

$$a = \cos\left(\frac{\pi}{s-2}\right)\left(\frac{\gamma}{s-2}\right)^{\frac{2}{s-2}} \frac{\Gamma(\frac{s-3}{s-2})}{\Gamma(\frac{s-1}{s-2})}\left[1 - \frac{A}{B}\tan\frac{\pi}{s-2}\right]. \tag{7.34}$$

Our implementation took advantage of (7.34) while the wavefunction was propagated using the log-derivative method with zero reference potential and modified Simpson's quadrature rule (see section 6.8). In Ref. 162, the ratio A/B was also derived in the semiclassical approximation, leading to a useful expression

$$a = \bar{a}\left[1 - \tan\frac{\pi}{s-2}\tan\left(\Phi - \frac{\pi}{2(s-2)}\right)\right], \tag{7.35}$$

$$\bar{a} = \cos\left(\frac{\pi}{s-2}\right)\left(\frac{\gamma}{s-2}\right)^{\frac{2}{s-2}} \frac{\Gamma(\frac{s-3}{s-2})}{\Gamma(\frac{s-1}{s-2})}, \tag{7.36}$$

where

$$\Phi = \int_{\sigma_0}^{\infty} \sqrt{2m[-V(r)]}\mathrm{d}r, \tag{7.37}$$

and σ_0 is the classical turning point of the potential at zero energy. The mean scattering length, $\bar{a}$, depends only on the reduced mass of the scattering particle and the long-range dispersion coefficient. It is a slowly varying function of the parameters of the potential. The factor in the brackets in equation (7.35) is a rapidly varying function of the potential that goes to infinity whenever there is a bound state of the potential at exactly zero energy.

The effective range expansion (7.20) may also be characterized by the bound state closest to the dissociation limit. Let its energy be $E = -\kappa^2/(2m)$. It satisfies

$$\frac{\mathrm{d}^2 u_\kappa}{\mathrm{d}r^2} - [\kappa^2 + 2mV(r)]u_\kappa(r) = 0 \tag{7.38}$$

with $u_\kappa(0) = 0$ and is asymptotically normalized as

$$u_\kappa(r) \approx \mathrm{e}^{-\kappa r}. \tag{7.39}$$

We also choose the following free-particle solutions

$$v_\kappa(r) = \mathrm{e}^{-\kappa r}, \quad v_k(r) = \frac{\sin(kr + \delta)}{\sin\delta} \tag{7.40}$$

of equations (7.38) and (7.21) respectively. Following the same procedure which led us to (7.25) and (7.27) and applying it to u's and v's, we obtain

$$(\kappa^2 + k^2)\int_0^{\infty} v_\kappa v_k \mathrm{d}r = k\cot\delta + \kappa \tag{7.41}$$

and, using the orthogonality between $u_\kappa(r)$ and $u(r)$,

$$k \cot \delta = -\kappa + \frac{1}{2}(\kappa^2 + k^2)\zeta, \tag{7.42}$$

where

$$\zeta = 2 \int_0^\infty (v_\kappa v_k - u_\kappa u_k) \mathrm{d}r. \tag{7.43}$$

If κ^2 and k^2 are small compared with the depth of $V(r)$, we may expand $k \cot \delta$ in $\kappa^2 + k^2$ and retain the first two terms. $v_k(r)$ may be expanded as

$$v_k(r) = c v_\kappa(r) + (\kappa^2 + k^2) f(r) + ..., \tag{7.44}$$

with the constant c to be determined. If k is replaced by $-i\kappa$ in the equation (7.40), v_k is identical to v_κ when $\cot \delta = -i$. Therefore $c = 1$ and (7.42) and (7.43) become

$$k \cot \delta = -\kappa + \frac{1}{2}(\kappa^2 + k^2)\rho + ... \tag{7.45}$$

and

$$\rho = 2 \int_0^\infty (v_\kappa^2 - u_\kappa^2) \mathrm{d}r. \tag{7.46}$$

Neglecting higher order terms in (7.45) and equating it with (7.27) and using (7.29) and a similar approximation for ρ in (7.46), we arrive to

$$\kappa = \frac{1}{a} + \frac{\rho \kappa^2}{2}, \quad r_0 = \rho. \tag{7.47}$$

We have thus expressed the scattering length in terms of the bound-state parameters. Using this connection it is easy to derive expressions for the scattering cross section in terms of the parameters in (7.47), see Ref. 161.

When inelastic scattering is possible, the depletion of flux from elastic channel may be described by a complex phase shift. In slow collisions, the elastic channel in the S matrix (see (7.6)) may be expanded and the complex phase shift for $l = 0$ expressed in terms of a complex scattering length, $a = \alpha - i\beta$, using (7.26),

$$S_{ii} \approx 1 + 2i\delta(k) = 1 - 2ik(\alpha - i\beta). \tag{7.48}$$

The imaginary part of the scattering length must be negative, $\beta > 0$, to ensure that $\sum_{i'} |S_{ii'}|^2 \leq 1$. The expressions for multichannel elastic and total inelastic cross sections

$$\sigma_{\text{elas}} = \frac{\pi}{k^2} |1 - S_{ii}|^2, \tag{7.49}$$

$$\sigma_{\text{inel}} = \frac{\pi}{k^2} \sum_{i' < i} |S_{ii'}|^2 = \frac{\pi}{k^2} \left[1 - |S_{ii}|^2\right], \tag{7.50}$$

using (7.48) become

$$\sigma_{\text{elas}} = 4\pi|a|^2 = 4\pi(\alpha^2+\beta^2), \tag{7.51}$$

$$\sigma_{\text{inel}} = -\frac{4\pi}{k}\text{Im}(a) = \frac{4\pi\beta}{k}. \tag{7.52}$$

These expressions were introduced in atom-molecule collisions by Balakrishnan et al. [42]. It is evident that the expressions (7.51) and (7.52) are consistent with the Wigner threshold laws and will be valid parametrizations of the cross sections wherever the Wigner laws apply for $l = 0$. Since in numerical applications either the S or $T = 1 - S$ matrix is usually calculated, the complex scattering length may be extracted from the entrance-channel matrix element by taking the limits

$$\alpha = \lim_{k\to 0}\frac{\text{Im}(T_{ii})}{2k}, \qquad \beta = \lim_{k\to 0}\frac{\text{Re}(T_{ii})}{2k}. \tag{7.53}$$

Using the connection between the scattering length and the bound states presented above, Forrey et al. [43] have derived expressions (valid when $\beta \ll \alpha$) for the energy and width of levels lying close to dissociation limit in the entrance channel in terms of the complex scattering length and effective range. Neglecting the effective range and expressing the scattering length in terms of its modulus and phase, $\phi = \arctan(\beta/\alpha)$, we obtain [42], using (7.47),

$$E = -\frac{1}{2m|a|^2}(\cos 2\phi + i\sin 2\phi) = E_m - \frac{i}{2}\Gamma_m, \tag{7.54}$$

as the energy of the uppermost level in the entrance channel. The energy is complex, meaning that the level is either quasibound or unbound and will decay to lower levels with a lifetime $\tau_m = 1/\Gamma_m$. Γ_m is called the width of state. The more accurate formula involving the effective range proved to work well for predicting the predissociation lifetimes of $He + H_2$ [43].

7.5 Resonant behaviour and eigenphase sum

Quasistationary states of a system are those that spend a considerable amount of time inside the system, but have a finite lifetime. The boundary condition at infinity of such a state is a diverging spherical wave and its energy is a complex quantity. The time dependent factor in the wavefunction of such a state is e^{-iEt}. By substituting (7.54) in that expression, it may be seen that the probability density inside the system is attenuated by a factor $e^{-\Gamma t}$ in time.

When particles are scattered at an energy close to one such quasistationary state, the phase shift and cross section exhibit a resonant behaviour. The origin of the resonant form will be described here following Ref. 157. The asymptotic form of the radial part of the wavefunction at large distances for $E < 0$ can be written in form

$$R_l = \frac{1}{r}\left[A_l(E)\exp\left(-\sqrt{-2mE}\right) + B_l(E)\exp\left(\sqrt{-2mE}\right)\right]. \tag{7.55}$$

A_l and B_l are function of the complex variable E. For real $E > 0$,

$$R_l = \frac{1}{r}\left[A_l(E)\mathrm{e}^{ikr} + B_l(E)\mathrm{e}^{-ikr}\right], \tag{7.56}$$

where $A_l(E) = B_l^*(E)$ and $k = \sqrt{2mE}$. Here $B_l(E)$ was taken on the upper edge of the cut on the physical sheet. The physical sheet is defined with $\mathrm{Re}(\sqrt{-E}) > 0$ and the cut is along the right half of the real axis. The condition that determines the quasistationary energy levels is

$$B_l\left(E_m - i\frac{\Gamma_m}{2}\right) = 0. \tag{7.57}$$

The wavefunction of the quasistationary states with the condition (7.57) originates from the outgoing wave in the asymptotic form (7.56). Therefore, $B_l(E)$ can be expanded in a series in $E - (E_m - i\Gamma_m/2)$ for $E > 0$ and small Γ_m. The first non-vanishing term is $B_l(E) = (E - E_m + i\Gamma_m/2)b_l$. Inserting it into (7.56) and comparing to the equation (7.5), we can extract the phase shift

$$\mathrm{e}^{2i\delta_l} = \mathrm{e}^{2i\delta_l^d}\frac{E - E_m - \frac{1}{2}i\Gamma_m}{E - E_m + \frac{1}{2}i\Gamma_m}. \tag{7.58}$$

Here δ_l^d is the value of the phase shift far from the resonance, i.e. where $|E - E_m| \gg \Gamma_m$. The formula (7.58) can be rearranged to give

$$\delta_l = \delta_l^d + \arctan\frac{\Gamma_m}{2(E_m - E)}. \tag{7.59}$$

When the energy is varied from $E \ll E_m$ to $E \gg E_m$, the phase shift increases by π. Neglecting the direct scattering, that is not involving the resonance, the phase shift in (7.59) leads to the Breit-Wigner formula,

$$\sigma_l = \frac{4\pi(2l+1)}{k^2}\frac{\Gamma_m^2}{4(E - E_m)^2 + \Gamma_m^2}. \tag{7.60}$$

In the above analysis it was assumed that the resonant region is not close to $E = 0$. The $E = 0$ is a branching point of the function $B_l(E)$ and an alternative expansion must be employed. For further analysis see Ref. 157.

The analysis of potential scattering resonances may be generalized to multichannel scattering resonances. The S matrix in the neighborhood of a resonance [163] denoted m is

$$S(E) = S_d(E) - \frac{ig_m(E)g_m^T(E)}{E - E_m(E) + \frac{1}{2}i\Gamma_m(E)}. \tag{7.61}$$

$S_d(E)$ is a complex unitary $n \times n$ matrix representing scattering that does not involve the metastable state, $g_m(E)$ is a complex column vector of order n and $E_m(E)$ and $\Gamma_m(E)$ are the energy and width of resonance. The vector $g_m(E)$ is related to $\Gamma(E)$ by

$$\Gamma_m(E) = \sum_i \Gamma_{mi}(E) = \sum_i |g_{mi}(E)|^2, \tag{7.62}$$

where $\Gamma_{mi}(E) = |g_{mi}(E)|^2$ is the partial width of channel i. The sum over i runs over all n open channels. The expression is derived in formal scattering theory within the isolated narrow resonance approximation, where it is assumed that $E_m(E)$, $\Gamma_m(E)$, and $g_m(E)$ are constant parameters characterizing resonance.

Having stated this result, we want to work backwards to prove that the formula (7.61) implies a Breit-Wigner form in eigenphase sum. Eigenphases, λ_i and λ_i^d, are defined through the relations

$$\begin{aligned} S(E) &= B(E)\Lambda^2(E)B^T, \\ S_d(E) &= B_d(E)\Lambda_d^2(E)B_d^T, \end{aligned} \tag{7.63}$$

where $B(E)$ and $B_d(E)$ are orthogonal matrices that diagonalize $S(E)$ and $S_d(E)$ respectively, and

$$\Lambda_{ij}(E) = \delta_{ij}\exp(i\lambda_i), \tag{7.64}$$

$$[\Lambda_d]_{ij}(E) = \delta_{ij}\exp(i\lambda_i^d), \tag{7.65}$$

are diagonal matrices. The eigenphase sums are

$$\varsigma(E) = \sum_{i=1}^{n} \lambda_i(E), \tag{7.66}$$

$$\varsigma_d(E) = \sum_{i=1}^{n} \lambda_i^d(E). \tag{7.67}$$

Now we perform a series of transformations following Ref. 163 in order to prove that

$$\varsigma(E) = \varsigma_d(E) + \arctan\left(\frac{\Gamma_m(E)}{2[E_m(E) - E]}\right) \tag{7.68}$$

follows from (7.61). The rapid variations are contained in the second term of the generalized Breit-Wigner formula (7.68) within the isolated narrow resonance approximation.

Equation (7.61) may be rewritten in form

$$S = X_d S_r X_d, \tag{7.69}$$

where

$$X_d = B_d \Lambda_d B_d^T, \tag{7.70}$$

$$S_r = 1 - \frac{i\Gamma_m w_m w_m^T}{E - E_m + \frac{1}{2} i\Gamma_m}, \tag{7.71}$$

and w_m is a column vector

$$w_m = \Gamma_m^{-1/2} X_d^\dagger g_m. \tag{7.72}$$

Now, relation (7.62) implies

$$w_m^T w_m = 1, \tag{7.73}$$

X_d is symmetric and unitary and the condition of unitarity of S implies that S_r must also be unitary, which together with (7.73) leads to the conclusion that w_m is real. This means that S_r may be written in form

$$S_r = B_r \Lambda_r^2 B_r^T, \tag{7.74}$$

with B_r orthogonal and

$$[\Lambda_r]_{ij}(E) = \delta_{ij} \exp(i\lambda_i^r) = \delta_{ij} c_i, \tag{7.75}$$

where

$$c_1 = 1 - \frac{i\Gamma_m}{E - E_m + \frac{1}{2} i\Gamma_m} = \exp\left[2i \arctan \frac{\Gamma_m}{2(E_m - E)}\right], \tag{7.76}$$

$$c_{j \neq 1} = 1. \tag{7.77}$$

Putting together equations (7.69), (7.71), and (7.74), we get

$$B\Lambda^2 B^T = (B_d \Lambda_d^2 B_d^T)(B_r \Lambda_r^2 B_r^T)(B_r \Lambda_r^2 B_r^T), \tag{7.78}$$

from where, by taking determinants of both sides, it follows that

$$|\Lambda^2| = |\Lambda_d^2||\Lambda_r^2|. \tag{7.79}$$

Using the definitions of the matrix elements, (7.65) and (7.77), we arrive to the generalized Breit-Wigner formula (7.68). Since the eigenphase sum increases by π when sweeping the energy through a resonance, plotting $\varsigma(E)$ against E is a convenient tool for locating resonances. Eigenphase sum is determined modulo π so that a fine mesh is needed to locate narrow resonances. We extracted the eigenphases from the diagonalized K matrix, which we obtained from the scattering calculations. The K matrix is related to the S matrix through

$$K(E) = i[1 - S(E)][1 + S(E)]^{-1}, \tag{7.80}$$

and its eigenvalues are tangents of eigenphases,

$$K(E) = B(E)[\tan \Lambda(E)]B^T(E). \tag{7.81}$$

The lifetime of a resonance, $\tau_m = 1/\Gamma_m$, may be determined by taking a derivative of (7.68) with respect to E. Then we obtain

$$\tau_m = 2\left(\frac{\partial \varsigma}{\partial E}\right)_{E=E_m}. \tag{7.82}$$

7.6 Langevin model

In this concluding section we derive a simple model due to Langevin, Gioumousis, and Stevenson [164] for reaction cross sections for reactions without a barrier. If the probability of a reactive encounter is one for all incident impact parameters $b \leq b_{\max}$ and zero for $b > b_{\max}$, the reaction cross section is

$$\sigma_{\text{reac}} = b_{\max}^2 \pi. \tag{7.83}$$

For the initial kinetic energy $E_{\text{K}} = mv^2/2$, the energy conservation implies

$$E_{\text{K}} = \frac{1}{2}m\dot{r}^2 + \frac{L^2}{2mr^2} + V(r), \tag{7.84}$$

where L is the orbital angular momentum $L = mvb$ and the motion is reduced to one dimension with an effective potential. It is assumed that there is no energy barrier for reaction, so the only barrier that needs to be surmounted is that due to the combined effect of the long-range centrifugal potential and the long-range attractive potential,

$$V_{\text{eff}} = \frac{E_{\text{K}}b^2}{r^2} + V(r) = \frac{E_{\text{K}}b^2}{r^2} - \frac{C_s}{r^s}. \tag{7.85}$$

At the maximum of the effective potential, $r_{\max}$, there must be enough kinetic energy left that reaction takes place. This condition determines the maximum value of the impact parameter,

$$[E_{\mathrm{K}} - V_{\mathrm{eff}}]_{r_{\max}} = 0. \tag{7.86}$$

Combining (7.85), (7.86), and (7.83), we obtain

$$\sigma_{\mathrm{reac}}(E_{\mathrm{K}}) = \pi \frac{s}{2} \left(\frac{2}{s-2}\right)^{\frac{s-2}{s}} \left(\frac{C_s}{E_{\mathrm{K}}}\right)^{\frac{2}{s}}. \tag{7.87}$$

The model predicts a decrease of reaction cross section with collision energy for reactions without a barrier.

For reactions proceeding over a barrier, $V(r)$ in the combined equations (7.85) and (7.86) may be replaced by the threshold energy E_{th} at a separation d. This leads to zero reaction cross section below the threshold and an increasing energy dependence above, $\sigma_{\mathrm{reac}}(E_{\mathrm{K}}) = \pi d^2(1 - E_{\mathrm{th}}/E_{\mathrm{K}})$.

The relevance of the Langevin model to cold collisions will be established in the next chapter.

Chapter 8

Ultracold collisions: $Li + Li_2$

8.1 Introduction

In this chapter we investigate the atom-diatom collisions in lithium at ultralow collision energies. We are interested in particular in the stability of molecules in the excited rovibrational states. Motivation for this work originates in the recent experimental efforts of creating stable ultracold molecular systems and molecular Bose-Einstein condensates.

Cold molecules have so far been produced from cold gases of atoms either by photoassociation or making use of magnetically tunable Feshbach resonances. Much of work has been concentrated on alkali atoms, so that lithium [52, 165], sodium [166, 167], potassium [168, 169], rubidium [170, 171], and cesium [29, 172] molecules have all been produced in both ways. First cold heteronuclear molecules were created in lithium by photoassociation [24]. Recently, molecular Bose-Einstein condensates have been created from degenerate Fermi gases of lithium [31, 32] and potassium [33]. In each of the above experiments, molecules have been created in rovibrational states close to dissociation. The crucial breakthrough that allowed creation of molecular condensates using fermionic isotopes was the finding that atom-molecule and molecule-molecule inelastic collisions are strongly suppressed in this case when the atom-atom scattering length is large and positive [165, 173, 174, 175]. It was explained in terms of Fermi statistics of the atoms [30] and the long-range nature of molecules. By contrast, weakly bound bosonic dimers have been found to be unstable against the decay into lower rovibrational states [21, 29, 171, 176, 177]. The energy released in the vibrationally and rotationally inelastic collisions is usually larger than the depth of traps used to store the atoms. For example, the depth of an optical trap in which the lithium molecules were produced from an atomic Fermi gas by Hulet and co-workers [173] was $\approx 7\mu$K. In this experiment atoms were converted to molecules with an efficiency of $\approx 50\%$, and it was assumed that the inelastic atom-molecule collisions are the main trap-loss mechanism. The inelastic rate coefficient was found to be $2-3$ orders of magnitude smaller than the one found in bosonic species, e.g. for Rb_2 [21] and Na_2 [177], $k_{\text{inel}} \approx 10^{-10}$ cm^{3}s^{-1}.

The possibility to create and trap state-selected molecules opens new prospects to perform collision and chemical reaction experiments at ultralow kinetic energies. Theoretical studies of such processes have so far been made on the following systems:

$He + I_2$ [178], $H + H_2$ [41, 42], $He + H_2$ [37, 43, 179, 180], $He + CO$ [35, 36, 181, 182], $He + O_2$ [183, 184], $Ar + H_2$ [185], $He + HF$ [186], $He + F_2$ [187], $He + N_2$ [188], and $F + H_2$ [11, 189–193], and also in ionic systems $He + He_2^+$ and $Ne + Ne_2^+$ [194]. All above systems, except ionic, proceed on a relatively weak potential. Calculations on these systems established the range of validity of Wigner threshold laws and provided first estimates of the magnitude of inelastic rate coefficients in the zero-energy limit. It was found that the the inelasticity is strongly dependent on the initial state of the molecule. Vibrational relaxation by a single quantum is generally more probable than double or triple de-excitations. Rotationally inelastic cross sections were found larger than the rovibrational ones and the product rotational distributions are peaked at lower j levels for low initial rotational states. For example, in the $H + H_2$ collisions [41], the Wigner threshold behaviour sets in at $\approx$ 10 mK and at even higher energies for vibrationally excited states. Inelastic rate coefficients vary as much as six orders of magnitude for different initial vibrational states of the molecule, between 10^{-17} cm^3s^{-1} for $v_i = 1$ and 10^{-10} cm^3s^{-1} for $v_i = 14$. Rotational levels were ignored in these calculations. Inelastic rate coefficients were found to be lower for heavier molecules and the onset of threshold behaviour usually between 0.1 mK and 10 mK. Rotational inelasticity was found to be as high as 10^{-10} cm^3s^{-1} for CO in the $v_i = 0$, $j_i = 1$ state. High inelastic rates were also found in the collisions starting from specific highly excited rotational states in H_2 [179] and O_2 [184] with helium, but they could also be as low as 10^{-17} cm^3s^{-1}. The highly state-specific energy transfer in these super-rotors was discussed in a series of papers [179, 180, 182, 184, 185, 195]. High rotationally inelastic rate coefficients, 10^{-9} cm^3s^{-1}, were also predicted for ionic systems [194], which do however proceed over the deep and highly anisotropic potential energy surfaces.

Chemical reactivity at ultralow energies has first been explored on the H + HF reaction by Balakrishnan et al. [11] and later on its isotopically substituted systems. These reactions proceed over a potential barrier and their efficiency is attributed to the quantum-mechanical tunneling process that becomes significant at low energies due to the long duration of the collision. The reactive rate coefficient was predicted to be $1.25 \cdot 10^{-12}$ cm^3s^{-1} [11] for $v_i = 0$, $j_i = 0$ at temperatures below 10 mK. The reaction of F with HD and D_2 gave lower rate coefficients because the efficiency of tunneling is lower in heavier systems [189–191].

The first study of an alkali atom-molecule system was made in the spin-polarized bosonic sodium, $^{23}Na + {}^{23}Na_2$ [196]. The potential energy surface [80] has a global minimum of -849 cm^{-1} at D_{3h} geometry with the bond distance of 4.406 Å. There is no barrier for atom exchange. Sodium potential is compared with other spin-polarized alkali trimers in Ref. 79. The cross sections were calculated for the $J = 0$ partial wave that is dominant at ultralow energies. Wigner laws govern the energy dependence below 10^{-5} K and the inelastic cross sections are larger than elastic below $10^{-4} - 10^{-3}$ K. The zero-energy limit of inelastic rate coefficient is $5.2 \cdot 10^{-10}$cm^{3}s^{-1}.

This chapter represents an extension of this work to another alkali system of experimental interest. Lithium is the lightest of alkalis which facilitates the computational cost of calculations. It comes in two isotopes with different nuclear spins which enables one to compare collisions in bosonic and fermionic systems. Collisions are investigated for the spin-stretched states of the lithium trimer, where the total spin of the system and its projection on a quantization axis acquire their maximum value. Atoms in such states can be magnetically trapped, although the present calculations do not assume the presence of external fields. The potential energy surface for lithium trimer is described in Chapter 2, 3, 4, and 5. We neglect the influence of the non-adiabatic couplings which are significant near the conical intersection at linear geometries. All the processes are studied with the aid of the reactive scattering code written by Launay and LeDourneuf [136, 138], which solves the Schrödinger equation for nuclei by the coupled channel method in hyperspherical coordinates, as described in Chapter 6.

We start by discussing the symmetry requirements following from the Pauli principle depending on the type of collision particles, fermions or bosons, involved. The other sections are each devoted to different processes: collisions in the bosonic and fermionic systems, and collisions in isotopic mixtures. We report on the convergence of our calculations, the vibrational and rotational relaxation cross sections for $J = 0$, and, in the case of three identical nuclei, the higher partial wave contributions and differential cross sections. With inclusion of 11 partial waves, cross sections are converged for collision energies below 500 mK. Finally, a simple classical Langevin model is used to make the semi-quantitative predictions of inelastic rate coefficients in other alkali systems.

Although the temperature is a thermodynamic quantity and the present chapter

deals with the individual state-to-state processes, the collision energies and the level separations are reported in Kelvins defined as the energy with respect to a reference energy divided by the Boltzmann constant. This convention is adopted widely in the cold-molecule literature.

8.2 Symmetry considerations

Working within the Born-Oppenheimer approximation, we have effectively separated the motion of electrons from the motion of nuclei so that their wavefunctions appear separately with the overall wavefunction in the form of a product. Here we consider the effect of the exchange of identical nuclei on the nuclear wavefunction and determine all the permitted states in the asymptotic region. An eigenstate of the nucleus-exchange operator in the asymptotic region will preserve the symmetry everywhere since the nuclear hamiltonian commutes with the nucleus-exchange operator.

All inelasticity of the collision is contained in the internal degrees of freedom of the molecule. Having the above in mind, the wavefunction of the diatomic molecule in the asymptotic region can be written as

$$\psi_{\text{total}} = \psi_{\text{electronic}} \times \psi_{\text{vibrational}} \times \psi_{\text{rotational}} \times \psi_{\text{nuclear spin}}. \tag{8.1}$$

We consider the symmetry under exchange of identical nuclei of each term in this product state separately.

In this work, we limit ourselves to the investigation of spin-stretched states, meaning that the total spin, the sum of the nuclear and electronic spins, and its projection on the quantization axis acquire their maximum value, $F = F_{\text{max}} = I + S$ and $|M_F| = F$. For alkali + alkali dimer systems, such collisions occur entirely on the electronic quartet surfaces with no contribution from doublet surfaces. This assumption determines the symmetry of the nuclear spin wavefunction to be even under exchange of identical nuclei regardless of the type of the nuclei in question.

The electronic wavefunction of the quartet ground state of three lithium atoms correlates with a ^2S state of the atom and a $^3\Sigma_u^+$ state of the molecule in its asymptotic limit. In the full nuclear permutation-inversion group of the molecule, the

operation of the exchange of two nuclei can be described as

$$(12) = (12)^* \times E^*, \tag{8.2}$$

where the operation E^* is the inversion of all particles, nuclei and electrons, through the molecular centre of mass. The action of the operator $(12)^*$ on the electronic wavefunction of the diatomic molecule is determined by the g or u character in the term symbol of the state ($D_{\infty h}$ group), while the action of E^* is determined by the sign $(+/-)$ in the term symbol [197]. The combined action therefore changes the sign of the electronic wavefunction of the $^3\Sigma_u^+$ state.

The exchange of identical nuclei does not induce any changes to the vibrational wavefunction. The rotational part of nuclear wavefunction transforms to $(-1)^j$ times the original, where j is the rotational quantum number. This can be seen by looking at the transformation of spherical harmonics under $\mathbf{r} \rightarrow -\mathbf{r}$. The overall wavefunction transforms to the original times $(-1)^{j+1}$.

In the case of Hund's coupling case (b), which applies to the triplet state of lithium dimer, the total mechanical rotation is a good quantum number. The deviations from the case (b) level pattern caused by the electronic orbital angular momenta are neglected. Fine and hyperfine structure of the rotational levels are also neglected. They have been experimentally measured in the $^3\Sigma_u^+$ state of Na_2 [198]. The dominant splittings come from electronic spin-spin (experimental value of the coupling constant for Na_2 is $\lambda = 4.34 \cdot 10^{-2}$ cm^{-1}) and spin-rotation interactions (experimental value of the coupling constant for Na_2 is $\gamma = 1.42 \cdot 10^{-3}$ cm^{-1}). Linton and co-workers have not been able to resolve the fine structure in the $^3\Sigma_u^+$ state of Li_2 with their experimental linewidths of ≈ 1 cm^{-1} [48]. The errors due to that are therefore expected to be small. It should also be noted here that the conventional spectroscopic symbols for different angular momenta are not the same as those used in this work.

Lithium appears in nature in two different isotopes. ^{6}Li (7.59%) has mass 10964.8974 m_e and nuclear spin 1. Integer nuclear spin means the ^{6}Li nucleus is a boson. In a cold dilute gas, where the probability of finding two atoms within the range of the interaction is low and therefore the electronic degrees of freedom are frozen out, the ^{6}Li atom is usually regarded as a composite fermion since its total spin, the sum of electronic and nuclear spin, is half-integer. The total wavefunction

of the dimer (8.1) must be symmetric under exchange of two identical bosons, meaning that only odd j levels can be populated in $^6Li_2$ in its spin-stretched state and $^3\Sigma_u^+$ electronic state. The change of sign in electronic part of the wavefunction is compensated by a change of sign in the nuclear wavefunction when two identical nuclei are exchanged. The nuclear wavefunction of lithium trimer $^6Li_3$ must be antisymmetric under exchange of two ^{6}Li nuclei everywhere, because the determined symmetry in the asymptotic region is a constant of motion as discussed in the beginning of this section.

^{7}Li (92.41%) has mass 12789.3934 m_e and nuclear spin 3/2. Its nucleus is therefore a fermion, although when viewed with the electrons (spin 1/2) as a whole, as is often done in the cold dilute gases, the atom is a composite boson. Following the same arguments as above, $^7Li_2$ can occupy only even j quantum states and the nuclear part of the wavefunction of lithium trimer must therefore be symmetric under the exchange of two ^{7}Li nuclei everywhere.

In the coupled channel calculations, restrictions on the symmetry of the wavefunction under the exchange of identical nuclei are implemented by employing a properly symmetrized set of basis functions. The basis functions that we use are expressed in terms of the pseudohyperspherical harmonics (6.51). In fact, as discussed in Chapter 6, it is the h functions (6.50) that determine the symmetry under exchange. The interchange of identical particles is accomplished by a reflection in the $\phi = 0$ plane, as is shown on a diagram in Figure 8.1, followed by a rotation around the body-fixed z axis by π. Namely,

- Interchange BC : $\phi \to -\phi$
- Interchange AB : $\phi \to 4\pi/3 - \phi$
- Interchange AC : $\phi \to 8\pi/3 - \phi$
- Cyclic permutation CAB : $\phi \to 2\pi/3 + \phi$
- Cyclic permutation BAC : $\phi \to 4\pi/3 + \phi$.

For the reactions in isotopic mixtures,

$$^6Li + {}^7Li_2 \to {}^7Li + {}^6Li^7Li, \tag{8.3}$$

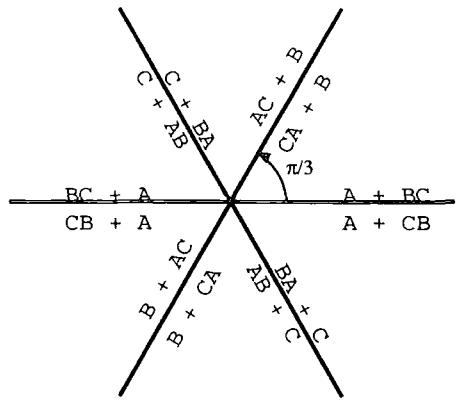

Figure 8.1: Diagram showing arrangements of three identical nuclei for a fixed θ in hyperspherical coordinate system. The in-plane azimuthal angle is ϕ and radial coordinate is the hyperradius ρ.

and

$$^7\mathrm{Li} + {}^6\mathrm{Li}_2 \rightarrow {}^6\mathrm{Li} + {}^6\mathrm{Li}^7\mathrm{Li}, \tag{8.4}$$

the wavefunction must have the appropriate symmetry with respect to the exchange of nuclei in the molecule BC in the incident arrangement of reaction (6.1). This is accomplished by choosing the basis functions with $\epsilon_P = +1$ ($h = \cos$) for the reaction (8.3) and basis functions with $\epsilon_P = -1$ ($h = \sin$) for the reaction (8.4). The amplitudes for the reverse reactions of those in (8.3) and (8.4) can be extracted from the same S matrix by making use of the principle of microscopic reversibility [148].

For collisions involving three identical nuclei,

$$^7\mathrm{Li} + {}^7\mathrm{Li}_2 \rightarrow {}^7\mathrm{Li} + {}^7\mathrm{Li}_2, \tag{8.5}$$

and

$$^6\mathrm{Li} + {}^6\mathrm{Li}_2 \rightarrow {}^6\mathrm{Li} + {}^6\mathrm{Li}_2, \tag{8.6}$$

the appropriate symmetry with respect to interchange of any two nuclei is set by requiring $\epsilon_P = +1$, if the wavefunction is to be symmetric under exchange, or $\epsilon_P = -1$, if the wavefunction is to be antisymmetric, and by simultaneously requiring the basis functions to be symmetric under a cyclic permutation. $\epsilon_P = +1$ is required for the reaction in (8.5), while $\epsilon_P = -1$ applies to the reaction (8.6). These results are summarized below ($\Omega\pi/2$ in the argument of trigonometric functions has been omitted for clarity).

- Three identical fermions: BF wavefunction is fully antisymmetric
  - $\sin 3\phi, \sin 9\phi, \ldots$ with $\epsilon_I = -1$, $\epsilon_P = -1$
  - $\sin 6\phi, \sin 12\phi, \ldots$ with $\epsilon_I = +1$, $\epsilon_P = -1$
- Three identical bosons: BF wavefunction is fully symmetric
  - $\cos 3\phi, \cos 9\phi, \ldots$ with $\epsilon_I = -1$, $\epsilon_P = +1$
  - $\cos 0\phi, \cos 6\phi, \ldots$ with $\epsilon_I = +1$, $\epsilon_P = +1$
- One boson and two fermions:
  - $\sin 1\phi, \sin 3\phi, \ldots$ with $\epsilon_I = -1$, $\epsilon_P = -1$
  - $\sin 2\phi, \sin 4\phi, \ldots$ with $\epsilon_I = +1$, $\epsilon_P = -1$
- One fermion and two bosons:
  - $\cos 1\phi, \cos 3\phi, \ldots$ with $\epsilon_I = -1$, $\epsilon_P = +1$
  - $\cos 2\phi, \cos 4\phi, \ldots$ with $\epsilon_I = +1$, $\epsilon_P = +1$

It is interesting to note that the convergence problem that might arise due to the Eckart singularity at the symmetric top geometries is never present when dealing with three identical fermions. The problem arises because the coupling matrix elements (6.56) of $\mathcal{R}$ (6.36) in the coupled equations (6.54) diverge for symmetric top configurations ($\theta = \pi/2$). The leading power in the expansion of $g_K^{\nu\Omega}$ for small deviations around $\theta = \pi/2$ is $\nu/2$, as can be seen by inserting the leading power term in the differential equation (6.49) and keeping first-order terms in power expansions about $\pi/2 - \theta$. There is a term in the expression for $\mathcal{R}$ (6.36) that is proportional to $1/\cos^2\theta$, which is singular. The contribution of this term to the coupling matrix element (6.56) behaves then as $(\pi/2 - \theta)^{\nu/2+\nu/2-2}$ for θ near $\pi/2$. From this result, it is clear that the divergence problems cannot occur when $\nu \geq 2$. As we have seen, the symmetry under exchange requires $\nu \geq 3$ for three identical fermions.

The problem with the Eckart singularity never occurs in the $J = 0$ partial wave since J_y in (6.36) couples only different projections Ω of J. In some types of reactions, the region where it could occur is inaccessible due to repulsiveness of the interaction potential. This is not the case in the quartet ground state surfaces of alkalis.

We adopt the notation J^{Π} for partial waves, where J is the total mechanical angular momentum of nuclei and Π is parity. J is equal to the sum of the orbital, l, and rotational, j, angular momenta. l and j are good quantum numbers in the asymptotic region. When molecule is initially in the rotational state j, the states with orbital angular momentum quantum number l satisfying the triangle inequality, $|J-j| \leq l \leq J+j$, couple with j into the partial wave of the total angular momentum J. The parity of initial state is $\epsilon_I = (-1)^{j+l}$ and it is conserved in course of collision. Tables 8.1 and 8.2 summarize the allowed l values for the scattering of three identical fermions from an initial $j = 1$ and for the scattering of three identical bosons from an initial $j = 0$ rotational level of the dimer. It is also indicated which values of Ω must be included in the basis set for each partial wave. Blocks of partial waves listed in the first row in Table 8.1 satisfy $\epsilon_I(-1)^J = +1$ and we call them parity favoured blocks. Parity blocks of partial waves in the second row satisfy $\epsilon_I(-1)^J = -1$ and we call them parity unfavoured. Parity favoured blocks include the basis functions with $\Omega = 0$, as can be seen from the form of the dependence of the wavefunction on the external hyperspherical coordinates (6.46), and as a consequence they include more basis functions than parity unfavoured blocks for a given partial wave J and accuracy.

FERMIONS: partial waves J^{Π}			
0^+	1^-	2^+	3^-
j=1, l=1 $\Omega = 0$	j=1, l=0,2 $\Omega = 0, 1$	j=1, l=1,3 $\Omega = 0, 1, 2$	j=1, l=2,4 $\Omega = 0, 1, 2, 3$
	1^+	2^-	3^+
	j=1, l=1 $\Omega = 1$	j=1, l=2 $\Omega = 1, 2$	j=1, l=3 $\Omega = 1, 2, 3$

Table 8.1: Partial wave analysis of the atom-diatom wavefunction of the fermionic system: initial rotational quantum number is $j = 1$; initial orbital angular momentum l and Ω quantum numbers included in the basis set are given.

The convergence parameter in the partial wave expansion is the orbital angular momentum $l_{\max}$, as can be confirmed with the actual calculations reported later in this chapter. The dominant contribution at ultracold temperatures is the one that comes from the partial wave containing $l = 0$, where the amplitudes are not hin-

BOSONS: partial waves J^{Π}			
0^+	1^-	2^+	3^-
j=0, l=0	j=1, l=1	j=0, l=2	j=0, l=3
$\Omega = 0$	$\Omega = 0, 1$	$\Omega = 0, 1, 2$	$\Omega = 0, 1, 2, 3$

Table 8.2: Partial wave analysis of the atom-diatom wavefunction of the bosonic system: initial rotational quantum number is $j = 0$; initial orbital angular momentum l and Ω quantum numbers included in the basis set are given.

dered by tunneling through the centrifugal barrier. For ultracold collisions involving three bosons, the partial wave 0^+ gives the dominant contribution. In case of three ultracold fermions, the partial wave 1^- contributes dominantly. It is evident from Table 8.1 and 8.2 that up to a given value of $l_{\max}$, more partial waves, J^{Π}, need to be included in the partial wave expansion for a fermionic system than for a bosonic system. This means that, for a given accuracy, calculations on fermionic systems are more computationally demanding.

8.3 Collisions in bosonic system

In this section we report the results of scattering calculations for the atom-exchange collision process

$$^7\mathrm{Li} + {}^7\mathrm{Li}_2 \rightarrow {}^7\mathrm{Li} + {}^7\mathrm{Li}_2, \tag{8.7}$$

involving three bosonic ^{7}Li nuclei at collision energies between 1 nK and 1 K.

Convergence parameters for the dominant $J = 0$ contribution to the cross sections are discussed in the next subsection. Vibrational relaxation cross sections for $J = 0$ and different initial states of the molecule are discussed in the subsequent subsection. This is followed by the partial wave convergence for $J = 0 - 10$. Product vibrational and rotational distributions and differential cross sections are reported for collision energies of 116 mK and 580 mK. Converged inelastic cross sections are compared with the classical Langevin model. Collisions involving an initially rotationally excited molecule are considered at the end of the section.

8.3.1 Convergence of cross sections: $J = 0$

Numerical solution of the Schrödinger equation for each partial wave must be converged with respect to the number of basis functions in the expansions and discretization steps in the integrations. The convergence parameters for the $J = 0$ partial wave are reported below.

The convergence of cross sections for the total angular momentum $J = 0$ with respect to the number of basis functions in equation (6.53) and the propagation distance in the hyperradial coordinate, $\rho_{\max}$, is studied by comparing the cross sections obtained using four different basis sets. The largest basis set consists of $N = 97$ basis functions which are asymptotically matched at $\rho_{\max} = 45\ a_0$ onto the rovibrational wavefunctions in Jacobi coordinates with $v = 0$, 1, 2, 3, 4, 5, 6, and 7, and with all the rotational levels up to $j_{\max} = 32$, 30, 28, 24, 22, 18, 14, and 10, for each vibrational manifold respectively. In this way, we included basis functions that correlate with all rovibrational states lying below the $v = 8$, $j = 0$ state in energy. Extending the basis set further would demand a corresponding increase in the propagation distance to ensure accurate projections (max. error for all states is 2 parts in 1000) between hyperspherical and Fock wavefunctions (6.78). The basis sets of $N = 84$ and $N = 70$ basis functions consist of all the hypersurface eigenfunctions matched onto the rovibrational levels up to and not including $v = 7$ ($j_{\max} = 32$, 28, 26, 22, 20, 16, 10) and $v = 6$ ($j_{\max} = 30$, 28, 24, 20, 16, 10) vibrational manifolds respectively.

Minimum propagation distance for a given basis set can be determined by setting a requirement for a good overlap at the matching distance between the wavefunctions in Fock and in hyperspherical coordinates (6.78). Projections improve with the propagation distance. With a slight compromise of the projections in the matching sector, the propagation distance can be reduced to $\rho_{\max} = 40\ a_0$ for the basis set $N = 84$.

Elastic and inelastic cross sections calculated using the basis sets described above are reported in Table 8.3. They converge monotonically with the basis set size. We believe that all the cross sections in the range of collision energies studied are converged to better than 10%, except in the regions of rapid variations with the collision energy.

The elastic and total inelastic cross sections for collisions with the molecule that

(v_i, v_f)	$N = 70$	$N = 84$	$N = 84$, $\rho_{\max} = 40a_0$	$N = 97$
(0,0)	$2.937 \cdot 10^{-12}$	$3.356 \cdot 10^{-12}$	$3.264 \cdot 10^{-12}$	$3.392 \cdot 10^{-12}$
(1,1)	$3.395 \cdot 10^{-12}$	$1.581 \cdot 10^{-12}$	$1.649 \cdot 10^{-12}$	$1.370 \cdot 10^{-12}$
(1,0)	$4.865 \cdot 10^{-9}$	$3.327 \cdot 10^{-9}$	$3.397 \cdot 10^{-9}$	$3.094 \cdot 10^{-9}$
(2,2)	$2.982 \cdot 10^{-13}$	$4.503 \cdot 10^{-13}$	$4.214 \cdot 10^{-13}$	$5.168 \cdot 10^{-13}$
(2,1)	$2.927 \cdot 10^{-10}$	$1.783 \cdot 10^{-10}$	$1.801 \cdot 10^{-10}$	$1.642 \cdot 10^{-10}$
(2,0)	$5.683 \cdot 10^{-10}$	$3.293 \cdot 10^{-10}$	$3.301 \cdot 10^{-10}$	$3.132 \cdot 10^{-10}$
(3,3)	$9.193 \cdot 10^{-13}$	$9.762 \cdot 10^{-13}$	$1.076 \cdot 10^{-12}$	$9.294 \cdot 10^{-13}$
(3,2)	$7.958 \cdot 10^{-10}$	$3.577 \cdot 10^{-10}$	$3.688 \cdot 10^{-10}$	$2.555 \cdot 10^{-10}$
(3,1)	$3.340 \cdot 10^{-10}$	$3.640 \cdot 10^{-10}$	$3.739 \cdot 10^{-10}$	$2.505 \cdot 10^{-10}$
(3,0)	$1.088 \cdot 10^{-9}$	$3.594 \cdot 10^{-9}$	$3.685 \cdot 10^{-9}$	$3.511 \cdot 10^{-9}$

Table 8.3: Convergence of vibrationally resolved cross sections, $\sum_{j_f} \sigma(v_i j_i \rightarrow v_f j_f)$ for $j_i = 0$ in cm^2, for ^{7}Li + ^{7}Li$_2$ at the collision energy of 0.928 nK. $\rho_{\max} = 45\ a_0$ for all bases unless otherwise indicated.

is initially in the $v_i = 1$ and $j_i = 0$ state are shown in Figure 8.2 against the collision energy between 1 nK and 1 K for the three bases, $N = 70$, 84, and 97, matched at $\rho_{\max} = 45\ a_0$. The profile of the energy dependence does not change significantly for the three basis sets and the error decreases with increasing collision energy which provides additional confidence in the results.

The rotationally resolved cross sections (state-to-state) from $(v, j) = (1, 0)$ to $(0, j_f)$ are shown in Figure 8.3 at the collision energy of 0.928 nK. The cross sections converge for all rotational levels. The results obtained using the smallest basis, $N = 70$, are in a significant disagreement with others for higher rotational levels.

The hyperradial coordinate was divided into sectors 0.1 a_0 wide with their centres extending from 5 a_0 up to $\rho_{\max}$. The log-derivative matrix is propagated within each sector in 8 steps per half the local WKB wavelength. The set of pseudohyperspherical harmonics used to evaluate the basis functions is limited by $K_{\max} = 239$ (1240 harmonics) in all sectors up to 30 a_0. Outside 30 a_0, $K_{\max}$ is linearly increased with the distance up to $K_{\max} = 359$ (2136 harmonics), at $\rho_{\max} = 45\ a_0$, in order to converge the hypersurface energies. Propagation outside 45 a_0 becomes expensive as pseudohyperspherical harmonics provide an increasingly inefficient basis. At $\rho_{\max}$, the channels close to threshold are matched onto the wavefunction propagated from a large distance inwards in the isotropic atom-molecule potential, $(V(\theta = 0) + 2V(\theta =$

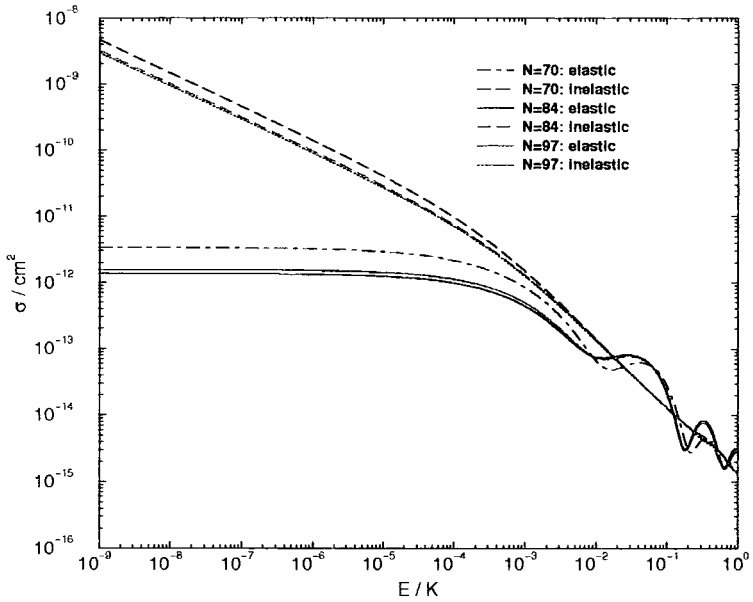

Figure 8.2: Convergence of elastic and inelastic cross sections for $^7\mathrm{Li} + {}^7\mathrm{Li}_2(v_i = 1, j_i = 0)$. N is the number of channels in the basis.

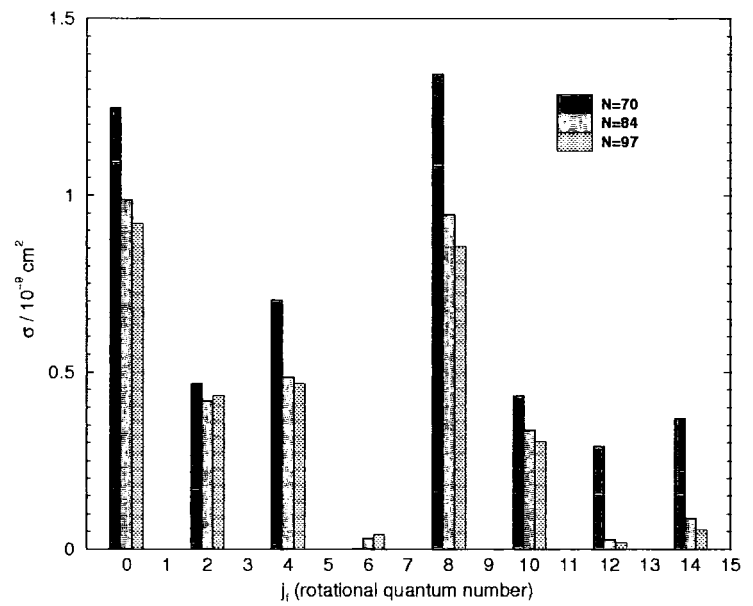

Figure 8.3: Convergence of inelastic state-to-state cross sections for $^7\mathrm{Li} + {}^7\mathrm{Li}_2(v_i = 1, j_i = 0)$ and $v_f = 0$ at the collision energy of 0.928 mK. N is the number of channels in the basis.

$\pi/2))/3$. The step-size in the one-channel backward propagation must be small. We took 40 steps per half the local WKB wavelength. The starting distance was chosen to be at the point where the isotropic potential is 10^{-6} times smaller than the centre of mass collision energy. This amounts to the distance of $\sim 10000\ a_0$ at 1 nK.

The adiabatic hypersurface energies corresponding to 97 channels employed in our calculations are plotted in Figure 8.4. They exhibit a deep minimum at 4.1 Å, which corresponds to the global minimum of the potential energy surface. The curves are smooth with numerous avoided crossings. At long range, they tend to the lithium rovibrational diatomic energies. The maximum of the hypersurface energies just below 6 Å is due to the curve crossing at linear geometries, while the saddle point at 7 Å corresponds to the minimum at linear configurations.

The integrations in $\theta \in [0, \pi/2]$ and $\phi \in [0, \pi/3]$ were performed by the four-point Gaussian-composite rules on the 300×200 grid. The range in ϕ is reduced because of the symmetry. There are three evaluations of coupling matrices (6.55, 6.56) within each sector which amounts to 180 000 potential evaluations per sector.

The asymptotic wavefunctions in Fock coordinates were expanded onto the basis of 80 primitives (sines). The quadratures in Fock angles used 200 points per corresponding range.

The matching at $\rho_{\max} = 45\ a_0$ corresponds to the atom-diatom distance of $R = 21.86$ Å when the diatom is at its equilibrium distance of ≈ 4.2 Å. The intermolecular potential is still substantially anisotropic at these distances. For $\theta = 0$ it is -0.2155 cm^{-1} while for $\theta = \pi/2$ it is -0.1525 cm^{-1}. It is assumed that this anisotropy of 0.063 cm^{-1} does not induce substantial rotational transitions at larger distances since the rotational spacing is greater than 1.25 cm^{-1} for all transitions involved in the reported results for $^7Li_2$ and 0.44 cm^{-1} for $^7Li^6Li$.

The largest basis set we have used here presents a limit in the size manageable with a reasonable computational effort. Any extension would increase the propagation distance, the number of harmonics (quadratic with ρ), and the number of integration points (i.e. potential evaluations), and would substantially increase the computer time. This basis ($N = 97$) was used in all the results reported in the subsequent sections.

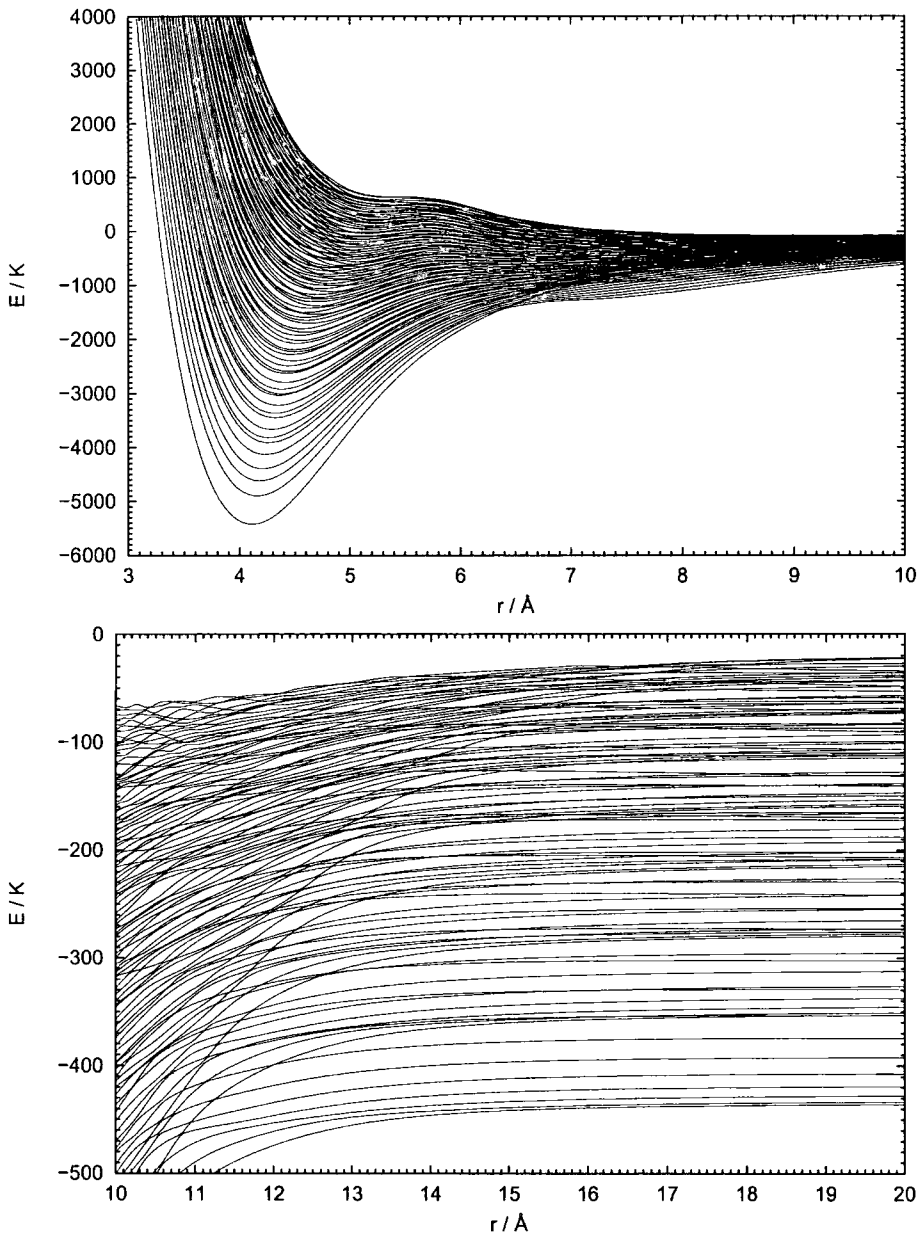

Figure 8.4: Eigenvalues ($N = 97$) of the hypersurface hamiltonian (6.47) for three ^{7}Li nuclei in the electronic quartet ground state.

8.3.2 Vibrational relaxation cross sections and rate coefficients: $J = 0$

In this subsection, we calculate the cross sections for atom-diatom collisions involving three ^{7}Li nuclei starting from a rotationless initial state, $j_i = 0$, and different initial vibrational levels. The dominant contribution to the cross sections at ultralow energies comes from the $J = 0^+$ partial wave since the approach is not suppressed by the centrifugal barrier. From $\mathbf{J} = \mathbf{j} + \mathbf{l}$, it follows that l_i=0.

The elastic and total inelastic cross sections of the $J = 0$ partial wave have been calculated at more than 150 collision energies between 1 nK and 1 K for $v_i = 0$, 1, 2, and 3. The results are plotted in Figures 8.5, 8.7, 8.9, and 8.10. The energy dependence of elastic cross sections is a constant at low collision energies, consistent with the Wigner law for elastic collisions (7.16) with $l_{i,f} = 0$. The energy dependence of inelastic cross sections for $v_i = 1$, 2, and 3, is linear on the logarithmic scale with a slope of $-1/2$ $(l_i - 1/2)$, as predicted by the Wigner laws (7.17). In this regime the elastic and inelastic cross sections can be parametrized by a complex scattering length, see (7.51) and (7.52). The convergence of the scattering length is shown in the insets of the figures. The plotted quantities are the right-hand sides of equations (7.53).

If the molecule is initially in its lowest rovibrational state, Figure 8.5, only elastic scattering is possible at energies below the $v = 0, j = 2$ threshold at 2.3 K. The threshold behaviour described by Wigner laws is reached in the mK region of collision energies. At higher energies, the cross section oscillates, dropping to zero at 37 mK and 300 mK, and exhibits a resonance profile at around 750 mK.

Scattering from the $v_i = 0$, $j_i = 0$ state is a process with one open channel which can be characterized by a phase shift, similar to potential scattering. We extracted the phase δ_0 from the K matrix (1×1) element being $\tan(\delta_0)$, see (7.81), and plotted it in Figure 8.6. It is clear from this plot that the cross section in Figure 8.5 drops to zero when the phase shift δ_0 passes through a multiple of π $(-\pi, -2\pi)$. The profile at $\approx$ 750 mK is associated with a rise of phase by $\approx \pi$ against the background and is therefore a resonance. A sharp drop in the region of the resonance may be associated with the phase rising through the value of -2π. The profile of the energy dependence of cross sections when the phase is close to a multiple of π is $\sim \sin^2(\delta_0)$,

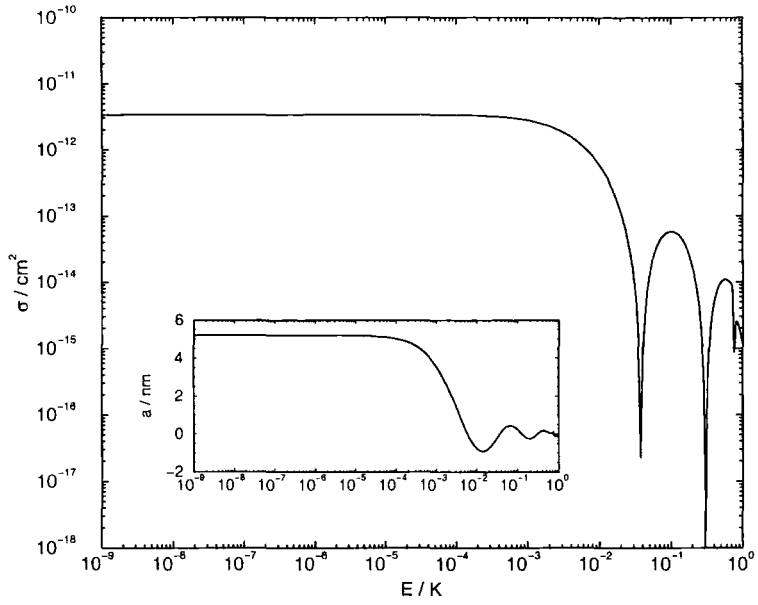

Figure 8.5: Energy dependence of elastic cross sections for $^7\mathrm{Li} + {}^7\mathrm{Li}_2(v_i = 0, j_i = 0)$. Convergence of scattering length shown in the inset.

as opposed to the lorentzian describing a resonant profile. The drop in cross sections is not expected to be measurable since higher partial waves will contribute at these energies. The position and the height of the centrifugal barrier for $l = 1$, as estimated from the isotropic dispersion and centrifugal potentials, $-C_6/R^6 + l(l+1)/2\mu R^2$, are $R \approx 94.3\ a_0$, which is the distance at which isotropic dispersion interaction dominates thus confirming our assumption, and $V_{\max} \approx 2.78$ mK. This means that above this energy higher partial waves will contribute significantly with the effect of washing out the features in the $J = 0$ cross sections.

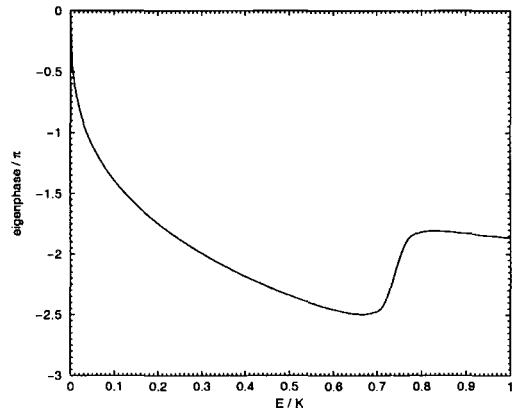

Figure 8.6: Energy dependence of eigenphase for $^7\mathrm{Li} + {}^7\mathrm{Li}_2(v_i = 0, j_i = 0)$.

The elastic cross sections for collisions involving the molecule in the $v_i = 1$, $j_i = 0$ state, in the same interval of collision energies, exhibit similar behaviour. The oscillations at the higher energy end in Figure 8.7 are analysed in terms of the individual eigenphases shown in Figure 8.8. There are nine open channels corresponding to even j levels from 0 to 14 of the $v = 0$ manifold and the elastic channel. The K matrix is diagonalized to obtain the tangents of the eigenphases on the diagonal (7.81). Each of the three minima in the elastic cross sections in Figure 8.7, at $\approx$ 13 mK, 175 mK, and 650 mK, can be associated with a zero of an eigenphase in Figure 8.8. Due to the coupling between channels, the features are not so pronounced and their positions are slightly displaced from the zeros of eigenphases. The eigenphase sum exhibits no sudden increase, but its first derivative oscillates indicating that there might be broad resonances lying under the background variations.

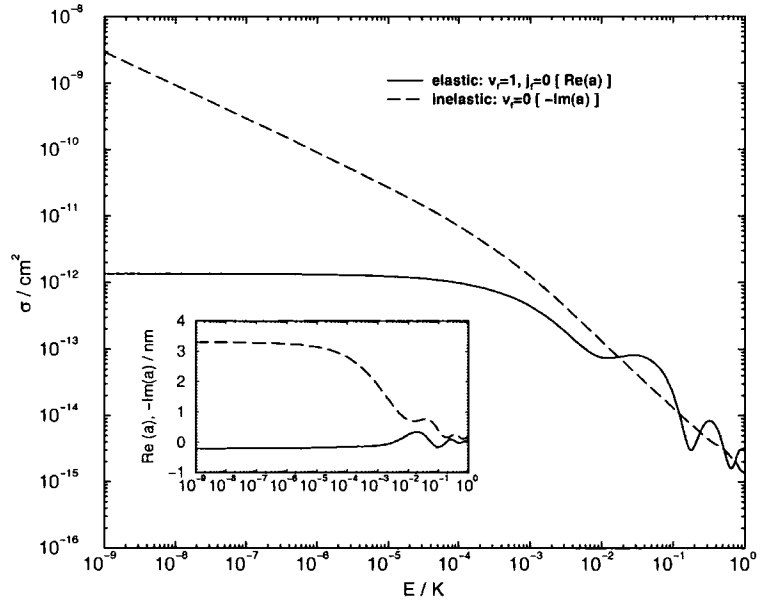

Figure 8.7: Energy dependence of elastic and inelastic cross sections for ^{7}Li+^{7}Li$_2$($v_i = 1, j_i = 0$). Convergence of complex scattering length shown in the inset.

The elastic cross sections for the initial rovibrational molecular states $v_i = 2, j_i = 0$ and $v_i = 3, j_i = 0$, shown in Figure 8.9 and 8.10, exhibit again similar oscillatory behaviour outside the Wigner regime. The eigenphase sum (not shown) remains entirely smooth, below 1 K, with no evidence of resonances.

The energy dependence of inelastic cross sections for all initial molecular vibrational levels studied, $v_i = 1$, 2, and 3, changes at mK collisional energies from the

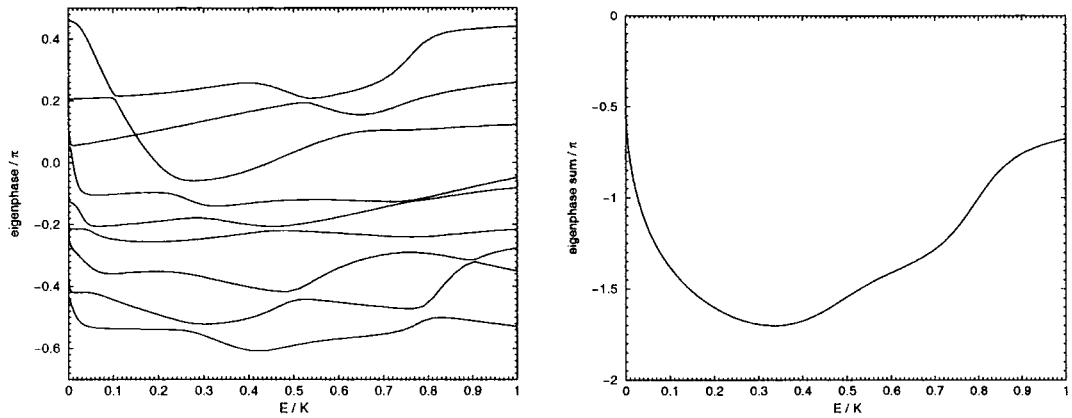

Figure 8.8: Energy dependence of eigenphases and eigenphase sum for ^{7}Li+^{7}Li$_2$($v_i = 1, j_i = 0$).

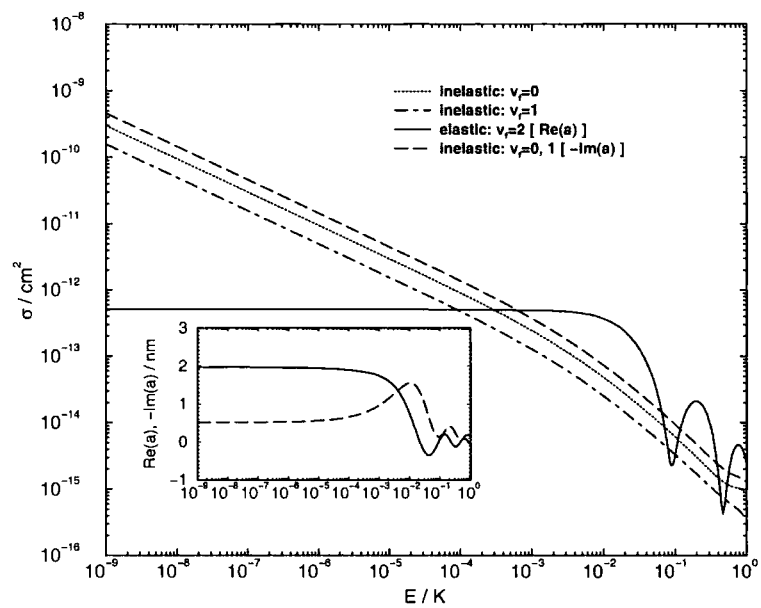

Figure 8.9: Energy dependence of elastic and inelastic cross sections for ^{7}Li+^{7}Li$_2$($v_i = 2, j_i = 0$).

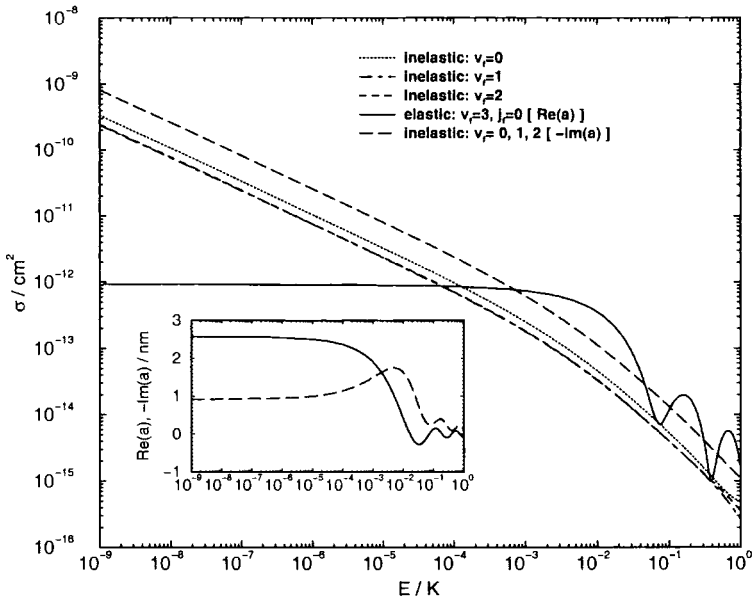

Figure 8.10: Energy dependence of elastic and inelastic cross sections for ^{7}Li + ^{7}Li$_2(v_i = 3, j_i = 0)$.

$-1/2$ power law, predicted by the Wigner law, to the -1 power law. The -1 power of the energy dependence comes from the kinematic factor in the expression for the cross section (6.75). The probability of inelastic transitions, $\sigma_{\rm inel}k^2/\pi$, and $\sigma_{\rm elas}k^2/\pi$ are shown in Figure 8.11 for $v_i = 1$ and 2. The probability increases with the collision energy according to the Wigner law until it saturates below unity, where the kinematic factor starts to dominate the energy dependence of inelastic cross sections. The elastic matrix element is less steady and it oscillates around the inelastic probability outside the Wigner regime, as is reflected in the cross sections.

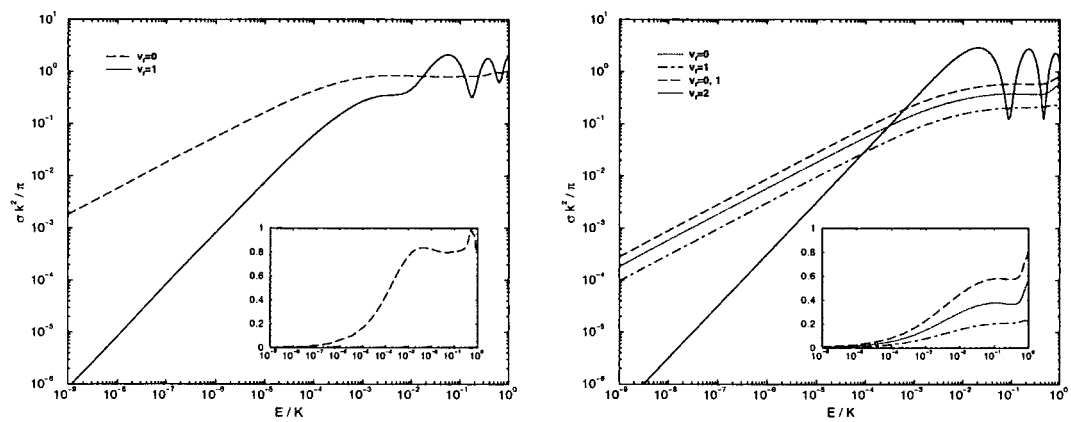

Figure 8.11: Energy dependence of elastic and the sum of inelastic matrix elements, $\sigma k^2/\pi$, for ^{7}Li + ^{7}Li$_2(v_i, j_i = 0)$ for $v_i = 1$ (left) and $v_i = 2$ (right).

There is no systematic dependence of the magnitude of cross sections on the initial vibrational level. The values of the elastic cross section at 1 nK are all within an order of magnitude and are $\approx 10^{-12}$ cm^2. The inelastic cross sections are all $\approx 10^{-9}$ cm^2 at 1 nK. The onset of threshold behaviour is at millikelvin temperatures for all initial states and the energy dependence of the cross sections is described by the Wigner laws (7.16, 7.17) at lower energies.

Vibrational distributions of the final molecular states $v_f < v_i$ are shown in Figure 8.9 and 8.10. The $v_f = 0$ state is the most probable outcome of the collision in each case. The partial cross sections for different final vibrational states do not change relative to each other over almost the entire range of collision energies studied here, although the individual cross sections vary over more than five orders of magnitude. This is also true for the ratios of the individual state-to-state cross sections. To demonstrate it, the product rotational distribution for $v_i = 1$ is plotted at 1 nK in Figure 8.12 and at ≈ 100 mK in Figure 8.13. The qualitative changes are small. The reason is that the energy dependence of inelastic cross sections in the studied range is dominated by the kinematic factor, $1/k^2$, and the energy normalisation resulting in the Wigner threshold laws. These factors influence all the partial cross sections equally.

Rotational distributions for $J = 0$, Figure 8.12, are irregular and oscillatory. Similar behaviour has been found earlier in the studies of $Na + Na_2$ collisions at ultracold temperatures [196], in the insertion reaction $C(^1D) + H_2 \rightarrow CH + H$ [199] for $J = 0$ at higher collision energies, and also in vibrational predissociation of Van der Waals complexes ($Ar-H_2$) [200]. A possible explanation is that the oscillatory behaviour arises from a rotational rainbow effect [201]. The energy released in the vibrationally inelastic process is partly converted to the translational motion and partly in the rotation of Li_2 molecule. Angular momentum transferred to the molecule is zero in the head-on collision and at T-shape geometries and large at $\theta = 45°$. In this model, the oscillations arise from the interference between the classical trajectories from either side of the maximum.

Elastic rate coefficients, $k = \sigma v$, vanish in the zero-energy limit, while inelastic rate coefficients tend to a constant, $\approx 10^{-10}$ cm^{3}s^{-1} for $v = 1 - 3$, see Appendix B. The ratio of inelastic and elastic rates at ultralow energies decreases with the collision energy, according to Wigner laws, until it reaches ≈ 1 in the millikelvin

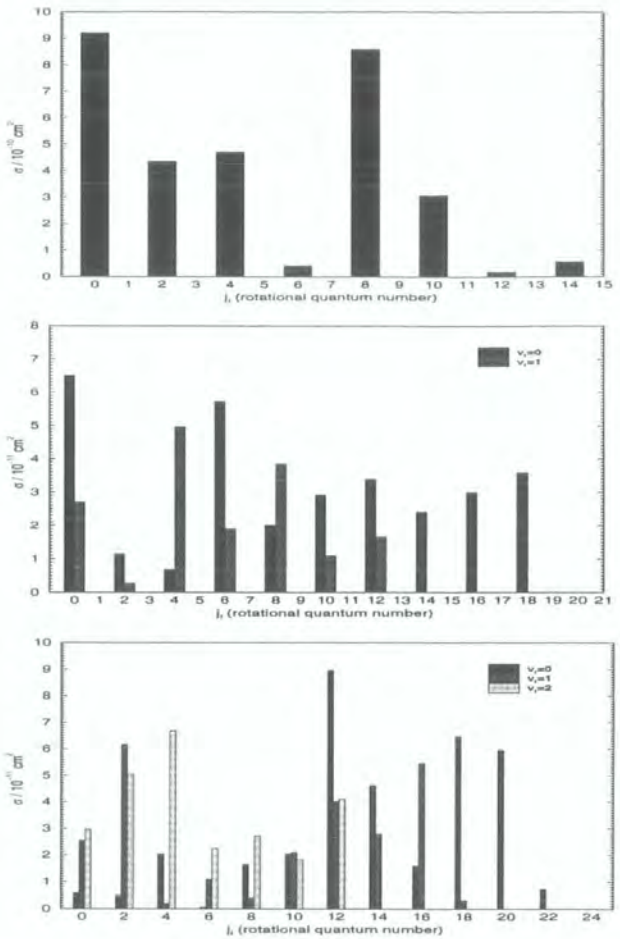

Figure 8.12: Final rotational distributions for $^7\mathrm{Li} + {}^7\mathrm{Li}_2(v_i, j_i = 0)$ at 0.928 nK for $v_i = 1$ (top), $v_i = 2$ (middle), and $v_i = 3$ (bottom).

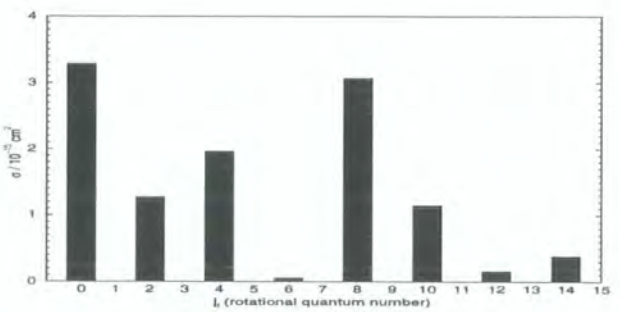

Figure 8.13: Final rotational distributions for $^7\mathrm{Li} + {}^7\mathrm{Li}_2(v_i = 1, j_i = 0)$ at 116 mK.

range. At higher collision energies, elastic and inelastic rates remain comparable.

Sympathetic and evaporative cooling of atoms and molecules depends on the ratio of elastic and inelastic rate coefficients which should preferably be large (> 100). Loss rates obtained in the experiments on ultracold bosonic molecules, cited in the introduction of the chapter, are consistent with the values obtained for bosonic lithium in this section, $\approx 10^{-10}$ cm^{3}s^{-1}. It must be emphasised that the reported rates in experiments are measured for high-lying rovibrational states on electronic doublet surfaces and in magnetic fields with samples confined in a trapping potential. In this view the agreement between the theoretical results of this chapter and experiments is satisfactory.

In comparison with the atom-exchange collision Na + Na_2 [196], elastic and inelastic cross sections at threshold, obtained here for lithium, differ by less than an order of magnitude. The dependence of cross sections on collision energy is qualitatively similar. The frequency of oscillations in the elastic cross section of sodium is higher, i.e. the phases evolve more rapidly, and threshold behaviour sets in at lower energies. This is a consequence of a lower de Broglie wavelength in sodium for a given collision energy due to the larger mass. Qualitative similarity of the results in the spin-polarized lithium and sodium systems suggests that an efficient cooling and trapping of atom-molecule mixtures is probably not possible even in other alkali systems. Formation rates in photoassociation experiments are currently $\approx 10^{-11}$ cm^{3}s^{-1}. Atomic and molecular clouds should quickly be separated after formation in order to prevent collisional losses.

In comparison with other ultracold processes, reviewed in the introduction of this chapter, the zero-energy limit of the inelastic rate coefficient for vibrationally excited molecules is high. There is no systematic dependence of the rate coefficients on the initial excitation of the molecule, unlike the above mentioned systems.

8.3.3 Vibrational relaxation cross sections and rate coefficients: $J > 0$

Accurate cross sections obtained from the coupled-channel equations in the total angular momentum basis must be converged with respect to the number of terms retained in the sum over J in (6.75) at a given collision energy. For the initial

molecular states having $j = 0$, the total angular momentum is $J = l$ and the parity is therefore $\epsilon_I = (-1)^J$.

We calculated the basis (eigenfunctions of the hypersurface hamiltonian (6.47)) for partial waves 0^+, 1^-, 2^+, ..., 10^+. The convergence parameters for $J > 0$ were kept same as for $J = 0$. For $\Omega > 0$ we included all the basis functions that converge in the same set of rovibrational states that were included for $\Omega = 0$, in the $J = 0$ calculations. This strategy repeatedly proved to yield converged results in the past [136, 138, 199, 202–204]. Since $j \geq \Omega$, the number of basis functions included for each Ω decreases. For Ω going from 0 to 10, it is 97, 89, 89, 81, 81, 73, 73, 65, 65, 57, and 57, respectively. Keeping $K_{\max}$ the same as for $J = 0$ for all sectors, the basis sets were calculated for both parities. The number of pseudohyperspherical harmonics for evaluating the basis functions varies in different sectors from 1220 ($\epsilon_I = -1$) to 2178 ($\epsilon_I = +1$) for $\Omega = 0$ and from 1045 to 1884 for $\Omega = 10$.

Coupled equations were propagated with the parameters set to the values already determined for $J = 0$. The number of channels for each partial wave J can easily be determined by summing the number of basis function for all $\Omega \leq J$. There are 827 channels for $J = 10$.

In order to examine the convergence of cross sections with respect to J, we show the elastic matrix elements and total inelastic probabilities, defined as $\sigma k^2/\pi$, as a function of J for several collision energies, and the initial dimer states $v_i = 1$ and 3, in Figure 8.14 and 8.15. The convergence does not depend significantly on the initial vibrational level. It is slower for elastic matrix elements compared to the total inelastic probabilities for higher collisional energies. At around 100 mK and below situation is reversed. The elastic cross sections decay faster than inelastic for $J \leq 4$ as the collision energy is lowered in the region where threshold laws are valid. The $J = 10$ partial wave contributes with 2.35% and 2.88% to the total elastic cross section at the collision energy of 580 mK for $v_i = 1$ and $v_i = 3$, respectively. The contribution of the $J = 10$ partial wave to the total inelastic cross section at 580 mK is substantially smaller, 0.0655% and 0.0558% for $v_i = 1$ and $v_i = 3$, respectively. This proves that the partial wave expansion is converged with respect to J for collision energies below 580 mK. The cut-off in J of the partial wave expansion for a given energy can easily be estimated from Figure 8.14 and 8.15.

Converged elastic and total inelastic cross sections for collisions involving a molecule

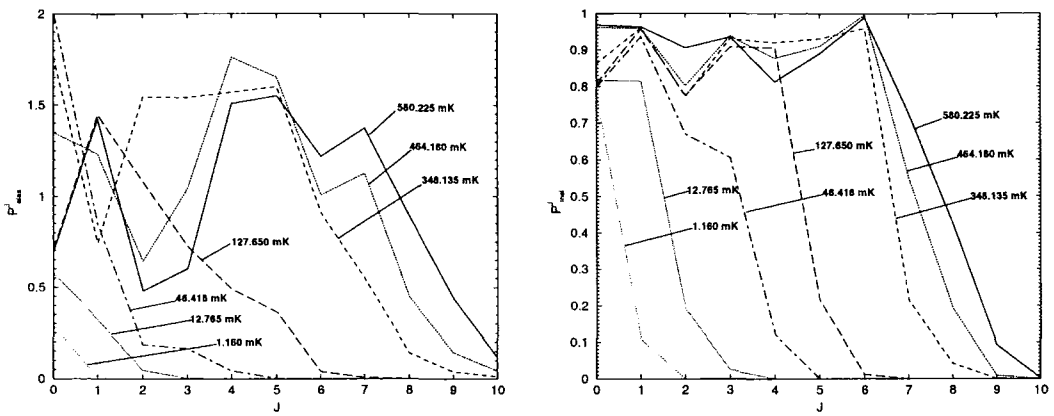

Figure 8.14: Elastic (left) and the sum of inelastic (right) matrix elements as a function of total angular momentum J for $^7\mathrm{Li} + {}^7\mathrm{Li}_2(v = 1, j = 0)$.

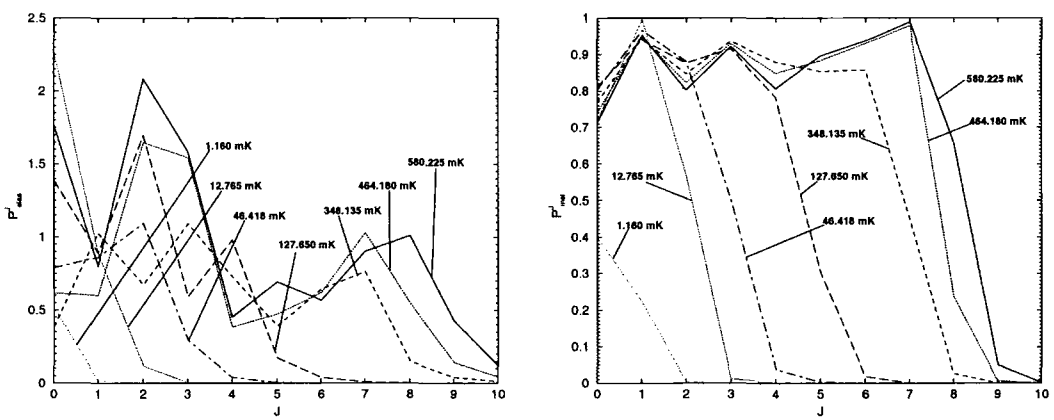

Figure 8.15: Elastic (left) and the sum of inelastic (right) matrix elements as a function of total angular momentum J for $^7\mathrm{Li} + {}^7\mathrm{Li}_2(v = 3, j = 0)$.

that is initially in the $v = 1, j = 0$ state are shown as a function of collision energy in the interval between 10 μK and 580 mK, in Figures 8.16 and 8.17. Contributions of all partial waves have been plotted separately. We can test now the range of collision energies for which the $J = 0$ cross sections give converged results. Contribution of other partial waves, but $J = 0$, make up 0.026% and 4.3% of the elastic cross section and 2% and 26.5% of the total inelastic cross section, at collision energies of 0.1 mK and 1 mK, respectively. This analysis indicates the magnitude of inaccuracy in the $J = 0$ cross sections, discussed in the last subsection.

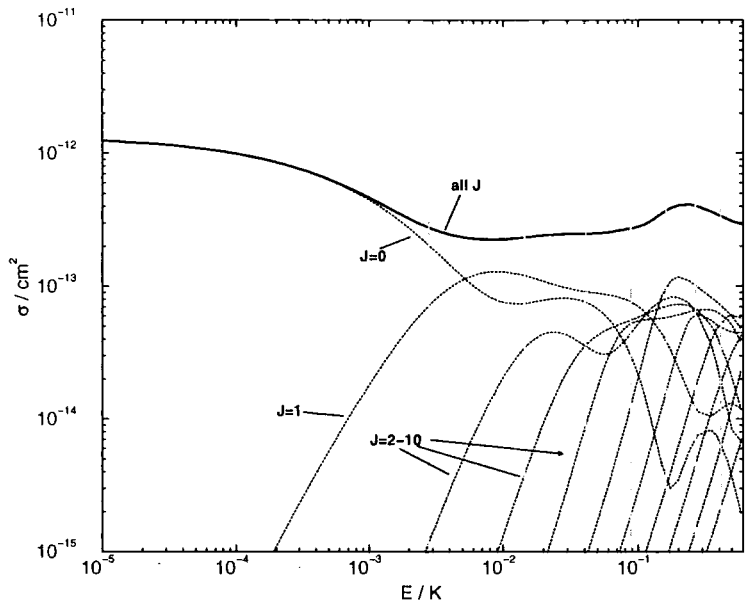

Figure 8.16: Energy dependence of elastic cross sections for $^7\mathrm{Li}+^7\mathrm{Li}_2(v_i = 1, j_i = 0)$: partial waves $J = 0 - 10$ and total.

Elastic cross sections for $J \geq 0$ show a linear rise in the dependence on collision energy on the log-log scale until a maximum is reached. When energies are further increased, they generally decrease in the oscillatory fashion, as has already been seen in the $J = 0$ calculations. The slope of the linear rise can be understood in terms of the Wigner laws (7.16). For $J = 0$ and 1, it is $2l$, where l is the orbital angular momentum, and $l = J$ for initially rotationless states. For $J \geq 2$ the slope should be 3, as was discussed in the previous chapter. Our calculations do follow the predictions for all J, except $J = 2$ and 3 have slopes between 2 and 3, but are bending towards 3 as the energy is being lowered.

Total inelastic cross section displays even simpler behaviour than the one seen for

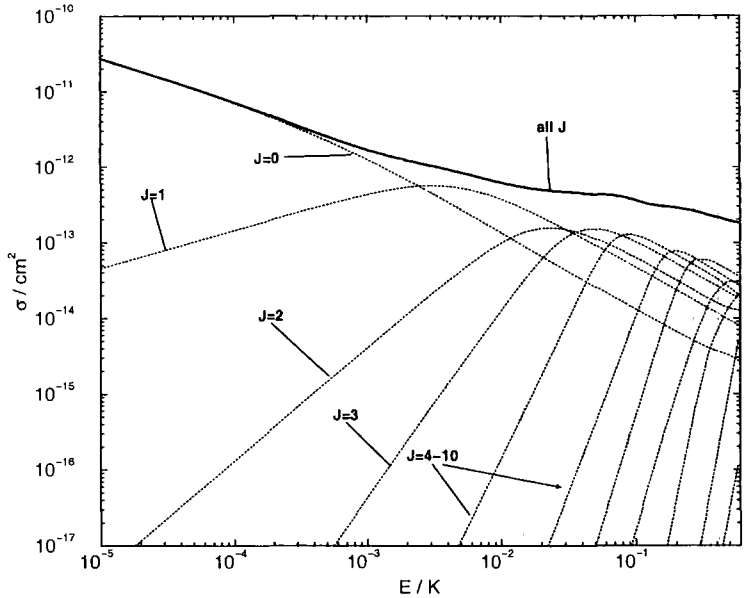

Figure 8.17: Energy dependence of inelastic cross sections for $^7\mathrm{Li} + {}^7\mathrm{Li}_2(v_i = 1, j_i = 0)$: partial waves $J = 0 - 10$ and total.

the elastic cross sections. The linear rise on the log-log scale with the slope of $l - 1/2$ ($l = J$), as the Wigner laws predict (7.17), until a maximum is reached, followed by a linear decrease (on the log-log scale) with the slope -1. It can be seen on the graphs of the inelastic probabilities, Figure 8.14 and 8.15, that the probabilities as a function of collision energy rise and then saturate attaining values close to unity, for all partial waves. The slope is then a result of the kinematic factor $1/k^2$ in the expression for the cross section (6.75). This was already discussed for the $J = 0$ results.

The cross sections for partial waves $J > 0$ at the energy at which they assume their maximum value contribute significantly to the overall cross sections. The positions of maxima can be associated with the heights of the barriers arising from the centrifugal potential in each partial wave. The positions and heights of the barriers can be estimated by maximizing the sum of centrifugal and the leading term of the dispersion potential, $-C_n/R^n + l(l+1)/2\mu R^2$. The estimates are then given by

$$V_{\max} = \frac{[\hbar^2 l(l+1)]^{\frac{n}{n-2}}}{\mu^{\frac{n}{n-2}}(nC_n)^{\frac{2}{n-2}}}\left(\frac{1}{2} - \frac{1}{n}\right), \tag{8.8}$$

$$R_{\max} = \left(\frac{nC_n\mu}{\hbar^2 l(l+1)}\right)^{\frac{1}{n-2}}. \tag{8.9}$$

Taking $n = 6$, $C_6 = 3085.54\ E_h a_0^6$, and $\mu = 2/3 m_{\mathrm{Li}}$, we obtain results in Table 8.4.

Positions of the barrier maxima are in the range where interactions are dominated by dispersion forces, thus confirming the validity of the assumption. Barrier heights are drawn as vertical lines in Figure 8.16 and 8.17 and are in accord with the positions of maxima in cross sections for $J \geq 0$. Threshold laws in each partial wave $J > 0$ set in at the collision energies just below the corresponding centrifugal barriers.

l	$V_{\max}/\mathrm{K}$	$R_{\max}/a_0$
1	$2.78 \cdot 10^{-3}$	94.25
2	$1.44 \cdot 10^{-2}$	71.62
3	$4.08 \cdot 10^{-2}$	60.22
4	$8.79 \cdot 10^{-2}$	53.00
5	$1.61 \cdot 10^{-1}$	47.89
6	$2.67 \cdot 10^{-1}$	44.02
7	$4.11 \cdot 10^{-1}$	40.97

Table 8.4: Estimates of the positions $R_{\max}$ and heights $V_{\max}$ of centrifugal barriers for the $^7\mathrm{Li} + {}^7\mathrm{Li}_2$ collision.

High total inelastic probabilities for all partial waves at energies above the barrier heights suggest applicability of the Langevin model, described in Chapter 7. An assumption of the Langevin model is that all the collisions at energies above the barrier result in a reaction, i.e. inelasticity as we have considered it here. With $n = 6$, equation (7.87) reads

$$\sigma_{\mathrm{inel}}(E) = \frac{3\pi}{2^{2/3}} \left(\frac{C_6}{E}\right)^{1/3}. \tag{8.10}$$

Total inelastic cross sections for $^7\mathrm{Li} + {}^7\mathrm{Li}_2(v_i = 1, j_i = 0)$ are compared to the predictions by the Langevin model for this reaction, with the atom-diatom C_6 taken same as above, and shown in Figure 8.18. The agreement is excellent above 30 mK. At this energy over 98% of the fully converged inelastic cross section is accounted for by partial waves $J = 0 - 3$ and 99.99% with the further inclusion of the $J = 4$ partial wave. This means that only three partial waves are needed for an agreement with a classical model. It is worth emphasising that the Langevin prediction is not dependent on the reduced mass of the system and depends solely on the isotropic long-range interactions of the collision partners.

To test that the agreement between our results and the model is not fortuitous, we have performed the full scattering calculations starting from the $v_i = 1, j_i = 0$

state of the dimer with another three potentials. Potential ACVTZ is calculated and constructed in the exactly same manner as the potential we have used so far (5Zuncp), but with the *ab-initio* energies calculated using the aug-cc-pCVTZ basis set, see Chapter 3. This basis set is substantially smaller and less accurate. Long range forms of both potentials, 5Zuncp and ACVTZ, are identical. We have also employed the potential of Colavecchia et al. [56] (COLA) and the pairwise-additive potential. Pairwise-additive parts of all potentials are identical. The energy dependence of elastic and total inelastic cross sections, with all partial wave contributions, for the three potentials are plotted in Figure 8.20. They are compared with the predictions of the Langevin model, using the appropriate C_6 coefficients, in Figure 8.18 and 8.19.

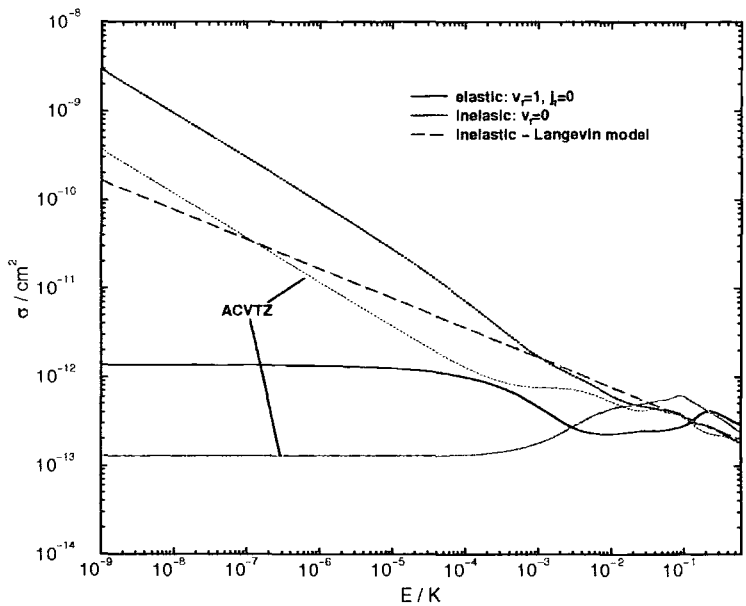

Figure 8.18: Elastic and total inelastic cross sections for $^7\mathrm{Li} + {}^7\mathrm{Li}_2(v_i = 1, j_i = 0)$ on the 5Zuncp and ACVTZ potentials (see text for description) and the inelastic cross sections in the Langevin model.

The agreement between the total inelastic cross sections calculated using the ACVTZ potential and the predictions by the Langevin model is again excellent above 30 mK. The agreement of the cross sections obtained by the COLA and pairwise-additive potentials with the Langevin model is poorer. The COLA results do seem to follow the $E^{-1/3}$ law above 5 mK, but the Langevin model overestimates the cross sections by $\approx 30\%$. Results obtained using the additive potential disagree more substantially with the model. It is possible that the agreement would be better at slightly higher

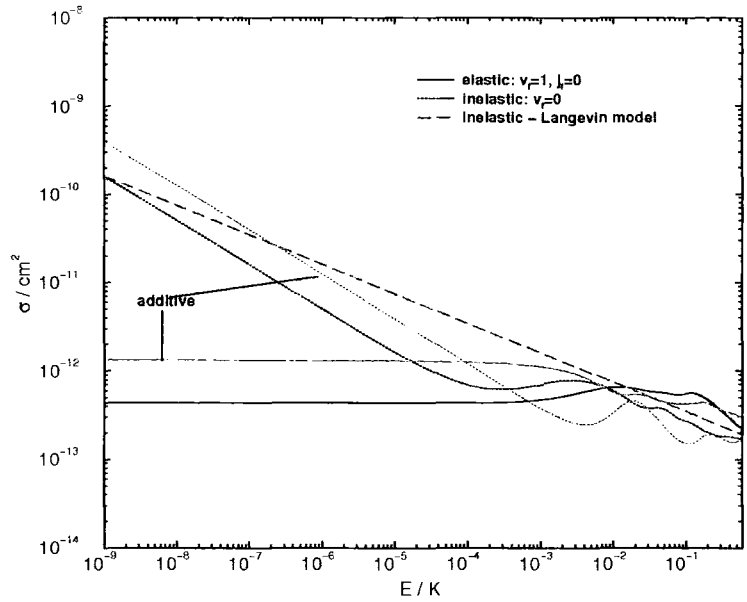

Figure 8.19: Elastic and total inelastic cross sections for $^7\mathrm{Li} + {}^7\mathrm{Li}_2(v_i = 1, j_i = 0)$ on the COLA and pairwise-additive potentials (see text for description) and the inelastic cross sections in the Langevin model.

energies than those converged in this study. The additive potential is shallower and differs substantially from the other potentials. Although the cross sections obtained in all four ways agree, within a factor of ≈ 1.5 above 10 mK, the differences in the ultracold limit can be larger than a factor of 10. The sensitivity of the cross sections in the zero-energy limit is addressed in more detail in Chapter 9.

The ratio of elastic and inelastic cross sections for $J = 0$ was discussed above in relation to the cooling dynamics of atom-molecule mixtures. Calculations predict that the elastic cross sections become larger than the inelastic outside the Wigner regime, for all potentials considered. This happens above 129 mK for 5Zuncp, 14.8 mK for ACVTZ, and 8 mK for COLA potential. The ratio $\sigma_{\mathrm{elas}}/\sigma_{\mathrm{inel}}$ can be as big as ≈ 1.6 for 5Zuncp and slightly over 2 for other potentials. When the inelastic probability is close to unity, which is an assumption in the Langevin model, the elastic probability must be close to zero. This means that the elastic cross sections will never be drastically different than the inelastic, where the Langevin model is valid.

Converged elastic and vibrationally resolved inelastic cross sections for the dimer that is initially in the $v_i = 2, j_i = 0$ state, with all partial wave contributions, are

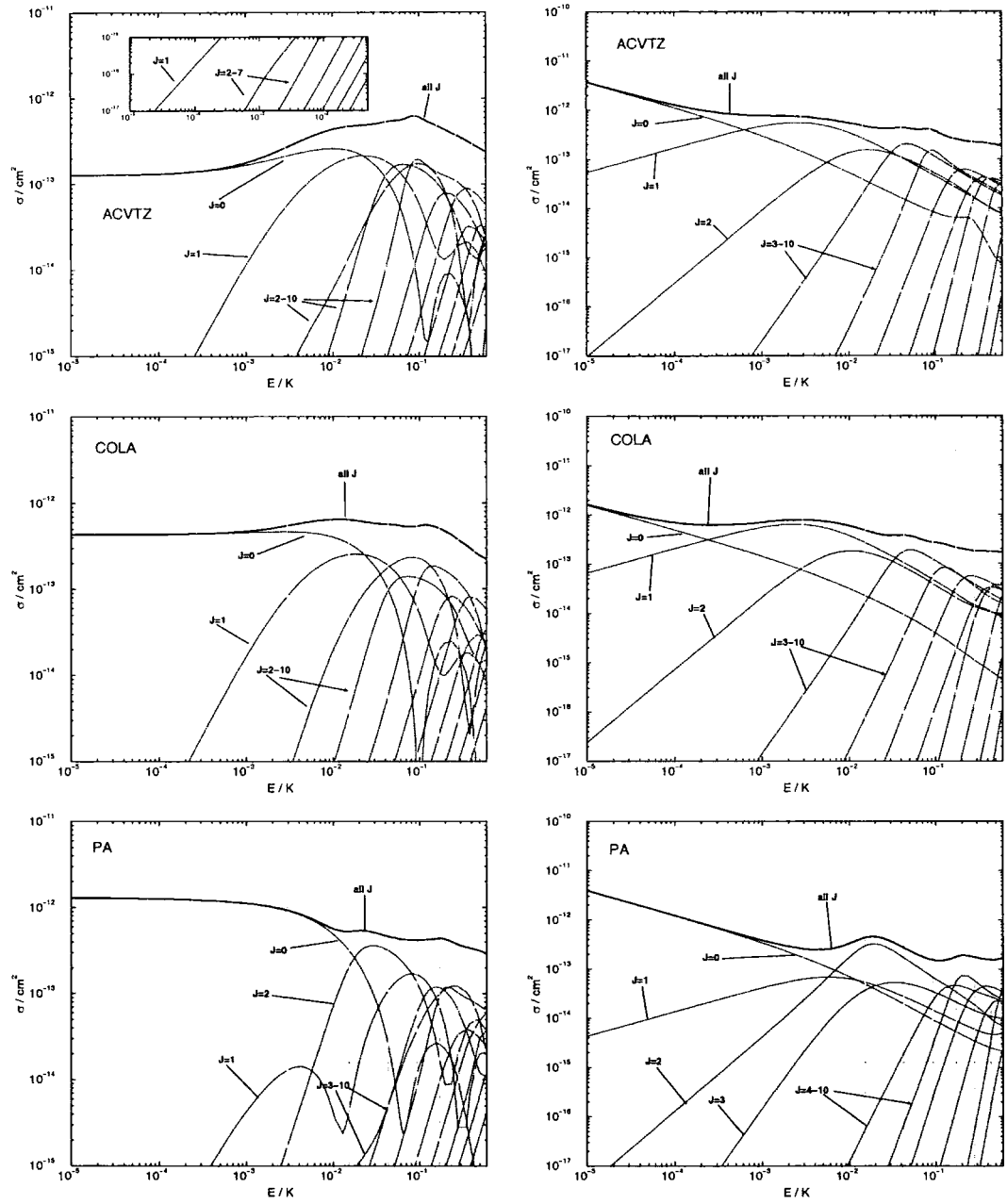

Figure 8.20: Energy dependence of elastic (left) and inelastic (right) cross sections for $^7\mathrm{Li} + {}^7\mathrm{Li}_2(v_i = 1, j_i = 0)$ on the ACVTZ (top row), COLA (middle row), and pairwise-additive (PA) potentials (bottom row): partial waves $J = 0 - 10$ and total.

plotted in Figure 8.21. Elastic and inelastic cross sections for the $v_i = 2, j_i = 0$ and $v_i = 3, j_i = 0$ are shown together with the Langevin predictions in Figure 8.22. The agreement with the model is excellent from 1 mK and 5 mK onwards for the $v_i = 2$ and $v_i = 3$ initial dimer states, respectively. The Langevin model relies on the high inelasticity which is also a valid assumption for collisions with molecules in the vibrationally excited states. Elastic cross sections for the $v_i = 2, j_i = 0$ are larger than the total inelastic ones above $\approx$ 15 mK by as much as factor of 2. For $v_i = 3, j_i = 0$, the elastic cross sections are never significantly larger than the total inelastic, but are comparable above $\approx$ 10 mK.

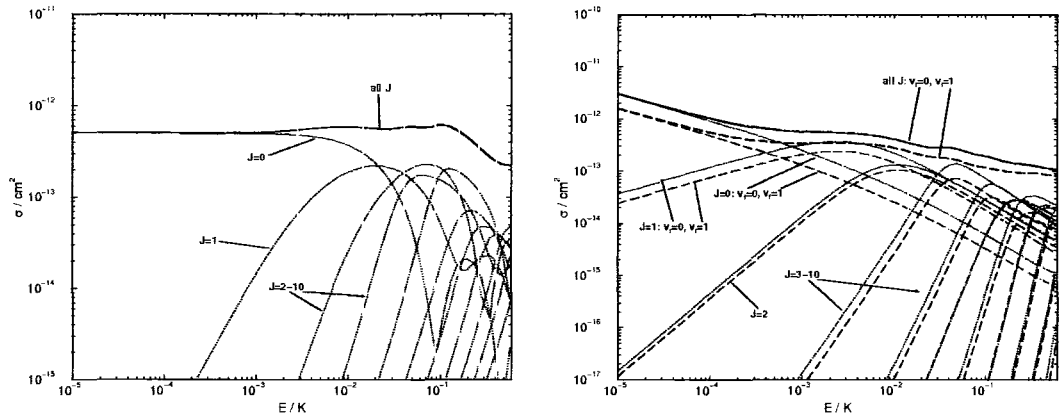

Figure 8.21: Energy dependence of elastic (left) and vibrationally resolved inelastic (right) cross sections for $^7\mathrm{Li} + {}^7\mathrm{Li}_2(v_i = 2, j_i = 0)$: partial waves $J = 0 - 10$ and total.

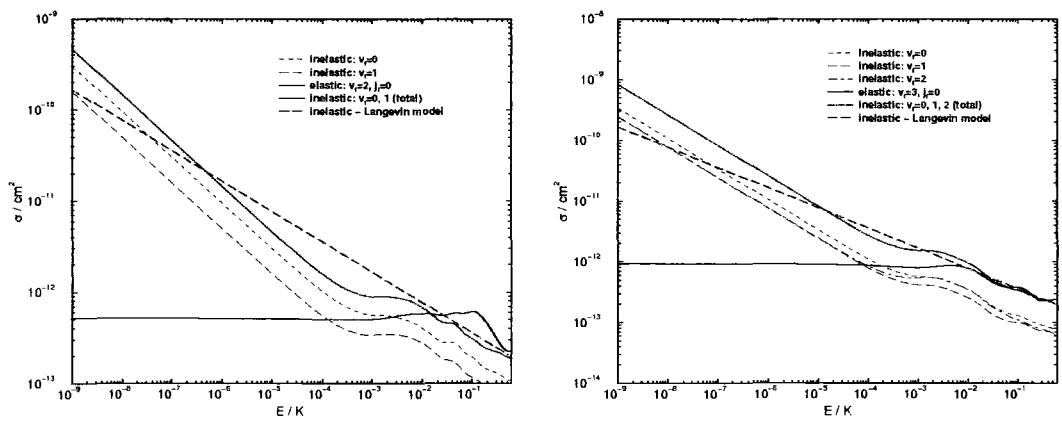

Figure 8.22: Elastic and inelastic (vibrationally resolved and total) cross sections for $^7\mathrm{Li} + {}^7\mathrm{Li}_2(v_i, j_i = 0)$, for $v_i = 2$ (left) and 3 (right), and the inelastic cross sections in the Langevin model.

Discrepancies between the Langevin model and the fully converged quantum calculations come from the fact that the probability of inelasticity is not constant as a function of collision energy above the centrifugal barrier and it is not exactly zero below. The high inelasticity above the barrier is provided by the large interstate couplings at short range. The decay of inelastic probabilities for $J > 0$ below the barrier, is fast only for higher partial waves. Resonances and other quantum effects, such as tunneling and quantum reflection, may be important at particular collision energies and could result in the deviations from the model.

8.3.4 Comparison with some insertion reactions

The reaction $^7Li + {}^7Li_2$ has no barrier for either linear or perpendicular approach. The potential energy surface involves a deep well and indicates a possible insertion reaction mechanism proceeding via complex formation. It is therefore interesting to compare the scattering results obtained above with some other insertion reactions that have been studied earlier at ordinary temperatures ($\sim$ 100 meV).

Using the same coupled channel method in hyperspherical coordinates, the following insertion reactions have been studied previously: $N(^2D)+H_2 \rightarrow NH+H$ [202], $O(^1D)+H_2 \rightarrow OH+H$ [203, 204], and $S(^2D)+H_2 \rightarrow SH+H$ [205]. These reactions are characterized by the high inelastic and reactive probabilities. The lowest vibrational level is the most populated and integral cross sections decrease with increasing v_f. The rotational product distributions are peaked at a high rotational quantum number for each v_f. The differential cross sections display a forward-backward symmetry. The above observations can be explained by formation of a collision complex whose decay is statistical [164]. This means that the probability of any decay mode of the complex is independent of the mode of its formation. It has recently been shown that the exact quantum results cited above are in excellent agreement with the results based on a quantum statistical theory [7]. If we assume that all product states are equally probable, the distribution of final states in vibrational and rotational levels would be proportional to the density of available states, which is proportional to the rotational degeneracy and density of translational states. Therefore, the density of quantum states for the total energy E in the system is

$$\rho(v_f, j_f) \sim (2j_f + 1)\sqrt{E - E_{v_f j_f}}. \tag{8.11}$$

The normalized statistical probability distribution for $^7Li + ^7Li_2$ at ultracold energies is shown in Figure 8.23.

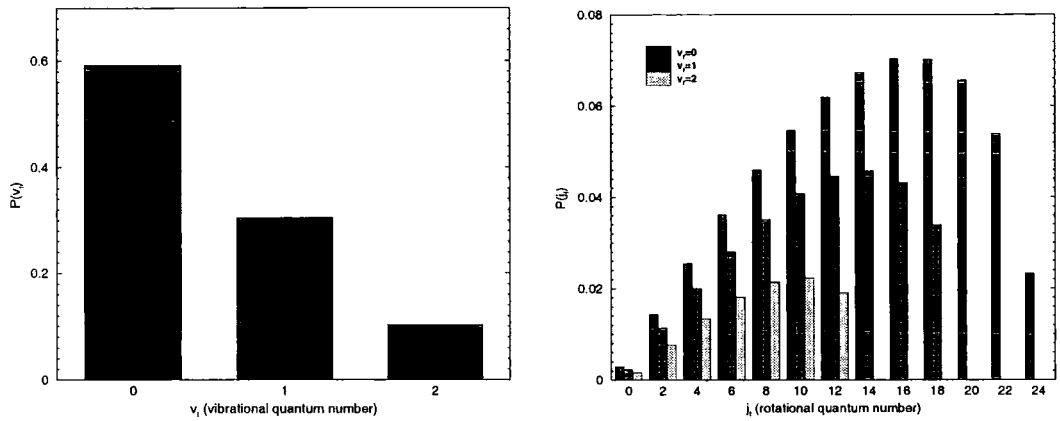

Figure 8.23: Vibrational (left) and rotational (right) prior distributions for $^7Li + ^7Li_2(v_i = 3, j_i = 0)$, at ultralow energies.

We have already seen that the rotational distributions at ultralow energies in Figure 8.12 sharply contrast with the statistical distribution in Figure 8.23. The rotational distributions and differential cross sections at 116 mK and 580 mK are shown in Figure 8.24 and 8.25, respectively, for $v_i = 1$, 2, and 3. Rotational distributions show that lower j values are more probable, unlike statistical predictions. The differential cross sections are forward-backward peaked with a preference for the forward direction. The ratio of the cross sections for forward and backward scattering is between 1 and 2. Sideways scattering is less probable than the scattering at the poles by a factor ranging between 2.3 and 3.8. Strong asymmetry is evident for collisions involving dimers in the $v_i = 1$, $j_i = 0$ state at 580 mK, where backward and sideways scattering are two times smaller than the forward peak. The symmetry in forward-backward scattering is usually explained in terms of the formation of a complex whose lifetime is determined by the width of the resonance at the particular energy. There is usually a sea of such resonances for reactions proceeding over a deep well in the potential. Angular distribution of products is governed by a particular partial wave J involved in the resonance. Cross terms involving different J, which break the symmetry in the direct reactions, in equation (6.74) vanish due to phase cancellations [7]. Only a few partial waves make a significant contribution at ultralow energies so that the statistical averaging over J does not work well. At 116 mK, partial waves $J = 3$ and 4 predominantly (2/3) contribute to the cross sections

for $v_i = 1$, with some contribution (1/3) also coming from $J = 1$ and 2. At 580 mK, the number of contributing partial waves is larger. The asymmetry in differential cross sections in the collision involving the dimer in the $v_i = 1$, $j_i = 0$ state at 580 mK is probably an effect of insufficient averaging of the J terms in (6.74). It should also be emphasised that all the insertion reactions cited above have a barrier for linear approach. In the case of the $Li + Li_2$ reaction, the insertion and abstraction mechanisms are both energetically possible and the two mechanisms may interfere.

We believe that at higher collision energies, the reaction mechanism will give evidence of complex formation and that it is likely that the vibrational and rotational distributions and differential cross sections assume features predicted by the statistical models.

8.3.5 Collisions involving rotationally excited states

It was found that collisions between atoms and rotationally excited diatoms can cause unusually efficient and specific energy transfer when the collision time is longer than the rotational period [206]. The general rule for this quasiresonant energy transfer is that the single transition dominates which approximately conserves the internal energy and satisfies $n_v \Delta v + n_j \Delta j = 0$, where n_v and n_j are small integers. It was explained in terms of the adiabatic invariance theory [207] with the assumption that the coupling between the degrees of freedom is not strong. This phenomenon was also shown to be present at ultralow collision energies [179, 180, 182, 184, 185, 195]. The inelastic rates for hydrogen molecules in the specific highly excited rotational states are dramatically suppressed for the energies below threshold of a quasiresonant transition [180]. It was predicted that helium may be used as a buffer gas to cool such rotationally excited molecules and that molecules can additionally be cooled by the evaporative cooling. Prospects for cooling oxygen molecules in the high rotational levels have also been investigated [195] and it was found that while the inelastic cross sections decrease with the initial rotational quantum number, pure rotational inelasticity is very efficient at all values of j [184]. High inelastic rate coefficients have also been found in other systems at ultralow collision energies [181, 190] and pure rotational transitions found to be more efficient than the rovibrational transitions.

It was suggested that quasiresonant energy transfer should be general feature

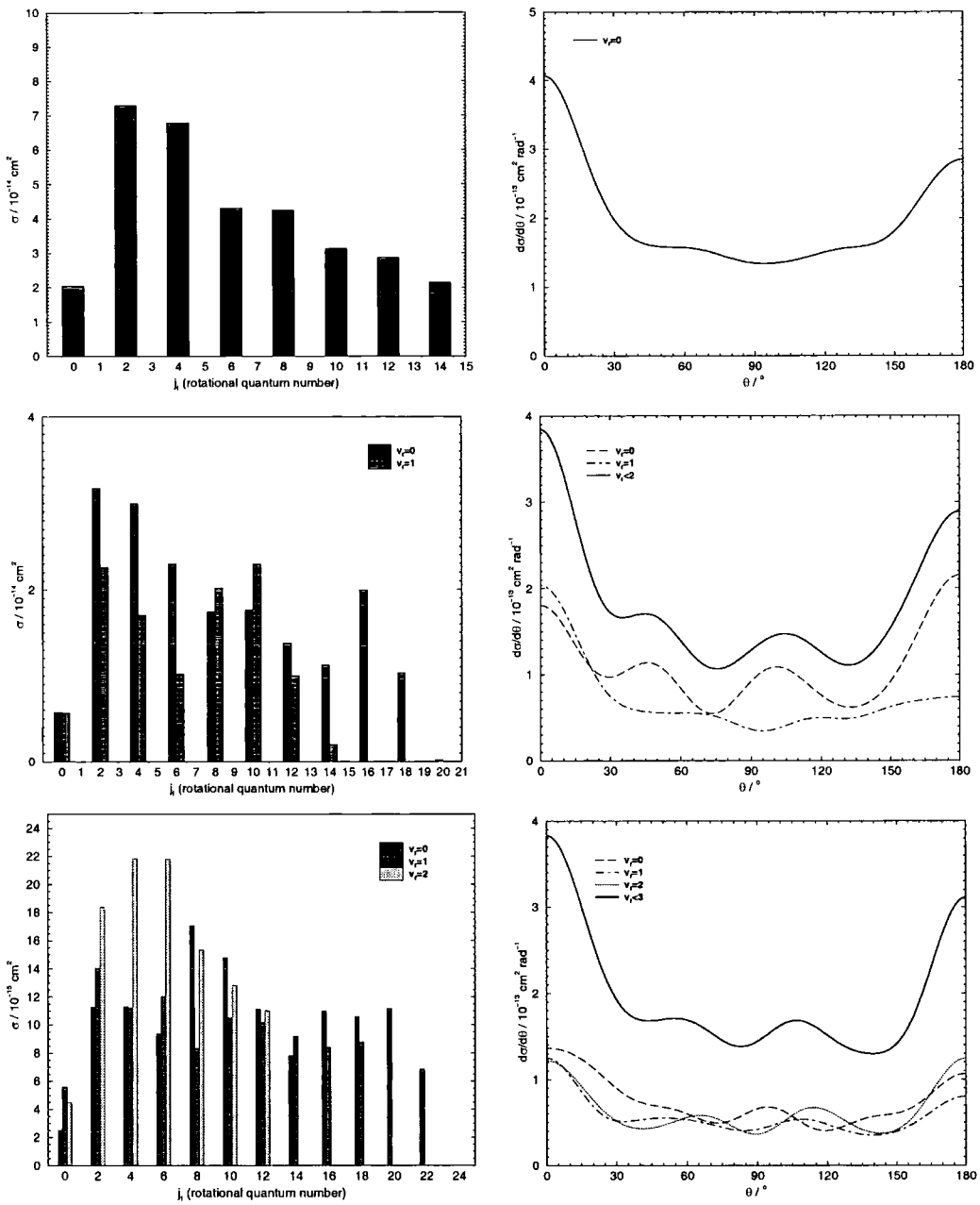

Figure 8.24: Final rotational distributions (left panels) and differential cross sections (right panels) for $^7\mathrm{Li} + {}^7\mathrm{Li}_2(v_i, j_i = 0)$ and $v_i = 1$ (top), 2 (middle), and 3 (bottom) at collision energy of 116 mK. Differential cross sections are integrated through the azimuthal angle and summed over the final states in each vibrational manifold and overall (solid line).

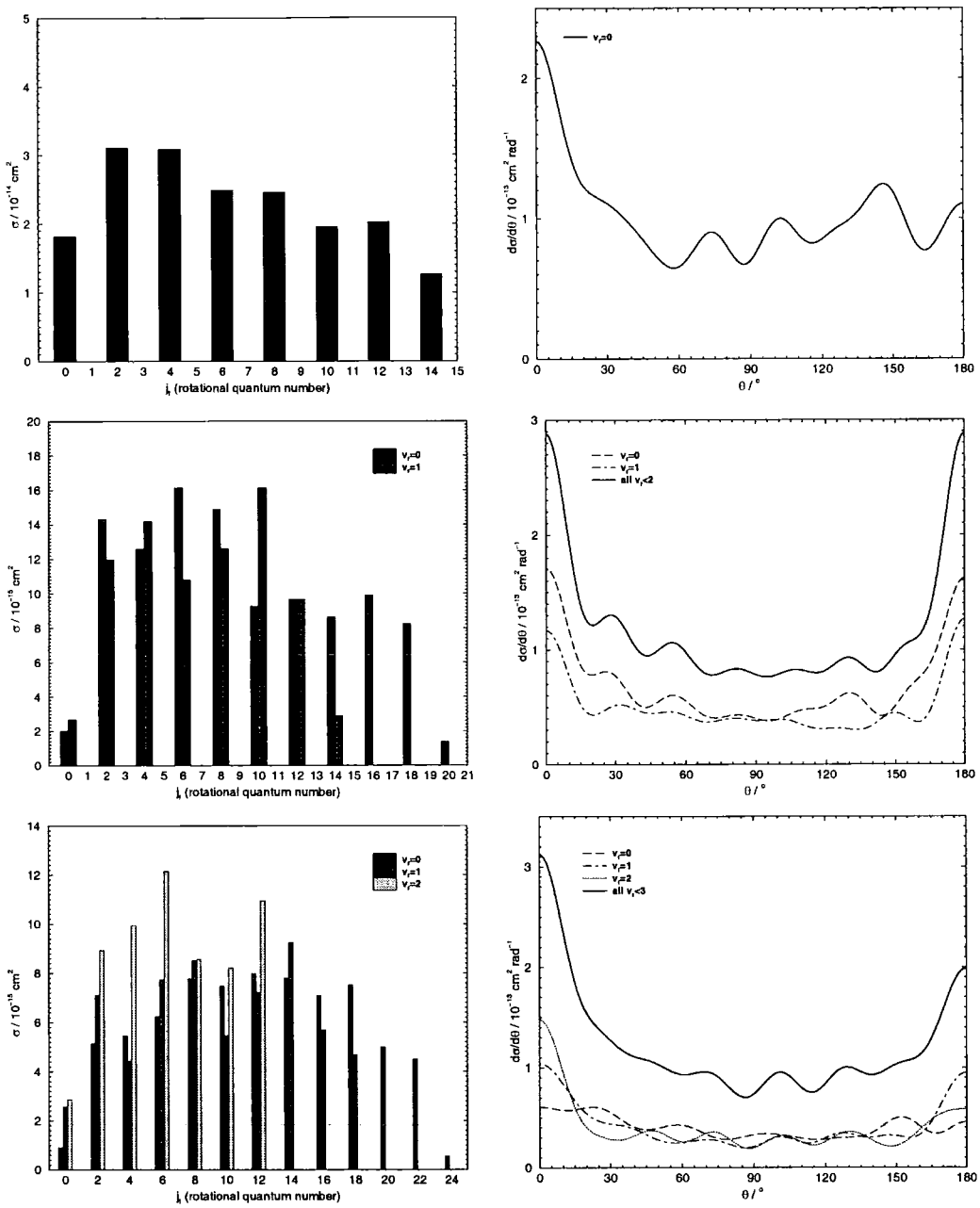

Figure 8.25: Final rotational distributions (left panels) and differential cross sections (right panels) for $^7\mathrm{Li} + {}^7\mathrm{Li}_2(v_i, j_i = 0)$ and $v_i = 1$ (top), 2 (middle), and 3 (bottom) at collision energy of 580 mK. Differential cross sections are integrated through the azimuthal angle and summed over the final states in each vibrational manifold and overall (solid line).

independent of the system [179], although it was predicted that quasiresonant rotational levels for lithium dimer in the electronic singlet state are above the dissociation limit [195]. We report here the calculations of the elastic and inelastic cross sections for atom-diatom collisions on the electronic quartet surface of lithium involving rotationally excited dimers. Only the dominant partial wave, that contains the $l_i = 0$ contribution, has been calculated in each case. For a molecule that is initially in the rotational level j_i, it was sufficient to use $J = j_i$ and the parity block $(-1)^{j_i}$ to estimate the cross sections in the Wigner regime.

We first investigate collisions with the dimer in the $v_i = 0$, $j_i = 2$. The energy dependence of elastic and inelastic cross sections is shown in Figure 8.26. There are four open channels in the partial wave $J = 2^+$: three elastic channels with $l = 0$, 2, and 4, and one inelastic channel $j = 0$, $l = 2$. The eigenphases and eigenphase sum are shown in Figure 8.27. The minimum in the elastic cross sections at $\approx$ 10 mK corresponds to a zero of an eigenphase and the peak at $\approx$ 90 mK is a resonance. The region between 0.6 K and 1.2 K of low inelastic cross sections is probably a combined effect of two overlapping broad resonances and an eigenphase being small and having two zeros in this energy interval. The ratio of inelastic and elastic cross sections for $v_i = 0$, $j_i = 2$ is smaller by an order of magnitude in comparison with collisions involving other rotationally excited molecules, see Table 8.5. This is probably a consequence of smaller amount of available phase space for inelasticity. The ultracold limit of the elastic cross section is high in this case. As will be discussed in the next chapter, cross sections are very sensitive to variations in the potential and variations in magnitude are larger for collisions involving fewer inelastic channels.

Product rotational distributions for collisions with the dimer in $v_i = 0$ and $j_i = 4$, 6, 8, and 10 are shown in Figure 8.28. We have calculated the product distributions for a range of initial states and found that the oscillatory structure present in the rovibrational transitions for the $J = 0$ partial wave persists (see the text pertaining to Figure 8.12). When the molecule is initially in a higher rotational level j_i, the higher j_f levels of the products tend to be more populated, like in the statistical models. A typical product-state distribution for a rovibrationally excited state is shown in Figure 8.29.

Elastic and total inelastic cross sections and rate coefficients for the collision

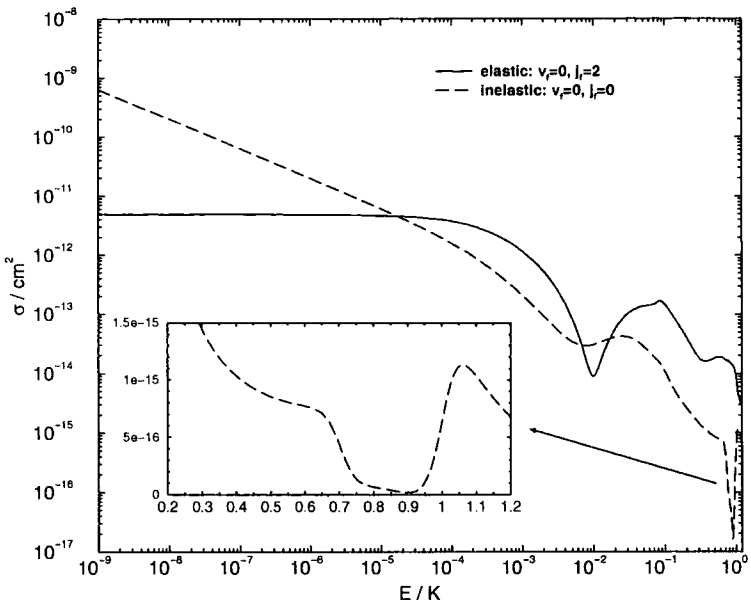

Figure 8.26: Energy dependence of elastic and inelastic cross sections for ^{7}Li + ^{7}Li$_2(v_i = 0, j_i = 2)$.

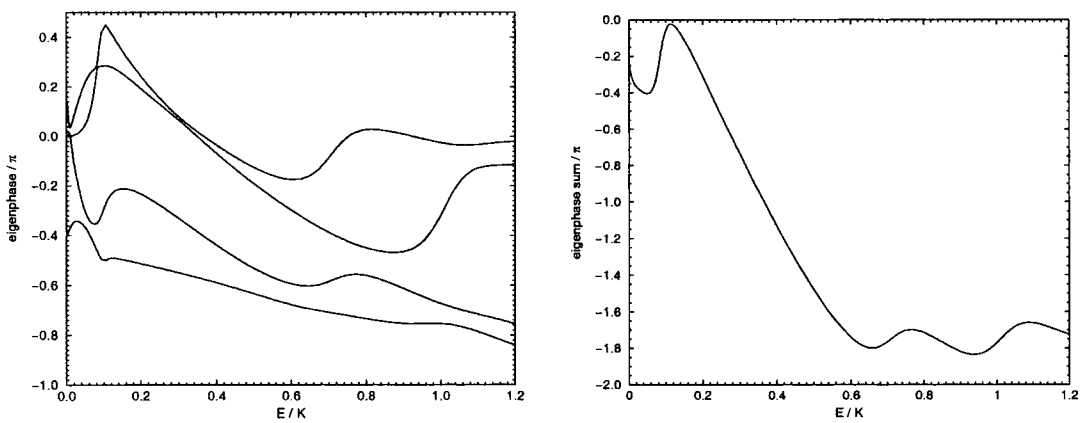

Figure 8.27: Energy dependence of eigenphases and eigenphase sum for ^{7}Li+^{7}Li$_2(v_i = 0, j_i = 2)$.

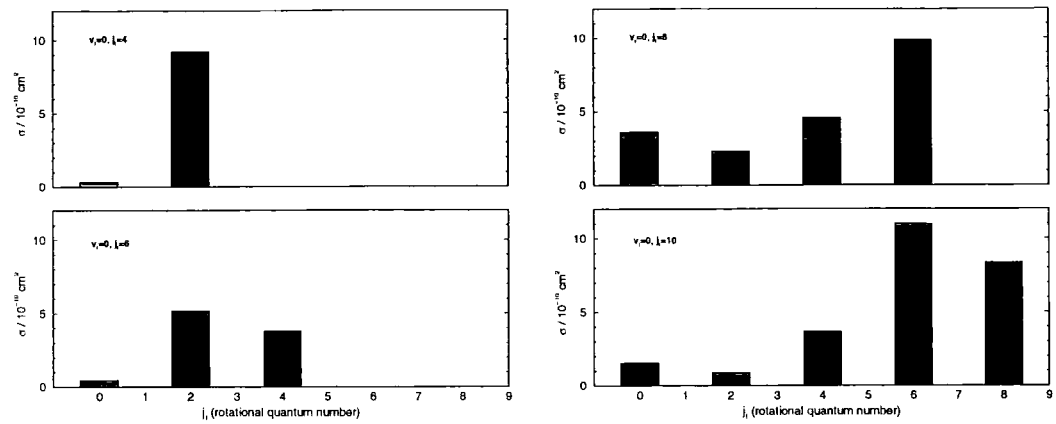

Figure 8.28: Final rotational distributions for $^7\mathrm{Li} + {}^7\mathrm{Li}_2(v_i = 0, j_i)$ at 0.928 nK for $j_i = 4$, 6, 8, and 10.

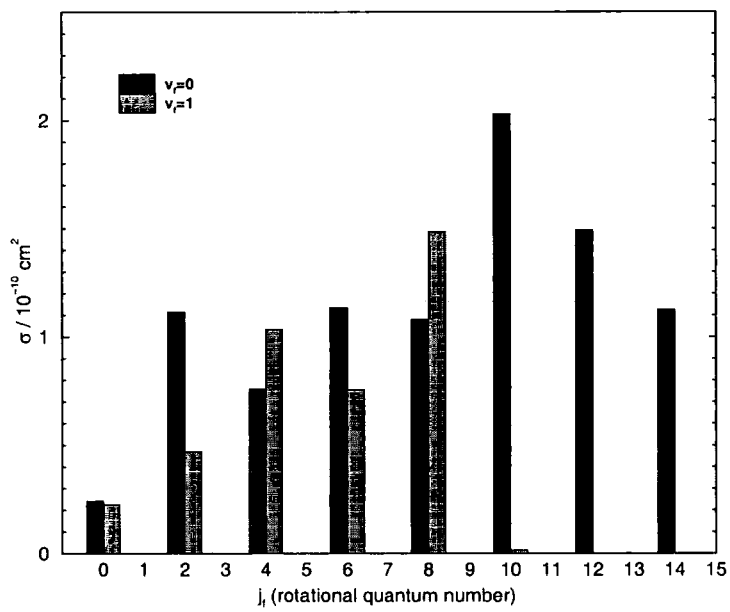

Figure 8.29: Final rotational distributions for $^7\mathrm{Li} + {}^7\mathrm{Li}_2(v_i = 1, j_i = 10)$ at 0.928 nK.

$^7Li + {}^7Li_2(v_i, j_i)$ at 0.928 nK, for a range of initial states of the dimer, are reported in Table 8.5, and the complex scattering lengths are given in Table 8.6. We have found no evidence of the quasiresonant behaviour in inelastic cross sections. There is no systematic dependence of the total inelastic cross sections on initial quantum numbers v_i and j_i. Pure rotational transitions are equally efficient as other rovibrational transitions, unlike the results cited above. This is, comparatively, a strong coupling case, where pure rotational and rovibrational transitions compete and the total inelastic probability is large (≈ 1) outside the Wigner regime.

v_i, j_i	σ_{elas} [cm^2]	σ_{inel} [cm^2]	k_{elas} [cm^{3}s^{-1}]	k_{inel} [cm^{3}s^{-1}]	$\sigma_{inel}/\sigma_{elas}$
0, 0	$3.39 \cdot 10^{-12}$	-	$6.16 \cdot 10^{-13}$	-	-
0, 2	$4.87 \cdot 10^{-12}$	$6.56 \cdot 10^{-10}$	$8.85 \cdot 10^{-13}$	$1.19 \cdot 10^{-10}$	135
0, 4	$3.90 \cdot 10^{-13}$	$9.55 \cdot 10^{-10}$	$7.09 \cdot 10^{-14}$	$1.73 \cdot 10^{-10}$	2450
0, 6	$7.72 \cdot 10^{-13}$	$9.42 \cdot 10^{-10}$	$1.40 \cdot 10^{-13}$	$1.71 \cdot 10^{-10}$	1220
0, 8	$1.57 \cdot 10^{-12}$	$2.04 \cdot 10^{-9}$	$2.85 \cdot 10^{-13}$	$3.71 \cdot 10^{-10}$	1300
0, 10	$9.26 \cdot 10^{-13}$	$2.55 \cdot 10^{-9}$	$1.68 \cdot 10^{-13}$	$4.63 \cdot 10^{-10}$	2750
1, 0	$1.37 \cdot 10^{-12}$	$3.09 \cdot 10^{-9}$	$2.49 \cdot 10^{-13}$	$5.61 \cdot 10^{-10}$	2260
1, 2	$2.05 \cdot 10^{-12}$	$3.00 \cdot 10^{-9}$	$3.72 \cdot 10^{-13}$	$5.45 \cdot 10^{-10}$	1460
1, 4	$8.00 \cdot 10^{-13}$	$1.14 \cdot 10^{-9}$	$1.45 \cdot 10^{-13}$	$2.07 \cdot 10^{-10}$	1425
1, 6	$8.46 \cdot 10^{-13}$	$1.43 \cdot 10^{-9}$	$1.54 \cdot 10^{-13}$	$2.60 \cdot 10^{-10}$	1690
1, 8	$1.74 \cdot 10^{-12}$	$1.96 \cdot 10^{-9}$	$3.16 \cdot 10^{-13}$	$3.56 \cdot 10^{-10}$	1130
1, 10	$1.38 \cdot 10^{-12}$	$1.53 \cdot 10^{-9}$	$2.51 \cdot 10^{-13}$	$2.78 \cdot 10^{-10}$	1110
2, 0	$5.17 \cdot 10^{-13}$	$4.77 \cdot 10^{-10}$	$9.39 \cdot 10^{-14}$	$8.67 \cdot 10^{-11}$	920
2, 2	$1.02 \cdot 10^{-12}$	$1.96 \cdot 10^{-9}$	$1.85 \cdot 10^{-13}$	$3.56 \cdot 10^{-10}$	1920
2, 4	$1.25 \cdot 10^{-12}$	$1.56 \cdot 10^{-9}$	$2.27 \cdot 10^{-13}$	$2.83 \cdot 10^{-10}$	1250
2, 6	$8.83 \cdot 10^{-13}$	$1.48 \cdot 10^{-9}$	$1.60 \cdot 10^{-13}$	$2.69 \cdot 10^{-10}$	1680
2, 8	$9.85 \cdot 10^{-13}$	$1.87 \cdot 10^{-9}$	$1.79 \cdot 10^{-13}$	$3.40 \cdot 10^{-10}$	1900
2, 10	$1.32 \cdot 10^{-12}$	$1.95 \cdot 10^{-9}$	$2.40 \cdot 10^{-13}$	$3.54 \cdot 10^{-10}$	1480
3, 0	$9.29 \cdot 10^{-13}$	$8.57 \cdot 10^{-10}$	$1.69 \cdot 10^{-13}$	$1.56 \cdot 10^{-10}$	920
3, 2	$1.06 \cdot 10^{-12}$	$1.43 \cdot 10^{-9}$	$1.93 \cdot 10^{-13}$	$2.60 \cdot 10^{-10}$	1350
3, 4	$1.16 \cdot 10^{-12}$	$2.42 \cdot 10^{-9}$	$2.11 \cdot 10^{-13}$	$4.40 \cdot 10^{-10}$	2090
3, 6	$1.77 \cdot 10^{-12}$	$2.61 \cdot 10^{-9}$	$3.22 \cdot 10^{-13}$	$4.74 \cdot 10^{-10}$	1470
3, 8	$2.55 \cdot 10^{-12}$	$3.85 \cdot 10^{-9}$	$4.63 \cdot 10^{-13}$	$6.99 \cdot 10^{-10}$	1510
3, 10	$1.27 \cdot 10^{-12}$	$1.96 \cdot 10^{-9}$	$2.31 \cdot 10^{-13}$	$3.56 \cdot 10^{-10}$	1540

Table 8.5: Elastic and total inelastic cross sections and rate coefficients for $^7Li + {}^7Li_2(v_i, j_i)$ at the collision energy of 0.928 nK for different initial states of the molecule.

v_i, j_i	Re(a) [nm]	−Im(a) [nm]	−Im(a)/Re(a)
0, 0	5.20	–	–
0, 2	−6.18	0.704	−0.114
0, 4	1.44	1.02	0.708
0, 6	2.27	1.00	0.441
0, 8	2.78	2.18	0.784
0, 10	0.0635	2.71	42.7
1, 0	−0.199	3.30	−16.6
1, 2	2.47	3.19	1.29
1, 4	2.21	1.22	0.552
1, 6	2.10	1.52	0.724
1, 8	3.08	2.09	0.679
1, 10	2.89	1.63	0.564
2, 0	1.96	0.509	0.260
2, 2	1.95	2.08	1.07
2, 4	2.68	1.67	0.623
2, 6	2.13	1.58	0.742
2, 8	1.96	1.99	1.02
2, 10	2.48	2.08	0.839
3, 0	2.56	0.914	0.357
3, 2	2.47	1.53	0.619
3, 4	1.62	2.58	1.59
3, 6	2.52	2.78	1.10
3, 8	1.87	4.10	2.19
3, 10	2.41	2.07	0.859

Table 8.6: Complex scattering lengths for $^7\mathrm{Li} + {}^7\mathrm{Li}_2(v_i, j_i)$ for different initial states of the molecule.

8.4 Collisions in fermionic system

This section deals with the fermionic analogue of the atom-exchange collision studied in the previous section,

$$^6\mathrm{Li} + {}^6\mathrm{Li}_2 \rightarrow {}^6\mathrm{Li} + {}^6\mathrm{Li}_2. \tag{8.12}$$

The process involves three fermionic ^{6}Li nuclei and we study atom-molecule collisions at energies between 1 nK and 1 K.

The results are presented in the similar order to that of the bosonic system. Calculations cover the elastic and inelastic cross sections for partial waves $J = 0^+ - 11^-$.

8.4.1 Convergence of cross sections: $J = 1^-$

The dominant contribution at ultracold collision energies in the atom-molecule collisions involving three fermions comes from the orbital angular momentum $l = 0$, when approach of the atom and molecule is not suppressed by the centrifugal barrier. We are primarily interested in the vibrational and rotational relaxation of the lithium dimer in collisions $^6\mathrm{Li} + {}^6\mathrm{Li}_2$. Here we test the convergence of the cross sections for the initial molecular states $v_i = 1$, 2, and 3 and the lowest rotational level $j_i = 1$. The dominant contribution is contained in the partial wave $J = 1^-$, as can be seen from Table 8.1.

Convergence parameters for bosonic and fermionic systems are similar, but the $J = 1^-$ partial wave makes the calculations on the fermionic system substantially more time-consuming than in the bosonic, where $J = 0^+$ contains the dominant contribution. The surface hamiltonian (6.47) needs to be diagonalized twice in each sector, for $\Omega = 0$ and 1, and the coupled equations contain functions of both Ω, so the size of the matrix propagated for each collision energy is larger.

Positions of the levels in $^6\mathrm{Li}_2$ are changed in comparison with $^7\mathrm{Li}_2$ due to the difference in masses of the nuclei and the quantum numbers allowed are different due to symmetry. We, therefore, test the convergence of cross sections with respect to the number of basis functions N, for $\Omega = 0$ and 1, and the propagation distance in hyperspherical coordinates, ρ_{max}. Other convergence parameters are kept unchanged from bosonic system.

The largest basis set employed here and limited by the requirement for good matching (one part in 1000) at the matching radius $\rho_{\max} = 45\ a_0$ contains $N = 85$ basis functions for $\Omega = 0$ and 85 basis functions for $\Omega = 1$. Asymptotically, they match onto the bound levels of the dimer with $v = 0$, 1, 2, 3, 4, 5, 6, and 7, and the rotational levels up to $j_{\max} = 31$, 27, 25, 23, 19, 17, 13, and 7, respectively. The cut-off in energy is just below the $v = 8$, $j = 0$ level of the dimer. The calculation of this basis set, keeping $K_{\max}$ same as for bosons, results in two diagonalisations per sector of the matrices that vary in size between 1220 and 2162 for $\Omega = 0$ and 1220 and 2154 for $\Omega = 1$. The other two basis sets comprise of $N = 74$ and $N = 64$ basis functions, for both Ω values, and match onto the bound states of dimer below the $v = 7, j = 0$ level ($j_{\max} = 29$, 27, 25, 21, 17, 13, 9) and below the $v = 6, j = 0$ level ($j_{\max} = 29$, 25, 23, 19, 15, 11), respectively.

Vibrationally resolved elastic and total inelastic cross sections are reported in Table 8.7. Variations of the cross sections with the basis set are smaller in comparison to the bosonic system, see Table 8.3, except for the elastic cross sections for $v = 0$, $j = 1$. The largest deviation of cross sections calculated using the $N = 85$ basis from those using the $N = 74$ basis is $\approx 13.3\%$. The propagation distance in the basis set using $N = 74$ channels can be reduced to $\rho_{\max} = 40\ a_0$ without losing substantially in the accuracy of the projections onto the Fock coordinates at that distance. The differences in the calculated cross sections extracted at $\rho_{\max} = 40\ a_0$ are within 10% of those obtained from matching at $\rho_{\max} = 45\ a_0$. Rotational spacing is larger in the dimer made of fermionic atoms compared to that of bosonic atoms, so neglecting rotational transitions at larger distances than the matching radius is a better approximation than in the bosonic system.

Individual inelastic state-to-state cross sections for the three basis sets and the dimer in the $v_i = 1$, $j_i = 1$ state are shown in Figure 8.30. We believe that all cross sections are converged to better than 10% except in the regions of rapid variation of cross sections with collision energy. The convergence slightly improves with increase in collision energy, outside the threshold region.

The adiabatic energies of the hypersurface hamiltonian (6.47) for $\Omega = 1$ are plotted as a function of hyperradius in Figure 8.31. They are raised in the energy compared to $\Omega = 0$. They vary smoothly with numerous avoided crossings.

The largest basis, $N = 85$, is employed in all the subsequent calculations.

(v_i, v_f)	$N = 64$	$N = 74$	$N' = 74$, $\rho_{\max} = 40\ a_0$	$N = 85$
(0,0)	$2.338 \cdot 10^{-11}$	$2.883 \cdot 10^{-12}$	$2.570 \cdot 10^{-12}$	$2.204 \cdot 10^{-12}$
(1,1)	$6.426 \cdot 10^{-13}$	$6.198 \cdot 10^{-13}$	$5.957 \cdot 10^{-12}$	$6.087 \cdot 10^{-13}$
(1,0)	$1.384 \cdot 10^{-9}$	$1.383 \cdot 10^{-9}$	$1.347 \cdot 10^{-9}$	$1.397 \cdot 10^{-9}$
(2,2)	$1.618 \cdot 10^{-12}$	$1.577 \cdot 10^{-12}$	$1.578 \cdot 10^{-12}$	$1.667 \cdot 10^{-12}$
(2,1)	$8.202 \cdot 10^{-10}$	$8.553 \cdot 10^{-10}$	$8.679 \cdot 10^{-10}$	$8.823 \cdot 10^{-10}$
(2,0)	$1.435 \cdot 10^{-9}$	$1.351 \cdot 10^{-9}$	$1.398 \cdot 10^{-10}$	$1.373 \cdot 10^{-9}$
(3,3)	$1.021 \cdot 10^{-12}$	$1.391 \cdot 10^{-12}$	$1.522 \cdot 10^{-12}$	$1.462 \cdot 10^{-12}$
(3,2)	$3.391 \cdot 10^{-10}$	$6.413 \cdot 10^{-10}$	$6.670 \cdot 10^{-10}$	$7.088 \cdot 10^{-10}$
(3,1)	$5.290 \cdot 10^{-10}$	$7.995 \cdot 10^{-10}$	$8.486 \cdot 10^{-10}$	$7.553 \cdot 10^{-10}$
(3,0)	$8.714 \cdot 10^{-10}$	$1.125 \cdot 10^{-9}$	$1.233 \cdot 10^{-9}$	$1.298 \cdot 10^{-9}$

Table 8.7: Convergence of vibrationally resolved cross sections, $\sum_{j_f} \sigma(v_i j_i \rightarrow v_f j_f)$ for $j_i = 1$ in cm^2, for ^{6}Li+ ^{6}Li$_2$ at the collision energy of 0.928 nK. $\rho_{\max} = 45\ a_0$ for all bases unless otherwise indicated.

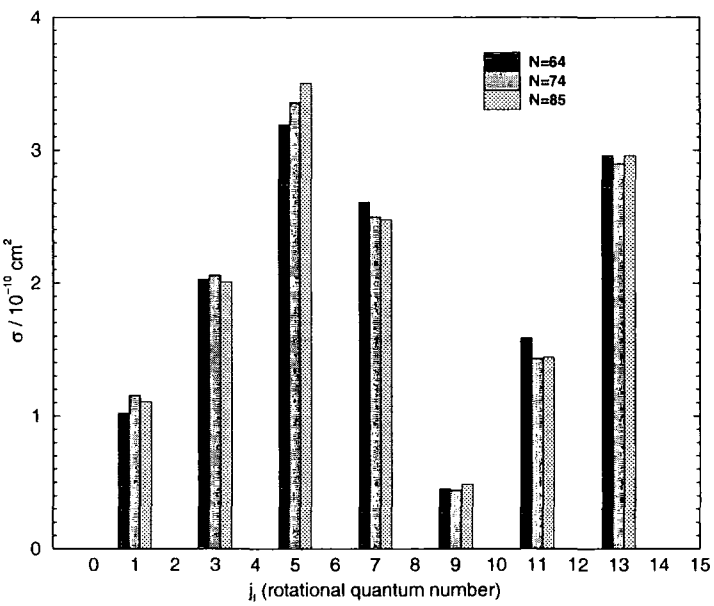

Figure 8.30: Convergence of inelastic state-to-state cross sections for $^6\mathrm{Li} + {}^6\mathrm{Li}_2(v_i = 1, j_i = 1)$ and $v_f = 0$ at the collision energy of 0.928 mK. N is the number of channels in the basis.

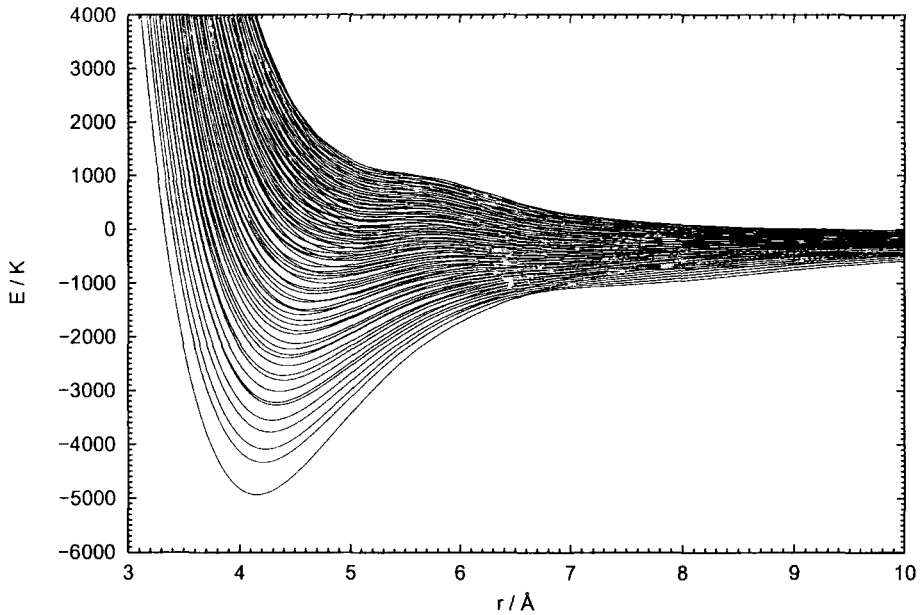

Figure 8.31: Eigenvalues ($N = 85$) of the hypersurface hamiltonian (6.47) for $\Omega = 1$ for three ^{6}Li nuclei in the electronic quartet ground state.

8.4.2 Vibrational relaxation cross sections and rate coefficients: $J = 1^-$

In this subsection we report the results of scattering calculations for atom-diatom collisions involving three identical ^{6}Li nuclei for the $J = 1^-$ partial wave. As discussed earlier, see Table 8.1, it contains contributions of the initial orbital angular momenta $l_i = 0$ and 2, when dimer is initially in the rotational ground state $j_i = 1$. There is no symmetry that would suppress the s-wave scattering, as in the scattering of two identical fermionic atoms.

We have calculated the elastic and inelastic cross sections for collisions involving the dimer in $v_i = 0$, 1, 2, and 3 and $j_i = 1$, in the collision energy interval from 1 nK to 1K at more than 150 energies. The energy dependence of the cross sections is plotted in Figure 8.32, 8.34, 8.35, and 8.36.

When the molecule is initially in the lowest bound state, $v_i = 0$, $j_i = 1$, only elastic scattering is possible in the collision energy range studied. The $v = 0$, $j = 3$ threshold is at 4.46 K. Elastic cross section in the zero-energy limit is similar to the corresponding one in the bosonic system. Threshold regime sets in at millikelvin energies. At higher energies the cross section exhibits several minima, but does not drop down to zero as in the bosonic system. The difference is that there are two open

channels in this case, corresponding to the initial and final orbital angular momenta $l = 0$ and 2. In the same figure are shown partial cross sections for scattering from and to individual open channels. The cross section $\sigma(l_i = 0 \rightarrow l_f = 0)$ dominates in the ultracold limit. The scattering length is defined in terms of the matrix element involved in this transition, $T_{l_i l_f}$, using equation (7.53). Its convergence is shown in the inset in Figure 8.32. The $\sigma(l_i = 0 \rightarrow l_f = 2)$ (same as $\sigma(l_i = 2 \rightarrow l_f = 0)$ due to the principle of microscopic reversibility and identical energy) and $\sigma(l_i = 2 \rightarrow l_f = 2)$ enter threshold regime below 10 mK with the energy dependence following the E^2 and E^3 laws, respectively. The cross sections, $\sigma(l_i = 0 \rightarrow l_f = 2)$ and $\sigma(l_i = 2 \rightarrow l_f = 2)$, exhibit minima at $\approx$ 200 mK and 650 mK. At each of these energies, an eigenphase passes through a multiple of π and the eigenphase sum increases, giving evidence of a resonance strongly modified by the variations of the background. They are shown in Figure 8.33. The other minimum, at $\approx$ 70 mK, may also be associated with a zero of an eigenphase, although the overall correspondence is weaker than in the bosonic system where only one channel is open for elastic scattering from the lowest rovibrational state.

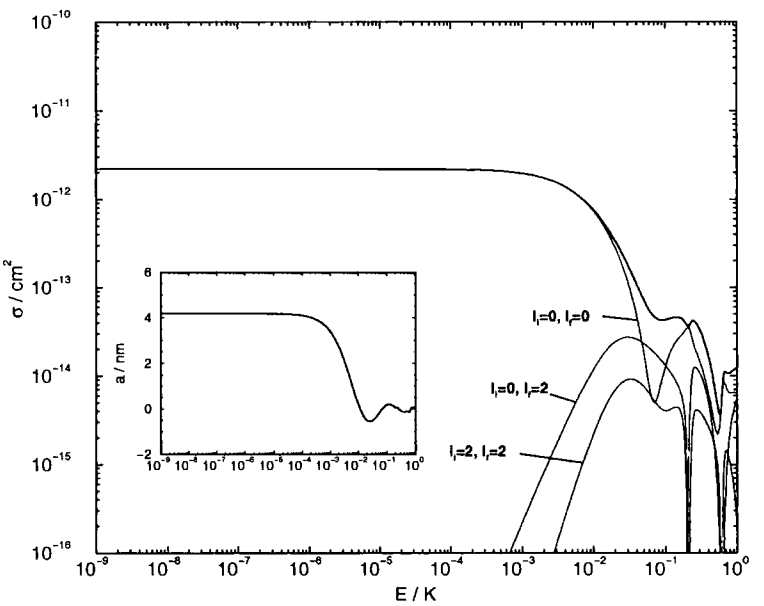

Figure 8.32: Energy dependence of cross sections for ^{6}Li + ^{6}Li$_2(v_i = 0, j_i = 1)$. Convergence of scattering length shown in the inset.

Energy dependence of elastic and inclastic cross sections for vibrationally excited dimers $v_i = 1 - 3$, shown in Figure 8.34, 8.35, and 8.36, follows Wigner laws below

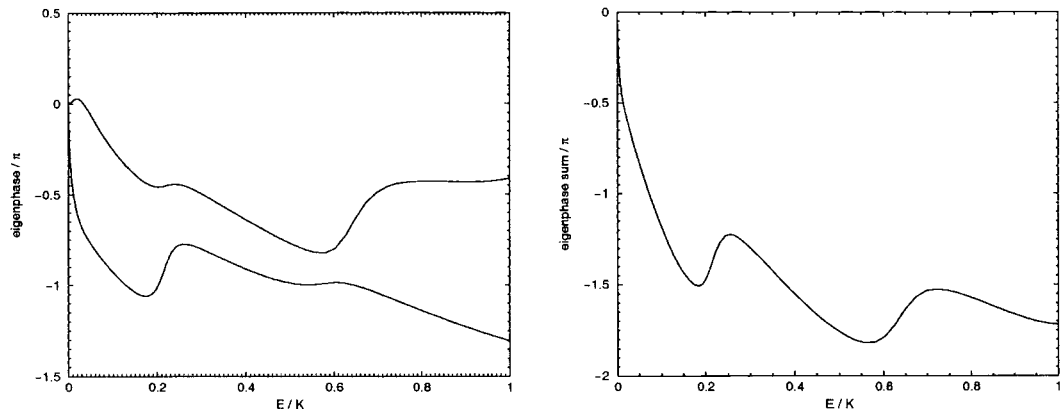

Figure 8.33: Energy dependence of eigenphases (left) and eigenphase sum (right) for $^6\mathrm{Li} + {}^6\mathrm{Li}_2(v_i = 0, j_i = 1)$.

millikelvin energies. At 1 nK, elastic cross sections are slightly lower than 10^{-12} cm^2. Total inelastic cross sections are about three orders of magnitude larger. At higher energies, outside the threshold regime, elastic cross sections for the partial wave $J = 1^-$ oscillate about the total inelastic ones. Undulations are less pronounced in comparison with the bosonic system because two, instead of one, open channels are involved. The $l = 2$ component starts contributing at energies above 10 mK. Inelastic probabilities saturate and energy dependence becomes dominated by the kinematic factor $1/k^2$ from the expression for cross section (6.75), as in the bosonic system. Convergence of the complex scattering lengths is shown in the insets on the figures. They are extracted from the elastic T matrix element with $l_{i,f} = 0$, using equation (7.53).

Vibrationally resolved cross sections for $v_i = 2$ and 3 favour lower vibrational levels with the constant relative magnitude below 10 mK. Final rotational distributions at 0.928 nK for $v_i = 1$, 2, and 3 are plotted in Figure 8.37. They all show oscillatory patterns already discussed above. The relative magnitudes do not change below the $l = 2$ threshold.

Elastic and inelastic cross sections for atom-molecule collisions involving three fermions are in the similar range as in the bosonic system, differing by less than an order of magnitude. Energy dependence is qualitatively similar and discussions of last section apply also to the fermionic system. As stated in the introduction of this chapter, it was observed that fermionic molecules in weakly bound states with a large positive atom-atom scattering length have long lifetimes [165, 173–175],

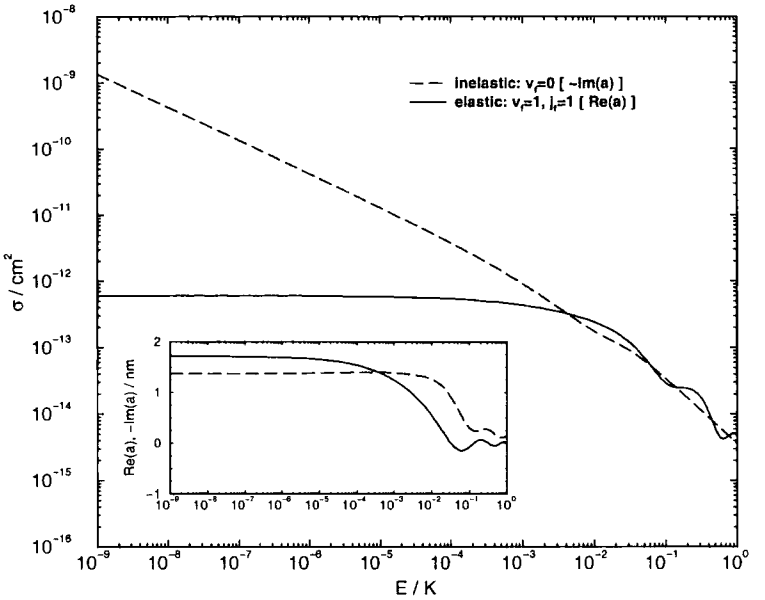

Figure 8.34: Energy dependence of elastic and inelastic cross sections for ^{6}Li + ^{6}Li$_2(v_i = 1, j_i = 1)$.

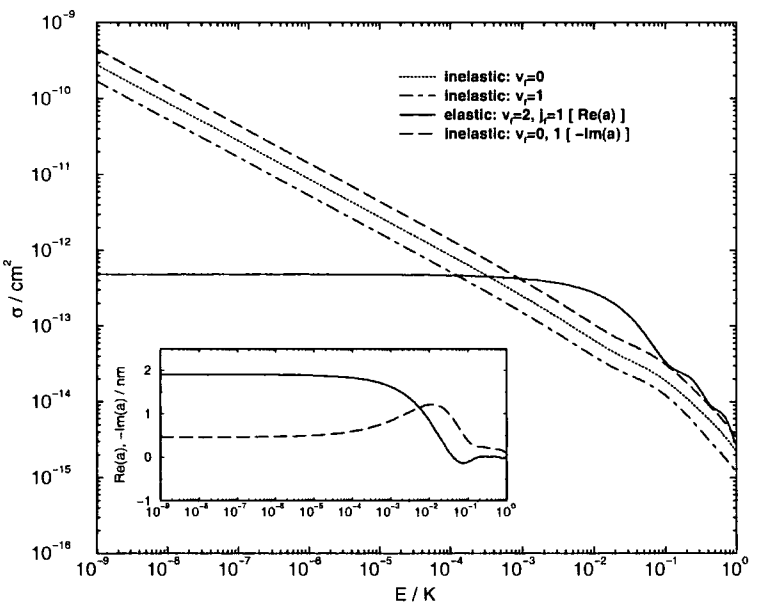

Figure 8.35: Energy dependence of elastic and inelastic cross sections for ^{6}Li + ^{6}Li$_2(v_i = 2, j_i = 1)$.

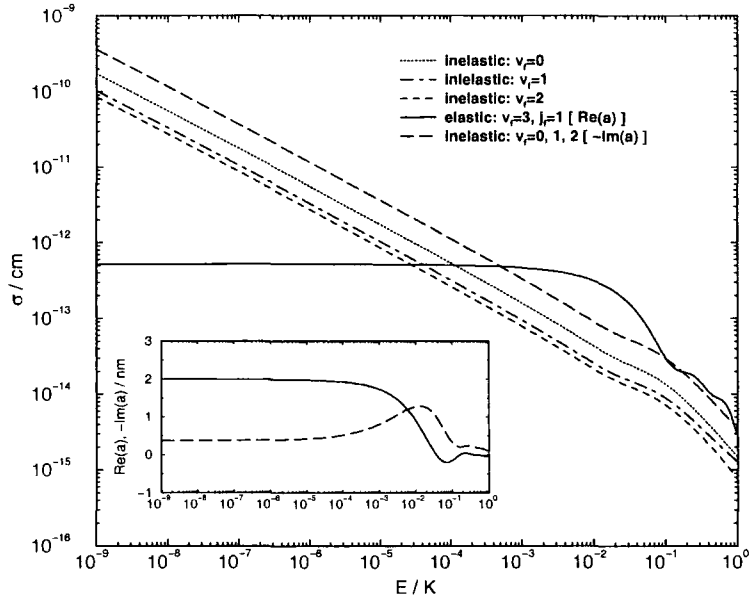

Figure 8.36: Energy dependence of elastic and inelastic cross sections for ^{6}Li + ^{6}Li$_2(v_i = 3, j_i = 1)$.

while, for example, in an experiment involving fermionic atoms, ^{40}K, with a smaller atom-atom scattering length collisional decay is rapid [169]. Our calculations for low-lying bound states contrast with the above results for weakly bound dimers. They do not depend on the atom-atom scattering length. Atom-atom scattering length is completely determined only if the long-range part of the diatomic potential is included in the system. Atoms interact with their long-range interactions near the three-body dissociation limit where the wavefunction for collisions in the deeply-bound states is negligible. That the inelastic rate coefficient never changes by several orders of magnitude for the fermionic atom-diatom systems, where the diatom is in a low-lying rovibrational level, will be evident from the potential sensitivity results in the next chapter.

8.4.3 Vibrational relaxation cross sections and rate coefficients: $J \neq 1^-$

We have seen in the study of the bosonic system that the maximum orbital angular momentum quantum number determines the convergence in the partial wave expansion of the wavefunction. For an initial rotational state of the molecule $j_i = 1$, there are three values of orbital angular momentum, $J - 1, J$, and $J + 1$, in each partial

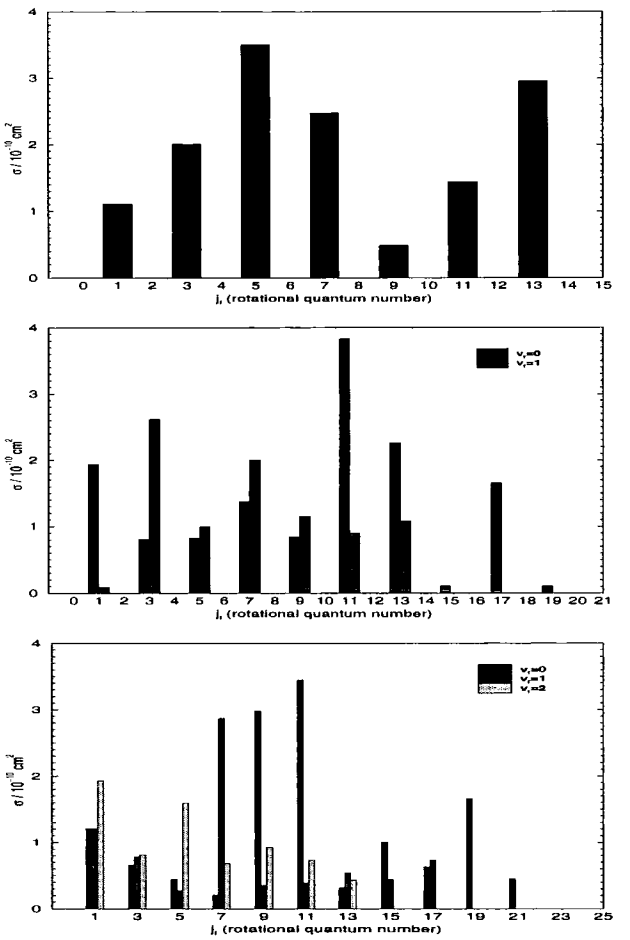

Figure 8.37: Final rotational distributions for $^6\mathrm{Li} + {}^6\mathrm{Li}_2(v_i, j_i = 1)$ at 0.928 nK for $v_i = 1$ (top), $v_i = 2$ (middle), and $v_i = 3$ (bottom).

wave $J > 0$. They divide according to parity into two blocks, $l = J - 1$ and $J + 1$ belong to the so-called parity favoured block of J and $l = J$ to the parity unfavoured block of J. We have included all the partial waves that include contributions from $l \leq 10$, namely: $0^+, 1^-, 2^+, 3^-, ..., 11^-$ (parity favoured series) and $1^+, 2^-, 3^+, ..., 10^-$ (parity unfavoured series). For each Ω value, we included all the basis functions that asymptotically converge in the same set of rovibrational states of the dimer that were included for $\Omega = 0$ and 1 earlier. The number of basis functions for $\Omega = 0$ to 11 is: 85, 85, 77, 77, 69, 69, 61, 61, 53, 53, 46, and 46. The basis sets have been calculated for both parities which resulted in diagonalisation of matrices with the dimensions ranging from 1180 to 2162 for $\Omega = 0$ and from 1027 to 1863 for $\Omega = 11$. The size of the log-derivative matrix that is propagated to solve the system of coupled equations for each partial wave at each collision energy varies between 85 for $J = 0^+$ to 782 for $J = 11^-$ in the parity favoured series and from 85 for $J = 1^+$ to 651 for $J = 10^-$ in the parity unfavoured series of partial wave blocks. The other convergence parameters were kept same as in the $J = 1^-$ calculations.

Elastic matrix elements and the total inelastic probabilities, $k^2\sigma/\pi$, for the molecule initially in $v = 1$ and $v = 3$ states are plotted as a function of J in Figure 8.38 and 8.39. Contributions of both parity blocks were added together for each partial wave J. Elastic cross sections for $J = 10$ and 11 partial waves at 580 mK contribute 3.06% and 0.863% to the overall elastic cross section for $v_i = 1$, and 1.67% and 0.457% for $v_i = 3$. The total inelastic cross sections at 580 mK are better converged. Cross sections for $J = 10$ and 11 partial waves contribute 0.0756% and 0.00268% for $v_i = 1$ and 0.242% and 0.00566% for $v_i = 3$ to the overall total inelastic cross section. Due to the different threshold laws, the situation reverses at ultracold temperatures and inelastic cross sections converge faster with J. Partial cross sections for each l drop off according to Wigner laws for collision energies below the centrifugal barriers for corresponding l's. Since fermions have lower mass than bosons in lithium, the barrier heights are higher at a given energy and the cross sections for fermions are, therefore, better converged here for a given l_{max}.

Elastic and inelastic cross sections for a molecule initially in the $v_i = 1$, $j_i = 1$ state are shown in Figure 8.40 as a function of collision energy in the interval between 10 μK and 580 mK. Contributions of all partial waves are plotted separately. The range of the applicability of threshold laws are related to the positions of centrifugal

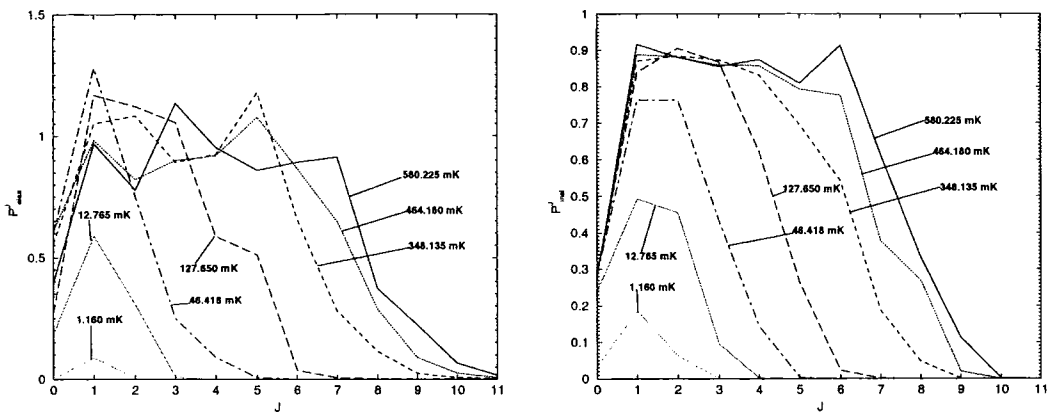

Figure 8.38: Elastic (left) and the sum of inelastic (right) matrix elements as a function of total angular momentum J for $^6\mathrm{Li} + {}^6\mathrm{Li}_2(v = 1, j = 1)$.

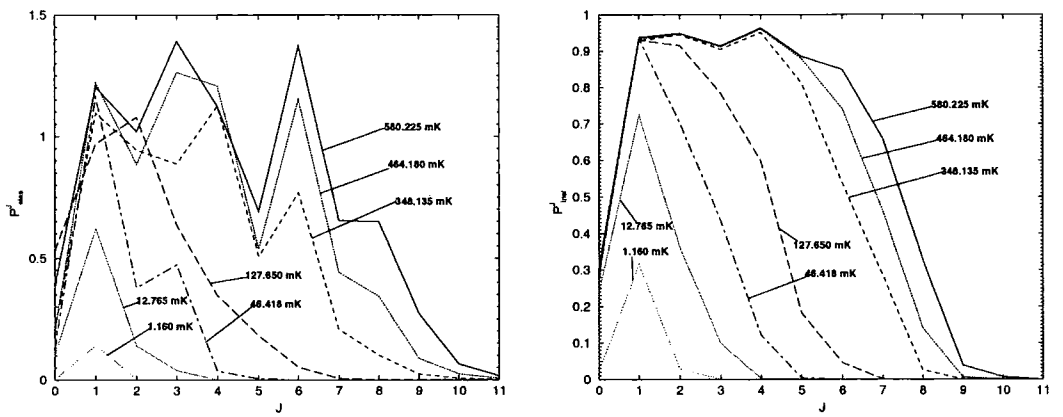

Figure 8.39: Elastic (left) and the sum of inelastic (right) matrix elements as a function of total angular momentum J for $^6\mathrm{Li} + {}^6\mathrm{Li}_2(v = 3, j = 1)$.

barriers for $l > 0$. The barrier maxima are plotted in the figure as vertical bars, as estimated using equation (8.9). They are 26% higher than the corresponding barriers in the bosonic system, given in Table 8.4.

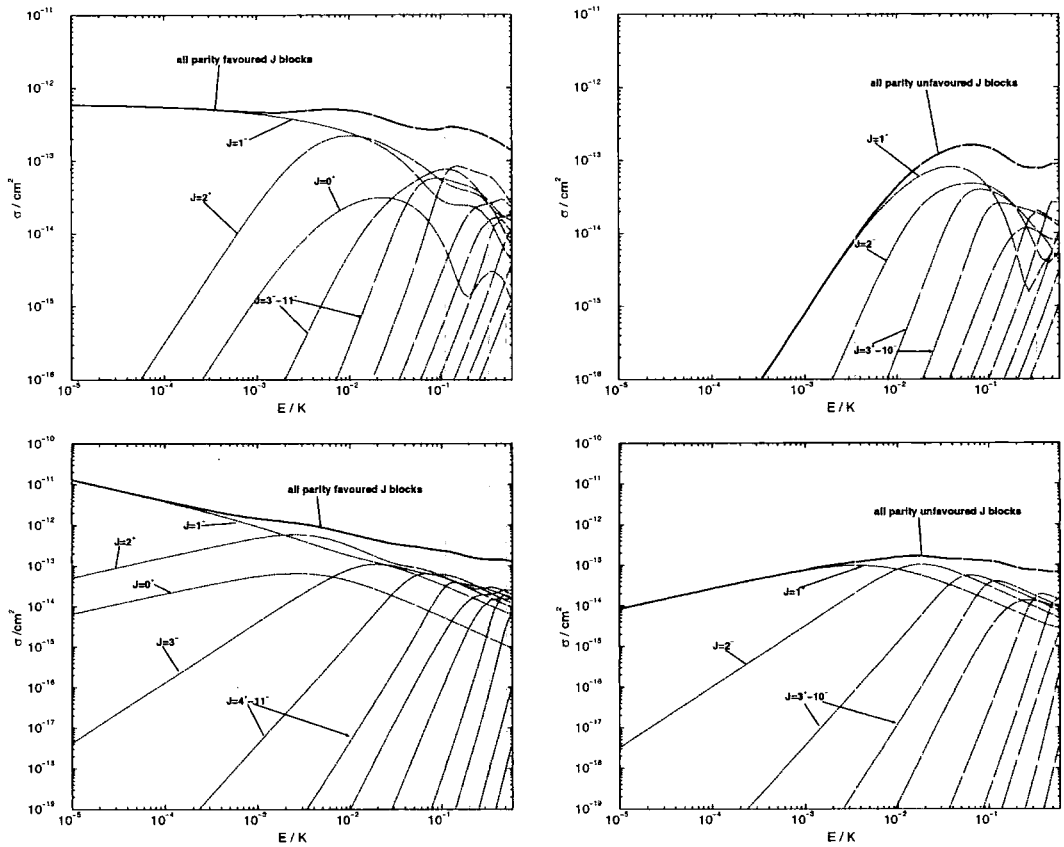

Figure 8.40: Energy dependence of elastic (top row) and inelastic (bottom row) cross sections for $^6\mathrm{Li} + {}^6\mathrm{Li}_2(v_i = 1, j_i = 1)$: partial waves $J = 0^+ - 11^-$ and total.

The energy dependence of inelastic cross sections in each partial wave $J > 1$ is again simply described by the threshold law $E^{l_i+1/2}$ below the centrifugal barrier and $l_i = J - 1$, and the E^{-1} law above the barrier for $l_i = J + 1$. The origin of the laws is described in the bosonic system. The contributions of different initial orbital angular momenta for $J = 0^+, 1^-, 2^+$ are plotted in Figure 8.41.

The probabilities for inelastic transitions for $J > 0$ are very high, $\approx 90\%$, below the cut-off in J and above 100 mK, see Figure 8.38 and 8.39. This suggests the applicability of the classical Langevin model. Elastic and vibrationally resolved and total inelastic cross sections are plotted together with the Langevin model predictions in Figure 8.42. The agreement between the model and the total inelastic cross sections is excellent already at millikelvin energies. Since the Langevin model depends on

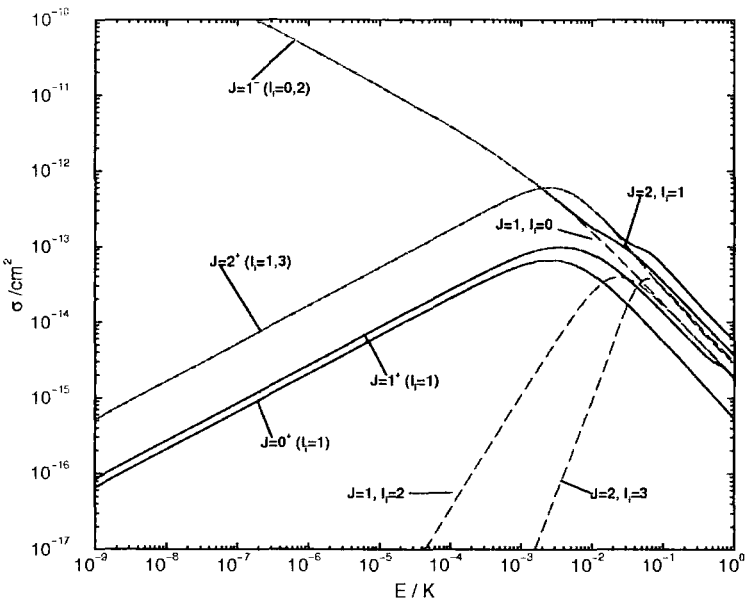

Figure 8.41: Energy dependence of partial inelastic cross sections for $^6\mathrm{Li} + ^6\mathrm{Li}_2(v_i = 1, j_i = 1)$. Cross sections are shown for partial waves $J = 0^+ - 2^+$ and different initial orbital angular momenta l_i.

the dispersion coefficient C_6 only, the difference between masses of lithium bosons and fermions and different level structure in the dimers makes little difference to the total inelastic rates at these collision energies.

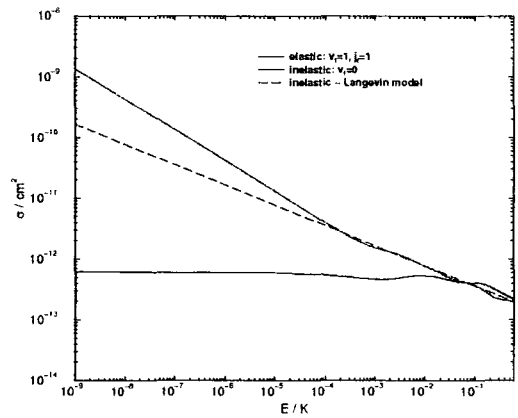

Figure 8.42: Elastic and total inelastic cross sections for $^6\mathrm{Li} + ^6\mathrm{Li}_2(v_i = 1, j_i = 1)$, and the inelastic cross sections in the Langevin model.

We check the accuracy of the $J = 1^-$ cross sections at 1 mK and 0.1 mK here. At 1 mK, contribution of all partial waves other than the $J = 1^-$ to the overall cross sections is 6.06% for elastic and 40.9% for inelastic. At 0.1 mK, the contributions are 0.0536% and 4.86% for the elastic and total inelastic cross sections, respectively.

In Figure 8.43, we show the partial wave contributions of elastic and inelastic cross sections for collisions with the dimer in the $v_i = 2$, $j_i = 1$ state. The energy dependence of inelastic cross section proves to be qualitatively simple again (see the discussion given above for $v_i = 1$). It may be noticed that the molecules do not preferentially scatter to the lowest vibrational state for all partial waves.

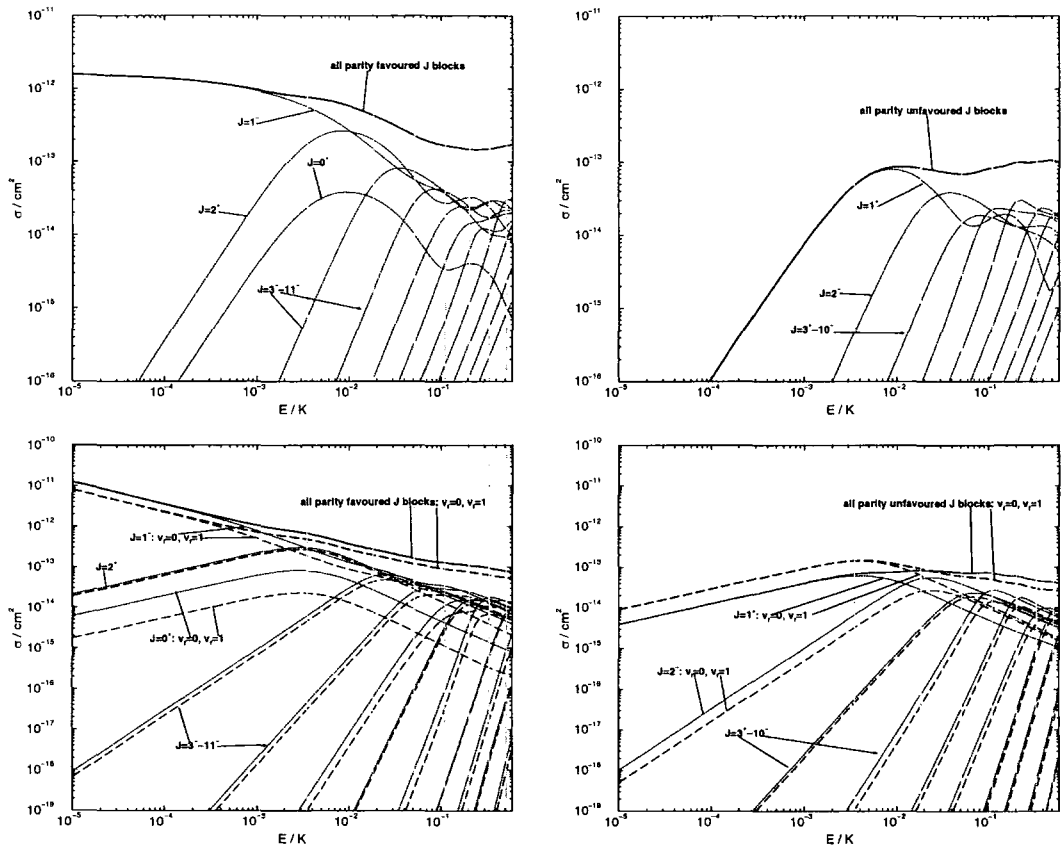

Figure 8.43: Energy dependence of elastic (top row) and inelastic (bottom row) cross sections for $^6\mathrm{Li} + {}^6\mathrm{Li}_2(v_i = 2, j_i = 1)$: partial waves $J = 0^+ - 11^-$ and total.

The elastic and vibrationally resolved and total inelastic cross sections for collisions with the dimer in its $v_i = 2$, $j_i = 1$ and $v_i = 3$, $j_i = 1$ states are shown in Figure 8.44. The agreement with the Langevin model is excellent for both initial dimer states above 10 mK. Elastic cross section becomes slightly larger than the inelastic at $\approx$ 60 mK, 290 mK, and 310 mK for the initial $v = 1$, 2, and 3 states, respectively. Since the inelastic probability is close to 1 when the Langevin model is valid, elastic probability must be close to zero, which leaves little room for differences, see equations (6.73) and (6.75).

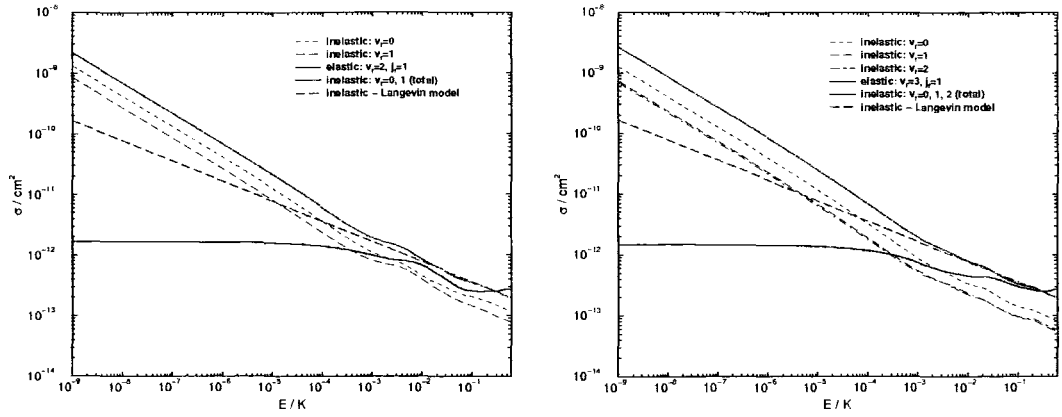

Figure 8.44: Elastic and inelastic (vibrationally resolved and total) cross sections for $^6Li + {}^6Li_2(v_i, j_i = 1)$, for $v_i = 2$ (left) and 3 (right), and the inelastic cross sections in the Langevin model.

8.4.4 Comparison with some insertion reactions

The observations made in the comparison of the scattering results for the bosonic system with some insertion reactions in subsection 8.3.4 apply for the fermionic system as well.

Final vibrational and rotational distributions, shown in Figure 8.45 and 8.46 at 116 mK and 580 mK respectively, for different initial dimer excitations v_i, are non-statistical. The lowest vibrational level is the most populated one. Oscillations observed in the rotational distributions in each partial wave are washed out in the sum over partial waves at higher collision energies, but distributions are not peaked at high j's, as one would expect using statistical arguments.

The only qualitative difference between the bosonic and fermionic systems is noticeable in the differential cross sections, shown in Figure 8.45 and 8.46 at 116 mK and 580 mK, for different initial dimer states v_i. The forward and backward peaks are less pronounced. The ratio of the differential cross sections at the poles and for the sideways scattering at 90° is in case of the bosonic system between 2.3 and 3.8, and it is between 1.5 and 2.1 for the fermionic system. That the forward and backward peak become wider and smaller with increasing j_i was already noticed in the $O(^1D) + H_2 \rightarrow OH + H$ reaction [6]. Differential cross sections in the figures show a slight preference for the forward scattering for most of the initial dimer states studied here. Ratio of forward and backward peaks ranges between 0.7 and

2.1. Again the asymmetry may result from the insufficient number of partial waves for the J averaging in equation (6.74) to be complete.

8.4.5 Collisions involving rotationally excited states

We have found no evidence of quasiresonant transitions in the bosonic system and we found the pure rotational and rovibrational state-to-state transitions equally efficient. The same is true in the fermionic system. Product rotational distributions for collisions of atoms and rotationally excited dimers are shown in Figure 8.47. There is again a slight preference for higher j_f levels, on top of the oscillatory behaviour discussed earlier (in connection with Figure 8.12). A typical product state distribution for collisions involving a rotationally and vibrationally excited dimer is shown in Figure 8.48.

Finally, we present the elastic and total inelastic cross sections and rate coefficients for collisions $^6\mathrm{Li} + {}^6\mathrm{Li}_2(v_i, j_i)$, for a range of initial states of the dimer, at the collision energy of 0.928 nK in Table 8.8. Complex scattering lengths are given in Table 8.9. For all initial dimer states, we found the inelastic cross sections to be about three orders of magnitude larger than elastic at 1 nK. There is no systematic dependence of the inelastic cross sections on initial quantum number v_i and j_i. Molecules of bosonic and fermionic lithium atoms in excited rovibrational states have comparable stability against collisional decay with an identical atom.

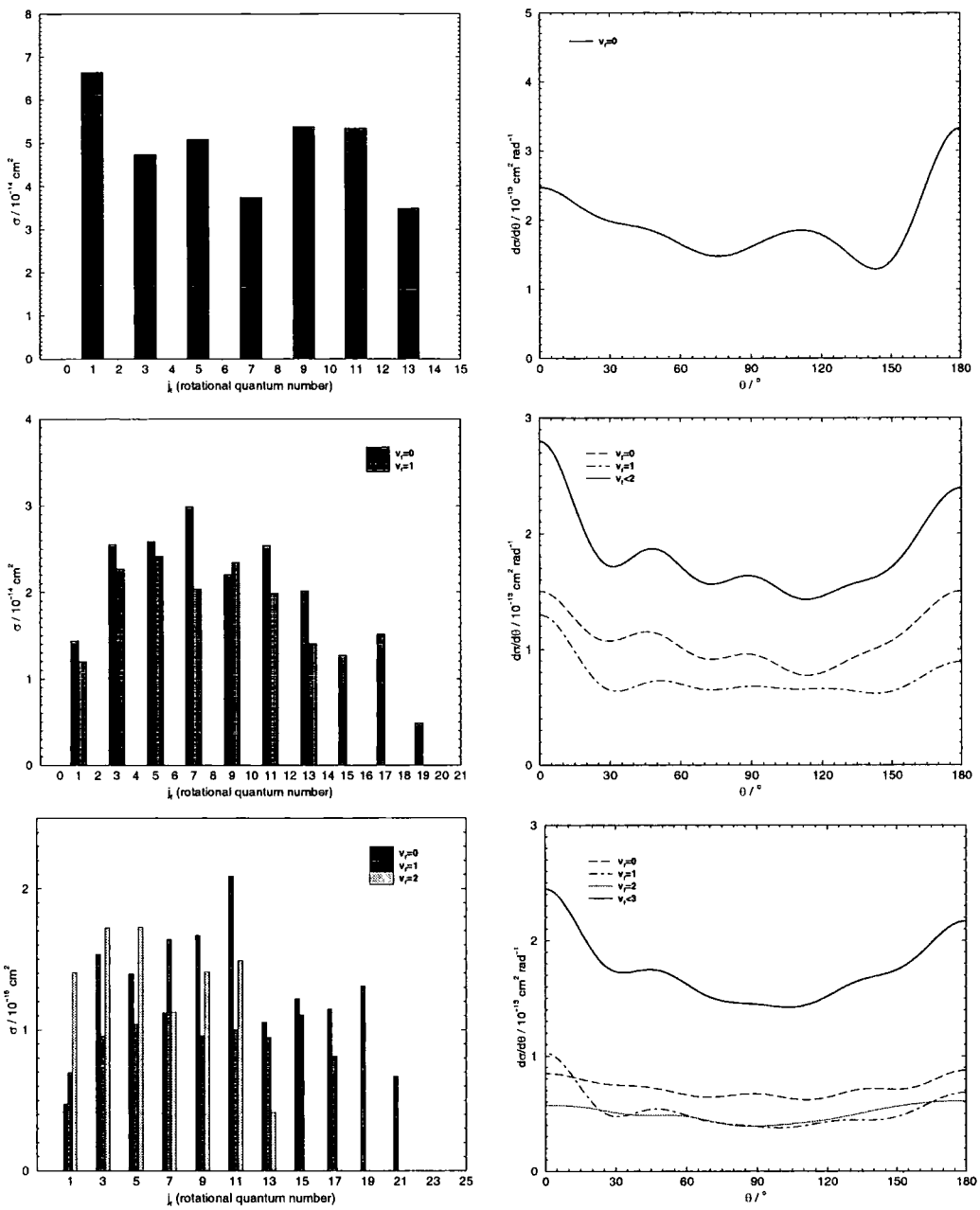

Figure 8.45: Final rotational distributions (left panels) and differential cross sections (right panels) for $^6\mathrm{Li} + {}^6\mathrm{Li}_2(v_i, j_i = 1)$ and $v_i = 1$ (top), 2 (middle), and 3 (bottom) at collision energy of 116 mK. Differential cross sections are integrated through the azimuthal angle and summed over the final states in each vibrational manifold and overall (solid line).

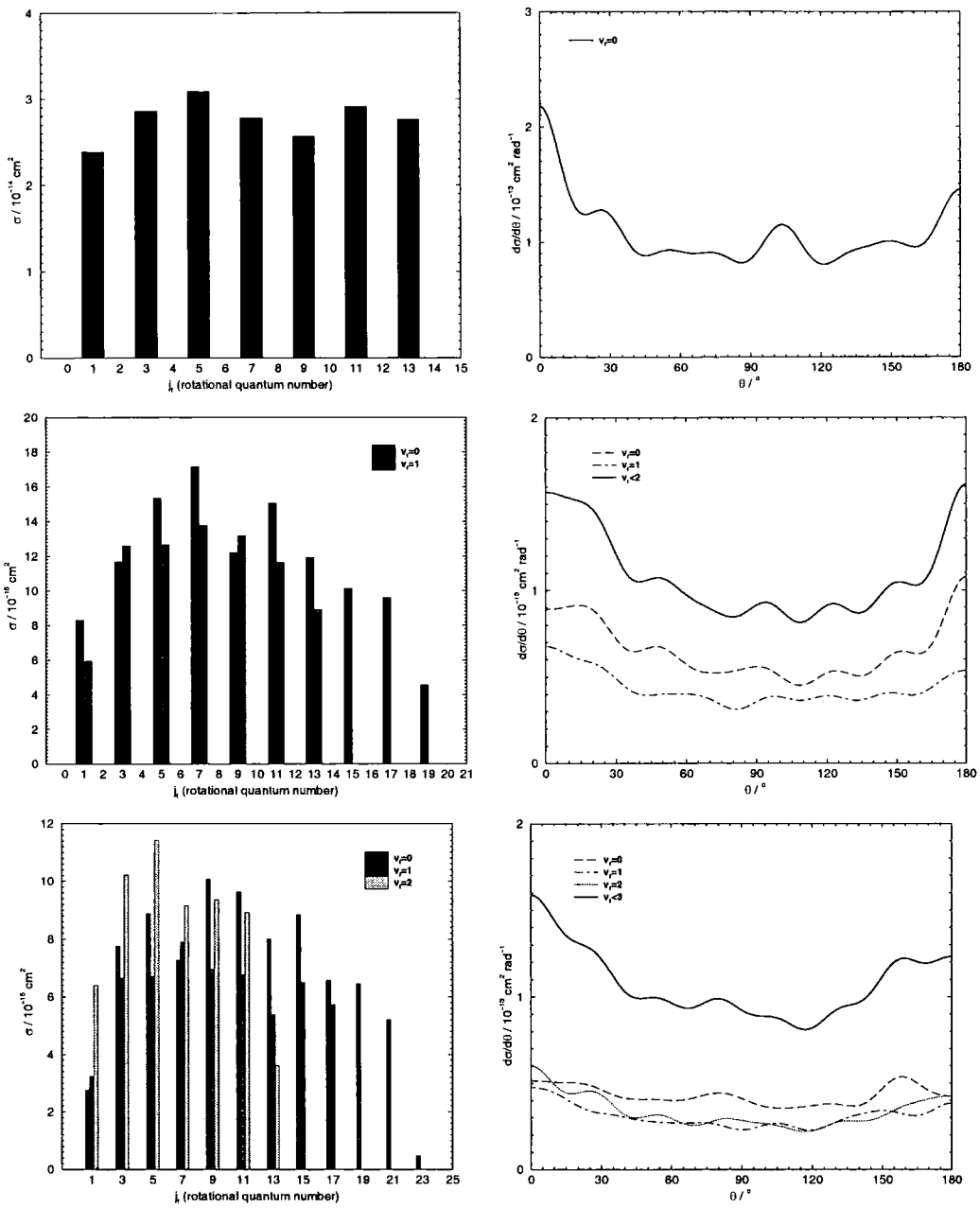

Figure 8.46: Final rotational distributions (left panels) and differential cross sections (right panels) for $^6\mathrm{Li} + {}^6\mathrm{Li}_2(v_i, j_i = 1)$ and $v_i = 1$ (top), 2 (middle), and 3 (bottom) at collision energy of 580 mK. Differential cross sections are integrated through the azimuthal angle and summed over the final states in each vibrational manifold and overall (solid line).

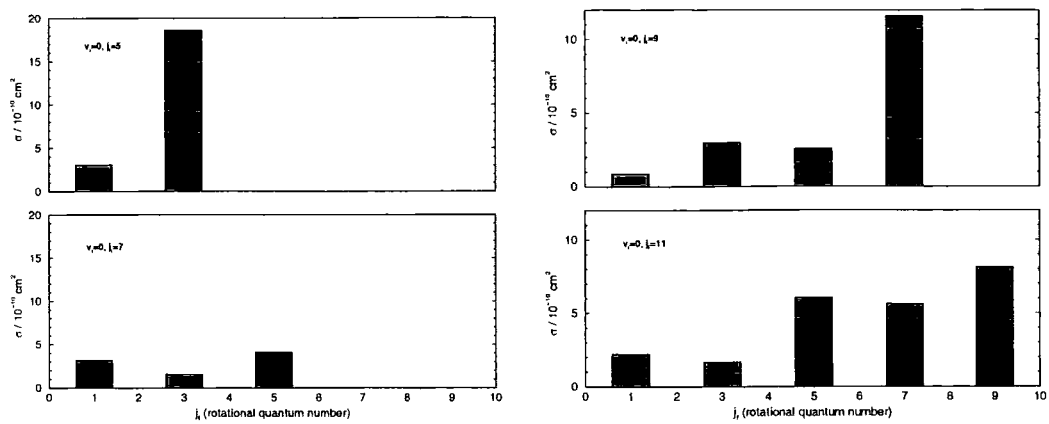

Figure 8.47: Final rotational distributions for $^6\mathrm{Li} + {}^6\mathrm{Li}_2(v_i = 0, j_i)$ at 0.928 nK for $j_i = 5$, 7, 9, and 11.

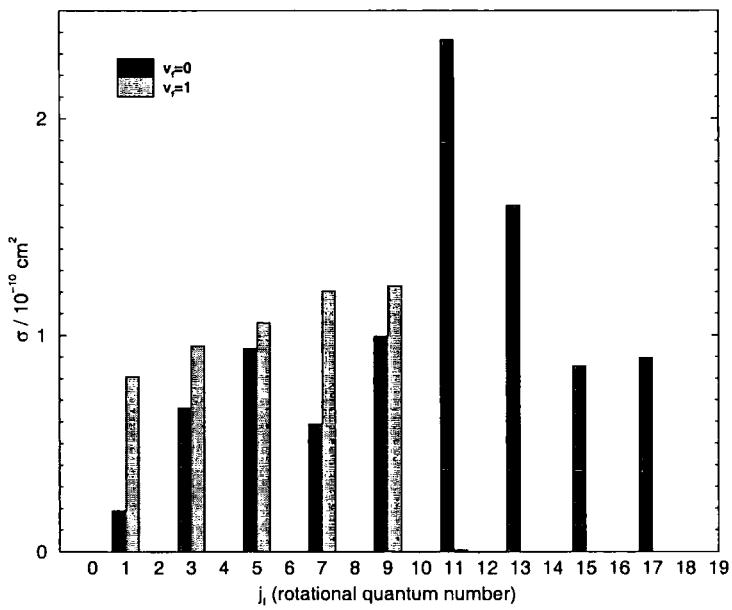

Figure 8.48: Final rotational distributions for $^6\mathrm{Li} + {}^6\mathrm{Li}_2(v_i = 1, j_i = 11)$ at 0.928 nK.

v_i, j_i	σ_{elas} [cm^2]	σ_{inel} [cm^2]	k_{elas} [cm^{3}s^{-1}]	k_{inel} [cm^{3}s^{-1}]	$\sigma_{\text{inel}}/\sigma_{\text{elas}}$
0, 1	$2.20 \cdot 10^{-12}$	-	$4.32 \cdot 10^{-13}$	-	-
0, 3	$1.11 \cdot 10^{-12}$	$2.62 \cdot 10^{-10}$	$2.18 \cdot 10^{-13}$	$5.14 \cdot 10^{-11}$	236
0, 5	$9.27 \cdot 10^{-13}$	$2.17 \cdot 10^{-9}$	$1.82 \cdot 10^{-13}$	$4.26 \cdot 10^{-10}$	2340
0, 7	$1.32 \cdot 10^{-13}$	$8.90 \cdot 10^{-10}$	$2.59 \cdot 10^{-14}$	$1.75 \cdot 10^{-10}$	6740
0, 9	$1.07 \cdot 10^{-12}$	$1.81 \cdot 10^{-9}$	$2.10 \cdot 10^{-13}$	$3.55 \cdot 10^{-10}$	1690
0, 11	$1.77 \cdot 10^{-12}$	$2.37 \cdot 10^{-9}$	$3.47 \cdot 10^{-13}$	$4.65 \cdot 10^{-10}$	1340
1, 1	$6.09 \cdot 10^{-13}$	$1.40 \cdot 10^{-9}$	$1.19 \cdot 10^{-13}$	$2.75 \cdot 10^{-10}$	2300
1, 3	$1.21 \cdot 10^{-12}$	$1.21 \cdot 10^{-9}$	$2.37 \cdot 10^{-13}$	$2.37 \cdot 10^{-10}$	1000
1, 5	$1.93 \cdot 10^{-12}$	$2.59 \cdot 10^{-9}$	$3.79 \cdot 10^{-13}$	$5.08 \cdot 10^{-10}$	1340
1, 7	$1.43 \cdot 10^{-12}$	$2.02 \cdot 10^{-9}$	$2.81 \cdot 10^{-13}$	$3.96 \cdot 10^{-10}$	1410
1, 9	$1.74 \cdot 10^{-12}$	$1.96 \cdot 10^{-9}$	$3.41 \cdot 10^{-13}$	$3.85 \cdot 10^{-10}$	1130
1, 11	$1.27 \cdot 10^{-12}$	$2.31 \cdot 10^{-9}$	$2.49 \cdot 10^{-13}$	$4.53 \cdot 10^{-10}$	1820
2, 1	$1.67 \cdot 10^{-12}$	$2.26 \cdot 10^{-9}$	$3.28 \cdot 10^{-13}$	$4.43 \cdot 10^{-10}$	1350
2, 3	$1.14 \cdot 10^{-12}$	$2.23 \cdot 10^{-9}$	$2.24 \cdot 10^{-13}$	$4.38 \cdot 10^{-10}$	1960
2, 5	$2.04 \cdot 10^{-12}$	$2.80 \cdot 10^{-9}$	$4.00 \cdot 10^{-13}$	$5.49 \cdot 10^{-10}$	1370
2, 7	$1.00 \cdot 10^{-12}$	$2.52 \cdot 10^{-9}$	$1.96 \cdot 10^{-13}$	$4.94 \cdot 10^{-10}$	2520
2, 9	$1.46 \cdot 10^{-12}$	$3.20 \cdot 10^{-9}$	$2.86 \cdot 10^{-13}$	$6.28 \cdot 10^{-10}$	2190
2, 11	$7.72 \cdot 10^{-13}$	$1.77 \cdot 10^{-9}$	$1.51 \cdot 10^{-13}$	$3.47 \cdot 10^{-10}$	2290
3, 1	$1.46 \cdot 10^{-12}$	$2.76 \cdot 10^{-9}$	$2.86 \cdot 10^{-13}$	$5.42 \cdot 10^{-10}$	1890
3, 3	$2.62 \cdot 10^{-12}$	$2.57 \cdot 10^{-9}$	$5.14 \cdot 10^{-13}$	$5.04 \cdot 10^{-10}$	981
3, 5	$1.87 \cdot 10^{-12}$	$2.71 \cdot 10^{-9}$	$3.67 \cdot 10^{-13}$	$5.32 \cdot 10^{-10}$	1450
3, 7	$1.31 \cdot 10^{-12}$	$2.77 \cdot 10^{-9}$	$2.57 \cdot 10^{-13}$	$5.43 \cdot 10^{-10}$	2110
3, 9	$1.17 \cdot 10^{-12}$	$2.10 \cdot 10^{-9}$	$2.30 \cdot 10^{-13}$	$4.12 \cdot 10^{-10}$	1790
3, 11	$6.92 \cdot 10^{-13}$	$2.00 \cdot 10^{-9}$	$1.36 \cdot 10^{-13}$	$3.92 \cdot 10^{-10}$	2890

Table 8.8: Elastic and total inelastic cross sections and rate coefficients for ^{6}Li + ^{6}Li$_2(v_i, j_i)$ at the collision energy of 0.928 nK for different initial states of the molecule.

v_i, j_i	Re(a) [nm]	−Im(a) [nm]	−Im(a)/Re(a)
0, 1	4.19	–	–
0, 3	2.96	0.260	0.0878
0, 5	1.68	2.14	1.27
0, 7	0.532	0.877	1.65
0, 9	2.31	1.78	0.772
0, 11	2.94	2.34	0.797
1, 1	1.72	1.38	0.803
1, 3	2.86	1.19	0.415
1, 5	2.98	2.55	0.856
1, 7	2.73	2.00	0.733
1, 9	2.21	2.28	1.03
1, 11	2.06	1.41	0.687
2, 1	2.88	2.22	0.772
2, 3	1.88	2.35	1.25
2, 5	2.94	2.76	0.940
2, 7	1.34	2.48	1.85
2, 9	1.30	3.15	2.43
2, 11	1.76	1.74	0.991
3, 1	2.05	2.72	1.33
3, 3	3.80	2.54	0.668
3, 5	2.78	2.67	0.961
3, 7	1.74	2.73	1.57
3, 9	2.23	2.07	0.929
3, 11	1.27	1.97	1.55

Table 8.9: Complex scattering lengths for $^6\mathrm{Li} + {}^6\mathrm{Li}_2(v_i, j_i)$ for different initial states of the molecule.

8.5 Collisions in isotopic mixtures

In this section, we study the reactive atom-diatom collisions in isotopic mixtures of lithium at collision energies below 1 K. There are four reactive collision systems that can be constructed from two lithium isotopes:

$$^7\mathrm{Li} + {}^6\mathrm{Li}^7\mathrm{Li}, \tag{8.13}$$

$$^6\mathrm{Li} + {}^7\mathrm{Li}_2, \tag{8.14}$$

$$^6\mathrm{Li} + {}^6\mathrm{Li}^7\mathrm{Li}, \tag{8.15}$$

$$^7\mathrm{Li} + {}^6\mathrm{Li}_2. \tag{8.16}$$

The novel feature in these systems is the possibility of a chemical reaction. The outcome of a collision can result in the formation of two different molecules. We call the process reactive when the products are different from the reactants, and we call it inelastic or elastic when the products and reactants are the same species. The ratio of cross sections for each of the outcomes is called the branching ratio.

Reactive processes in the systems (8.13) and (8.16) are exothermic because of the difference in zero-point energy of the reactant and product molecules (see the level diagram in Appendix A). From the viewpoint of formation of cold molecular systems from atoms or in the presence of atoms, it is interesting to note that a reaction is possible even from the molecular ground state and is likely to result in trap loss.

In this section we present the elastic, inelastic and reactive cross sections for the above systems, (8.13)−(8.16), where the dimer is in a low-lying rovibrational state. We are particularly interested in the sum of all transitions that lead to a kinetic energy release. The sum of all inelastic and reactive cross sections, we call, in this section, the loss cross section.

The symmetry under exchange of identical nuclei and how to implement it has already been discussed at the beginning of this chapter. First two systems, (8.13) and (8.14), consist of two bosons and a fermion and they share a common basis for use in the scattering calculations. Transition probabilities of the two processes at a given energy are related by the principle of microscopic reversibility [148]. The same is valid for the systems of two fermions and one boson, (8.15) and (8.16).

8.5.1 Convergence of cross sections

Convergence has not been studied separately for the isotopically mixed systems. We adopt discretization parameters and the cut-off in the basis set size from bosonic and fermionic systems with small modifications. The range of $\phi \in [0, \pi]$ is now full, so the grid size for integrations in θ and ϕ is taken to be 300×600. Matching is performed onto the states of two different arrangements at 45 a_0. The cut-off in energy was again somewhat below the $v = 8$, $j = 0$ level in each product diatomic as it gave converged results in scattering calculations in bosonic and fermionic systems. The sector size and step size were taken the same.

We have computed scattering cross sections for the $J = 0^+$ and 1^- partial waves for both systems and they are presented in the following subsections.

For the system of two bosons and a fermion, we included in our basis the hypersurface states that match onto the rovibrational states of the ^{6}Li^{7}Li molecule up to $j_{\max} = 32$, 29, 26, 23, 20, 17, 13, and 7, and the states of the ^{7}Li$_2$ molecule up to $j_{\max} = 32$, 30, 28, 24, 22, 18, 14, and 10, for $v = 0 - 7$, respectively. This leads to 272 channels for $\Omega = 0$, see Figure 8.49, and 256 for $\Omega = 1$. The evaluation of the basis functions was performed with the cut-off $K_{\max}$ in each sector taken from our earlier calculations. The size of the basis of pseudo-hyperspherical harmonics varied between 3660 and 6488.

For the system of two fermions and a boson, we included states that asymptotically match onto the rovibrational states of ^{6}Li^{7}Li up to $j_{\max} = 32$, 29, 27, 24, 21, 17, 14, and 9 for $v = 0 - 7$, respectively, and the states of ^{6}Li$_2$ up to $j_{\max} = 31$, 27, 25, 21, 19, 15, 11, and 7, in the same notation. This leads to 263 channels for $\Omega = 0$ and 255 for $\Omega = 1$. Evaluation in the pseudohyperspherical harmonics basis ranged in the diagonalization of matrices whose size varied again between 3660 and 6488.

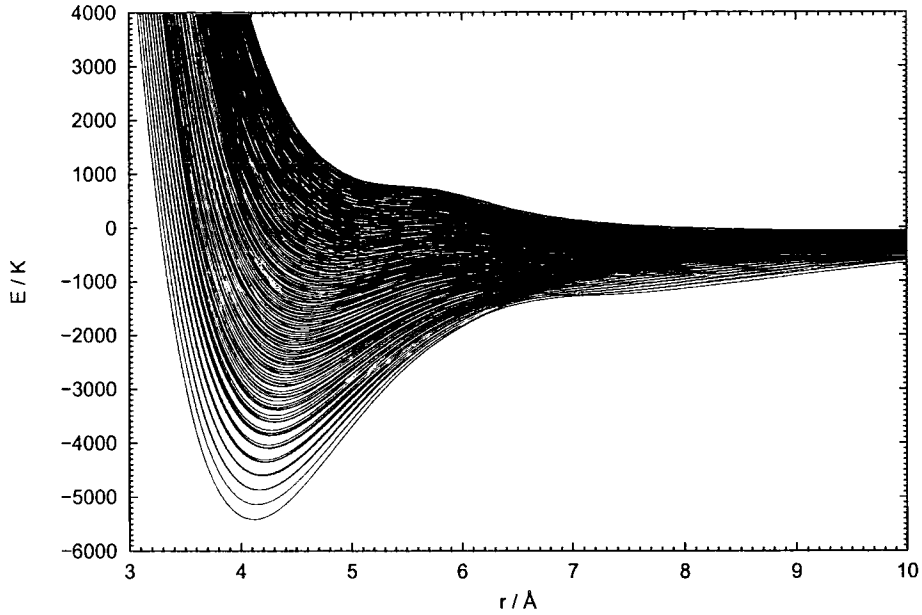

Figure 8.49: Eigenvalues ($N = 272$) of the hypersurface hamiltonian (6.47) for $\Omega = 0$ for the system of two bosonic and one fermionic nuclei in the electronic quartet ground state.

8.5.2 Vibrational relaxation cross sections and rate coefficients: ^{7}Li + ^{6}Li^{7}Li

We start by analysing the collision of bosonic lithium atom with a heteronuclear molecule,

$$^7\mathrm{Li} + {}^6\mathrm{Li}^7\mathrm{Li}(v_i, j_i) \rightarrow \begin{cases} {}^7\mathrm{Li} + {}^6\mathrm{Li}^7\mathrm{Li}(v_f, j_f) \\ {}^6\mathrm{Li} + {}^7\mathrm{Li}_2(v_f, j_f) \end{cases} . \tag{8.17}$$

Two different product molecules are possible. Heteronuclear lithium can have even and odd j rotational levels populated, while molecules from bosonic atoms populate only even j levels.

When the molecule is initially in the $v = 0$, $j = 0$ state and the collision energy is below 2.485 K ($v = 0$, $j = 2$ threshold), the accessible states in a non-reactive collision are the $v = 0$, $j = 0$ and $j = 1$, the latter being 0.825 K above the ground state of ^{6}Li^{7}Li. In a reactive collision, the ground state of ^{7}Li$_2$, $v = 0$, $j = 0$, and the $v = 0$, $j = 2$ state, are accessible, the former being 1.822 K below the ground state of ^{6}Li^{7}Li, and the latter 0.477 K above. The level diagram is shown in Appendix A.

The energy dependence of state-to-state cross sections for partial wave $J = 0$ are shown on the log-log and lin-log scales in Figure 8.50. Reactive cross sections in

the Wigner regime are particularly low in comparison with the inelastic in bosonic and fermionic systems. This is also reflected in the imaginary part of the scattering length that is much smaller than its real part, see Table 8.13, unlike the bosonic and fermionic lithium systems, but similar to the weakly coupled systems studied by Dalgarno and co-workers, cited in the introduction of this chapter. The imaginary part of the scattering length was found to be smaller than the real part in all cases where the number of inelastic (loss) channels was small, e.g. in the collisions involving the dimer in $v = 0$, $j = 2$ state in the bosonic system, and $v = 0$, $j = 3$ in the fermionic system. Inelastic and reactive cross sections at higher collision energies, when both events are possible, are comparable in magnitude.

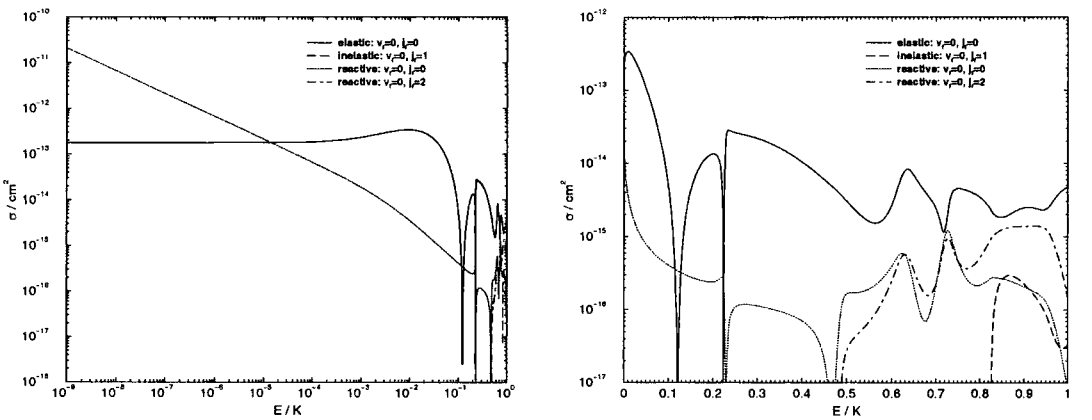

Figure 8.50: Energy dependence of elastic, inelastic and reactive cross sections for $^7\mathrm{Li} + {}^6\mathrm{Li}^7\mathrm{Li}(v_i = 0, j_i = 0)$ on the log-log scale (left) and lin-log scale (right).

Elastic and reactive cross sections are plotted on the linear scales in Figure 8.51. The structure in the energy dependence is analysed in terms of the individual eigenphases and eigenphase sum, shown in Figure 8.52. At 225 mK, there is a clear isolated Feshbach resonance. There is another resonance at $\approx$ 470 mK just below the threshold for the $v = 0$, $j = 2$ state, and there are two overlapping resonances at $\approx$ 630 mK and 725 mK. The cusp in the eigenphase sum at 825 mK corresponds to the opening of the $v = 0$, $j = 1$ channel in the reactant arrangement. The first minimum in the elastic cross section can evidently be associated with the zero of an eigenphase and is not a resonance.

Next, we examine the effect of initial rotation of dimer. Partial wave $J = 1^-$ contains the dominant contribution for the collisions involving dimer in the $j = 1$ rotational level. Product rotational distributions of collision involving dimers in the

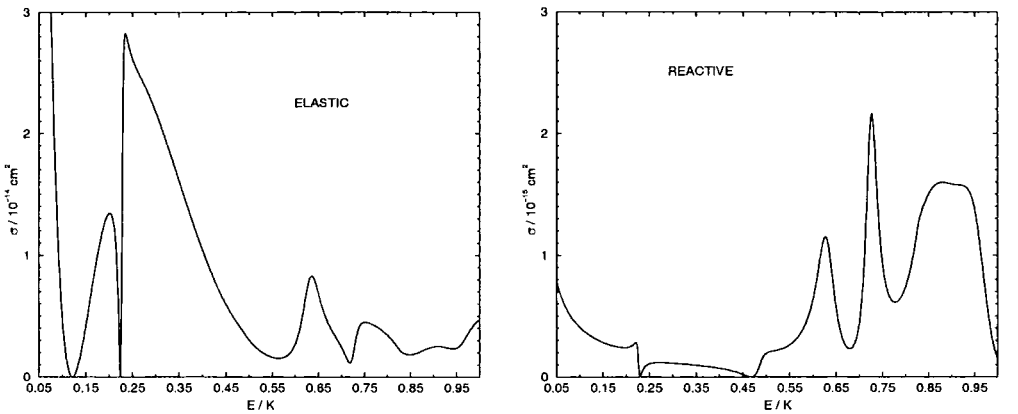

Figure 8.51: Energy dependence of elastic (left) and reactive (right) cross sections for ^{7}Li + ^{6}Li^{7}Li($v_i = 0, j_i = 0$).

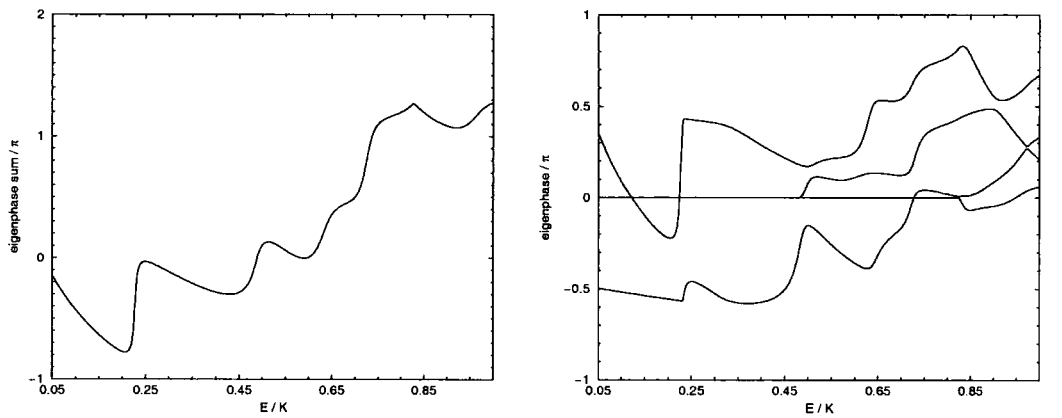

Figure 8.52: Energy dependence of eigenphase sum (left) and individual eigenphases (right) for ^{7}Li + ^{6}Li^{7}Li($v_i = 0, j_i = 0$).

$j_i = 0$ and $j_i = 1$ level are compared for $v_i = 1$ and $v_i = 2$ at 0.928 nK in Figure 8.53. Distributions are oscillatory in each case. The shape is strongly dependent on the initial level. Rotational excitation in the initial dimer state $v_i = 1$ produces an increase in the elastic, inelastic and reactive cross sections, while for the $v_i = 2$ level, it produces a decrease in the magnitude of cross sections. Results are summarized in Table 8.10 and 8.11.

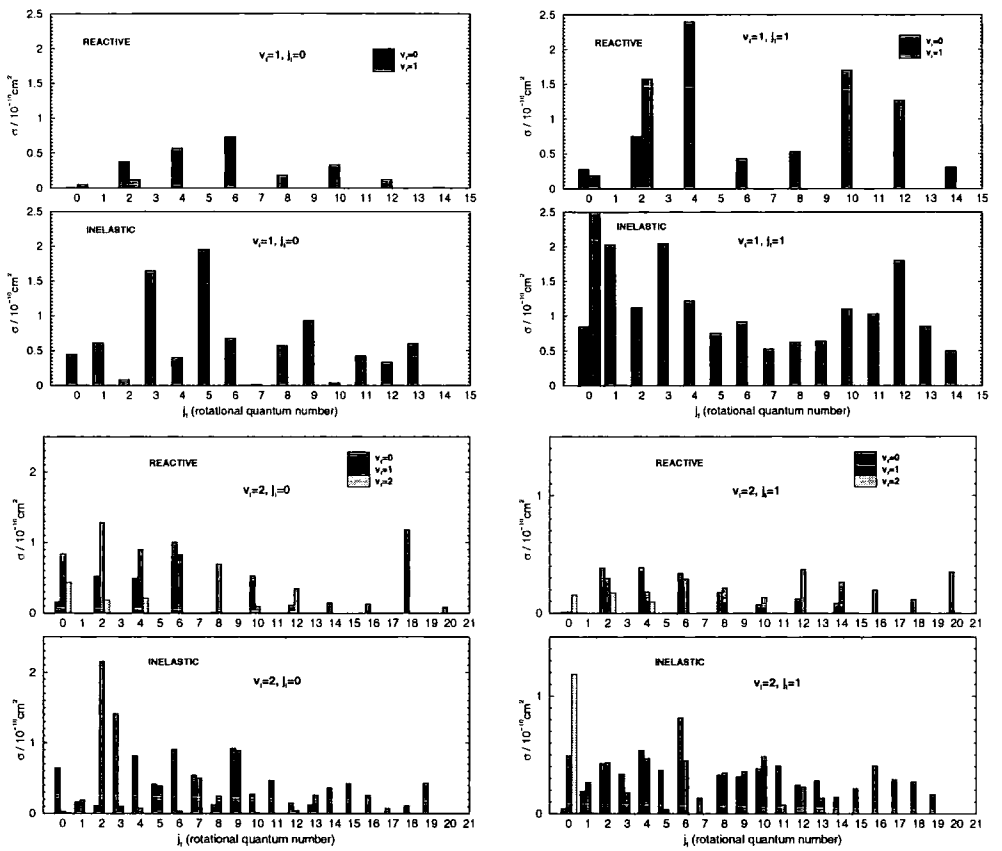

Figure 8.53: Final rotational distributions for $^7\mathrm{Li} + {}^6\mathrm{Li}^7\mathrm{Li}(v_i, j_i)$ at 1 nK for $v_i = 1$, $j_i = 0$ (top left) and $v_i = 1$, $j_i = 1$ (top right), $v_i = 2$, $j_i = 0$ (bottom left) and $v_i = 2$, $j_i = 1$ (bottom right).

Vibrational distributions for the initial state $v_i = 2$, $j_i = 0$ and $j_i = 1$ are compared in Figure 8.54. Lower vibrational levels in the inelastic and reactive arrangements tend to be more populated. This means that oscillatory patterns on average give similar contributions in each vibrational manifold and the number of available states does give a rough estimate of vibrational distributions.

Statistical predictions for branching ratios predict that the heteronuclear dimer is a more likely outcome in the collisions (8.17). Using relationship (8.11), $\sigma_{\mathrm{inel}}/\sigma_{\mathrm{reac}}$

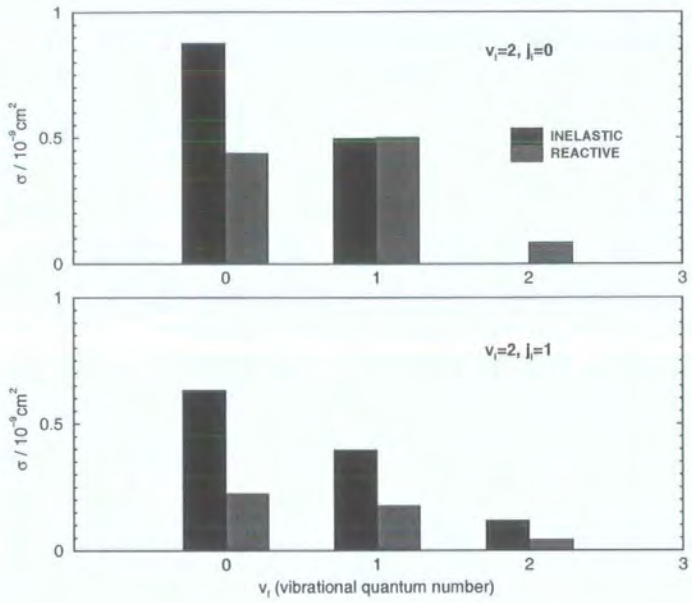

Figure 8.54: Final vibrational distributions for ^{7}Li + ^{6}Li^{7}Li($v_i = 2, j_i$) at 1 nK for $j_i = 0$ (top) and $j_i = 1$ (bottom).

v_i, j_i	σ_{elas} [cm^2]	$\sigma_{\text{inel}}^{\text{vib-rot}}$ [cm^2]	$\sigma_{\text{inel}}^{\text{rot}}$ [cm^2]	σ_{reac} [cm^2]
0, 0	$1.77 \cdot 10^{-13}$	-	-	$2.20 \cdot 10^{-11}$
1, 0	$1.32 \cdot 10^{-12}$	$8.79 \cdot 10^{-10}$	-	$2.56 \cdot 10^{-10}$
2, 0	$1.32 \cdot 10^{-12}$	$1.37 \cdot 10^{-9}$	-	$1.02 \cdot 10^{-9}$
3, 0	$1.09 \cdot 10^{-12}$	$1.30 \cdot 10^{-9}$	-	$8.74 \cdot 10^{-10}$
0, 1	$4.81 \cdot 10^{-12}$	-	$4.30 \cdot 10^{-10}$	$2.32 \cdot 10^{-9}$
1, 1	$1.52 \cdot 10^{-12}$	$1.60 \cdot 10^{-9}$	$2.47 \cdot 10^{-10}$	$9.47 \cdot 10^{-10}$
2, 1	$9.09 \cdot 10^{-13}$	$1.03 \cdot 10^{-9}$	$1.19 \cdot 10^{-10}$	$4.45 \cdot 10^{-10}$
3, 1	$9.51 \cdot 10^{-13}$	$1.60 \cdot 10^{-9}$	$7.11 \cdot 10^{-11}$	$6.28 \cdot 10^{-10}$

Table 8.10: Elastic, inelastic (pure rotational and rovibrational) and reactive cross sections for ^{7}Li + ^{6}Li^{7}Li(v_i, j_i) at 0.928 nK.

v_i, j_i	k_{elas} [cm^{3}s^{-1}]	k_{loss} [cm^{3}s^{-1}]
0, 0	$3.26 \cdot 10^{-14}$	$4.05 \cdot 10^{-12}$
1, 0	$2.43 \cdot 10^{-13}$	$2.09 \cdot 10^{-10}$
2, 0	$2.43 \cdot 10^{-13}$	$4.40 \cdot 10^{-10}$
3, 0	$2.01 \cdot 10^{-13}$	$4.00 \cdot 10^{-10}$
0, 1	$8.85 \cdot 10^{-13}$	$5.06 \cdot 10^{-10}$
1, 1	$2.80 \cdot 10^{-13}$	$5.14 \cdot 10^{-10}$
2, 1	$1.67 \cdot 10^{-13}$	$2.93 \cdot 10^{-10}$
3, 1	$1.75 \cdot 10^{-13}$	$4.23 \cdot 10^{-10}$

Table 8.11: Elastic and loss rate coefficients for ^{7}Li + ^{6}Li^{7}Li(v_i, j_i) at 0.928 nK.

is 1.752, 1.742, and 1.574, for $v_i = 1$, 2, and 3, respectively, for the dimer that is initially in $j_i = 0$ at 1 nK. These branching ratios may be compared with the values in Table 8.12. The preference for the heteronuclear dimer is present in all above cases, but the values depart strongly from those of the statistical model. For the case $v_i = 0$, $j_i = 1$, the statistical model also predicts preferential formation of the dimer composed of bosonic atoms, $\sigma_{\text{inel}}/\sigma_{\text{reac}} = 0.199$ at ultralow energies.

The loss cross sections are about three orders of magnitude higher than the elastic cross sections for vibrationally excited heteronuclear dimers. The consequences of that in ultracold atom-molecule mixtures were discussed earlier in the bosonic and fermionic systems. Complex scattering lengths for the collisions studied in this subsection are summarized in Table 8.13.

v_i, j_i	$\sigma_{\text{inel}}/\sigma_{\text{reac}}$	$\sigma_{\text{loss}}/\sigma_{\text{elas}}$
0, 0	-	124
1, 0	3.43	860
2, 0	1.34	1810
3, 0	1.49	1990
0, 1	0.185	572
1, 1	1.95	1840
2, 1	2.58	1750
3, 1	2.66	2420

Table 8.12: Branching ratios and ratios of loss and elastic cross sections for ^{7}Li + ^{6}Li^{7}Li(v_i, j_i) at 0.928 nK.

v_i, j_i	Re(a) [nm]	−Im(a) [nm]
0, 0	1.19	0.0233
1, 0	3.01	1.19
2, 0	2.04	2.52
3, 0	1.86	2.29
0, 1	5.46	2.90
1, 1	1.85	2.94
2, 1	2.10	1.68
3, 1	1.71	2.15

Table 8.13: Complex scattering lengths for ^{7}Li + ^{6}Li^{7}Li(v_i, j_i).

8.5.3 Vibrational relaxation cross sections and rate coefficients: ^{6}Li + ^{7}Li$_2$

We proceed by studying the collisions of the dimer made of bosonic lithium atoms with a fermionic atom,

$$^6\text{Li} + {}^7\text{Li}_2(v_i, j_i) \rightarrow \begin{cases} {}^6\text{Li} + {}^7\text{Li}_2(v_f, j_f) \\ {}^7\text{Li} + {}^6\text{Li}^7\text{Li}(v_f, j_f) \end{cases} . \tag{8.18}$$

This collision includes the reverse process to the reaction in (8.17). Product molecules of the collisions (8.17) and (8.18) are same. Initial energetics is different. It is interesting to see the differences this implies.

The collision with the dimer that is initially in the $v = 0$, $j = 0$ state does not lead to a reaction below 1.822 K. For collisions with the vibrationally excited dimers, we report the cross sections and rate coefficients in Table 8.14. The magnitudes are similar to the other vibrationally excited systems studied in this chapter, with no systematic dependence on the initial v quantum number. Complex scattering lengths are given for comparison in Table 8.16.

We compare the product rotational and vibrational distributions for the collision (8.18), shown in Figure 8.55, with the ones for the collision (8.17), shown in Figure 8.53 and 8.54, for $v_i = 2$, $j_i = 0$. The oscillatory patterns are qualitatively different. The initial level $v = 2$, $j = 0$ of the ^{7}Li$_2$ is 3.35% lower than the same level in ^{6}Li^{7}Li, which amounts to 7.12 K. Oscillatory patterns are also different to those for the collision of the same molecule but with the different isotope, shown in Figure 8.12. There is no strong preference for even or odd final rotational levels in the product

heteronuclear dimer.

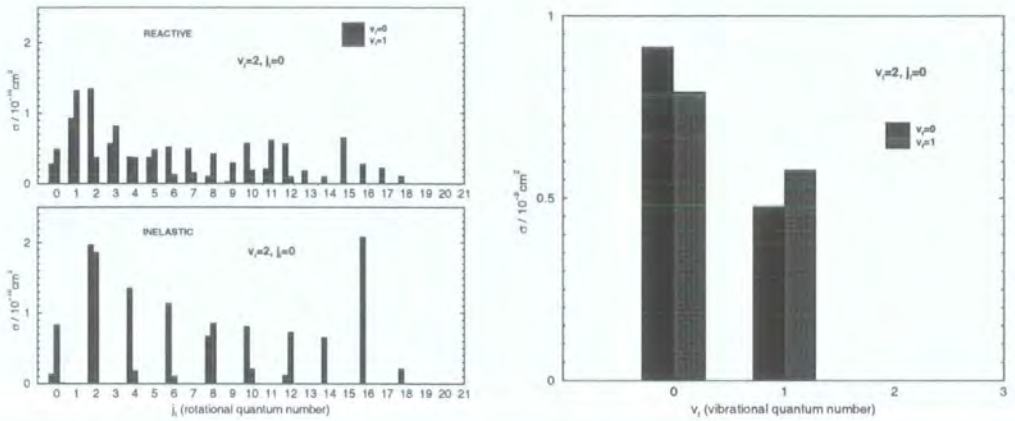

Figure 8.55: Final rotational (left) and vibrational (right) distributions for $^6\mathrm{Li} + {}^7\mathrm{Li}_2(v_i = 2, j_i = 0)$ at 0.928 nK.

v_i, j_i	σ_{elas} [cm^2]	σ_{inel} [cm^2]	σ_{reac} [cm^2]	k_{elas} [cm^{3}s^{-1}]	k_{loss} [cm^{3}s^{-1}]
0, 0	$1.29 \cdot 10^{-12}$	-	-	$2.47 \cdot 10^{-13}$	-
1, 0	$1.33 \cdot 10^{-12}$	$5.70 \cdot 10^{-10}$	$8.85 \cdot 10^{-10}$	$2.55 \cdot 10^{-13}$	$2.79 \cdot 10^{-10}$
2, 0	$1.14 \cdot 10^{-12}$	$1.39 \cdot 10^{-9}$	$1.37 \cdot 10^{-9}$	$2.18 \cdot 10^{-13}$	$5.28 \cdot 10^{-10}$
3, 0	$1.51 \cdot 10^{-12}$	$1.00 \cdot 10^{-9}$	$1.42 \cdot 10^{-9}$	$2.89 \cdot 10^{-13}$	$4.63 \cdot 10^{-10}$

Table 8.14: Elastic, inelastic and reactive cross sections and rate coefficients for $^6\mathrm{Li} + {}^7\mathrm{Li}_2(v_i, j_i)$ at 0.928 nK.

Branching ratios and ratios of loss and elastic cross sections are given for different initial vibrational states of the dimer at the collision energy of 0.928 nK in Table 8.15. Statistical predictions for the branching ratio, using (8.11) are 1.751, 1.781, and 1.618, for $v_i = 1$, 2, and 3, respectively. Loss cross sections are again about three orders of magnitude larger than the elastic at 1 nK.

8.5.4 Vibrational relaxation cross sections and rate coefficients: $^6\mathrm{Li} + {}^6\mathrm{Li}^7\mathrm{Li}$

Another possibility we investigate here is the collision of the heteronuclear lithium dimer with a fermionic lithium atom,

$$^6\mathrm{Li} + {}^6\mathrm{Li}^7\mathrm{Li}(v_i, j_i) \rightarrow \begin{cases} {}^6\mathrm{Li} + {}^6\mathrm{Li}^7\mathrm{Li}(v_f, j_f) \\ {}^7\mathrm{Li} + {}^6\mathrm{Li}_2(v_f, j_f) \end{cases} . \tag{8.19}$$

v_i, j_i	$\sigma_{\rm reac}/\sigma_{\rm inel}$	$\sigma_{\rm loss}/\sigma_{\rm elas}$
0, 0	-	-
1, 0	1.55	1090
2, 0	0.990	2410
3, 0	1.42	1600

Table 8.15: Branching ratios and ratios of loss and elastic cross sections for ^{6}Li + ^{7}Li$_2(v_i, j_i)$ at 0.928 nK.

v_i, j_i	Re(a) [nm]	$-$Im(a) [nm]
0, 0	3.20	-
1, 0	2.90	1.47
2, 0	1.16	2.79
3, 0	2.45	2.45

Table 8.16: Complex scattering lengths for ^{6}Li + ^{7}Li$_2(v_i, j_i)$.

Heteronuclear lithium can populate even and odd j rotational levels, while fermionic molecule populates only odd levels. The ground state heteronuclear molecules are stable against such collisions up to the collision energy of 0.825 K, where the $v = 0$, $j = 1$ level of the heteronuclear dimer becomes energetically accessible.

We show the product rotational and vibrational distributions for collisions with the dimer in the $v_i = 2$ state and in $j_i = 0$ and $j_i = 1$ rotational levels in Figure 8.56 and 8.57. The shape of the inelastic rotational distributions is different from the one in Figure 8.53, that involved the same dimer in collision with a different (bosonic) lithium isotope. Vibrational distributions show preference for lower vibrational quantum numbers.

Elastic, inelastic and reactive cross sections and rate coefficients are reported in Table 8.17 and 8.18. Again, there is little new that can be said in an attempt to compare them with the values in Table 8.10, for the collision of the same molecule with a bosonic atom. The effect of the rotational excitation is such that the patterns in rotational distributions drastically change, see Figure 8.56. Cross sections for pure rotational transitions are comparable to other state-to-state transitions and the values of cross sections in the zero-energy limit unpredictably change, but stay within an order of magnitude, as in all the above vibrationally excited systems we studied. Complex scattering lengths are reported in Table 8.20.

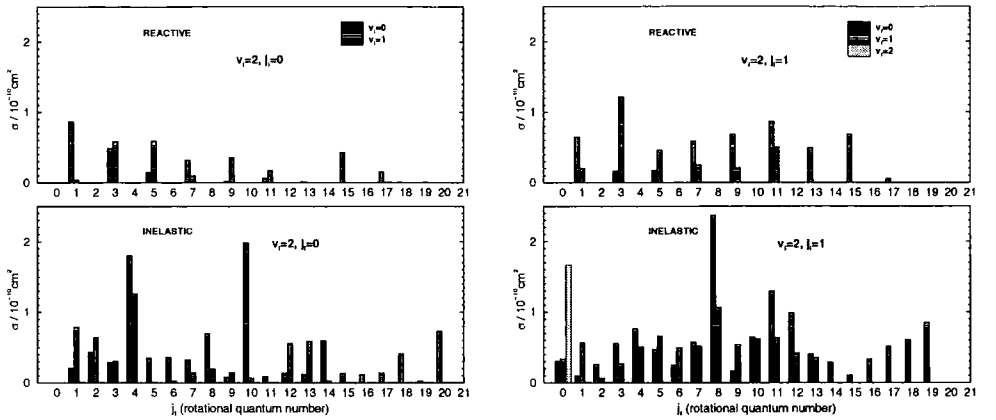

Figure 8.56: Final rotational distributions for $^6\mathrm{Li} + ^6\mathrm{Li}^7\mathrm{Li}(v_i = 2, j_i)$ at 0.928 nK for $j_i = 0$ (left) and $j_i = 1$ (right).

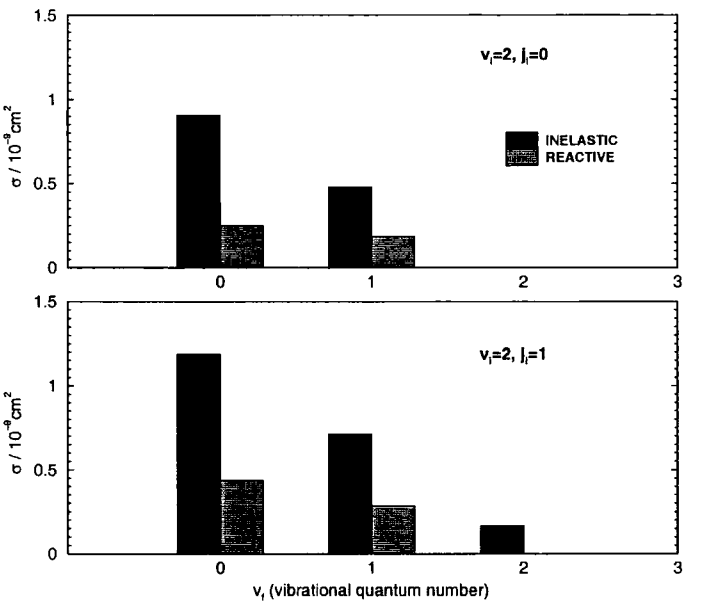

Figure 8.57: Final vibrational distribution for $^6\mathrm{Li} + ^6\mathrm{Li}^7\mathrm{Li}(v_i = 2, j_i)$ at 0.928 nK for $j_i = 0$ (top) and $j_i = 1$ (bottom).

v_i, j_i	σ_{elas} [cm^2]	$\sigma_{\text{inel}}^{\text{vib-rot}}$ [cm^2]	$\sigma_{\text{inel}}^{\text{rot}}$ [cm^2]	σ_{reac} [cm^2]
0, 0	$4.71 \cdot 10^{-12}$	-	-	-
1, 0	$6.43 \cdot 10^{-13}$	$1.15 \cdot 10^{-9}$	-	$2.12 \cdot 10^{-10}$
2, 0	$1.12 \cdot 10^{-12}$	$1.39 \cdot 10^{-9}$	-	$4.37 \cdot 10^{-10}$
3, 0	$1.54 \cdot 10^{-12}$	$1.34 \cdot 10^{-9}$	-	$9.49 \cdot 10^{-10}$
0, 1	$2.74 \cdot 10^{-12}$	-	$5.84 \cdot 10^{-10}$	-
1, 1	$7.56 \cdot 10^{-13}$	$1.88 \cdot 10^{-9}$	$1.60 \cdot 10^{-10}$	$2.72 \cdot 10^{-10}$
2, 1	$1.19 \cdot 10^{-12}$	$1.90 \cdot 10^{-9}$	$1.67 \cdot 10^{-10}$	$7.21 \cdot 10^{-10}$
3, 1	$1.27 \cdot 10^{-12}$	$1.47 \cdot 10^{-9}$	$8.30 \cdot 10^{-11}$	$7.76 \cdot 10^{-10}$

Table 8.17: Elastic, inelastic (pure rotational and rovibrational) cross sections for $^6\text{Li} + {}^6\text{Li}^7\text{Li}(v_i, j_i)$ at 0.928 nK.

v_i, j_i	k_{elas} [cm^{3}s^{-1}]	k_{loss} [cm^{3}s^{-1}]
0, 0	$9.12 \cdot 10^{-13}$	-
1, 0	$1.25 \cdot 10^{-13}$	$2.64 \cdot 10^{-10}$
2, 0	$2.17 \cdot 10^{-13}$	$3.53 \cdot 10^{-10}$
3, 0	$2.98 \cdot 10^{-13}$	$4.43 \cdot 10^{-10}$
0, 1	$5.31 \cdot 10^{-13}$	$1.13 \cdot 10^{-10}$
1, 1	$1.46 \cdot 10^{-13}$	$4.48 \cdot 10^{-10}$
2, 1	$2.30 \cdot 10^{-13}$	$5.40 \cdot 10^{-10}$
3, 1	$2.46 \cdot 10^{-13}$	$4.51 \cdot 10^{-10}$

Table 8.18: Elastic and loss rate coefficients for $^6\text{Li} + {}^6\text{Li}^7\text{Li}(v_i, j_i)$ at 0.928 nK.

Branching ratios and ratios of loss and elastic cross sections are given in Table 8.19. Branching ratios predicted by the statistical model, using 8.11, are 2.182, 2.285, and 2.017, for $v_i = 1$, 2, and 3, and $j_i = 0$, respectively. Quantitative departures from the statistical model are large, but the heteronuclear dimer is preferentially formed in the reaction in each case studied. Loss cross sections are about three orders of magnitude larger than elastic, except in case of the collision involving dimer initially in the $v = 0$, $j = 1$ state, with one available inelastic channel.

v_i, j_i	$\sigma_{\text{inel}}/\sigma_{\text{reac}}$	$\sigma_{\text{loss}}/\sigma_{\text{elas}}$
0, 0	-	-
1, 0	5.42	2110
2, 0	3.18	1630
3, 0	1.41	1490
0, 1	-	213
1, 1	7.50	3070
2, 1	2.87	2350
3, 1	2.00	1830

Table 8.19: Branching ratios and ratios of loss and elastic cross sections for ^{6}Li + ^{6}Li^{7}Li(v_i, j_i) at 0.928 nK.

v_i, j_i	Re(a) [nm]	−Im(a) [nm]
0, 0	6.12	-
1, 0	1.81	1.36
2, 0	2.36	1.82
3, 0	2.66	2.29
0, 1	4.64	0.586
1, 1	0.828	2.31
2, 1	1.32	2.79
3, 1	2.16	2.33

Table 8.20: Complex scattering lengths for ^{6}Li + ^{6}Li^{7}Li(v_i, j_i).

8.5.5 Vibrational relaxation cross sections and rate coefficients: $^7Li + {}^6Li_2$

Finally, we look at the collision of a dimer composed of fermionic atoms with a bosonic atom,

$$^7\mathrm{Li} + {}^6\mathrm{Li}_2(v_i, j_i) \rightarrow \begin{cases} {}^7\mathrm{Li} + {}^6\mathrm{Li}_2(v_f, j_f) \\ {}^6\mathrm{Li} + {}^6\mathrm{Li}{}^7\mathrm{Li}(v_f, j_f) \end{cases} . \tag{8.20}$$

This collision includes the reverse process to the reaction in (8.19). Due to the differences of zero-point energies, the collision of atom with the ground-state dimer (8.20) may result in an exothermic reaction.

The accessible states for the collision involving a ground state dimer below the collision energy of 2.322 K (threshold for the $v = 0$, $j = 3$ state of $^6Li^7Li$) are the states of the heteronuclear dimer $v = 0$, $j = 0$, 1, and 2. They are 2.643 K, 1.818 K, and 0.1573 K below the ground state of the reactant molecule respectively. The level diagram is shown in Appendix A.

The energy dependence of the elastic and reactive cross sections for partial wave $J = 1^-$ are shown in Figure 8.58. We again find that the reactive cross sections in the zero-energy limit are about an order of magnitude lower in comparison with cases where more inelastic channels are available, see Table 8.21. The imaginary part of the scattering length is also small in comparison with the collisions involving vibrationally excited dimers, see Table 8.23.

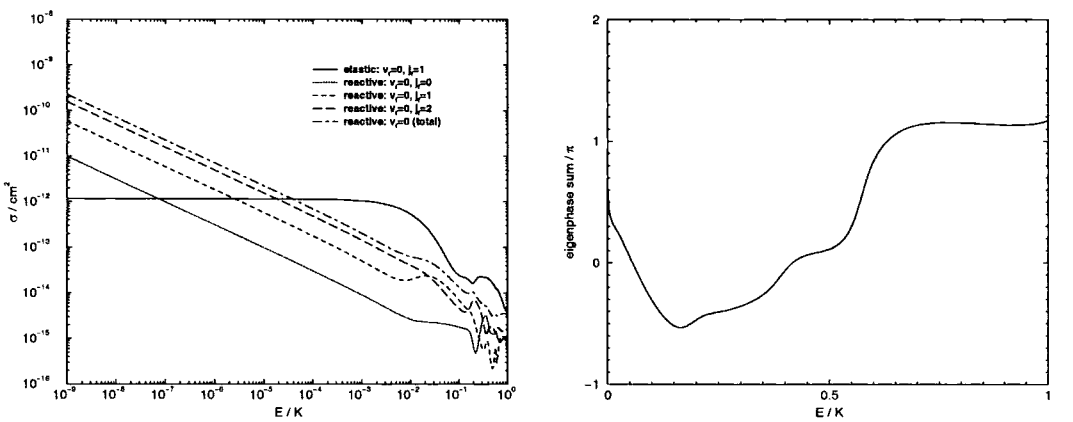

Figure 8.58: Energy dependence of elastic and reactive cross sections (left) and eigenphase sum (right) for $^7Li + {}^6Li_2(v_i = 0, j_i = 1)$.

The energy dependence of the eigenphase sum in Figure 8.58 gives evidence of

resonances at collision energies of $\approx$ 200 mK, 370 mK and 570 mK. They may be associated with the features in the reactive cross sections, shown in Figure 8.59 on the linear scales.

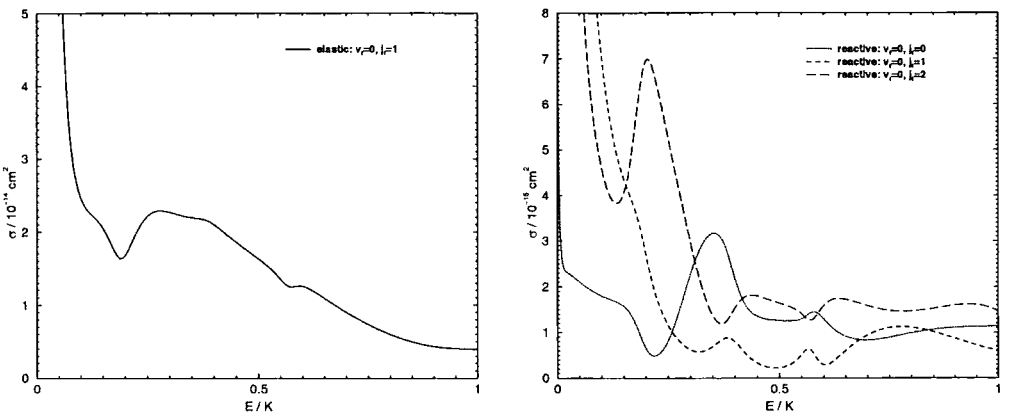

Figure 8.59: Energy dependence of elastic (left) and reactive (right) cross sections for ^{7}Li + ^{6}Li$_2$($v_i = 0, j_i = 1$) (linear scales).

Collisions involving vibrationally excited dimers usually have a high inelastic rate coefficient as in the collisions involving other isotopic combinations, see Table 8.21. We again show an example of the oscillatory product rotational distributions in Figure 8.60 for the case of the $v = 2$, $j = 1$ initial dimer state. Vibrational distribution in Figure 8.60 shows that lower vibrational levels are more likely to be populated in collisions at ultralow energies.

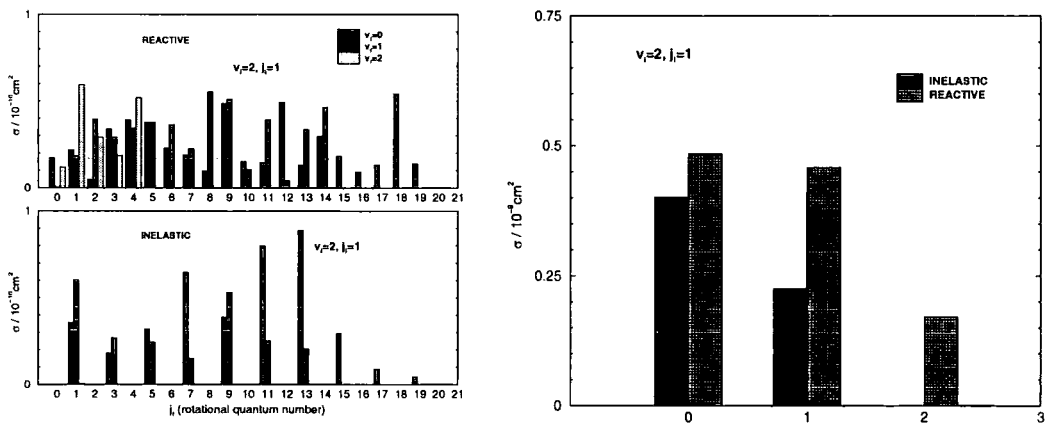

Figure 8.60: Final rotational (left) and vibrational (right) distributions for ^{7}Li + ^{6}Li$_2$($v_i = 2, j_i = 1$) at 0.928 nK.

Branching ratios for different initial states of the dimer at collision energy of 0.928 nK are given in Table 8.22. The values depart from the statistical predictions

v_i, j_i	σ_{elas} [cm^2]	σ_{inel} [cm^2]	σ_{reac} [cm^2]	k_{elas} [cm^{3}s^{-1}]	k_{loss} [cm^{3}s^{-1}]
0, 1	$1.17 \cdot 10^{-12}$	-	$2.34 \cdot 10^{-10}$	$2.18 \cdot 10^{-13}$	$4.37 \cdot 10^{-11}$
1, 1	$1.62 \cdot 10^{-12}$	$1.00 \cdot 10^{-9}$	$1.76 \cdot 10^{-9}$	$3.02 \cdot 10^{-13}$	$5.15 \cdot 10^{-10}$
2, 1	$6.61 \cdot 10^{-13}$	$2.66 \cdot 10^{-10}$	$1.12 \cdot 10^{-9}$	$1.23 \cdot 10^{-13}$	$2.58 \cdot 10^{-10}$
3, 1	$8.05 \cdot 10^{-13}$	$5.29 \cdot 10^{-10}$	$1.07 \cdot 10^{-9}$	$1.50 \cdot 10^{-13}$	$2.98 \cdot 10^{-10}$

Table 8.21: Elastic, inelastic, and reactive cross sections and rate coefficients for $^7\text{Li} + {}^6\text{Li}_2(v_i, j_i)$ at 0.928 nK.

of 2.220, 2.184, and 1.984, but show preference for the formation of heteronuclear dimer with more available states. Loss rates are about three orders of magnitude more efficient than the elastic rates.

v_i, j_i	$\sigma_{\text{reac}}/\sigma_{\text{inel}}$	$\sigma_{\text{loss}}/\sigma_{\text{elas}}$
0, 1	-	200
1, 1	1.76	1710
2, 1	4.20	2100
3, 1	2.02	1990

Table 8.22: Branching ratios and ratios of loss and elastic cross sections for $^7\text{Li} + {}^6\text{Li}_2(v_i, j_i)$ at 0.928 nK.

v_i	Re(a) [nm]	$-$Im(a) [nm]
0, 1	3.04	0.244
1, 1	2.17	2.86
2, 1	1.41	1.81
3, 1	1.91	1.66

Table 8.23: Complex scattering lengths for $^7\text{Li} + {}^6\text{Li}_2(v_i, j_i)$.

8.6 Other atom-diatom alkali collisions

We conclude this chapter by making estimates on the inelastic rate coefficients for other atom-diatom alkali systems in the electronic quartet states. We found that the classical Langevin model gives semi-quantitatively good description of the inelastic

rate coefficients outside the Wigner regime,

$$k = \frac{3\pi}{2^{1/6}} \frac{C_6^{1/3}}{\mu^{1/2}} E^{1/6}, \tag{8.21}$$

where C_6 is the atom-molecule dispersion coefficient and μ is the atom-molecule reduced mass. The inelastic rate coefficients for different systems will then be proportional to $C_6^{1/3}/\mu^{1/2}$. The resulting inelastic rate coefficients for ^{23}Na, ^{40}K, ^{87}Rb and ^{133}Cs are lower than that for lithium by factors of 1.81, 1.75, 2.43, and 2.65, respectively, using C_6 coefficients equal to twice the atomic dispersion coefficients from [208]. The lower bound of applicability of the model may be estimated from the centrifugal barrier heights for $l = 3$, which are 6.86 mK, 1.89 mK, 0.537 mK, and 0.235 mK, for Na, ..., Cs, respectively. The applicability of the model relies on the assumption that the inelastic probability is high. This implies that the elastic rate coefficient will not differ by a large factor from the inelastic. Alkali molecules in low rovibrational states, whether made of bosonic or fermionic atoms, must quickly be removed from the presence of atoms to prevent collisional loss.

The zero-energy limits of elastic cross sections and inelastic rate coefficients will be discussed in more detail in the next chapter.

Chapter 9

Potential sensitivity analysis: $Li + Li_2$

9.1 Introduction

The cross sections for elastic atom-atom collisions in the limit of zero collision energy are determined in terms of a single parameter, the scattering length. Scattering length is very sensitive to the details of the interaction potential and its properties and dependence on potential are well established [162]. Only with the best available *ab-initio* potentials and the lightest diatomic systems, a theoretical prediction of the scattering length is within reach today [209]. Otherwise, one must build some experimental information in the potential or adjust the potential to reproduce the experimentally determined value of the scattering length in order to obtain a potential that describes accurately low-energy phenomena.

Atom-molecule collisions in the zero collision-energy limit may be parametrized by a complex scattering length, whose imaginary part is proportional to the inelastic probability current density. The dependence of cross sections and scattering length for ultracold atom-molecule collisions on the potential energy surface has been recently reported for the $Na + Na_2$ system [210]. Our aim in this chapter is to explore the sensitivity of cross sections in the bosonic and fermionic lithium systems at ultracold energies on changes in the potential. This will provide an insight in how good the potential energy surface needs to be to give us quantitatively accurate results. It is also desirable to estimate how much one can rely on the quantitative aspects of the results of the previous chapter.

A simple model that describes the behaviour of the complex scattering length at low collision energies was given [185] by a radially symmetric complex square well potential:

$$U(r) = 2\mu V(r) = \begin{cases} -(U_1 + iU_2), & r < a \\ 0, & r > a \end{cases} . \tag{9.1}$$

The phase shift δ_0 (for $l = 0$) is determined to be

$$\delta_0 = -ka + \arctan\left(\frac{k}{\kappa}\tan\kappa a\right), \tag{9.2}$$

with

$$\kappa^2 = k^2 + U_1 + iU_2, \tag{9.3}$$

by matching the logarithmic derivatives of the interior solution, $j_l(\kappa r)$ valid for $r < a$, and the general potential-free exterior solution, $j_l(kr) - \tan(\delta_l) n_l(kr)$ valid for $r > a$,

at $r = a$ [156]. From the complex phase shift (9.2), the complex scattering length, $\alpha - i\beta$, is obtained by equating the real and imaginary components in (7.48):

$$\alpha = a - \frac{\lambda_1 \tan(\lambda_1 a)\mathrm{sech}^2(\lambda_2 a) + \lambda_2 \tanh(\lambda_2 a)\sec^2(\lambda_1 a)}{(\lambda_1^2 + \lambda_2^2)[1 + \tan^2(\lambda_1 a)\tanh^2(\lambda_2 a)]} \tag{9.4}$$

$$\beta = \frac{\lambda_1 \tanh(\lambda_2 a)\sec^2(\lambda_1 a) - \lambda_2 \tan(\lambda_1 a)\mathrm{sech}^2(\lambda_2 a)}{(\lambda_1^2 + \lambda_2^2)[1 + \tan^2(\lambda_1 a)\tanh^2(\lambda_2 a)]} \tag{9.5}$$

where

$$\lambda = \lambda_1 + i\lambda_2 = \sqrt{U_1 + iU_2}. \tag{9.6}$$

When $U_2 \ll U_1$, $\lambda_1 \approx \sqrt{U_1}$ and $\lambda_2 \approx U_2/2\sqrt{U_1}$. The relations (9.4) and (9.5) are plotted in Figure 9.1 for different $\lambda_2 a$.

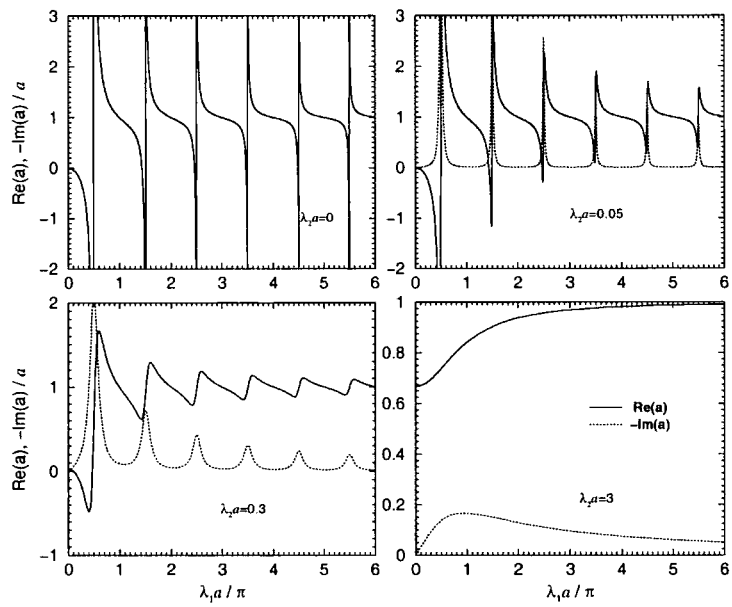

Figure 9.1: Dependence of the complex scattering length for a complex square well potential of range a on the potential through $\lambda_1 + i\lambda_2 = \sqrt{U_1 + iU_2}$.

In the case $\lambda_2 a = 0$, the imaginary part of the scattering length is zero and the real part has familiar behaviour (7.35) with poles at zero-energy resonances. In the case of a weak coupling the poles in the real part are removed and the ratio of imaginary and real part is fairly constant except at the positions of resonances, as noted in Ref. 185. When the imaginary part of the potential is further increased and system is more coupled, the sharp tangent-like profiles of the real part become more blunt.

Having these results in mind, we analyzed the sensitivity of elastic and inelastic cross sections for the collisions $\mathrm{Li} + \mathrm{Li}_2(v_i, j_i = 0) \rightarrow \mathrm{Li} + \mathrm{Li}_2(v_f, j_f)$, for $v_i = 0$,

1, 2, and 3, at the collision energy of 0.928 nK to small changes in the potential. We studied the case of three identical ^{7}Li and ^{6}Li nuclei in the next two sections, respectively. The study of mixed reactions in this manner is prohibitively expensive in terms of computer time at present.

The problem is set once we decided in what way we make the changes in potential energy surface and how to parametrize them. The additive part of the three-body potential energy surface can be quite well determined from the experimental data by procedures like RKR, as was done for the lithium molecule by Linton et al. [48] and is built into our potential. The most relevant part of the potential for atom-molecule collisions with the molecule in low-lying vibrational states is the bottom of the diatomic potential. This part is accurately determined by an RKR potential reproducing the energies of low-lying bound states. The *ab-initio* determination of the two-body potential is also more accurate than the nonadditive part of the three-body potential since less nuclei and electrons are involved. Therefore, the least-known part of the potential is the nonadditive contribution. We decided to change the lithium three-body potential by multiplying the nonadditive part by a scaling factor λ,

$$V_{\mathrm{tot}}(r_1, r_2, r_3) = V_2(r_1) + V_2(r_2) + V_2(r_3) + \lambda V_3(r_1, r_2, r_3). \tag{9.7}$$

Changes in the well depth and position of the minima at D_{3h} and $D_{\infty h}$ geometries for several values of parameter λ are displayed in Table 9.1. The changes in the parameter that are considered are small since the nonadditive part is extremely large at D_{3h} geometries (see Chapter 2 and 3).

	D_{3h}		$D_{\infty h}$	
λ	r_{min} / Å	V_{min} / cm^{-1}	r_{min} / Å	V_{min} / cm^{-1}
1.01	3.1045	−4010.1452	3.7596	−950.8434
1	3.1111	−3958.4507	3.7624	−947.3968
0.9999	3.1115	−3957.9360	3.7624	−947.3624
0.999	3.1117	−3953.3049	3.7627	−947.0530
0.99	3.1176	−3907.1844	3.7653	−943.9666

Table 9.1: Dependence of the potential minimum and its position at D_{3h} and $D_{\infty h}$ geometries on the scaling factor λ of the nonadditive part of the potential.

9.2 Bosonic system

We first performed scattering calculations at collision energy of 0.928 nK on three identical ^{7}Li nuclei on a number of potentials. The scaling parameter λ of the nonadditive part of potential was varied in the range $\lambda \in [0.98, 1.02]$. We took 70 steps in range $[0.995, 1.005]$, and slightly longer steps outside this region. The total number of potentials studied was 111.

The dependence of the elastic cross sections, for a molecule that is initially in its ground state, on the scaling factor λ at the collision energy of 0.928 nK is shown in Figure 9.2. The corresponding scattering length is plotted in Figure 9.3. It is characterized by the familiar tangent profiles around a mean (7.35). Only the range $[0.995, 1.005]$ is shown, because the chosen grid is not dense enough outside it to capture the detail of the dependence.

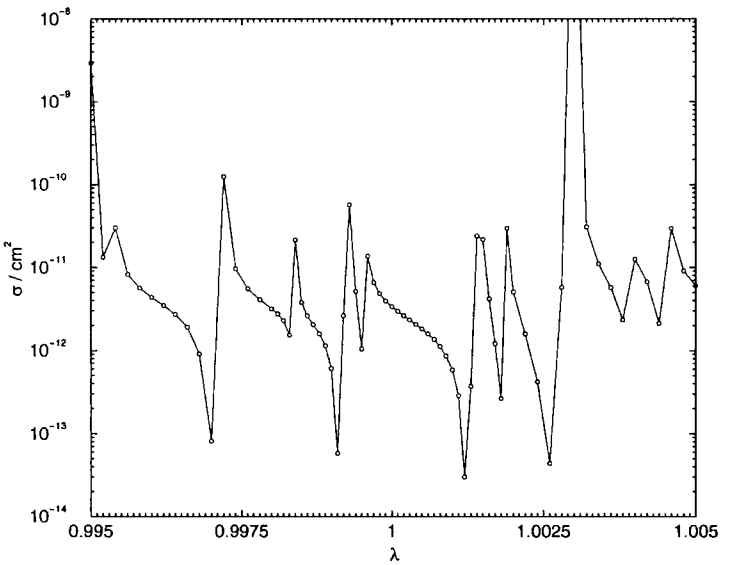

Figure 9.2: Dependence of the elastic cross sections for $^7\mathrm{Li} + {}^7\mathrm{Li}_2(v_i = 0, j_i = 0)$ on the scaling factor λ of the nonadditive part of the potential.

We estimated the mean scattering length using (7.36) and obtained $\bar{a} = 2.154$ nm using the isotropic atom-molecule dispersion coefficient $C_6 = 3085.54\, E_h a_0^6$, evaluated at the diatomic equilibrium distance ≈ 4.2 Å from the fit discussed in Chapter 5. The mean, estimated as the zero of the tangent curves, is slightly dependent on the potential as can be seen in Figure 9.3 and is ≈ 3.5 nm in the vicinity of $\lambda = 1$. The anisotropy of the potential is neglected in formula (7.36) and it only gives the correct order of magnitude. The poles may be interpreted as zero-energy resonances [162].

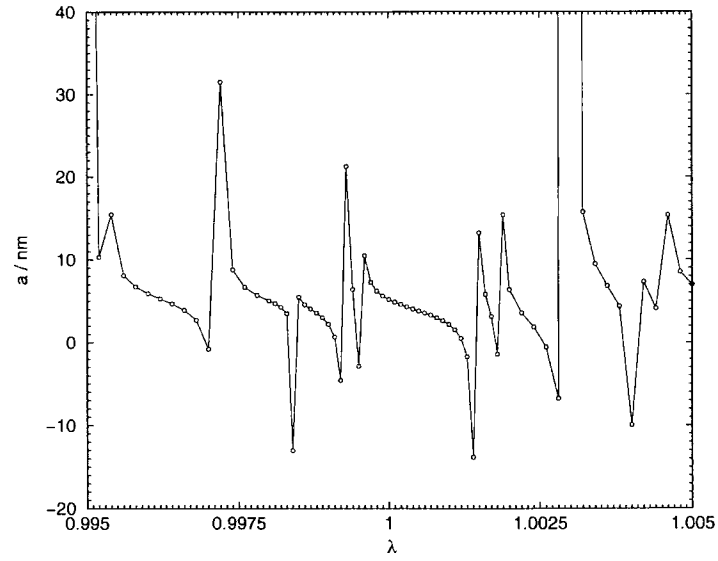

Figure 9.3: Dependence of the scattering length for $^7Li + {}^7Li_2(v_i = 0, j_i = 0)$ on the scaling factor λ of the nonadditive part of the potential.

The profiles of the dependence of scattering length on potential correspond to the case $\lambda_2 a = 0$ in Figure 9.1, i.e. where the imaginary potential is zero and only the elastic channel open.

The frequency of oscillations of elastic cross section with λ varies significantly over the short range of λ values on which the calculations were performed. A relatively flat region between the poles can be only as wide as a step of 0.0001 in λ which corresponds to 0.5 cm^{-1} at the global minimum of the potential, i.e., as little as one part in 10 000. This means that *ab-initio* calculations cannot at present give us any quantitative information about the magnitude of the elastic cross sections of atom and molecule in its ground state for this system at ultralow collision energies where the Wigner threshold laws apply.

The elastic and total inelastic cross sections for collisions of an atom with a molecule which is initially vibrationally excited are shown in Figures 9.4 and 9.5, respectively. The variation of cross sections over the range is again oscillatory. The amplitude and frequency are both reduced compared to the case where the molecule was in its ground state and the results become less sensitive to the potential with increasing initial vibrational excitation. The overall behaviour is similar to that in sodium trimer [210], although the nonadditive part of potential is much stronger in lithium and results in higher sensitivity.

The maximum relative deviation of elastic cross sections of scaled potentials relative to the elastic cross section of the non-scaled potential ($\lambda = 1$) in the whole set of the studied potentials is 191%, 110%, and 38.0%, for $v_i = 1, 2$, and 3, respectively. The maximum relative deviation of the inelastic cross sections is 67.9%, 219%, and 57.9%, respective to the same set of initial vibrational levels. The ranges over which the cross sections vary in the set of studied potentials, reported in Table 9.2, decrease in a monotonic fashion for all initial levels, except the relative range of inelastic cross sections for $v_i = 2$. The frequency of oscillations with λ is monotonically decreasing with v_i.

v_i	$\Delta\sigma_{\text{elas}}$ [cm^2]	$\sigma_{\text{elas}}^{\text{mid}}$ [cm^2]	$\Delta\sigma_{\text{elas}}/\sigma_{\text{elas}}^{\text{mid}}$
1	$3.844 \cdot 10^{-12}$	$2.063 \cdot 10^{-12}$	1.863
2	$7.329 \cdot 10^{-13}$	$7.192 \cdot 10^{-13}$	1.019
3	$6.201 \cdot 10^{-13}$	$9.723 \cdot 10^{-13}$	0.638
	$\Delta\sigma_{\text{inel}}$ [cm^2]	$\sigma_{\text{inel}}^{\text{mid}}$ [cm^2]	$\Delta\sigma_{\text{inel}}/\sigma_{\text{inel}}^{\text{mid}}$
1	$4.186 \cdot 10^{-9}$	$3.088 \cdot 10^{-9}$	1.356
2	$1.250 \cdot 10^{-9}$	$8.982 \cdot 10^{-10}$	1.392
3	$7.251 \cdot 10^{-10}$	$9.910 \cdot 10^{-10}$	0.732

Table 9.2: Range of variation of elastic and inelastic cross sections $\Delta\sigma$, centred on σ^{mid}, for $^7\text{Li} + {}^7\text{Li}_2(v_i, j_i = 0)$. Scaling factor of the nonadditive part of potential $\lambda \in [0.98, 1.02]$.

Next, we would like to give a quantitative measure of local sensitivity of cross sections. If we were able to determine the potential with such great accuracy that the cross section variation on a smooth change in the potential, from ours to the exact, falls within one oscillatory cycle, the accuracy of the calculations could be estimated from the maximum slope of the dependence of cross sections on the parameter characterizing the change. For example, if we were interested in the elastic and total inelastic cross sections from the $v_i = 1$ state of lithium dimer, the above condition would roughly imply the determination of the scaling factor to within 0.004 ($\approx$ 10 oscillations within the studied range), which corresponds to determination of the global minimum with an error of ≈ 20 cm^{-1} or 0.5%. We calculated crudely the maximum modulus of the slope in the dependence of cross sections on the scaling factor of the nonadditive part of potential, $\Delta\sigma/\Delta\lambda$, and also relative change of the

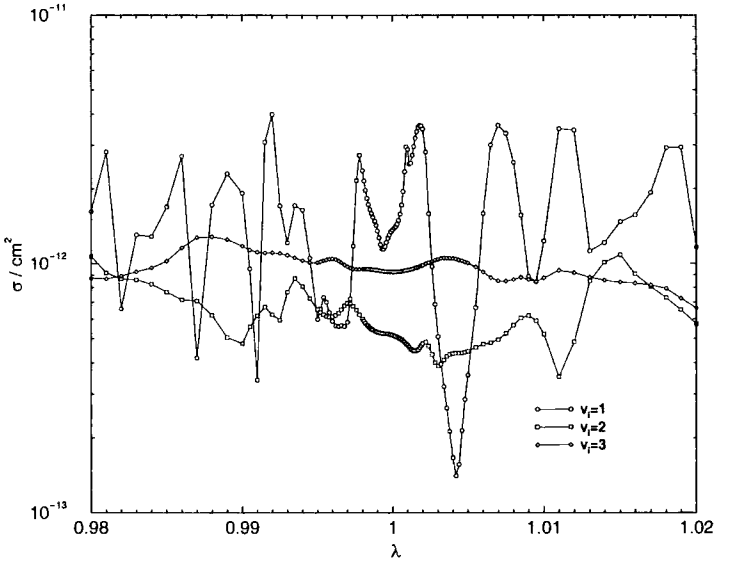

Figure 9.4: Dependence of the elastic cross sections for $^7\mathrm{Li} + {}^7\mathrm{Li}_2(v_i, j_i = 0)$ on the scaling factor λ of the nonadditive part of the potential.

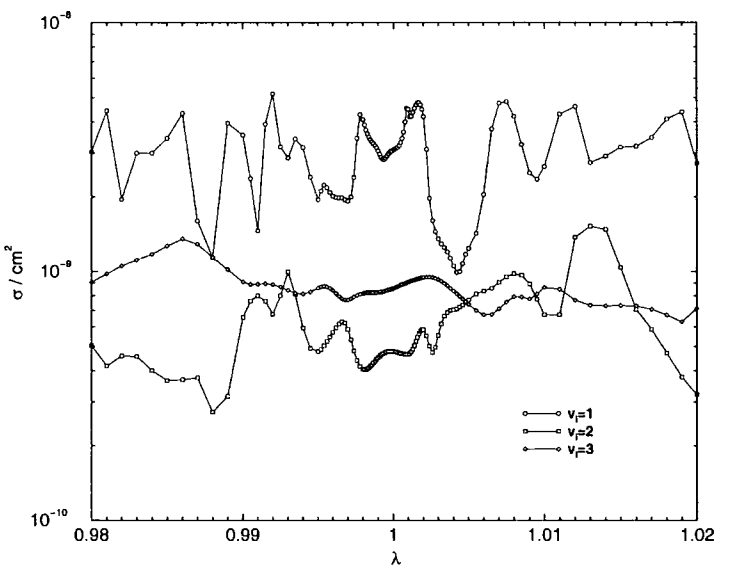

Figure 9.5: Dependence of the total inelastic cross sections for $^7\mathrm{Li} + {}^7\mathrm{Li}_2(v_i, j_i = 0)$ on the scaling factor λ of the nonadditive part of the potential.

cross sections with respect to a step in λ, $(\Delta\sigma/\Delta\lambda)/\sigma$. We report it in Table 9.3. The dependence of cross sections on the potential monotonically flattens as initial excitation is increased. Global minimum of the potential V_{min} varies with the scaling factor as $\Delta V_{\text{min}}/\Delta\lambda \simeq 5150$ cm^{-1} over the range studied. This means that an error of 1 cm^{-1} in the well depth could result in errors as high as 62%, 11%, and 2.4% in elastic, or 44%, 14%, and 2.6% in inelastic cross sections for $v_i = 1, 2$, and 3, respectively.

v_i	$\Delta\sigma_{\text{elas}}/\Delta\lambda$ [cm^2]	$\Delta\sigma_{\text{inel}}/\Delta\lambda$ [cm^2]	$(\Delta\sigma_{\text{elas}}/\Delta\lambda)/\sigma$	$(\Delta\sigma_{\text{inel}}/\Delta\lambda)/\sigma$
1	$6.125 \cdot 10^{-9}$	$5.702 \cdot 10^{-6}$	3203	2245
2	$3.656 \cdot 10^{-10}$	$7.063 \cdot 10^{-7}$	547	698
3	$1.346 \cdot 10^{-10}$	$1.462 \cdot 10^{-7}$	124	135

Table 9.3: Maximum absolute and relative change of elastic and inelastic cross sections for $^7\text{Li} + {}^7\text{Li}_2(v_i, j_i = 0)$ per step in the scaling factor of the nonadditive part of potential, $\lambda \in [0.98, 1.02]$.

We have also tested the dependence of the collision cross section on the potential by employing potentials that are significantly different at short range. The ACVTZ potential was constructed in the same manner as our original potential used until now and described in Chapters 3, 4, and 5, with the only difference that the RCCSD(T) energies were calculated using aug-cc-pCVTZ basis set. We used the same long range part of potential. The COLA potential is the potential obtained by Colavecchia et al. [56]. We also performed calculations on the pairwise additive potential, obtained by setting $\lambda = 0$. Potential characteristics at the minima in D_{3h} and $D_{\infty h}$ are summarized in Table 9.4.

	D_{3h}		$D_{\infty h}$	
potentials	r_{min} / Å	V_{min} / cm^{-1}	r_{min} / Å	V_{min} / cm^{-1}
ACVTZ	3.1250	−3873.3724	3.7801	−930.2916
COLA	3.1016	−4112.4633	3.7423	−1005.4543
additive	4.1727	−1001.1000	4.1322	−692.8993

Table 9.4: Potential minima and their positions at D_{3h} and $D_{\infty h}$ geometries for the Li_3 potentials described in the text.

The elastic and inelastic cross sections for the three different potentials at 0.928

nK are listed in Table 9.5, together with the relative deviations from the values obtained using our original potential. The relative changes in elastic and inelastic cross sections always bear the same sign, but are substantial. This result is not surprising since the potentials are quite different. The cross sections for $v_i = 3$ have the most consistent values for the different potentials. The ratio $\sigma_{\text{inel}}/\sigma_{\text{elas}}$ for ACVTZ potential is the most similar to the values obtained by original potential. It is interesting to note that the purely additive potential, although it is vastly different from others, does not give entirely different results compared to the results with other potentials. This could be rationalized by noting that the long-range parts of all potentials considered here are very similar and that it is the long range which predominantly determines the mean value of the scattering length in atom-atom scattering. If a similar statement is true for atom-molecule scattering, the mean should not be very different for considered potentials. In the Van der Waals systems, the exact value oscillates depending on the binding energy and lifetime of virtual states close to dissociation limit and is sensitive to the potential [42, 43]. These resonant structures in the zero-energy limit are washed out, in our system, as the initial excitation of molecule is increased and more inelastic channels open. This enables a more precise determination of cross sections for higher vibrational levels and makes them less dependent on the potential energy surface.

The loss of flux from elastic to inelastic channels is described by the imaginary part of potential in the complex square well potential model described above. The scattering lengths, extracted from the diagonal T matrix element at 0.928 nK, are plotted Figure 9.6. When the molecule is initially in the $v_i = 1$ state, the real part of the scattering length is predominantly lower than its imaginary part, opposed to what the complex-square-well model predicts, see Figure 9.1. The maxima in the imaginary part of the scattering length do still follow the sharp variations in its real part and can be associated with virtual states appearing near the dissociation limit as the potential is varied. When the molecule is initially in the $v_i = 2$ and 3 states, the scattering length recovers the behaviour obtained in the complex-square-well model with $\lambda_2 a \simeq 1$. The real part of the scattering length is consistently larger than its imaginary part and the ratio is fairly constant as is shown in the Figure 9.7. The ratio of the imaginary and real parts of the scattering length for the three additional potentials described above is reported in Table 9.6. The results obtained using the

	ACVTZ				
v_i	σ_{elas} [cm^2]	σ_{inel} [cm^2]	$\sigma_{\text{inel}}/\sigma_{\text{elas}}$	$\Delta\sigma_{\text{elas}}$ [%]	$\Delta\sigma_{\text{inel}}$ [%]
1	$1.29 \cdot 10^{-13}$	$3.85 \cdot 10^{-10}$	2980	−90.6	−87.5
2	$1.03 \cdot 10^{-12}$	$1.51 \cdot 10^{-9}$	1470	99.9	216
3	$1.38 \cdot 10^{-12}$	$1.36 \cdot 10^{-9}$	985	48.4	58.8
	COLA				
v_i	σ_{elas} [cm^2]	σ_{inel} [cm^2]	$\sigma_{\text{inel}}/\sigma_{\text{elas}}$	$\Delta\sigma_{\text{elas}}$ [%]	$\Delta\sigma_{\text{inel}}$ [%]
1	$4.35 \cdot 10^{-13}$	$1.64 \cdot 10^{-10}$	377	−68.2	−94.7
2	$4.13 \cdot 10^{-12}$	$2.67 \cdot 10^{-9}$	646	699	461
3	$9.82 \cdot 10^{-13}$	$1.87 \cdot 10^{-9}$	1900	5.73	118
	additive				
v_i	σ_{elas} [cm^2]	σ_{inel} [cm^2]	$\sigma_{\text{inel}}/\sigma_{\text{elas}}$	$\Delta\sigma_{\text{elas}}$ [%]	$\Delta\sigma_{\text{inel}}$ [%]
1	$1.31 \cdot 10^{-12}$	$4.11 \cdot 10^{-10}$	311	−4.15	−86.7
2	$1.67 \cdot 10^{-14}$	$2.42 \cdot 10^{-10}$	14500	−96.8	−49.3
3	$1.96 \cdot 10^{-12}$	$9.59 \cdot 10^{-10}$	489	111	11.9

Table 9.5: Elastic and total inelastic cross sections for $^7\text{Li} + {}^7\text{Li}_2(v_i, j_i = 0)$ using ACVTZ, COLA, and additive potentials, with comparison to potential described in Chapter 5. See text for details.

	ACVTZ		
v_i	Re(a) / nm	−Im(a) / nm	−Im(a)/ Re(a)
1	0.926	0.411	0.443
2	2.37	1.61	0.679
3	2.98	1.45	0.487
	COLA		
v_i	Re(a) / nm	−Im(a) / nm	−Im(a)/ Re(a)
1	1.85	0.175	0.0947
2	4.97	2.85	0.573
3	1.96	1.99	1.013
	additive		
v_i	Re(a) / nm	−Im(a) / nm	−Im(a)/ Re(a)
1	3.20	0.439	0.137
2	2.58	2.57	0.999
3	3.81	1.02	0.269

Table 9.6: Complex scattering lengths for $^7\text{Li}+{}^7\text{Li}_2(v_i, j_i = 0)$ using ACVTZ, COLA, and additive potentials, described in the text.

ACVTZ potential are the most similar to those obtained using our original potential, as is expected based on the similarity of potentials.

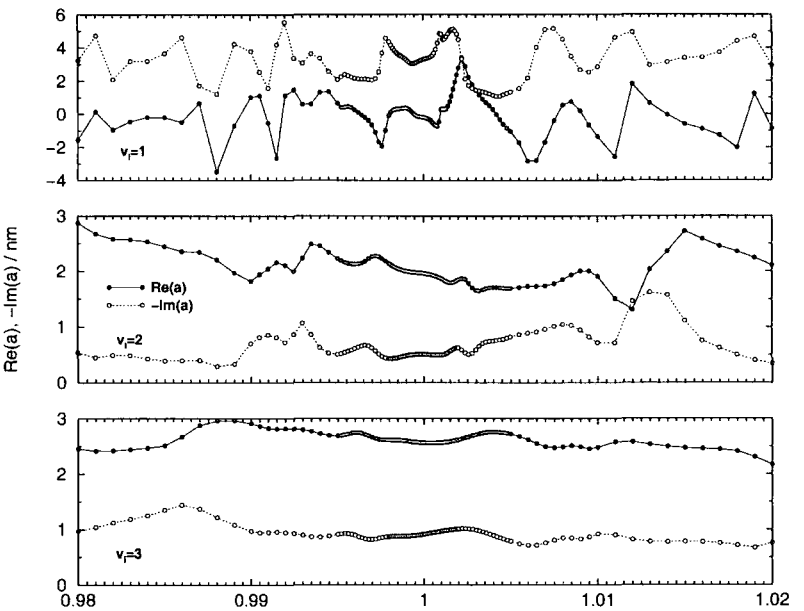

Figure 9.6: Dependence of the complex scattering length for ^{7}Li + ^{7}Li$_2(v_i, j_i = 0)$, with $v_i = 1$, 2, and 3, on the scaling factor λ of the nonadditive part of the potential.

The elastic and inelastic cross sections, shown in Figures 9.4 and 9.5, have a remarkably similar dependence on the potential. The ratio of inelastic to elastic cross sections is therefore expected to be more stable with respect to potential variation. As inelastic collisions represent a trap loss mechanism, and elastic ones are important for efficiency of evaporative cooling, the ratio should preferably be small ($\ll 1$). It is plotted in Figure 9.8. The oscillatory behaviour is diminished, but is still spread over an order of magnitude. At the maxima of elastic and inelastic cross sections, the ratio is at a minimum. This means that, if we had means to tune the potential, at the maxima of elastic cross sections, the ratio would be more favourable. But the ratio is consistently large and extremely unfavourable for cooling and storage of such atom-molecule mixtures.

Finally, we briefly report on the partial and state-to-state cross sections. Vibrationally resolved cross sections for the ^{7}Li +^{7}Li$_2(v_i, 0)$ collisions for $v_i = 2$ and 3 are plotted in Figure 9.9. Partial cross sections vary more than the total inelastic cross sections since the latter is a sum and the summation averages out the undulations. It is clear that over the plotted range the single, double, and triple de-excitations

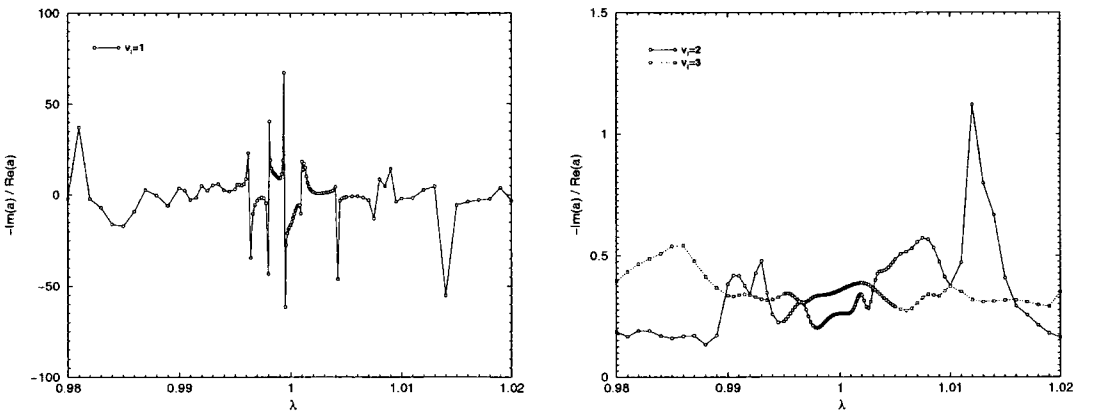

Figure 9.7: Dependence of $-\mathrm{Im}(a)/\mathrm{Re}(a)$ on the scaling factor λ of the nonadditive part of the potential, where a is complex scattering for $^7\mathrm{Li} + {}^7\mathrm{Li}_2(v_i, j_i = 0)$, with $v_i = 1$ (left), 2, and 3 (right).

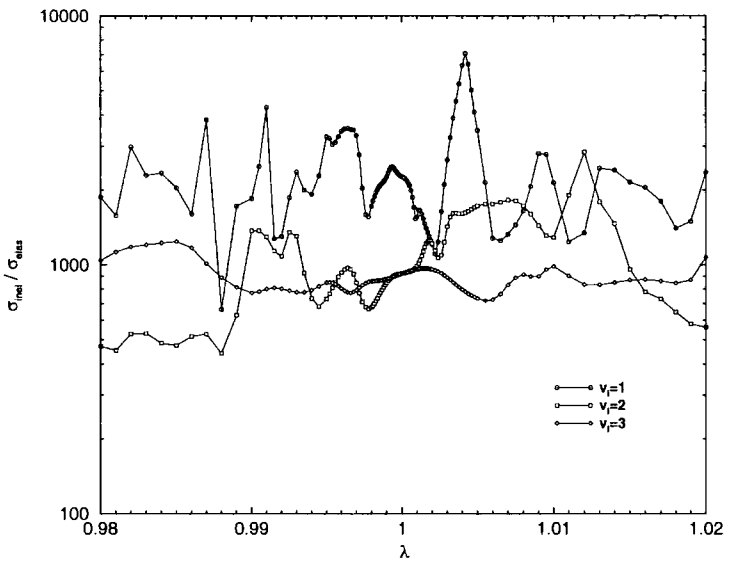

Figure 9.8: Dependence of the ratio of total inelastic and elastic cross sections for $^7\mathrm{Li} + {}^7\mathrm{Li}_2(v_i, j_i = 0)$, with $v_i = 1$, 2, and 3, on the scaling factor λ of the nonadditive part of the potential.

compete and the potential must be determined very accurately to be able to order them in magnitude.

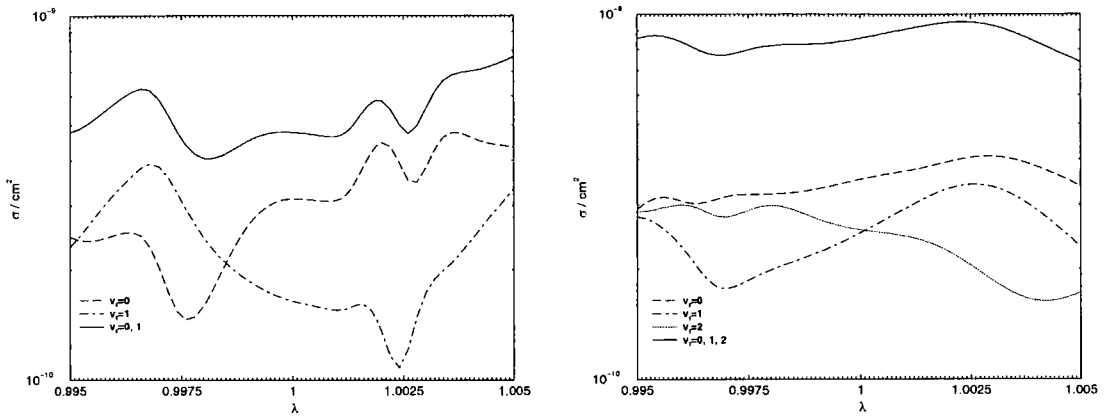

Figure 9.9: Dependence of vibrationally resolved cross sections for $^7\mathrm{Li} + {}^7\mathrm{Li}_2(v_i, j_i = 0) \rightarrow {}^7\mathrm{Li} + {}^7\mathrm{Li}_2(v_f, \mathrm{all}\, j_f)$ for $v_i = 2$ (left) and 3 (right), and all accessible v_f's, on the scaling factor λ of the nonadditive part of the potential.

Rotational distributions for several scaling factors λ are shown in Figures 9.11 and 9.12, for the $v_i = 1$ and 3 states of the molecule, respectively. They are very sensitive to potential. The relative populations and interference patterns are changed for both initial states of molecule with a small change in λ. The variations of several state-to-state cross sections with λ are shown in Figure 9.10. The underlying structure of the summed cross sections is smoothly and rapidly varying and the more we sum, the more these undulations are statistically averaged out and the calculated quantities becoming more certain, i.e. less potential dependent.

9.3 Fermionic system

In this section, we calculate the cross sections at 0.928 nK in the fermionic system on a number of scaled potentials and perform a sensitivity analysis in an analogous manner to the bosonic system in the last section. We took 90 steps in the scaling factor λ of the nonadditive part of the potential with $\lambda \in [0.98, 1.02]$, with more steps in the central part of the range.

Since the chosen grid was not as dense, the detail of the λ-dependence of elastic cross sections for collisions of an atom and a molecule in its ground state was not fully captured and is not shown here. The results do not differ significantly from

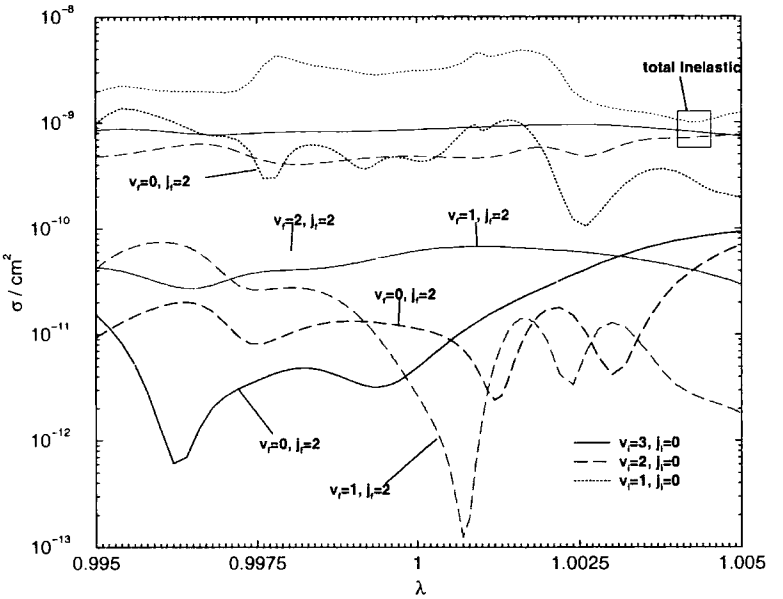

Figure 9.10: Dependence of state-to-state cross sections for $^7\mathrm{Li} + {}^7\mathrm{Li}_2(v_i, j_i = 0) \rightarrow {}^7\mathrm{Li} + {}^7\mathrm{Li}_2(v_f, j_f)$ on the scaling factor λ of the nonadditive part of the potential. Several examples are shown.

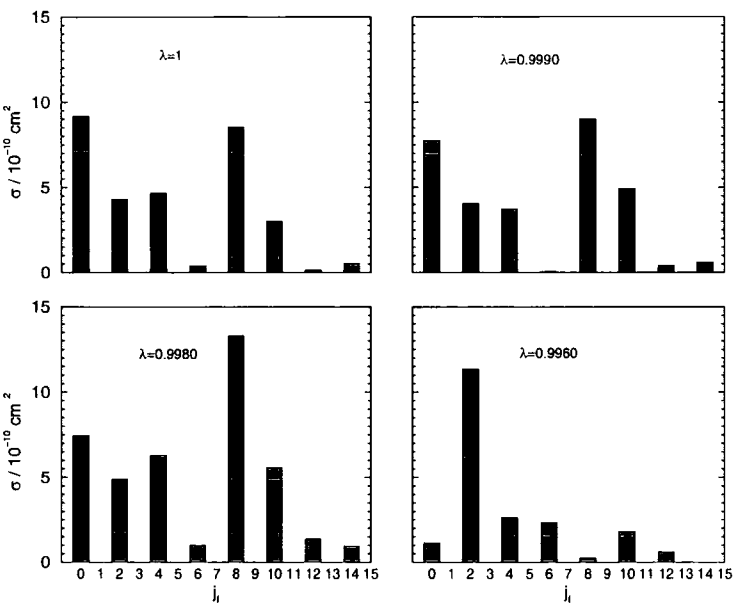

Figure 9.11: Rotational distribution of final states for $^7\mathrm{Li} + {}^7\mathrm{Li}_2(v_i = 1, j_i = 0) \rightarrow {}^7\mathrm{Li} + {}^7\mathrm{Li}_2(v_f = 0, j_f)$ for several values of the scaling factor λ of the nonadditive part of the potential.

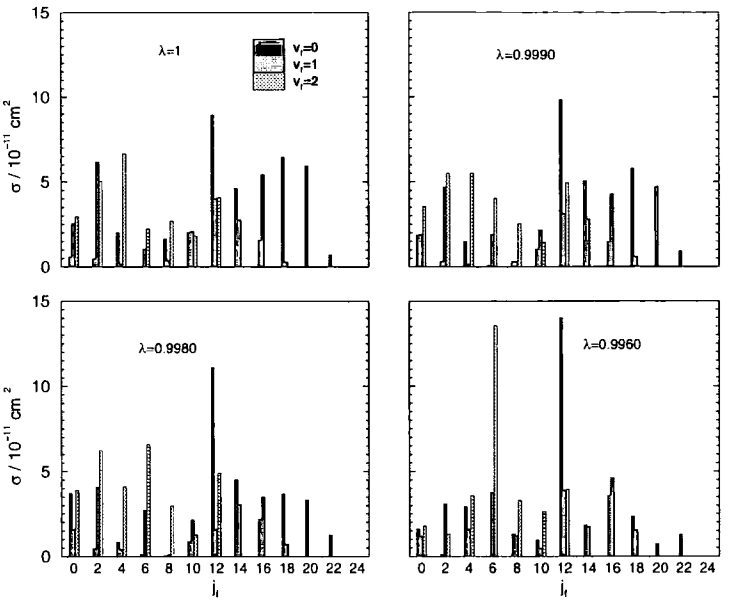

Figure 9.12: Rotational distribution of final states for $^7\mathrm{Li} + {}^7\mathrm{Li}_2(v_i = 3, j_i = 0) \rightarrow {}^7\mathrm{Li} + {}^7\mathrm{Li}_2(v_f, j_f)$ for several values of the scaling factor λ of the nonadditive part of the potential.

bosonic system qualitatively. The mean scattering length, from formula (7.36), is $\approx$ 4% smaller than in the bosonic system which is not visible on a logarithmic scale, see Figure 9.2. It is visible from our results that Gribakin's formula (7.36) underestimates the scattering length extracted from our calculations.

The dependence of elastic and inelastic cross sections on λ, for $v_i = 1$, 2, and 3, are shown in Figures 9.13 and 9.14. The frequency and amplitude of oscillations are generally decreasing with initial molecular excitation. We proceed by giving the quantitative measures of potential sensitivity introduced in the previous section. The maximum deviation of elastic cross sections from that of the non-scaled potential, in the set of potentials studied, is 288%, 86.4%, and 40.6%, for $v_i = 1$, 2, and 3, respectively. For the total inelastic cross sections the maximum deviation is 161%, 54.4%, and 38.0%, for the same set of initial molecular states. The ranges in which the cross sections vary and the widths relative to the cross sections in the centre of the range are tabulated in Table 9.7. Most of reported numbers decrease with the initial molecular excitation as in the bosonic system. The highest absolute and relative change in cross sections per step in λ is given in Table 9.8. This can be used with $\Delta V_{\mathrm{min}}/\Delta\lambda \simeq 5150\ \mathrm{cm}^{-1}$ to estimate how much the cross sections can

change when the change in the potential results in ≈ 1 cm^{-1} at the global minimum. The estimated relative changes of elastic cross sections are 65%, 8.3%, and 5.4%, for $v_i = 1$, 2, and 3, respectively. The corresponding set of numbers for inelastic cross sections is 56%, 6.4%, and 3.6%. Comparison to the bosonic system does not reveal significant qualitative differences.

v_i	$\Delta\sigma_{\text{elas}}$ [cm^2]	$\sigma_{\text{elas}}^{\text{mid}}$ [cm^2]	$\Delta\sigma_{\text{elas}}/\sigma_{\text{elas}}^{\text{mid}}$
1	$2.050 \cdot 10^{-12}$	$1.339 \cdot 10^{-12}$	1.531
2	$1.693 \cdot 10^{-12}$	$2.260 \cdot 10^{-13}$	0.749
3	$1.129 \cdot 10^{-12}$	$1.492 \cdot 10^{-13}$	0.756
	$\Delta\sigma_{\text{inel}}$ [cm^2]	$\sigma_{\text{inel}}^{\text{mid}}$ [cm^2]	$\Delta\sigma_{\text{inel}}/\sigma_{\text{inel}}^{\text{mid}}$
1	$3.149 \cdot 10^{-9}$	$3.088 \cdot 10^{-9}$	1.553
2	$2.180 \cdot 10^{-9}$	$2.119 \cdot 10^{-9}$	1.029
3	$1.423 \cdot 10^{-9}$	$2.425 \cdot 10^{-9}$	0.587

Table 9.7: Range of variation of elastic and inelastic cross sections $\Delta\sigma$, centred on σ^{mid}, for ^{6}Li $+^6$Li$_2(v_i, j_i = 1)$. Scaling factor of the nonadditive part of potential $\lambda \in [0.98, 1.02]$.

v_i	$\Delta\sigma_{\text{elas}}/\Delta\lambda$ [cm^2]	$\Delta\sigma_{\text{inel}}/\Delta\lambda$ [cm^2]	$(\Delta\sigma_{\text{elas}}/\Delta\lambda)/\sigma$	$(\Delta\sigma_{\text{inel}}/\Delta\lambda)/\sigma$
1	$5.402 \cdot 10^{-9}$	$6.283 \cdot 10^{-6}$	3357	2900
2	$1.013 \cdot 10^{-9}$	$6.934 \cdot 10^{-7}$	430	332
3	$4.965 \cdot 10^{-10}$	$4.310 \cdot 10^{-7}$	280	184

Table 9.8: The maximum absolute and relative change of elastic and inelastic cross sections for ^{6}Li$+^6$Li$_2(v_i, j_i = 1)$ per step in the scaling factor of the nonadditive part of potential, $\lambda \in [0.98, 1.02]$.

The dependence of the scattering length, extracted from the T matrix at 0.928 nK, on λ is plotted in Figure 9.15. The real part of scattering length is mainly greater than the imaginary part for all initial levels we studied. In comparison with the results obtained in the bosonic system in the last section, the imaginary part of the scattering length is higher. The ratio $-\text{Im}(a)/\text{Re}(a)$, shown in Figure 9.16, is therefore also higher. This quantity is expected to be less dependent on the potential except at the positions of resonances [185].

The ratio of inelastic and elastic cross sections is shown in Figure 9.17 as a

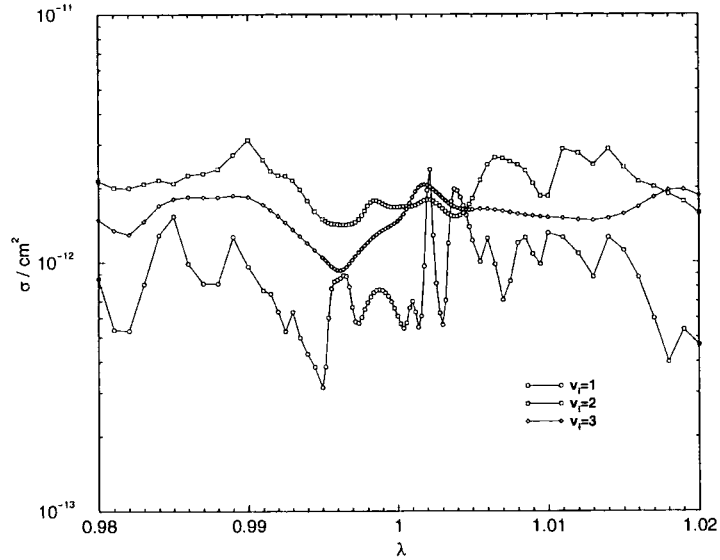

Figure 9.13: Dependence of the elastic cross sections for $^6\mathrm{Li} + {}^6\mathrm{Li}_2(v_i, j_i = 1)$ on the scaling factor λ of the nonadditive part of the potential.

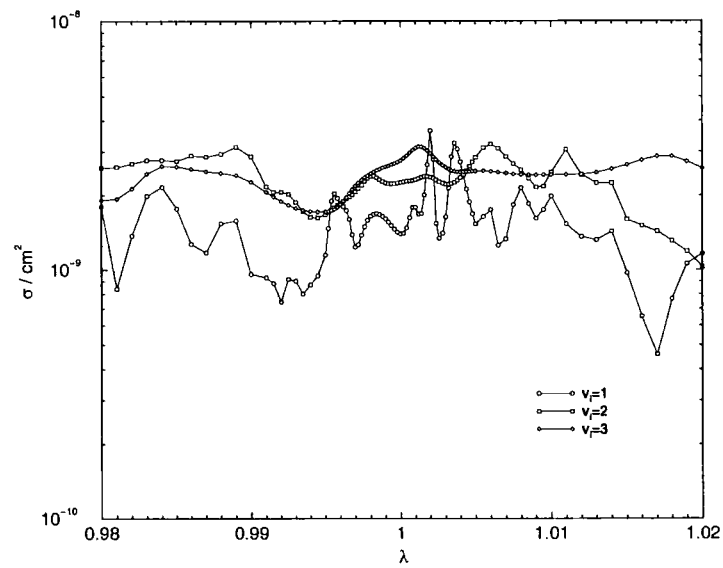

Figure 9.14: Dependence of the total inelastic cross sections for $^6\mathrm{Li} + {}^6\mathrm{Li}_2(v_i, j_i = 1)$ on the scaling factor λ of the nonadditive part of the potential.

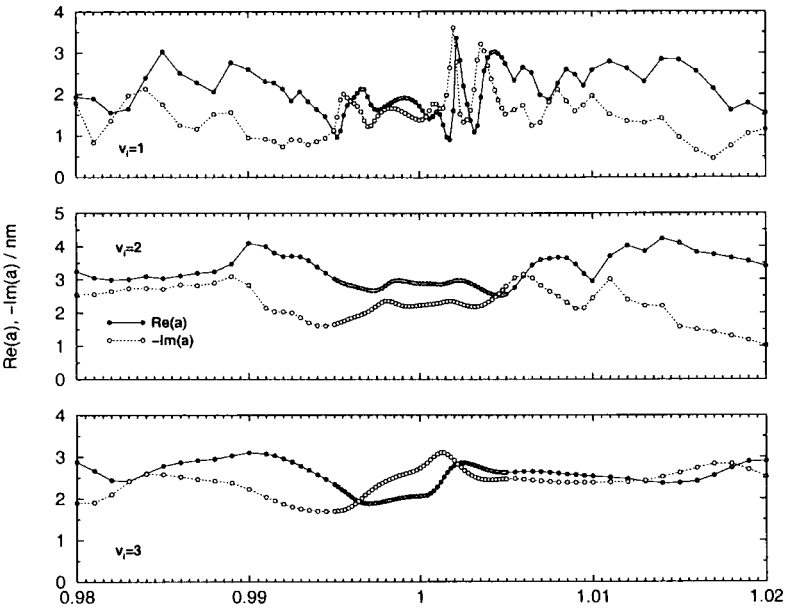

Figure 9.15: Dependence of the complex scattering length for $^6\mathrm{Li} + {}^6\mathrm{Li}_2(v_i, j_i = 1)$, with $v_i = 1$, 2, and 3, on the scaling factor λ of the nonadditive part of the potential.

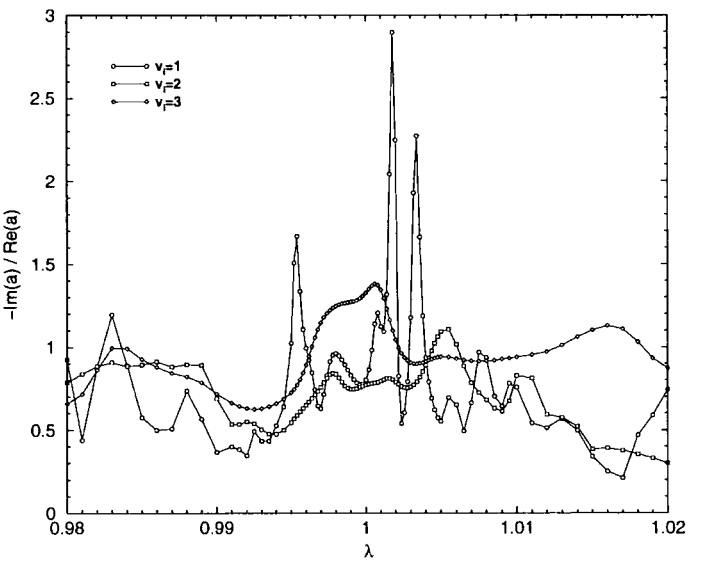

Figure 9.16: Dependence of $-\mathrm{Im}(a)/\mathrm{Re}(a)$ on the scaling factor λ of the nonadditive part of the potential, where a is complex scattering for $^6\mathrm{Li} + {}^6\mathrm{Li}_2(v_i, j_i = 1)$, with $v_i = 1$, 2, and 3.

function of the scaling factor λ. The importance of this quantity was emphasized above. Our calculations deliver the value of $\approx$ 1000 with a reasonable certainty, which is unfavourable for storage and cooling of such atom-molecule mixtures.

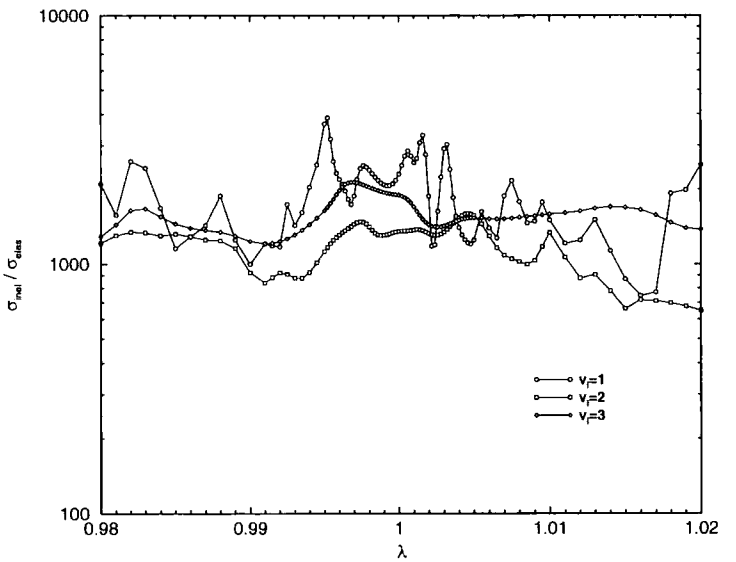

Figure 9.17: Dependence of the ratio of total inelastic and elastic cross sections for $^6\mathrm{Li} + {}^6\mathrm{Li}_2(v_i, j_i = 1)$, with $v_i = 1$, 2, and 3, on the scaling factor λ of the nonadditive part of the potential.

The dependence of the vibrationally resolved cross section on λ is plotted in Figure 9.18. The total inelastic cross section is dominated by transitions to the ground vibrational state of the molecule. The partial cross sections exhibit a stronger dependence on the potential. The same was observed in the bosonic system. The weaker dependence of the summed quantities on potential results from statistical averaging of the underlying structure.

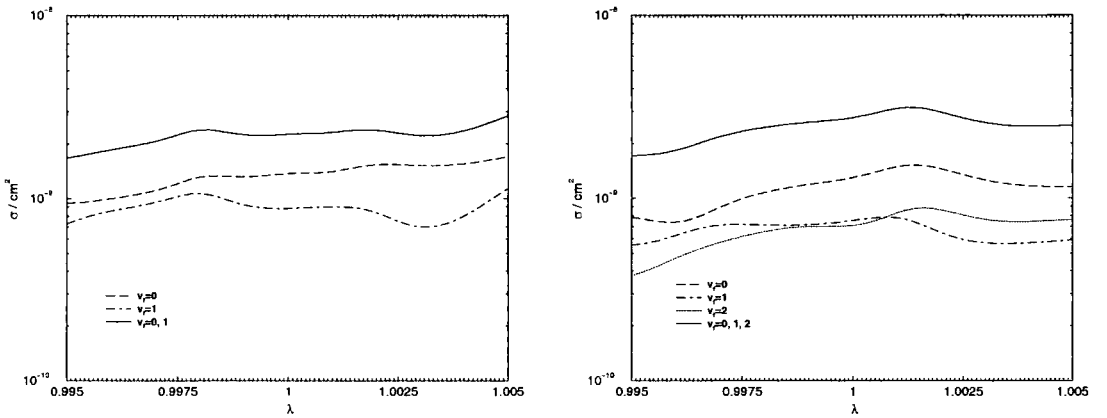

Figure 9.18: Dependence of vibrationally resolved cross sections for $^6\mathrm{Li}+^6\mathrm{Li}_2(v_i, j_i = 1) \rightarrow {}^6\mathrm{Li} + {}^6\mathrm{Li}_2(v_f, \mathrm{all}\, j_f)$ for $v_i = 2$ (left) and 3 (right), and all accessible v_f's, on the scaling factor λ of the nonadditive part of the potential.

Chapter 10

Conclusions

We have generated the potential energy surface of lithium trimer in the electronic quartet ground state. The surface allows barrierless atom-exchange reactions. It has a deep global minimum of ≈ 4000 cm^{-1} at equilateral geometries and a saddle point at linear geometry. The nonadditive forces are found to be large, especially near the equilibrium geometries. They increase the three-atom potential well depth by a factor of 4 and reduce the equilibrium interatomic distance by 1.07 Å. The nonadditive forces originate principally from chemical bonding arising from *sp* mixing effects.

Another surface of A' symmetry in C_s meets the ground state surface at linear geometries at short range. Part of the seam, near $D_{\infty h}$ geometries with $r_1 = r_2 = r_3 = 3.1$ Å, is in an energetically accessible region for cold collisions. Inside the seam, the lowest A' surface correlates with $^4\Pi$ rather than $^4\Sigma$ state.

We established the relationship between the non-additive dispersion coefficients, that arise in the perturbation expansion of nonadditive dispersion interactions between three identical S-state atoms, and the coefficients in the asymptotic expansion of atom-molecule dispersion coefficients in powers of bond length. The results are summarized in Table 5.6 and 5.7. Using this connection we propose a model to represent the long-range dispersion interactions in a symmetric form for scattering calculations on reactive triatomic systems. The form describes accurately the atom-diatom potential at long range and it takes as input the atom-molecule dispersion coefficients as a function of distance.

Scattering calculations on the ^{7}Li + ^{7}Li$_2$ and ^{6}Li + ^{6}Li$_2$ systems indicate that the inelastic rate coefficients at limitingly low temperatures are large, often above 10^{-10} cm^{3}s^{-1}. The elastic rate coefficients are three orders of magnitude lower than inelastic at the collision energy of 1 nK. Atom-molecule mixtures, at the densities found in Bose-Einstein condensates of alkalis that were recently produced, would last only a fraction of a second. No systematic dependence of cross sections on the initial molecular states was found. The energy dependence of cross sections follows Wigner laws in mK regime. Cross sections in the Wigner regime are extremely sensitive to the details of potential energy surface. The range of variations is less than an order of magnitude for small changes in the potential and is reduced for the higher initial vibrational levels of molecule. The results are qualitatively similar for bosonic and fermionic systems.

The partial wave expansion at collision energy of 500 mK converges at $J = 10$.

The distributions of product states are not statistical and the forward-backward symmetry in differential cross sections is broken at some collision energies. The fermionic system has a flatter angular dependence of cross sections, possibly due to its rotational excitation. The classical Langevin model describes semi-quantitatively the energy-dependence of inelastic cross sections above ≈ 50 mK. The only parameter in the model is the atom-molecule C_6 coefficient. At these energies elastic cross sections are of same order of magnitude as inelastic cross sections.

Reactions in isotopic mixtures of lithium may be exothermic even from the molecular ground state. The sum of inelastic and reactive rate coefficients is $1-2$ orders of magnitude smaller than those in systems involving an initially vibrationally excited dimer. Reactivity at ultralow collision energies in this system is as efficient as inelasticity, depending roughly on the number of available states, although the departures from a simple statistical model are large.

The work on collisions in lithium contrasts with that of Balakrishnan et al. on the $F + H_2$ system [11] and van der Waals systems in that the Li_3 system is barrierless and involves a deep well. Our results may also be contrasted with those of Petrov et al. [30] on inelastic rate coefficients in fermionic atom-diatom systems for weakly bound dimer states. This work is an extension of the research on insertion reactions [6] previously undertaken only at high collision energies.

The research leaves many open ends. We mention some of the possible future directions below. An interesting thing to do in the future would be the diabatization of the quartet potential energy surfaces and the coupled dynamics calculations on diabatic surfaces. This would reveal how much influence the conical intersection has on the dynamics. With an increase of computer power, it would be instructive to see whether the system becomes statistical at higher temperatures with inclusion of more partial waves. Including external fields in the dynamics calculations would enable a more realistic modelling of the low-temperature experiments and possibly bring novel phenomena to light.

Appendix A

Energy-level diagram of lithium dimer

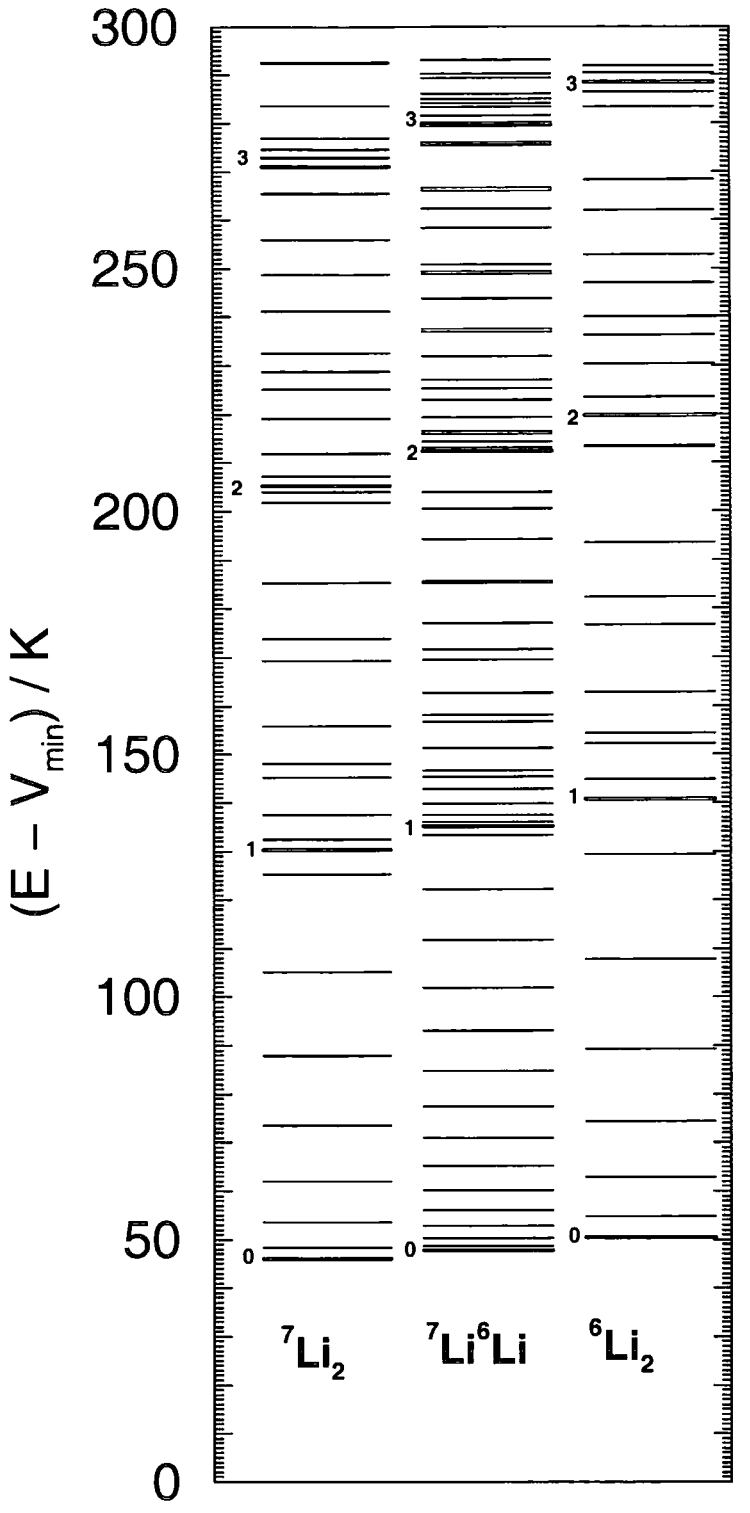

Figure A.1: Rovibrational energy levels of all isotopic variants of Li_2. Numbers in the graph indicate the beginning of corresponding vibrational manifolds.

Appendix B

Rate coefficients in bosonic and fermionic systems

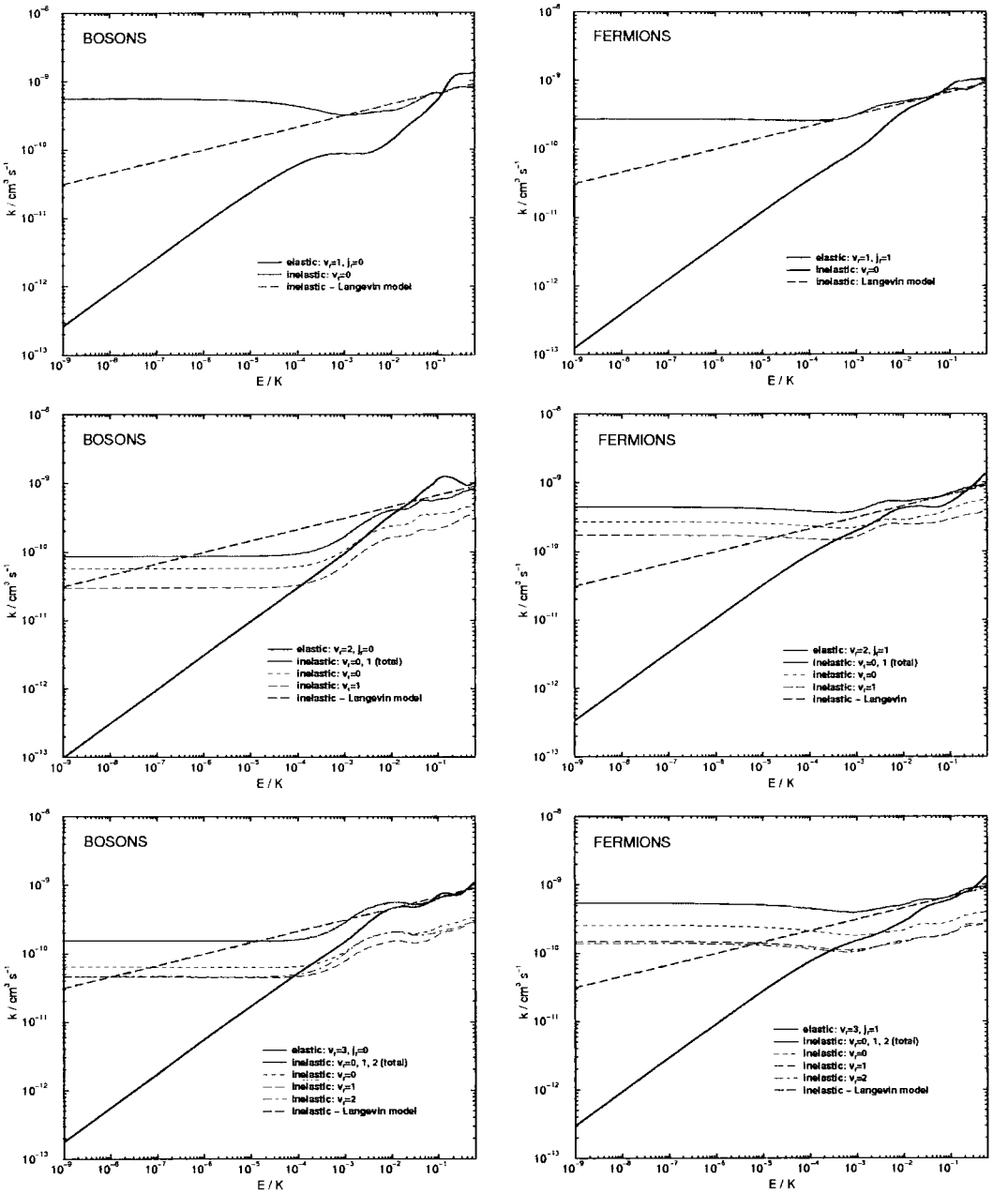

Figure B.1: Energy dependence of elastic and inelastic rate coefficients for Li + $Li_2(v_i, j_i)$ in bosonic (left column) and fermionic (right column) systems and the Langevin model predictions. (Initial dimer state v_i, j_i is: v_i = row number, j_i = column number − 1).

Appendix C

Publications and conferences

C.1 Publications

Pavel Soldán, Marko T. Cvitaš, Jeremy M. Hutson, Pascal Honvault, Jean-Michel Launay, Quantum dynamics of ultracold Na + Na_2, Phys.Rev. Lett. **89**, 153201 (2002)

Pascal Honvault, Jean-Michel Launay, Pavel Soldán, Marko T. Cvitaš, Jeremy M. Hutson, Quantum dynamics of ultracold alkali + alkali dimer collisions, in Interactions of cold atoms and molecules, edited by P. Sóldan, J. M. Hutson, M. T. Cvitaš, C. S. Adams, CCP6 Daresbury (2002)

Pavel Soldán, Marko T. Cvitaš, Jeremy M. Hutson, Three-body nonadditive forces between spin-polarized alkali-metal atoms, Phys. Rev. A **67**, 054702 (2003)

Marko T. Cvitaš, Antonio Šiber, Vibrations of a chain of Xe atoms in a groove in a carbon nanotube bundle, Phys. Rev. B **67**, 193401 (2003)

Marko T. Cvitaš, Pavel Soldán, Jeremy M. Hutson, P. Honvault, J.-M. Launay, Ultracold Li + Li_2 collisions: bosonic and fermionic cases, Phys. Rev. Lett. **94**, 033201 (2005)

C.2 Conferences, workshops, summer schools

Aug 15 – Aug 25, 2001: Charles Coulson Summer School on the Quantum Dynamics of Molecular Systems, University of Oxford (University College), Oxford

Dec 6 2000: Theoretical Chemistry Day, University College London, London

Mar 28 2001: Spectroscopy in Action: Molecular Dynamics and Structure, University of Oxford, Oxford

Mar 28 – Apr 1 2001: EU Network Meeting on Reaction Dynamics University of Oxford, Oxford

Apr 9 – Apr 12 2001: CCP6 Workshop on Time-Dependent Quantum Dynamics, University of Bristol, Bristol

Apr 18 – Apr 20 2001: Faraday Discussion 118: Cluster Dynamics, University of Durham, Durham

Mar 3 – Mar 8 2002: Cold Molecules 2002 : Ultra-Cold Molecules and Bose-Einstein Condensation, Les Houches, France

Sep 19 – Sep 22 2002: CCP6 Workshop: Interactions of Cold Atoms and Molecules University of Durham, Durham

Jul 9 2003: ANUMOCP XIII (Annual Northern Universities Meeting on Chemical Physics), University of Durham, Durham

Mar 30 – Apr 3 2004: Bose-Einstein Condensation: from Atoms to Molecules, University of Durham, Durham

Bibliography

[1] Y. T. Lee, Science **236**, 793 (1987)

[2] P. Casavecchia, N. Balucani, G. G. Volpi, Annu. Rev. Phys. Chem. **50**, 347 (1999)

[3] K. Liu, Annu. Rev. Phys. Chem. **52**, 139 (2001)

[4] S.C. Althorpe, F. Fernandez-Alonso, B. D. Bean, J.D. Ayers, A. E. Pomerantz, R. N. Zare, E. Wrede, Nature **416**, 67 (2002)

[5] S. C. Althorpe, D. C. Clary, Annu. Rev. Phys. Chem. **54**, 493 (2003)

[6] P. Honvault, J.-M. Launay, in Theory of chemical reaction dynamics, edited by A. Lagana, G. Lendvay, NATO Science Series **145**, 187, Kluwer (2004)

[7] E. J. Rackham, T. Gonzales-Lezana, D. E. Manolopoulos, J. Chem. Phys. **119**, 12895 (2003)

[8] H. L. Bethlem, G. Meijer, Int. Rev. Phys. Chem **22**,73 (2003)

[9] C. E. Wieman, D. E. Pritchard, D. J. Wineland, Rev. Mod. Phys. **71**, 253 (1999)

[10] J. Weiner, V. S. Bagnato, S. Zilio, P. S. Julienne, Rev. Mod. Phys. **71**, 1 (2003)

[11] N. Balakrishnan, A. Dalgarno, Chem. Phys. Lett. **341**, 652 (2001)

[12] M. H. Andersen, J. R. Ensher, M. R. Matthews, C. E. Wieman, E. A. Cornell, Science **269**, 198 (1995)

[13] C. C. Bradley, C. A. Sackett, J. J. Tollett, R. G. Hulet, Phys. Rev. Lett. **75**, 1687 (1995)

[14] K. B. Davis, M. O. Mewes, M. R. Andrews, N. J. Druten, D. S. Durfee, D. M. Kurn, W. Ketterle, Phys. Rev. Lett. **75**, 3969 (1995)

[15] B. DeMarco, D. S. Jin, Science **285**, 1703 (1999)

[16] B. D. Esry, C. H. Greene, J. P. Burke, Phys. Rev. Lett. **83**, 1751 (1999)

[17] F. Dafolvo, S. Giorgini, L. P. Pitaevskii, S. Stringari, Rev. Mod. Phys. **71**, 463 (1999)

[18] J. T. Bahns, P. L. Gould, W. C. Stwalley, Adv. At. Mol. Opt. Phys. **42**, 171 (2000)

[19] P. D. Lett, P. S. Julienne, W. D. Phillips, Annu. Rev. Phys. Chem. **46**, 423 (1995)

[20] W. C. Stwalley, H. Wang, J. Mol. Spect. **195**, 194 (1999)

[21] R. Wynar, R. S. Freeland, D. J. Han, C. Ryu, D. J. Heinzen, Science **287**, 1016 (2000)

[22] E. R. I. Abraham, W. I. McAlexander, C. A. Sackett, R. G. Hulet, Phys. Rev. Lett. **74**, 1315 (1995)

[23] D. Jaksch, V. Venturi, J. I. Cirac, C. J. Williams, P. Zoller, Phys. Rev. Lett. **89**, 40402 (2002)

[24] U. Schlöder, C. Silber, C. Zimmermann, Appl. Phys. B **73**, 801 (2001)

[25] M. W. Mancini, G. D. Telles, A. R. L. Caires, V. S. Bagnato, L. G. Marcassa, Phys. Rev. Lett. **92**, 133203 (2004)

[26] A. J. Kerman, J. M. Sage, S. Sainis, T. Bergeman, D. DeMille, Phys. Rev. Lett. **92**, 153001 (2004)

[27] C. Haimberger, J. Kleinert, M. Bhattacharya, N. P. Bigelow, Phys. Rev. A **70**, 021402 (2004)

[28] E. A. Donley, N. R. Claussen, S. T. Thompson, C. E. Wieman, Nature **417**, 529 (2002)

[29] J. Herbig, T. Kraemer, M. Mark, T. Weber, C. Chin, H.-C. Nägerl, R. Grimm, Science **301**, 1510 (2003)

[30] D. S. Petrov, C. Salomon, G. V. Shlyapnikov, Phys. Rev. Lett. **93**, 090404 (2004)

[31] S. Jochim, M. Bartenstein, A. Altmeyer, G. Hendl, S. Riedl, C. Chin, J. H. Denschlag, R. Grimm, Science **302**, 2101 (2003)

[32] M. W. Zwierlein, C. A. Stan, C. H. Schnuck, S. M. F. Raupach, S. Gupta, Z. Hadzibabic, W. Ketterle, Phys. Rev. Lett. **91**, 250401 (2003)

[33] M. Greiner, C. A. Regal, D. S. Jin, Nature **426**, 537 (2003)

[34] J. D. Weinstein, R. deCarvalho, T. Guillet, B. Friedrich, J. M. Doyle, Nature **395**, 148 (1998)

[35] C. Zhu, N. Balakrishnan, A. Dalgarno, J. Chem. Phys. **115**, 1335 (2001)

[36] N. Balakrishnan, A. Dalgarno, R. C. Forrey, J. Chem. Phys. **113**, 621 (2000)

[37] N. Balakrishnan, R. C. Forrey, A. Dalgarno, Phys. Rev. Lett. **80**, 3224 (1998)

[38] Interactions of cold atoms and molecules, edited by P. Sóldan, J. M. Hutson, M. T. Cvitaš, C. S. Adams, CCP6 Daresbury (2002)

[39] M. Gupta, D. Herschbach, J. Phys. Chem. A **105**, 1626 (2001)

[40] M. S. Elioff, J. J. Valentini, D. W. Chandler, Science **302**, 1940 (2003)

[41] N. Balakrishnan, R. C. Forrey, A. Dalgarno, Chem. Phys. Lett. **280**, 1 (1997)

[42] N. Balakrishnan, V. Kharchenko, R. C. Forrey, A. Dalgarno, Chem. Phys. Lett. **280**, 5 (1997)

[43] R. C. Forrey, N. Balakrishnan, V. Kharchenko, A. Dalgarno, Phys. Rev. A **58**, 2645 (1998)

[44] D. D. Konowalow, M. L. Olson, Chem. Phys. **21**, 393 (1977); J. Chem. Phys. **71**, 450 (1979)

[45] U. Kaldor, Chem. Phys. **140**, 1 (1990)

[46] M. D. Halls, H. B. Schlegel, M. J. DeWitt, G. W. F. Drake, Chem. Phys. Lett. **339**, 427 (2001)

[47] L. Li, A. M. Lyrra, Spectrochimica Acta A **55**, 2147 (1999)

[48] C. Linton, F. Martin, A. J. Ross, I. Russier, P. Crozet, A. Yiannopoulou, L. Li, A. M. Lyrra, J. Mol. Spectrosc. **196**, 20 (1999); F. Martin, R. Bacis, J. Vergès, C. Linton, G. Bujin, C. H. Cheng, E. Stad, Spectrochimica Acta A **44**, 1369 (1988)

[49] C. Linton, T. L. Murphy, F. Martin, R. Bacis, J. Vèrges, J. Chem. Phys. **91**, 6036 (1989)

[50] W. T. Zemke, W. C. Stwalley, J. Phys. Chem. **97**, 2053 (1993)

[51] R. Côtè, A. Dalgarno, M. J. Jamieson, Phys. Rev. A **50**, 399 (1994)

[52] E. R. I. Abraham, N. W. M. Ritchie, W. I. McAlexander, R. G. Hulet, J. Chem. Phys. **103**, 7773 (1995)

[53] E. R. I. Abraham, W. I. McAlexander, H. T. C. Stoof, R. G. Hulet, Phys. Rev. A **53**, 3092 (1996)

[54] E. R. I. Abraham, W. I. McAlexander, J. M. Gerton, R. G. Hulet, R. Côtè, A. Dalgarno, Phys. Rev. A **55**, 3299 (1997)

[55] E. R. I. Abraham, W. I. McAlexander, J. M. Gerton, R. G. Hulet, R. Côtè, A. Dalgarno, Phys. Rev. A **53**, 3713 (1996)

[56] F. D. Colavecchia, J. P. Burke Jr., W. J. Stevens, M. R. Salazar, G. A. Parker, R. T Pack, J. Chem. Phys. **118**, 5484 (2003)

[57] W. Meyer, M. Keil, A. Kudell, M. A. Baig, W. Demtröder, J. Chem. Phys. **115**, 2590 (2001); M. Keil, H.-G. Krämer, A. Kudell, M. A. Baig, J. Zhu, W. Demtröder, W. Meyer, J. Chem. Phys. **113**, 7414 (2000); H.-G. Krämer, M. Keil, C. B. Suarez, W. Demtröder, W. Meyer, Chem. Phys. Lett. **99**, 212 (1999)

[58] R. T Pack, J. O. Hirschfelder, J. Chem. Phys. **49**, 4009 (1968); *ibid.* **52**, 521 (1969)

[59] F. Jensen, Introduction to computational chemistry, John Wiley & Sons (1999)

[60] P. Knowles, M. Schütz, H.-J. Werner, in Modern methods and algorithms in quantum chemistry, edited by J. Grotendorst, John von Neumann Institute for Computing, Jülich (2000)

[61] T. Helgaker, P. Jørgensen, J. Olsen, Molecular electronic-structure theory, John Wiley & Sons (2000)

[62] MOLPRO 2000.1 is a package of *ab initio* programs written by H.-J. Werner and P. Knowles with contribution form others.

[63] Gaussian 98, Revision A.9, M. J. Frisch, et al., Gaussian, Inc., Pittsburgh PA, 1998

[64] H.-J. Werner, P. J. Knowles, J. Chem. Phys. **82**, 5053 (1985); P. J. Knowles, H.-J. Werner, Chem. Phys. Lett. **115**, 259 (1985); H.-J. Werner, W. Meyer, J. Chem. Phys. **73**, 2342 (1980); H.-J. Werner, W. Meyer, J. Chem. Phys. **74**, 5794 (1981); H.-J. Werner, Adv. Chem. Phys. LXIX, 1 (1987)

[65] H.-J. Werner, P. J. Knowles, J. Chem. Phys. **89**, 5803 (1988); P. J. Knowles, H.-J. Werner, Chem. Phys. Lett. **145**, 514 (1988); H.-J. Werner, E. A. Reinsch, J. Chem. Phys. **76**, 3144 (1982); H.-J. Werner, Adv. Chem. Phys. LXIX, 1 (1987)

[66] P. J. Knowles, C. Hampel, H. J. Werner, J. Chem. Phys. **99**, 5219 and 2000 (1993), ibid. **112**, 3106 (Erratum); J. D. Watts, J. Gauss, R. J. Bartlett, J. Chem. Phys. **98**, 8718 (1993)

[67] EMSL Gaussian Basis Set Order Form, web site:
http://www.emsl.pnl.gov/forms/basisform.html

[68] P. W. Atkins, M. S. Child, C. S. G. Phillips, Tables for group theory, Oxford University Press (1988)

[69] T. J. Lee, P. R. Taylor, Int. J. Quantum Chem. Symp. **23**, 199 (1989)

[70] T. J. Lee, A. P. Rendell, P. R. Taylor, J. Phys. Chem. **94**, 5463 (1990)

[71] J. A. Klos, G. Chalasiński, M. M. Szcześniak, H.-J. Werner, J. Chem. Phys. **115**, 3085 (2001)

[72] B. M. Axilrod, E. Teller, J. Chem. Phys. **11**, 299 (1943)

[73] J. A. Barker, Mol. Phys. **57**, 755 (1986)

[74] V. F. Lotrich, K. Szalewicz, J. Chem. Phys. **106**, 9688 (1997)

[75] J. W. Kress, J. J. Carberry, G. C. Kuczynski, Mol. Phys. **36**, 717 (1978)

[76] I. G. Kaplan, J. Hernández-Cobos, I. Ortega-Blake, O. Novaro, Phys. Rev. A **53**, 2493 (1996)

[77] I. G. Kaplan, S. Roszak, J. Leszczynski, J. Chem. Phys. **113**, 6245 (2000)

[78] C. W. Bauschlicher, Jr., P. S. Bagus, B. N. Cox, J. Chem. Phys. **77**, 4032 (1982)

[79] P. Soldán, M. T. Cvitaš, J. M. Hutson, Phys. Rev. A **67**, 054702 (2003)

[80] J. Higgins, T. Hollebeek, J. Reho, T.-S. Ho, K. K. Lehmann, H. Rabitz, G. Scoles, M. Gutowski, J. Chem. Phys. **112**, 5751 (2000)

[81] I. Roeggen, J. Almlöf, J. Chem. Phys. **102**, 7095 (1995)

[82] A. E. Reed, R. B. Weinstock, F. Weinhold, J. Chem. Phys. **83**, 735 (1985)

[83] F. T. Smith, Phys. Rev. **179**, 111 (1969)

[84] C. A. Mead, D. G. Truhlar, J. Chem. Phys. **77**, 6090 (1982)

[85] A. J. Dobbyn, P. J. Knowles, Mol. Phys. **91**, 1107 (1997)

[86] T. H. Dunning, J. Chem. Phys. **90**, 1007 (1989)

[87] D. E. Woon, T. H. Dunning, J. Chem. Phys. **103**, 4572 (1995)

[88] M. A. Iron, M. Oren, J. M. L. Martin, Mol. Phys. **101**, 1345 (2003)

[89] cc-pCVXZ basis sets for alkali metals by M. A. Iron, M. Oren, J. M. L. Martin, web site: http://theochem.weizmann.ac.il/web/papers/group12.html

[90] Z.-C. Yan, G. W. F. Drake, Phys. Rev. A **52**, 3711 (1995)

[91] C. E. Moore, Atomic energy levels Vol. 1, U.S. National Bureau of Standards (1971)

[92] R. W. Molof, H. L. Schwartz, T. M. Miller, B. Bederson, Phys. Rev. A **10**, 1131 (1974)

[93] Z.-C. Yan, J. F. Babb, A. Dalgarno, G. W. F. Drake, Phys. Rev. A **54**, 2824 (1996)

[94] S. F. Boys, F. Bernardi, Mol. Phys. **19**, 553 (1970)

[95] Z.-C. Yan, A. Dalgarno, J. F. Babb, Phys. Rev. A **55**, 2882 (1997)

[96] W. H. Press, B. P. Flannery, S. A. Teukolsky, W. T. Vetterling, Numerical Recipes, Cambridge University Press (1988)

[97] C. Boisseau, E. Audouard, J. Vigué, Europhys. Lett. **41**, 349 (1998); C. Boisseau, E. Audouard, J. Vigué, V. V. Flambaum, Eur. Phys. J. D **12**, 199 (2000)

[98] M. Meuwly, J. M. Hutson, J. Chem. Phys. **110**, 8338 (1999)

[99] P. G. Hajigeorgiou, R. J. Le Roy, J. Chem. Phys. **112**, 3949 (2000); J. Y. Seto, R. J. Le Roy, J. Vergès, C. Amiot, J. Chem. Phys. **113**, 3067 (2000)

[100] G. C. Schatz, Rev. Mod. Phys. **61**, 669 (1989)

[101] T.-S. Ho, H. Rabitz, J. Chem. Phys. **104**, 2584 (1996)

[102] T. Hollebeek, T.-S. Ho, H. Rabitz, Annu. Rev. Phys. Chem. **50**, 537 (1999)

[103] P. Sóldan, J. M. Hutson, J. Chem. Phys. **112**, 4415 (2000)

[104] T.-S. Ho, H. Rabitz, J. Chem. Phys. **113**, 3960 (2000)

[105] A. J. C. Varandas, J. N. Murrell, Chem. Phys. Lett. **84**, 440 (1981)

[106] J. Hernández, I. G. Kaplan, J. N. Murrell, Mol. Phys **92**, 63 (1997)

[107] M. J. Cohen, J. N. Murrell, Chem. Phys. Lett. **260**, 371 (1996)

[108] T. Ishida, G. C. Schatz, J. Comput. Chem. **24**, 1077 (2003)

[109] J. Ischtwan, M. A. Collins, J. Chem. Phys. **100**, 8080 (1994)

[110] G. G. Maisuradze, D. L. Thompson, J. Phys. Chem. A **107**, 7118 (2003)

[111] T. Ishida, G. C. Schatz, J. Chem. Phys. **107**, 3558 (1997)

[112] T. Ishida, G. C. Schatz, Chem. Phys. Lett. **298**, 285 (1998)

[113] M. J. T. Jordan, K. C. Thompson, M. A. Collins, J. Chem. Phys. **103**, 9669 (1995)

[114] J. M. M. Howson, Ph.D. Thesis, University of Durham (1999)

[115] M. R. Salazar, Chem. Phys. Lett. **359**, 460 (2002)

[116] M. R. Salazar, R. L. Bell, J. Comput. Chem. **19**, 1431 (1998)

[117] J. Weiner, V. S. Bagnato, S. Zilio, P. S. Julienne, Rev. Mod. Phys. **71**, 1 (1999)

[118] A. D. Buckingham, P. W. Fowler, J. M. Hutson, Chem. Rev. **88**, 963 (1988)

[119] D. E. Stogryn, Mol. Phys. **22**, 81 (1971)

[120] P. Piecuch, Mol. Phys. **59**, 1067 (1986); **59**, 1085 (1986); **59**, 1097 (1986)

[121] A. J. Stone, The theory of intermolecular forces, Clarendon Press, Oxford (1996)

[122] S. H. Patil, K. T. Tang, J. Chem. Phys. **106**, 2298 (1997)

[123] M. Rérat, B. Bussery-Honvault, Mol. Phys. **101**, 373 (2003)

[124] R. J. Bell, J. Phys. B: Atom. Molec. Phys. **3**, 751 (1970)

[125] M. B. Doran, I. J. Zucker, J. Phys. C: Solid St. Phys **4**, 307 (1971)

[126] W. L. Bade, J. Chem. Phys. **28**, 282 (1958)

[127] M. Merawa, M. Rérat, B. Bussery-Honvault, J. Mol. Struc.-Theochem **633**, 137 (2003)

[128] G. A. Parker, R. B. Walker, B. K. Kendrick, R. T Pack, J. Chem. Phys. **117**, 6083 (2002)

[129] K. T. Tang, J. P. Toennies, J. Chem. Phys. **80**, 3726 (1984)

[130] T. I. Sachse, K. T. Tang, J. P. Toennies, Chem. Phys. Lett. **317**, 346 (2000); A. R. Cooper, J. M. Hutson, J. Chem. Phys. **98**, 5337 (1993); M. Bulski, G. Chalasinski, J. Chem. Phys. **86**, 936 (1987)

[131] W. L. Bade, J. Chem. Phys. **27**, 1280 (1957)

[132] R. J. Wheatley, W. J. Meath, Mol. Phys. **80**, 25 (1993); P. J. Knowles, W. J. Meath, Chem. Phys. Lett. **124**, 164 (1986)

[133] A. Kuppermann, G. C. Schatz, J. Chem. Phys. **62**, 2502 (1975)

[134] G. C. Schatz, J. Phys. Chem. **100**, 12839 (1996)

[135] G. A. Parker, R. T Pack, B. J. Archer, R. B. Walker, Chem. Phys. Lett. **137**, 564 (1987)

[136] J.-M. Launay, M. Le Dourneuf, Chem. Phys. Lett. **163**, 178 (1989)

[137] R. T Pack, G. A. Parker, J. Chem. Phys **87**, 3888 (1987)

[138] J.-M. Launay, M. Le Dourneuf, Chem. Phys. Lett. **169**, 473 (1990)

[139] D. Skouteris, J. F. Castillo, D. E. Manolopoulos, Comput. Phys. Comm. **133**, 128 (2000)

[140] F. T. Smith, J. Chem. Phys. **31**, 1352 (1959)

[141] R. N. Zare, Angular momentum, John Wiley & Sons (1988)

[142] B. R. Johnson, J. Chem. Phys. **73**, 5051 (1980)

[143] B. R. Johnson, J. Chem. Phys. **79**, 1906, 1916 (1980)

[144] F. T. Smith, Phys. Rev. **120**, 1058 (1960)

[145] A. M. Arthurs, A. Dalgarno, Proc. R. Soc. Lond. A **256**, 540 (1960)

[146] J. J. Sakurai, Modern quantum mechanics, Addison-Wesley Publishing Company (1994)

[147] R. T Pack, J. Chem. Phys. **60**, 633 (1974)

[148] M. S. Child, Molecular collision theory, Dover Publications (1996)

[149] V. Fock, D. Kon. Nors. Vidensk. Selsk. Forh. **31**, 138 (1958)

[150] J. M. Hutson, Comp. Phys. Comm. **84**, 1 (1994)

[151] B. R. Johnson, J. Chem. Phys. **69**, 4678 (1978)

[152] E. B. Stechel, R. B. Walker, J. C. Light, J. Chem. Phys **69**, 3518 (1978)

[153] B. R. Johnson, J. Comput. Phys. **13**, 445 (1973); F. Mrugala, D. Secrest, J. Chem. Phys. **79**, 5960 (1983); D. E. Manolopoulos, J. Chem. Phys. **85**, 6425 (1986); M. H. Alexander, D. E. Manolopoulos, J. Chem. Phys **86**, 2044 (1987)

[154] F. D. Colavecchia, F. Mrugala, G. A. Parker, R. T Pack, J. Chem. Phys **118**, 10387 (2003)

[155] D. E. Manolopoulos, Ph. D. Thesis, University of Cambridge (1988)

[156] C. J. Joachain, Quantum collision theory, Elsevier Science Publishers (1983)

[157] L. D. Landau, E. M. Lifshitz, Quantum mechanics (Non-relativistic theory), Butterworth Heinemann (1977)

[158] E. P. Wigner, Phys. Rev. **73**, 1002 (1948)

[159] H. R. Sadeghpour, J. L. Bohn, M. J. Cavagnero, B. D. Esry, I. I. Fabrikant, J. H. Macek, A. R. P. Rau, J. Phys. B: At. Mol. Opt. Phys. **33**, 93 (2000)

[160] U. Fano, A. R. P. Rau, Atomic collisions and spectra, Academic Press (1986)

[161] T.-Y. Wu, T. Ohmura, Quantum theory of scattering, Prentice-Hall International (1962)

[162] G. F. Gribakin, V. V. Flambaum, Phys. Rev. A **48**, 546 (1993)

[163] C. J. Ashton, M. S. Child, J. M. Hutson, J. Chem. Phys. **78**, 4025 (1983)

[164] R. D. Levine, R. B. Bernstein, Molecular reaction dynamics, Oxford University Press (1974)

[165] J. Cubizolles, T. Bourdel, S. J. J. M. F. Kokkelmans, G. V. Shlyapnikov, C. Salomon, Phys. Rev. Lett. **91**, 240401 (2003)

[166] P. D. Lett, K. Helmerson, W. D. Phillips, L. P. Ratliff, S. L. Rolston, M. E. Wagshul, Phys. Rev. Lett. **71**, 2200 (1993)

[167] K. Xu, T. Mukaiyama, J. R. Abo-Shaeer, J. K. Chin, D. E. Miller, W. Ketterle **91**, 210402 (2003)

[168] H. Wang, P. L. Gould, W. C. Stwalley, Phys. Rev. A **53**, R1216 (1996)

[169] C. A. Regal, C. Ticknor, J. L. Bohn, D. S. Jin, Nature **424**, 47 (2003)

[170] J. D. Miller, R. A. Cline, D. J. Heinzen, Phys. Rev. Lett. **71**, 2204 (1993)

[171] S Dürr, T. Volz, A. Marte, G. Rempe, Phys. Rev. Lett. **92**, 020406 (2004)

[172] A. Fioretti, D. Comparat, A. Crubellier, O. Dulieu, F. Masnou-Seeuws, P. Pillet, Phys. Rev. Lett. **80**, 4402 (1998)

[173] K. E. Strecker, G. B. Partridge, R. G. Hulet, Phys. Rev. Lett. **91**, 080406 (2003)

[174] C. A. Regal, M. Greiner, D. S. Jin, Phys. Rev. Lett. **92**, 83201 (2004)

[175] S. Jochim, M. Bartenstein, A. Altmeyer, G. Hendl, C. Chin, J. H. Denschlag, R. Grimm, Phys. Rev. Lett. **91**, 240402 (2003)

[176] J. Stenger, S. Inouye, W. R. Andrews, H. J. Miesner, D. M. Stamper-Kurn, W. Ketterle, Phys. Rev. Lett. **82**, 2422 (1999)

[177] T. Mukaiyama, J. R. Abo-Shaeer, K. Xu, J. K. Chin, W. Ketterle, Phys. Rev. Lett. **92**, 180402 (2004)

[178] D. W. Schwenke, D. G. Truhlar, J. Chem. Phys. **83**, 3454 (1985)

[179] R. C. Forrey, N. Balakrishnan, A. Dalgarno, M. R. Haggerty, E. J. Heller, Phys. Rev. Lett. **82**, 2657 (1999)

[180] R. C. Forrey, Phys. Rev. A **63**, 051403 (2001)

[181] E. Bodo, F. A. Gianturco, A. Dalgarno, Chem. Phys. Lett. **353**, 127 (2002)

[182] P. M. Florian, M. Hoster, R. C. Forrey, Phys. Rev. A **70**, 032709 (2004)

[183] N. Balakrishnan, A. Dalgarno, J. Phys. Chem. A **105**, 2348 (2001)

[184] K. Tilford, M. Hoster, P. M. Florian, R. C. Forrey, Phys. Rev. A **69**, 052705 (2004)

[185] J. C. Flasher, R. C. Forrey, Phys. Rev. A **65**, 032710 (2002)

[186] T. Stoecklin, A. Voronin, J. C. Rayez, Chem. Phys. **294**, 117 (2003)

[187] T. Stoecklin, A. Voronin, J. C. Rayez, Phys. Rev. A **68**, 032716 (2003)

[188] T. Stoecklin, A. Voronin, J. C. Rayez, Phys. Rev. A **66**, 042703 (2002)

[189] E. Bodo, F. A. Gianturco, A. Dalgarno, J. Chem. Phys. **116**, 9222 (2002)

[190] E. Bodo, F. A. Gianturco, A. Dalgarno, J. Phys. B: At. Mol. Opt. Phys. **35**, 2391 (2002)

[191] N. Balakrishnan, A. Dalgarno, J. Phys. Chem. A **107**, 7101 (2003)

[192] E. Bodo, F. A. Gianturco, N. Balakrishnan, A. Dalgarno, J. Phys. B: At. Mol. Opt. Phys. **37**, 3641 (2004)

[193] T. Stoecklin, A. Voronin, J. C. Rayez, Chem. Phys. **298**, 175 (2004)

[194] E. Bodo, E. Scifoni, F. Sebastianelli, F. A. Gianturco, A. Dalgarno, Phys. Rev. Lett. **89**, 283201 (2002)

[195] R. C. Forrey, Phys. Rev. A **66**, 023411 (2002)

[196] P. Soldán, M. T. Cvitaš, J. M. Hutson, P. Honvault, J.-M. Launay, Phys.Rev. Lett. **89**, 153201 (2002)

[197] P. R. Bunker, P. Jensen, Molecular Symmetry and Spectroscopy, NRC Research Press Ottawa (1998)

[198] A. Färbert, W. Demtröder, Chem. Phys. Lett. **264**, 225 (1997)

[199] B. Bussery-Honvault, P. Honvault, J.-M. Launay, J. Chem. Phys. **115**, 10701 (2001)

[200] J. M. Hutson, C. J. Ashton, R. J. Le Roy, J. Phys. Chem. **87**, 2713 (1983)

[201] R. Schinke, P. McGuire, J. Chem. Phys. **71**, 4201 (1979)

[202] P. Honvault, J.-M. Launay, J. Chem. Phys. **111**, 6665 (1999)

[203] P. Honvault, J.-M. Launay, J. Chem. Phys. **114**, 1057 (2001)

[204] F. J. Aois, L. Bañares, J. F. Castillo, M. Brouard, W. Denzer, C. Vallance, P. Honvault, J.-M. Launay, A. J. Dobbyn, P. J. Knowles, Phys. Rev. Lett. **86**, 1729 (2001)

[205] P. Honvault, J.-M. Launay, Chem. Phys. Lett. **370**, 371 (2003)

[206] B. Stewart, P. D. Magill, T. P. Scott, J. Derouard, D. E. Pritchard, Phys. Rev. Lett. **60**, 282 (1988); P. D. Magill, B. Stewart, N. Smith, D. E. Pritchard, Phys. Rev. Lett. **60**, 1943 (1988)

[207] W. J. Hoving, R. Parson, Chem. Phys. Lett. **158**, 222 (1989)

[208] A. Derevianko, W. R. Johnson, M. S. Safranova, J. F. Babb, Phys. Rev. Lett. **82**, 3589 (1999)

[209] F. X. Gadea, T. Leininger, A. S. Dickinson, Eur. Phys. J. D **15**, 251 (2001); F. X. Gadea, T. Leininger, A. S. Dickinson, J. Chem. Phys. **117**, 7122 (2002); A. S. Dickinson, F. X. Gadea, T. Leininger, J. Phys. B **37**, 587 (2004)

[210] G. Quéméner, P. Honvault, J.-M. Launay, Eur. Phys. J. D **30**, 201 (2004)